

Proceedings of the Cardiff University Engineering Research Conference 2023

EDITORS

Emiliano Spezi
Michaela Bray

Proceedings of the Cardiff University Engineering Research Conference 2023



School of Engineering

Ysgol Peirianeg

EDITORS

Emiliano Spezi
Michaela Bray

Proceedings of the Cardiff University Engineering Research Conference 2023 is an open access publication from Cardiff University Press, which means that all content is available without charge to the user or his/her institution. You are allowed to read, download, copy, distribute, print, search, or link to the full texts of the articles in this publication without asking prior permission from the publisher or the author.

Original copyright remains with the contributing authors and a citation should be made when all or any part of this publication is quoted, used or referred to in another work.

E. Spezi and M. Bray, *Proceedings of the Cardiff University Engineering Research Conference 2023*, Cardiff University School of Engineering, Cardiff, UK, 2024.
doi.org/10.18573/conf1

Cardiff University Engineering Research Conference 2023 was organised by the School of Engineering and held from 12 to 14 July 2023 at Cardiff University.

The work presented in these proceedings has been peer reviewed and approved by the conference organisers and associated scientific committee to ensure high academic standards have been met.

First published 2024

Cardiff University Press
Cardiff University, PO Box 430
1st Floor, 30-36 Newport Road
Cardiff CF24 0DE

cardiffuniversitypress.org

Editorial design and layout by
Academic Visual Communication

ISBN: 978-1-9116-5349-3 (PDF)



This work is licensed under the Creative Commons Attribution - NoCommercial - NoDeriv 4.0 International licence.

This license enables reusers to copy and distribute the material in any medium or format in unadapted form only, for noncommercial purposes only, and only so long as attribution is given to the creator.

<https://creativecommons.org/licenses/by-nc-nd/4.0/>

Contents

Engineering for Health

- 3 Generalizability of Deep Learning Models on Brain Tumour Segmentation
- 6 A Tool for Radiotherapy Plan Evaluation Analysis: generalise Uniform Ideal Dose (gUIDE)
- 11 Investigating the Feasibility of MRI Auto-segmentation for Image Guided Brachytherapy
- 15 Label-free Volumetric Imaging of Synthetic Cell Chassis using Optical Coherence Tomography
- 19 Evaluation of Radiomic Analysis over the Comparison of Machine Learning Approach and Radiomic Risk Score on Glioblastoma
- 23 Inter-planner Variability in Expert Driven Pareto-guided Automated Planning Solutions

Civil Infrastructure

- 29 A 3D Coupled Finite Element Model for Self-Healing Quasi-Brittle Materials
- 34 Pinball Tendons Crack Closure Technology
- 39 Smart Activation System for the Hybrid Tendons Crack Closure Technology
- 44 3D-Printed Mini-vascular Networks for Self-healing Lime-based Mortars
- 48 Agricultural Waste as a Cementitious Material — Rice Husk Ash
- 52 Waste Foundry Sand (WFS) as Aggregate Replacement for Green Concrete
- 55 Biomimetic Materials in Construction Industry: the Necessity of Simulation
- 58 Characterisation of Innovative Mortar Formulations for the Restoration of Roman Mosaics
- 62 Modelling Buildings During Flood Inundation Using TELEMAC-2D
- 66 Shrinkage Potential and Water Transport Properties of Self-compacting Concrete at Different Temperatures
- 70 Determining Surface Velocity Coefficients in Headwater Streams for Natural Flood Management
- 75 Simulating Flood Hazard in Wye Valley during Storm Dennis using Hec-Ras
- 80 Influence of Healing Agents and Concrete Environment on PLA 3D Printed Mini-vascular Networks for Self-healing Concrete Structures

Advanced Manufacturing

- 86 Accelerating Multi-step Sparse Reward Reinforcement Learning
- 91 Safety for Human-Robot Interaction with a Shared Autonomy
- 95 A Novel Hybrid Bees Regression Convolutional Neural Network (BA-RCNN) Applied to Porosity Prediction in Selective Laser Melting Parts
- 100 The Research on Mechanical Properties and Compressive Behavior of Graphene Foam with Multi-scale Model
- 105 Developing Antibacterial Nanocomposites
- 109 Microwave Resonator-based Microfluidic Sensors Fabricated Using 3D-Printing Technology
- 113 Using DCGAN and WGAN-GP to Generate Artificial Thermal RGB Images for Induction Motors
- 118 Altering the Tribological Properties of Laser Powder Bed Fusion Materials through Various Methods: A Review
- 123 Development of a Net Zero Route for the Circular Production of Additive Manufacturing Powders
- 128 A Study on the Surface Chemistry of Laser Textured Parts

Sustainable Energy

- 135 Modelling and Simulation of a Hydrogen-Based Energy Storage System
- 140 Acoustic Noise Emission Detection and Location Analysis from a Scaled Laminated Transformer
- 145 Measuring the Coupled Effect of Heat and Stress on the Magnetic Properties of Electrical Steel
- 148 Development of a Multi-Community Peer-to-Peer Electricity Trading Mechanism
- 153 Double-ended Fault Location Method with Reduced Measurements
- 158 Spectroscopic Measurements of Light Emissions from High Current Arcs
- 163 Influence of Fuel Hydrogen Content and Atomisation Quality on Ultrafine Non-volatile Particulate Matter Emissions in RQL Gas Turbine Technology
- 168 Numerical Wave Flume with Lattice Boltzmann Method for Wave Energy Converters
- 173 Mathematical Modelling to Optimise an Urban Electric Vehicle Charging System
- 176 Plasma-assisted Ammonia Combustion: The Effect of Equivalence Ratio on NO Emissions
- 181 Exploring the Potential of Ammonia/Hydrogen Trigenation Cycle

Compound Semiconductors and Applications

- 187 Numerical Investigation of Size Effects in Tension and Torsion of Micro-scale Copper Wires using a Strain Gradient Modified Johnson-Cook Constitutive Model
- 191 Electro-Thermal Coupling for Simulation of 52 kV Polymeric Bushing with Nonlinear ZnO Microvaristor Under Different Environmental Conditions

Foreword

It is with great pleasure that we welcome you to the Proceedings of the Cardiff University Engineering Research Conference 2023. The conference was established for the first time in 2023 as part of a programme to sustain the research culture, environment, and dissemination activities of the School of Engineering at Cardiff University in the United Kingdom. The conference served as a platform to celebrate advancements in various engineering domains researched at our School, explore and discuss further advancements in the diverse fields that define contemporary engineering.

The structure of the conference programme reflected the multidimensional nature of our research and was built around the priority research areas for the School:

Engineering for Health forms a cornerstone of our discussions, recognizing the pivotal role technology plays in revolutionizing healthcare. We are applying the latest research in medical engineering to push the boundaries in areas where innovation has the potential to transform patient care.

Civil Infrastructure takes centre stage as we improve the sustainability and resilience of infrastructure across the UK and the globe. We work on developing sustainable and resilient total lifecycle solutions across a wide range of domains including construction, structures, energy, geo-environmental and water infrastructure systems. From creating new nano-scale smart materials to macro-scale urban interventions.

Advanced Manufacturing represents cutting-edge research into materials, systems and transformative technologies to transform engineering and economic performance in the transport, energy generation and manufacturing industries. Our research in this area focuses on developing smart materials and structures, and sustainable manufacturing processes that help create a sustainable and greener economy.

Sustainable Energy stands as a testament to our commitment to a greener, more efficient future. We aim to advance energy technology and play a key role in addressing the increasing demand for sustainable and low carbon technologies while reducing environmental impact and ensuring a sustainable environment. Our work helps to drive forward net-zero solutions for achieving the government carbon targets.

Compound Semiconductors and Applications represents the cutting edge of electronics, a critical driver of progress in the digital age. We explore the latest developments in compound semiconductor materials, advanced characterisation techniques, quantum optics and novel circuit design methodologies and their diverse applications. We anticipate breakthroughs that will power the next generation of computing, communication, and sensing technologies.

These proceedings are a testament to the shared vision of engineers and researchers from our School as they are working to address the challenges of today and set a course towards a brighter tomorrow. We extend our gratitude to all participants, presenters, and sponsors for their invaluable contributions to this endeavour and look forward to hosting this event again in 2024.

Professor Emiliano Spezi
Organizing Committee Chair
Cardiff University School of Engineering
Research Conference 2023

Dr Michaela Bray
Organizing Committee Deputy Chair
Cardiff University School of Engineering
Research Conference 2023

Acknowledgements

We gratefully acknowledge everyone who has contributed to the conference through their participation and submission of papers as well as our many colleagues that have organised, reviewed, and made possible the rich diversity of interests and high standards represented by this event.

Particular thanks is given to the Conference Organising Committee and to the Scientific Committee, as well as to Cardiff University Press for supporting the publication of these proceedings.

CONFERENCE ORGANISING COMMITTEE

Emiliano Spezi (<i>Chair</i>)	Arif Mohammad
Michaela Bray (<i>Deputy Chair</i>)	Debajyoti Bhaduri
Julia Kennedy	Mo Alnajideen
Saif Sami	Jose Hernandez
Geraint Lewis	Yue Zhou
Gina Goddard-Bell	Morteza Shafiekhani

CONFERENCE SCIENTIFIC COMMITTEE

Agustin Valera Medina (<i>Chair</i>)	David Kennedy
Daniel Pugh	Michael Packianather
Sam Evans	Heungjae Choi

CONFERENCE EVENT SUPPORT

Samantha Jones	Bryn Walton
Daiana Condrea	Sina Sayadi Moghadam
Han Wei	Yali Jiang
Ahmad Alhamdan	

Engineering for Health



Engineering for Health

- 3 Generalizability of Deep Learning Models on Brain Tumour Segmentation
- 6 A Tool for Radiotherapy Plan Evaluation Analysis: generalise Uniform Ideal Dose (gUIDE)
- 11 Investigating the Feasibility of MRI Auto-segmentation for Image Guided Brachytherapy
- 15 Label-free Volumetric Imaging of Synthetic Cell Chassis using Optical Coherence Tomography
- 19 Evaluation of Radiomic Analysis over the Comparison of Machine Learning Approach and Radiomic Risk Score on Glioblastoma
- 23 Inter-planner Variability in Expert Driven Pareto-guided Automated Planning Solutions

Duman A

*Cardiff University
School of Engineering*

Sun X

*Cardiff University
School of Computer Science and Informatics*

Powell J

*Velindre NHS Trust
Department of Oncology, Cardiff*

Spezi E

*Cardiff University
School of Engineering*

Thomas S

*Velindre NHS Trust
Department of Oncology, Cardiff*

ENGINEERING FOR HEALTH

Generalizability of Deep Learning Models on Brain Tumour Segmentation

Brain tumour segmentation is a hard and time-consuming task to be conducted in the process of radiotherapy planning. Deep Learning (DL) applications have a significant improvement in image segmentation tasks. In this work, we apply DL models such as 2D and 2.5D U-NET to the segmentation task of a brain tumour on the BraTS 2021 dataset and our local dataset. The 2.5D network is a modified version of 2D U-NET by using three slices as an input for each magnetic resonance imaging (MRI) sequence. We achieve the best segmentation results with 2.5D U-NET on BraTS with Dice scores of 86.97%, 91.27% and 94.42% for enhancing tumour, tumour core and whole tumour respectively. On the other hand, our best segmentation result of the GTV delineation on the local dataset is a Dice score of 78.51% for 2D U-NET. Although the result of GTV contours is not improved by 2.5D for the local dataset due to non-fixed voxel size, the Dice scores of ET, TC and WT are improved by the proposed 2.5D U-NET for the BraTS dataset.

*Keywords:
Glioblastoma, autosegmentation,
brain tumour segmentation,
radiotherapy planning.*

*Corresponding author:
DumanA@cardiff.ac.uk*



A. Duman , J. Powell, S. Thomas, X. Sun, and E. Spezi, ‘Generalizability of Deep Learning Models on Brain Tumour Segmentation’, *Cardiff University School of Engineering Research Conference 2023*, Cardiff, UK, 2023, pp. 3-5.

doi.org/10.18573/conf1.b

INTRODUCTION

Brain tumours are one of the most lethal types of cancer [1]. Glioblastoma (GBM) is a aggressive, rapidly developing and fatal type of glioma that originates from glial cells. The median survival time for GBM patients is 15 months after diagnosis [2]. Brain tumour segmentation is the process of separating the tumour from healthy brain tissue. Brain tumour segmentation is a challenging task due to the heterogeneous nature of the tumour tissue [3] and Magnetic Resonance Imaging (MRI) is a commonly used imaging technique in brain because it provides high-quality, high-contrast and detailed images of soft tissues. Accurate tumour segmentation is critical for diagnosis and therapy planning [4]. In radiotherapy, the optimal delivery of high-dose radiation to the tumour while sparing healthy tissues depends on the accuracy of segmentation. Manual segmentation is time-consuming, subjective, and non-reproducible. Automated segmentation is proposed to decrease labour-intensive work, provides objective and reproducible results [5]. Deep Learning (DL) models are one of solutions developed to segment tumours automatically.

In clinical practice the poor generalizability of DL models is a major barrier [6]. Particularly for medical image segmentation tasks, models have demonstrated good performance when using uniform datasets, but their ability to generalise to new and unseen data remains a challenge. In brain tumour segmentation, the generalizability of DL models needs to be evaluated for different datasets consisting of MRI scans with variable settings such as resolution (pixel spacing and slice thickness) and matrix size. Such validation is essential for enhancing the robustness and usefulness of DL models in clinical applications. Ideally, models with high generalizability could be developed when training datasets contain a significant number of high-quality images from different centres using variety of imaging settings.

Despite high number of publications dealing with DL-based tasks including segmentation, due to generalizability as a primary issue, the models transferred to clinic are very few [7]. In this study, we investigated the generalizability of DL models with different configurations on GBM segmentation task across different datasets.

MATERIALS AND METHODS

In this study we utilised a large dataset of publicly accessible MRI scans and reference segmentations (BraTS 2021) and a local dataset. GBMs are segmented according to the BraTS challenge as enhancing tumour (ET), tumour core (TC), and entire tumour (WT) regions [8]. The BraTS 2021 dataset has a fixed voxel size (1x1x1mm) and fixed matrix size (240x240x155). However, clinical datasets including our local glioma scans have variable voxel sizes and matrix sizes for each MRI sequence.

In this research, we used U-NET, a convolutional neural network architecture designed for biomedical image segmentation tasks. The U-NET architecture consists of an encoder network, which down samples the input image extracting salient features, and a decoder network, which up samples the feature maps back to the original image resolution and generates the segmentation mask. This arrangement gives the network its characteristic U shape [9]. Tumour segmentation was carried out using a region-focused selection (RFS) method [10] that combines several single 2D U-NET and 2.5D U-NET architectures trained on BraTS tumour regions and validated with Gross Tumour

Volumes (GTV) of the local dataset. Fig. 1 shows 4 image sequences namely: FLAIR, T1, T1ce and T2. The BraTS and the local dataset cover 1251 patients and 53 patients respectively.

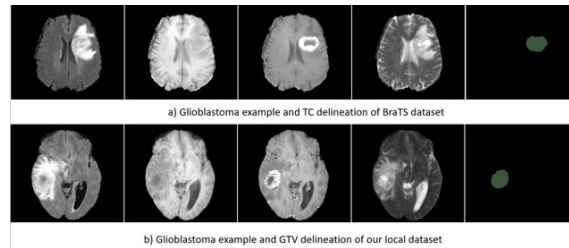


Fig. 1. Examples in BraTS 2021 (Fig. 1a) and our local dataset (Fig. 1b). From left to right; FLAIR, T1, T1ce, T2 sequences and their corresponding segmentation masks.

In the 2.5D model, for each sequence we used 3 channels including: (a) current slice (n), (b) previous slice (n-1) and (c) following slice (n+1). This is shown in Fig. 2. Due to the local dataset having different voxel and matrix sizes for each patient, each scan of the local dataset was resampled to match the BraTS 2021 data format and specifications. Each channel used a 2D image of size (240x240).

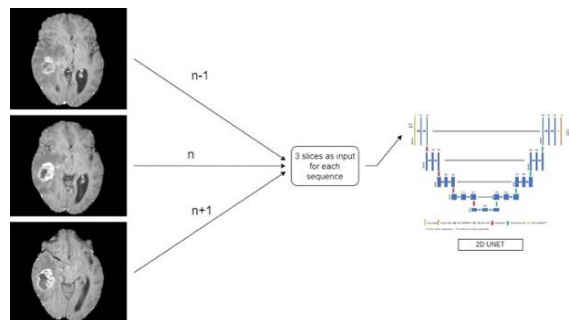


Fig. 2. A 3-slice example of the T1ce sequence for the local dataset.

The RFS method use three types of U-NET models for image segmentation, i.e., Binary class, Multi-label, and Multiclass models. In the case of binary-class models, three separate binary-class models were used for segmenting three regions (ET, TC, and WT), separately. The input and output of each binary-class model corresponded to only one of the regions. In both cases of multilabel and multiclass models, only a single model was used for the segmentation of all the three regions. The difference between the multilabel and multiclass models is that the former uses the overlapping class masks among ET, TC and WT, while the latter takes non-overlapping class masks. Both binary and multilabel models used the sigmoid function, while the multiclass model used the softmax function at the last layer of the U-NET.

The z-score technique was used to normalise images. Multiclass, Multi-label, and Binary class single 2D and 2.5D U-NET architectures were trained on individual tumour regions with the BraTS 2021 dataset. The Dice Similarity Coefficient (DSC) was utilised to assess the similarity between the contours generated by the DL models and the reference contours.

The trained models were then combined with a union RFS (u-RFS) model. The u-RFS model was used to improve the DL-based GTV segmentation for both 2D and 2.5D models.

RESULTS

For our local dataset, the comparison of 2D U-NET and 2.5D U-NET predictions is shown in Fig. 3.

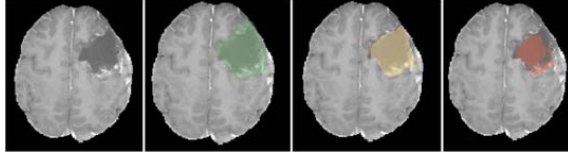


Fig. 3. GTV segmentation of the local dataset. From left to right; T1ce sequence, reference contour, 2D U-NET prediction and 2.5D U-NET prediction for.

In Table 1, the results show that 2.5D U-NET models outperform 2D U-NET models for each DL method and for both ET and WT regions.

DL method	ET(%) (2D)	ET(%) (2.5D)	WT(%) (2D)	WT(%) (2.5D)
Multiclass	84.99	86.76	91.65	93.81
Multilabel	82.29	84.01	92.24	94.42
Binary class	85.19	86.97	92.18	94.35

Table 1. DSC results of ET and WT (BraTS dataset).

In Table 2, the results show that 2.5D U-NET models outperform 2D U-NET models for the TC region. However, the 2D model outperforms the 2.5D model for the GTV region. u-RFS provided the best DSC score with 78.51% when applied to the 2D model.

DL method	TC(%) (2D)	TC(%) (2.5D)	GTV(%) (2D)	GTV(%) (2.5D)
Multiclass	89.71	91.27	78.43	70.35
Multilabel	87.27	88.78	77.91	69.88
Binary class	89.48	91.03	78.22	70.16
u-RFS		78.51	70.42	

Table 2. DSC results for TC (BraTS dataset) and for GTV (local dataset).

DISCUSSION AND CONCLUSIONS

The results presented in this work show that 2.5D models outperform 2D models for the segmentation of GBM on the BraTS dataset. This is because of the additional information provided by the imaging data feeding into the 3 channels used in the model equating to 12 channels in total compared to 4 channels used in the 2D model. However, the 2.5D model did not generalise well when applied to our local dataset that included scans with different voxel and matrix sizes compared to the BraTS 2021 dataset.

If only one model will be developed, the RFS method can be utilised for the selection of the best method when considering only one region. The u-RFS method proved to be useful in improving the performance of both 2D and 2.5D models. The u-RFS can be applied to any DL model to increase segmentation results.

Acknowledgments

This work was sponsored by the Turkish Ministry of National Education.

Conflicts of interest

The authors have no conflict of interest to declare.

REFERENCES

- [1] L. M. DeAngelis, 'Brain Tumors', *N Engl J Me*, vol. 344, no. 2, pp. 114–123, 2001. doi.org/10.1056/nejm200101113440207
- [2] R. L. Siegel, K. D. Miller, and A. Jemal, 'Cancer statistics, 2019', *CA Cancer J Clin*, vol. 69, no. 1, pp. 7–34, Jan. 2019. doi.org/10.3322/CAAC.21551
- [3] S. Bakas *et al.*, 'Advancing The Cancer Genome Atlas glioma MRI collections with expert segmentation labels and radiomic features', *Sci Data*, vol. 4, no. 1, p. 170117, 2017. doi.org/10.1038/sdata.2017.117
- [4] P. Kickingereder *et al.*, 'Automated quantitative tumour response assessment of MRI in neuro-oncology with artificial neural networks: a multicentre, retrospective study', *Lancet Oncol*, vol. 20, no. 5, pp. 728–740, May 2019. doi.org/10.1016/S1470-2045(19)30098-1
- [5] G. P. Mazzara, R. P. Velthuizen, J. L. Pearlman, H. M. Greenberg, and H. Wagner, 'Brain tumor target volume determination for radiation treatment planning through automated MRI segmentation', *Int J Radiat Oncol Biol Phys*, vol. 59, no. 1, pp. 300–312, 2004. doi.org/10.1016/j.ijrobp.2004.01.026
- [6] K. Yasaka and O. Abe, 'Deep learning and artificial intelligence in radiology: Current applications and future directions', *PLoS Med*, vol. 15, no. 11, p. e1002707, 2018. doi.org/10.1016/j.ijrobp.2004.01.026
- [7] C. J. Kelly, A. Karthikesalingam, M. Suleyman, G. Corrado, and D. King, 'Key challenges for delivering clinical impact with artificial intelligence', *BMC Med*, vol. 17, no. 1, p. 195, 2019. doi.org/10.1186/s12916-019-1426-2
- [8] B. H. Menze *et al.*, 'The Multimodal Brain Tumor Image Segmentation Benchmark (BRATS)', *IEEE Trans Med Imaging*, vol. 34, no. 10, pp. 1993–2024, 2015. doi.org/10.1109/TMI.2014.2377694
- [9] O. Ronneberger, P. Fischer, and T. Brox, 'U-net: Convolutional networks for biomedical image segmentation', in *International Conference on Medical image computing and computer-assisted intervention*, 2015, pp. 234–241. doi.org/10.1007/978-3-319-24574-4_28
- [10] A. Duman, P. Whybra, J. Powell, S. Thomas, X. Sun, and E. Spezi, 'Transferability of deep learning models to the segmentation of gross tumour volume in brain cancer', in *ESTRO 2023 Conference (Accepted)*, 2023.

Cagni E

Cardiff University, School of Engineering
Azienda USL-ICCS di Reggio Emilia

Lewis A

Cardiff University
School of Computer Science and Informatics

Valeria T

Azienda USL-ICCS di Reggio Emilia

Spezi E

Cardiff University
School of Engineering

Andrea B

Azienda USL-ICCS di Reggio Emilia

ENGINEERING FOR HEALTH

A Tool for Radiotherapy Plan Evaluation Analysis: generalise Uniform Ideal Dose (gUIDE)

In radiotherapy, treatment planning is the process in which the appropriate dose distribution is planned for a specific patient. However, there is no consensus on what the 'optimal' plan should be and on how to measure plan quality. The purpose of this study was to develop a tool called a 'generalized Uniform Ideal Dose' (gUIDE) that produces an 'ideal' dose distribution based on single patient anatomy and dose prescription. By comparing the clinical achieved dose distribution with gUIDE a quantitative measure of plan quality can be derived. gUIDE is based on an exponential function of dose fall-off outside the tumor volume. The algorithm does not require any specification of the treatment machine but only patient geometry information. gUIDE fall-off parameter was properly derived in a simple geometry dose profile. Overall, gUIDE showed a lower DVH than the DVH generated using the clinical treatment planning system, as it was expected for a baseline ideal condition. In the clinical validation, although the statistical test showed significant differences between the two groups, overall values were similar for all structures between gUIDE and PlanIQ. A baseline dose gUIDE was implemented, optimised and evaluated. gUIDE could be accurate enough to be used as baseline to help in the plan evaluation process.

Keywords:

Radiotherapy, medical physics, dose distribution, treatment plan evaluation, radiotherapy plan comparison, machine learning.

Corresponding author:

CagniE@cardiff.ac.uk



E. Cagni, V. Trojani, A. Botti, G. Lewis, and E. Spezi, 'A Tool for Radiotherapy Plan Evaluation Analysis: generalise Uniform Ideal Dose (gUIDE)', *Cardiff University School of Engineering Research Conference 2023*, Cardiff, UK, 2023, pp. 6-10.

doi.org/10.18573/conf1.c

INTRODUCTION

There are several steps in the radiotherapy process, where human actions can bring variability in the quality of the delivered treatment. One example lies in contouring variations among radiation oncologists in defining organs at risk (OARs) and tumour areas (target) on the planning CT images of the patient. Concerning medical physicists, we can find the most variation in the plan dose distribution optimisation process. Treatment plan optimisation differences can lead to dosimetrically different plan solutions mainly due to differences between planners in their skills, dedication, ambition, and in time spent on planning. Other steps in the radiotherapy process where human action introduces variation are the different perceptions of plan quality and the consequent different choices of which plan to approve for treatment. There is wide variability in the assessment of treatment plan quality (defined as the ability of the planners and plans to meet the specified goals). Indeed, there is no consensus on what the 'optimal' plan parameters should be for the different treatment sites and on how to measure plan quality quantitatively. In Cagni *et al.* [1], significant variations in plan quality evaluation among radiation oncologists and medical physicists belonging to the same department was found.

Tools have been previously defined based on physical dose distribution, such as dose volume histogram (DVH) or dosimetric endpoints. A dose volume histogram (DVH) shows what portion of the volume of a structure receives a certain amount of dose and is a convenient 2D tool to compare two or more treatment plans for the same patient. In addition, 1D tools, such as specific dosimetric endpoints, such as maximum dose (Dmax) or mean dose (Dmed) received to a specific organ are used.

However, in both 1D and 2D representation, spatial information is lost. The process of plan evaluation also necessarily involves the visual assessment of a 3D dose distribution on patient CT images made by a clinician. Since the ideal plan solution for a certain patient is not *a priori* known, traditional clinical methods of evaluation of treatment plan have been based on the clinical experience.

Ahmed *et al.* [2] use the CT images and DICOM RT structure set of the patient to generate a synthetic dose distribution based on first principle assumptions and series of energy-specific dose-spread calculations. This 3D dose distribution is 'ideal' and is intentionally unachievable. This tool has been implemented in PlanIQ commercial software v2.1 (Sun Nuclear Corp., Melbourne, FL). However, the user can only visualise and export the 2D and 1D information of this ideal dose and not its spatial 3D distribution matrix.

In this study, we developed a tool called a 'generalized Uniform Ideal DosE' (gUIDE). This tool produces an 'ideal' dose distribution based on single patient anatomy and dose prescription. gUIDE can be used as a baseline dose in clinical plan quality assessment. By comparing the clinical dose distribution with our gUIDE dose, we can compute a quantitative measure of plan quality. The novelty of gUIDE is its simple formulation designed to be easily built for every patient and used as baseline to improve the robustness of treatment plan comparison.

MATERIALS AND METHODS

gUIDE tool

This tool was implemented using Matlab version R2020b (Mathworks, Natick, USA). The process of the gUIDE computation is composed of three steps and it is described in Fig. 1.

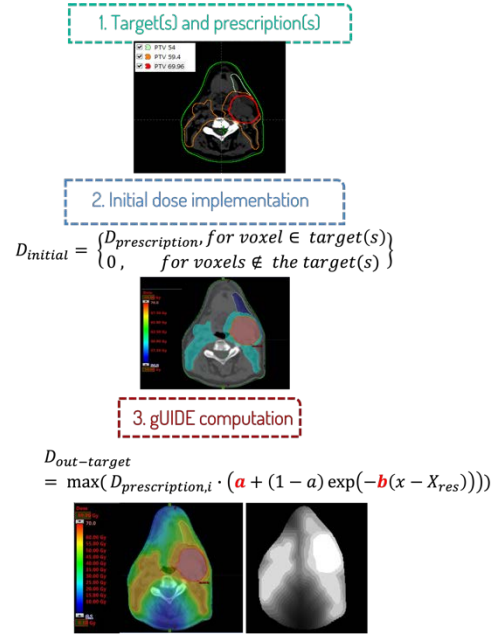


Fig. 1. The process of gUIDE creation.

The algorithm does not require any specification of the treatment machine or beam energy. The inputs needed for the gUIDE tool to generate the dose distribution are the CT simulation scan volume, the structure sets (OARs and tumour volumes), the dose prescription levels and the clinical treatment planning system (TPS) dose grid spatial resolution.

The starting point for gUIDE is the specification of target volume(s) and their prescription(s) together with calculation parameters on patient CT. The initial version of the ideal dose is a basic 3D dose grid (with the user specified resolution parameters) which provides 100% coverage of each of the target volumes with its associated prescribed dose. As the PTV is initially specified in the coordinates and the resolution space of the CT simulation scan, an interpolation of the mask (PTV contours) is carried out to map the mask in the 3D dose grid space. Then the dose grid points $[x,y,z]$ corresponding to the voxels of the dose matrix, are assigned a dose value. In this first step, the dose values are assigned following a simple binary target coverage grid:

$$D_{initial} = \begin{cases} D_p, & \text{for voxels} \in \text{the target}(s) \\ 0, & \text{for voxels} \notin \text{the target}(s) \end{cases} \quad (1)$$

After this, the algorithm assigns the dose to the non-target voxels. This is achieved by creating successive expansions of the target in an iterative process: the dimension of the expansion margins used in every iteration is equal to the highest dose grid resolution. Then, the voxels inside the expansion are given the prescribed target dose, multiplied by a negative exponential factor depending on the distance of the specific expansion with respect to the target, following this relationship:

$$D_{out} = D_p \cdot (a + (1-a) \exp(-b(x - X_{res}))) \quad (2)$$

Where, D_{out} is the dose assigned to every voxel inside the n th expansion, D_p is the target prescription for that sub-dose; a is the plateau parameter describing the minimum percentage of dose showing in the 3D dose map; as our ideal dose needed to be as low as possible, this parameter was set to 0.01; b is the fall-off parameter, determining the steepness of the dose descent; X_{res} is the dose grid resolution, set equal to the maximum resolution of the map (in this work, 3 mm); x is the distance from the target for that specific expansion which is computed by $x=i, X_{res}$, where i is the number of the iteration.

The rationale behind equation (2) formulation was based on the Eclipse Treatment Planning System (Varian Medical Systems, CA), normal tissue objective (NTO) definition, used to decrease the dose outside target region during the optimisation [3]. In the presence of multiple targets, the final gUIDE is composed of the maximum values among all gUIDE sub-doses. The resulting dose derived from the above formula is thus composed of dose steps as it is a collection of isodoses decreasing exponentially with their distance from the target.

Tuning setup and validation strategy

gUIDE dose descent is parametrized with a fall-off variable, which needs to be tuned. We devised a tuning and validation setup using virtual CT scans of a cylindrical phantom with water density. We employed two model geometries, shown in Fig. 2. In both configurations, the centres of the targets were placed at the centre of the phantom with the OAR placed next to the target. We studied two possible configurations: the first one (conf. A) where the PTV (i.e. the target) was comprised of a cylinder with a diameter of 8 cm, with a cylindrical OAR next to it with a diameter of 4 cm. The OAR was placed tangential to the target's surface as we wanted to explore how steep the dose descent would be if the system's priority forced it to a single direction. The second setting (conf. B) had a similar geometry, with a cylindrical PTV with a diameter of 5 cm, with a cylindrical OAR next to it with a diameter of 3 cm. We thought these two configurations were enough to be able to properly model the dimensions of PTVs and OARs typical of a H&N site; for other sites, different configuration setups to tune the dose descent parameters might need to be configured (i.e. a different target site with different OARs for sites like breast).

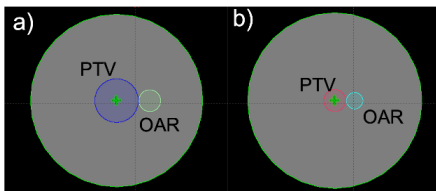


Fig. 2. Configuration A (a) and configuration B (b) used in the model tuning and validation.

Two treatment plans were generated on the two configurations. The dose prescription in these model geometries were 2 Gy to be delivered to the conf. A and conf. B PTVs. The optimization objectives, carried out in the aforementioned TPS, were the same for both configurations. The aim in this plan was to ensure near-perfect conformity of the prescription dose to the target and a dose homogeneity within $\pm 10\%$. For the OAR, the goal was to make the mean dose as low as possible. After the final dose

calculation was completed, we extracted the dose profiles taken in the perpendicular direction passing in the middle of the OAR (and starting from the target). Then, we fitted the resulting dose profiles using an exponential function having the same form and parameters as the one described in Eq. 2.

The steepest dose profiles were then recorded and fitted using the gUIDE equation, parametrized with the fall-off parameter (b) and the plateau parameter (a). However, as the plateau parameter takes into consideration the low-gradient effects which we are not interested in modelling, we did not use it in our fit. In fact, only the fall-off parameter of the Eq. 2, used in the dose descent in gUIDE, was used in our tuning strategy. Said parameter was set as the mean among the values found from every analyzed configuration.

gUIDE computation for clinical case

Our gUIDE was used on 15 clinical head and neck cancer patient datasets to extract their ideal dose distribution. To assess the feasibility of our results, gUIDE doses were compared with a "benchmark" ideal dose, generated by a commercial tool, planIQ (Sun Nuclear Corp, Melbourne, FL). PlanIQ allows the user to create a feasibility DVH (fDVH), introduced by Ahmed *et al.* [2], able to generate a synthetic feasible ideal DVH for a given patient, using a similar approach of gUIDE. For the purpose of our future applications and based on the considerations reported in the introduction section, 3D dose distribution is mandatory for our study, thus necessitating the implementation of an independent system. Our comparison with the benchmark was performed for spinal cord, brainstem, left and right parotids, oral cavity, mandible, oesophagus and larynx.

RESULTS

gUIDE tuning setup

In Fig. 3, a horizontal dose profile, passing through the middle of the PTV and OAR associated with the 2 configurations described in Fig.2 are reported. The graph can be divided in two parts. The first one (above the black line, shaded in orange) concerns the doses over 0.4 Gy, i.e. 20% of the maximum value (2 Gy in this case) is the part of the graph which was used in the fit and in the validation, as it describes the fall-off parameter. The other part of the graph simply shows that, for lower doses, the gUIDE differs from the experimental data, but it is expected as in the gUIDE modelling, the low gradient effects [2] were not taken into consideration. The fits exhibited a mean $R^2 > 0.98 \pm 0.01$ and the final fall-off parameter was set as $b=1.9$.

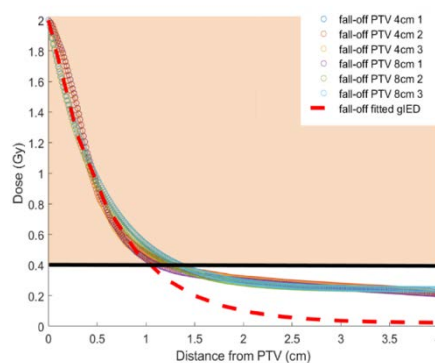


Fig. 3: Results from the fall-off parameter tuning.

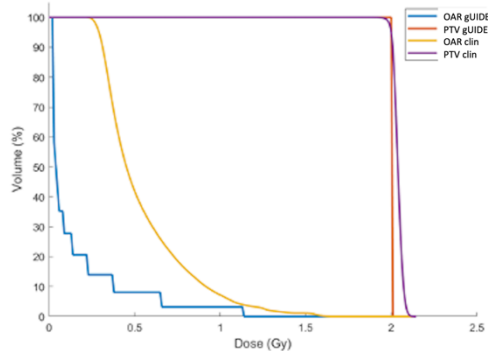


Fig. 4. Dose distributions from two examples of the dose calculation in configuration A and B. The red arrow shows the direction the dose profile was taken for the tuning of the gUIDE fall-off parameter.

Fig. 4 shows for configuration A (PTV=8 cm), the obtained DVHs related to the two involved structures. As expected, the PTV DVH for the gUIDE is a step function where all the prescription dose is delivered to the PTV, while the OAR DVH is composed of steps as a result of the isodoses with descending values implementation. The PTV DVH of configuration A cannot reach the step function given to the gUIDE, by definition. Regarding the DVHs, it is expected that the gUIDE would be lower as the tuning was performed using the steepest one-dimensional dose descent in the OAR while in the real dose distribution the OARs receive the sum of various profile contributions.

gUIDE validation for clinical cases

In the comparison between gUIDE and planIQ clinical cases, the median DVHs for both cases, together with their 10-90 percentiles are shown in Fig. 5. Overall, the results are quite similar, even if for some OARs the differences between the two methods are more evident, such as larynx. However, the paired two-sided Wilcoxon signed rank test on the mean doses of all 8 OARs considered in the comparison (area under the DVH curve) showed different median values for the two DVH sets, with a p-value << 0.05.

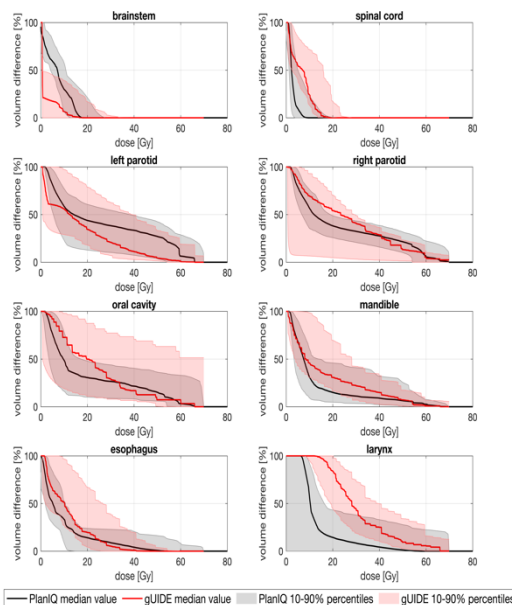


Fig. 5. PlanIQ and gUIDE DVHs difference for principal OARs structure in term median DVHs for the 15 patients with 10-90% percentiles.

Fig. 6 shows this comparison in terms of boxplots commercial PlanIQ (upper panel) and gUIDE (lower panel) mean dose values. Although the statistical test showed significant difference between the two groups, overall values are quite similar for all OARs in the two approaches.

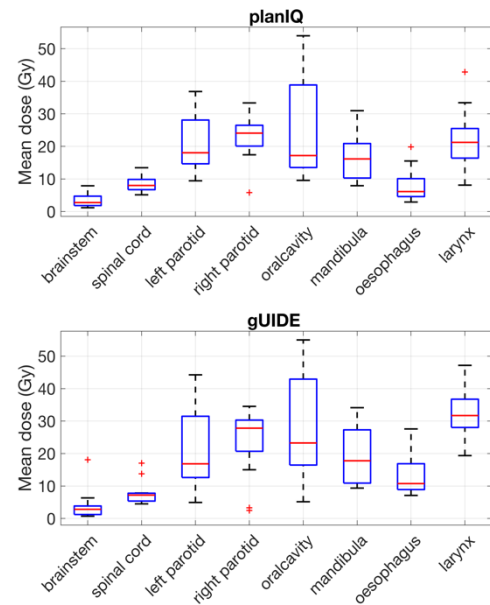


Fig. 6. Boxplots of planIQ and gUIDE DVH area under the curve distribution sorted by OAR. For each box, the central mark represents the median value, while the bottom and top edges of the box are the 25th and 75th percentiles over 15 patients, respectively.

DISCUSSION

In this study an ideal dose, called gUIDE was developed. gUIDE was optimised in a simple geometrical situation and tested on data from a cohort of 15 head and neck cancer patients, through a comparison with a commercial software system.

As the process of evaluation also necessarily involves the visual assessment of a 3D dose distribution, it was thought that the computation of a ‘baseline dose’, which is not attainable but represents the closest option to the ideal (but physically impossible) situation, could help improve the modelling of the evaluation process. The best achievable dose to specific anatomic regions was not known a priori by the automatic planning system or the evaluation. gUIDE considers the unique patient anatomy and how that plays a significant role in the best achievable doses. The comparison of these theoretical and synthetic (but patient-specific limits) could give more insight into the evaluation process and could help in highlighting the different personal preferences that observers could employ when evaluating a plan. One key aspect of this study was the very simple formulation of gUIDE, that make it easy to implement and use in a clinical practice. gUIDE formulation presents some limitations because the low-gradient effect, which affects the lower dose is not considered. Nevertheless, gUIDE does not represent a physically achievable dose, but it is intended to be used as a baseline for actual dose distributions comparison.

By using this ideal dose, based on the anatomy of a single patient, together with the dosimetric features (1D endpoints

and 2D DVH metrics) belonging to the different plans (which are strongly influenced by each patient's unique anatomy), the behavioural patterns of the evaluators during the scoring process can be investigated using machine learning (ML) techniques. gUIDE could provide partial but fundamental information about the quality of obtained dose distributions in different patient anatomies and geometries.

In an on-going study, due to the limited number of samples (treatment plans) to model for the clinical set of patients considered in the application, gUIDE has been applied to improve the information of the dataset without adding features for ML classification. Preliminary results of this on-going study showed that the ML approach using gUIDE gives more complete information in comparison to the use of the ML tool without any patient's anatomy and dose distribution information. Results of this application are currently under further study.

CONCLUSIONS

In this study, a baseline dose gUIDE was implemented, optimised and evaluated. From our results, gUIDE could be accurate enough to be used as baseline to help in the plan evaluation process.

Further applications of gUIDE include using it in the ML tool to investigate the process of plan quality assessment among several evaluators in a limited dataset of plans. This could be the basis of useful information for a departmental-wide discussion to improve the consistency of plan quality assessment.

Conflicts of interest

The authors declare no conflict of interest.

REFERENCES

- [1] E. Cagni *et al.*, 'Variations in Head and Neck Treatment Plan Quality Assessment Among Radiation Oncologists and Medical Physicists in a Single Radiotherapy Department', *Front Oncol*, vol. 11, p. 706034, 2021. doi: 10.3389/fonc.2021.706034
- [2] S. Ahmed *et al.*, 'A method for a priori estimation of best feasible DVH for organs-at-risk: Validation for head and neck VMAT planning', *Medical Physics*, vol. 44, no. 10, pp. 5486–5497, Oct. 2017. doi: 10.1002/mp.12500
- [3] *Eclipse photon and electron algorithms reference guide*, March 2015, available at <https://www.myvarian.com>

Doherty C

*Velindre NHS Trust,
Department of Oncology, Cardiff*

Hutton M

*The Christie NHS Foundation Trust
Manchester*

Duman A

*Cardiff University
School of Engineering*

Spezi E

*Cardiff University
School of Engineering*

Chuter R

*The Christie NHS Foundation Trust
Manchester*

ENGINEERING FOR HEALTH

Investigating the Feasibility of MRI Auto-segmentation for Image Guided Brachytherapy

A feasibility study has been performed to investigate the viability of applying auto-segmentation methods to the delineation of regions of interest (ROIs) in the treatment of cervical cancer using Image Guided Brachytherapy (IGBT). The introduction of auto-segmentation in IGBT aims to improve outlining consistency while improving patient experience by reducing the time taken to plan treatments. An anonymised database of MRI images and corresponding clinical ROI outlines was curated, categorised by brachytherapy treatment applicator type. This database was then used to train and test an auto-segmentation model to contour the Bladder using three established algorithms, U-Net, SegNet and PSPNet. Quantitatively the U-Net model was found to produce contours geometrically closest to the original manual contours with a mean Dice Similarity Coefficient (DSC) of 0.942 compared to 0.919 and 0.879 for SegNet and PSPNet respectively and a mean Mean Distance to Agreement (mDTA) value of 0.46mm compared to 0.66mm and 0.89mm for SegNet and PSPNet. Visual assessment of the resulting contours demonstrated good agreement for the U-Net and SegNet produced outlines, particularly in the region of clinical significance, with greater variations seen at the extremities of the contour. In conclusion this feasibility study has shown that auto-segmentation methods can be applied to MRI IGBT contour delineation with a method established to facilitate further investigations in the application to all clinical ROIs and brachytherapy applicator types.

*Keywords:
Image Guided Brachytherapy,
auto-segmentation, MRI.*

*Corresponding author:
Ceri.Doherty@wales.nhs.uk*



C. Doherty, A. Duman, R. Chuter, M. Hutton and E. Spezi, 'Investigating the Feasibility of MRI Auto-segmentation for Image Guided Brachytherapy', *Cardiff University School of Engineering Research Conference 2023*, Cardiff, UK, 2023, pp. 11-14.

doi.org/10.18573/conf1.d

INTRODUCTION

Manual contouring of organs at risk (OARs) and target volumes is standard practice for radiotherapy treatment planning at most clinical centres [1, 2]. Manual delineation is time consuming, subjective and cumbersome, with its ease dependent on the efficiency of the contouring tools available [3, 4]. This manual contouring is a significant source of variability within the treatment planning process due to inter or intra-observer variations [1, 2, 5, 6].

Brachytherapy is a radiotherapy treatment that uses sealed radioactive sources to treat cancers by placing the sources close to, or within the tumour. This allows a high radiation dose to be delivered to the tumour, and reduces the dose received by the surrounding healthy tissues when compared to conventional external beam radiotherapy (EBRT) [7, 8]. At Velindre Cancer Centre the Image Guided Brachytherapy (IGBT) process for cervical cancer uses an MR safe intracavitary Venezia applicator (Elekta AB, Sweden). The Venezia applicator comprises an Intrauterine Tube (IUT) and two Lunar Ovoids. The IUT is inserted into the patient's uterus through the cervix under ultrasound image guidance and the lunar ovoids are positioned within the vagina, flush against the cervix.

Our current clinical brachytherapy planning process, from Magnetic Resonance Imaging (MRI) to treatment, typically takes two to three hours. One of the more time consuming aspects is the outlining of the tumour and OARs on the MRI images, locally taking on average 55 minutes [2, 4]. As brachytherapy utilises the inverse square law the dose falloff from a source results in steep dose gradients across surrounding OARs. Therefore a slight difference in target volume outlining can have significant impact on surrounding OAR toxicity or tumour coverage [9].

IGBT for cervical cancer has advanced to planning on MRI datasets alone, with no CT necessary due to the lack of requirement for electron density information [10]. Although MRI images have significantly improved soft tissue contrast compared to CT images they are also subject to increased variability across image acquisitions which causes auto-segmentation challenges [2]. There was little evidence found in the literature of the use of auto-segmentation for brachytherapy, particularly for gynaecological cancers with MRI.

MATERIALS AND METHODS

IGBT with paraxial MRI started at Velindre Cancer Centre in late 2014 with over 160 patients treated since then, totalling over 460 outlined image sets. Since 2014 we have used a varying range of brachytherapy treatment applicators by which the image sets have been categorised. The applicator type chosen for clinical insertion can be dependent on disease location and/or patient anatomy. The anonymised outlined MRI image sets were used to establish a 'gold standard' database on which to train and develop the auto-segmentation solution.

The clinical MRI dataset is in the form of DICOM image files and DICOM RSTRUCT files which store the outlined regions of interest (ROIs). For cervical cancer IGBT these are the target volumes of Cervix, Gross Tumour Volume (GTV) and the High Risk Clinical Target Volume (HR-CTV), which is created as a union of the GTV and Cervix. The OARs outlined are the Bladder, Bowel and Rectum. Once collated, the ROI naming convention standardised and the datasets

anonymised these were converted from DICOM files to NIfTI files and subsequently into PNG image files and masks for each ROI.

Existing python code for a range of established auto-segmentation algorithms, including SegNet, Unet and PSPnet, was then adapted to suit this database including image orientation and required number of ROIs [11, 12]. The database was split into training and testing subsections with 90% for training and 10% for testing. For this proof of concept stage the model was primarily trained and tested on the bladder as this is typically the most well defined of these ROIs with greatest contrast at the organ boundaries.

In this feasibility study the Venezia applicator database was used for the training of each of the auto-segmentation models as this was both the largest dataset and the current clinical applicator set used for the majority of patients. The results will later be tested on the Multi-Channel Vaginal Applicator (MCVA) dataset to test if the trained model is independent of applicator or needs to be trained per applicator type. As the applicators are inserted into the patient they have the potential to deform the ROIs and therefore it may be that the trained model is not transferrable between database subsets.

RESULTS

For the bladder there was greater than 2000 PNG image files in the Venezia Applicator dataset. This is equal to each slice with a bladder outline defined on the 104 clinical patient MRI scans. In the 10% testing subset a total of 217 slices were output which equated to 10 full bladder ROI contours.

The Dice Similarity Coefficient (DSC) results and mean Distance to Agreement (mDTA) for each of the 10 patients for the SegNet, U-Net and PSPNet auto-segmentation models are outlined in Tables 1 and 2 respectively. The DSCs were calculated using Eq. 1 where A and B represent the two contour sets, the resulting auto-segmentation model contour and the original manual clinical contour, where $|A \cap B|$ is equivalent to the intersection of the contour sets. For DSC, a measure of overlap, a value of 0 indicates no overlap between the contours and 1 is a perfect overlap. The distance to agreement (DTA) is defined as the shortest distance from a point on the surface of one contour (A) to the surface of another (B). The Mean distance to agreement (mDTA) is the mean of all the DTA distances, where the smaller the mDTA the greater the similarity between the two contour sets.

$$(1) DSC = \frac{2 \times |A \cap B|}{|A| + |B|}$$

It can be seen that the DSC values ranged from 0.849 to 0.955 across all model types with the greatest mean DSC for U-Net (0.942, range: 0.924-0.955), then SegNet (0.919, range: 0.877-0.940) and lastly PSPNet (0.879, range: 0.902-0.849). Similarly the U-Net model was found to produce the lowest mean mDTA value, 0.456mm, compared to 0.662mm for Segnet and 0.894 for PSPNet.

Patient	Auto-Segmentation Model		
	SegNet	U-Net	PSPNet
1	0.917	0.942	0.863
2	0.909	0.924	0.890
3	0.930	0.936	0.883
4	0.924	0.948	0.862
5	0.877	0.953	0.882
6	0.938	0.946	0.902
7	0.940	0.955	0.902
8	0.903	0.926	0.849
9	0.928	0.946	0.866
10	0.928	0.940	0.892
Mean	0.919	0.942	0.879

Table 1: DSC values for Bladder ROIs for the three different Auto-Segmentation models

Patient	Auto-Segmentation Model		
	SegNet	U-Net	PSPNet
1	0.691	0.476	1.049
2	0.617	0.500	0.756
3	0.467	0.477	0.807
4	0.509	0.432	0.906
5	1.822	0.740	1.480
6	0.377	0.330	0.610
7	0.487	0.345	0.727
8	0.608	0.474	0.944
9	0.485	0.339	0.839
10	0.562	0.443	0.820
Mean	0.662	0.456	0.894

Table 2: mDTA values (mm) for Bladder ROIs for the three different Auto-Segmentation models.

Output files were initially produced as PNG mask files. These were converted to DICOM RT structure files containing each auto-segmentation model contour as well as the original clinical Bladder outline. The resulting structure files were then viewed in the clinical treatment planning system, Oncentra Brachy (Elekta AB, Sweden), overlaid on the original MRI images. Fig.2a & Fig.2b show the axial and sagittal views respectively of the bladder contours for the clinical and three subsequent auto-segmentation models for patient two. As well as having the lowest mean DSC values the produced PSPNet contours were visually assessed, by a clinical scientist authorised in IGBT OAR review and plan checking, to be clinically unsuitable due to the pixelated nature of the generated outlines.

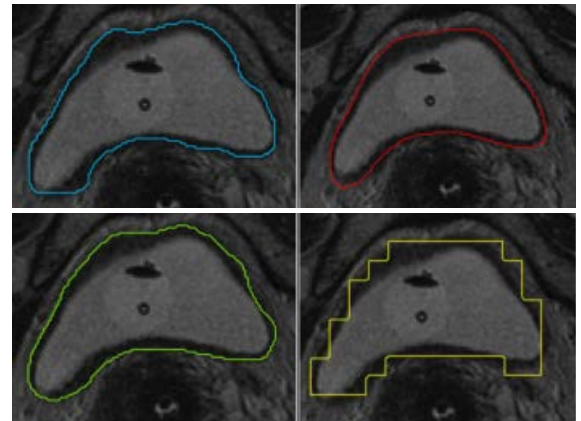


Fig. 1 : Axial Bladder slices for the Clinical (Blue) and SegNet (Red), U-Net (Green) and PSPNet (Yellow) auto-segmentation models for Patient 2.

Both the SegNet and U-Net generated contours were noted to be clinically acceptable for the majority of axial slices, particularly in the mid region of the ROI. However, greater differences were seen compared to the clinical contours at both the superior and inferior extremities of the volume, particularly at the superior aspect of the bladder. It can be seen in Fig.2b that both the SegNet and U-Net contours have failed to outline the apex aspect of the bladder which is raised due to the presence of the catheter tube. The SegNet contour, seen in Red, has also inadvertently outlined some regions of bowel superior to the bladder. For Brachytherapy this may not be clinically significant as the doses reported to the bladder are the highest dose to 2cc (D2cc), and are therefore in the region closest to the treatment applicators within the uterus, typically adjacent to the mid-section of the bladder.

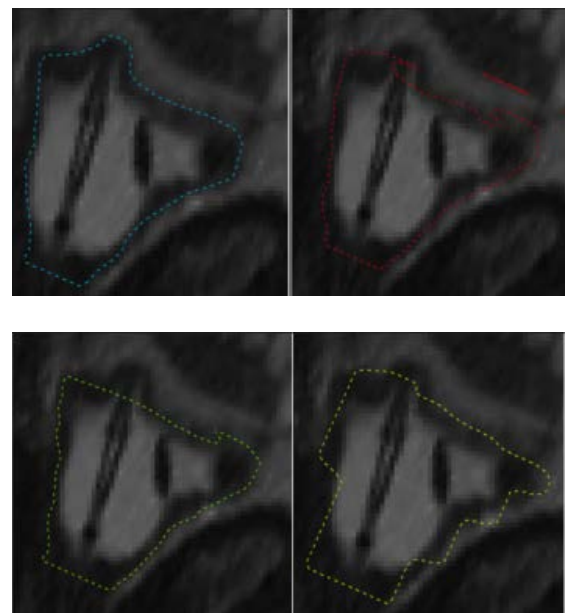


Fig. 2: Sagittal Bladder slices for the Clinical (Blue) and SegNet (Red), U-Net (Green) and PSPNet (Yellow) auto-segmentation models for Patient 2.

DISCUSSION

At this stage preliminary results have shown the possibility to utilise auto-segmentation methods for MRI IGBT cervical cancer treatments. The results have shown that bladder outlines of an acceptable clinical standard in the high dose region can be produced. For this ROI the U-Net and SegNet auto-segmentation algorithms have shown promise and it is anticipated further refinement of the algorithm training will see greater accuracy in the subsequent contours.

This feasibility study has produced a collated database of anonymised IGBT MRI images with standardised ROI naming and a consistent MRI protocol, categorised by brachytherapy applicator type. Although initial results are limited to one ROI a method of data processing, auto-segmentation model training and testing has been established which can now be expanded to include all relevant ROIs and applicator types.

The aim of implementing auto-segmentation into the clinical environment is to both reduce manual outlining variability while also reducing the time taken to produce clinically acceptable contours. This envisioned efficiency aims to improve patient experience by reducing the time the patient has to wait on the ward, with the applicators inserted and unable to move, while the treatment is planned. Increased consistency in outlining by minimising human variation will consequently increase the accuracy and consistency of dose reporting. The auto-segmented contours, such as those produced in this feasibility study, could with minor manual adaptations still lead to significant time savings in the IGBT clinical pathway.

Auto-segmented contouring quality can be quantified in both spatial accuracy and dose calculation accuracy, with each highly dependent on the other [2]. Although spatial accuracy is primarily evaluated in the literature and in this feasibility study to date uncertainties in patient and applicator positioning and anatomical changes may mean that deviations in contours spatially may not have the anticipated outcome on dose distributions and consequently treatment efficacy [2]. Dose assessments to understand the clinical significance in any outlining variations will further inform algorithm requirements.

Conflicts of interest

The authors declare no conflict of interest.

Research approval

This research project is approved by the HRA and Health and Care Research Wales (HCRW), IRAS project ID 300935, REC reference: 21/HCRW/0033.

REFERENCES

- [1] I. Simmat, P. Georg, D. Georg, W. Birkfellner, G. Goldner, and M. Stock, 'Assessment of accuracy and efficiency of atlas-based autosegmentation for prostate radiotherapy in a variety of clinical conditions', *Strahlenther Onkol*, vol. 188, no. 9, pp. 807–815, Sep. 2012. doi.org/10.1007/s00066-012-0117-0
- [2] G. Sharp *et al.*, 'Vision 20/20: Perspectives on automated image segmentation for radiotherapy: Perspectives on automated image segmentation for radiotherapy', *Med Phys*, vol. 41, no. 5, p. 050902, Apr. 2014. doi.org/10.1118/1.4871620
- [3] L.C. Anders, F. Stieler, K. Siebenlist, J. Schäfer, F. Lohr, and F. Wenz, 'Performance of an atlas-based autosegmentation software for delineation of target volumes for radiotherapy of breast and anorectal cancer', *Radiotherapy and Oncology*, vol. 102, no. 1, pp. 68–73, Jan. 2012. doi.org/10.1016/j.radonc.2011.08.043
- [4] V. Valentini, L. Boldrini, A. Damiani, and L.P. Muren, 'Recommendations on how to establish evidence from auto-segmentation software in radiotherapy', *Radiotherapy and Oncology*, vol. 112, no. 3, pp. 317–320, Sep. 2014. doi.org/10.1016/j.radonc.2014.09.014
- [5] S. Ghose *et al.*, 'A review of segmentation and deformable registration methods applied to adaptive cervical cancer radiation therapy treatment planning', *Artificial Intelligence in Medicine*, vol. 64, no. 2, pp. 75–87, Jun. 2015. doi.org/10.1016/j.artmed.2015.04.006
- [6] J. Yang, C. Wei, L. Zhang, Y. Zhang, R.S. Blum, and L. Dong, 'A statistical modeling approach for evaluating auto-segmentation methods for image-guided radiotherapy', *Computerized Medical Imaging and Graphics*, vol. 36, no. 6, pp. 492–500, Sep. 2012. doi.org/10.1016/j.compmedimag.2012.05.001
- [7] S. Nag *et al.*, 'The American Brachytherapy Society recommendations for low-dose-rate brachytherapy for carcinoma of the cervix', *International Journal of Radiation Oncology-Biology-Physics*, vol. 52, no. 1, pp. 33–48, Jan. 2002. doi.org/10.1016/S0360-3016(01)01755-2
- [8] K. Saarilahti, P. Arponen, L. Vaalavirta, and M. Tenhunen, 'The effect of intensity-modulated radiotherapy and high dose rate brachytherapy on acute and late radiotherapy-related adverse events following chemoradiotherapy of anal cancer', *Radiotherapy and Oncology*, vol. 87, no. 3, pp. 383–390, Jun. 2008. doi.org/10.1016/j.radonc.2008.04.011
- [9] S. Nouranian, S.S. Mahdavi, I. Spadinger, W.J. Morris, S.E. Salcudean, and P. Abolmaesumi, 'A Multi-Atlas-Based Segmentation Framework for Prostate Brachytherapy', *IEEE Trans Med Imaging*, vol. 34, no. 4, pp. 950–961, Apr. 2015. doi.org/10.1109/TMI.2014.2371823
- [10] J.C.A. Dimopoulos *et al.*, 'Recommendations from Gynaecological (GYN) GEC-ESTRO Working Group (IV): Basic principles and parameters for MR imaging within the frame of image based adaptive cervix cancer brachytherapy', *Radiotherapy and Oncology*, vol. 103, no. 1, pp. 113–122, Apr. 2012. doi.org/10.1016/j.radonc.2011.12.024
- [11] L. Zongyi, *Research on Medical Image Segmentation Based on Dense Attention Guide SEU-Net*, Cardiff University School of Computer Science and Informatics, 2021.

Dimitriou P

Cardiff University
School of Engineering

Birchall J

Welsh School of Pharmacy and
Pharmaceutical Science, Cardiff University

Castell O

Welsh School of Pharmacy and
Pharmaceutical Science, Cardiff University

Li J

Cardiff University
School of Engineering

ENGINEERING FOR HEALTH

Label-free Volumetric Imaging of Synthetic Cell Chassis using Optical Coherence Tomography

Bottom-up, chemically formed synthetic cells are usually imaged by optical microscopy, and the cell sizes and shapes are mostly estimated from acquired 2D images. The three-dimensional (3D) structures of a compartmentalised synthetic cell can be analysed by axially stacking 2D images, typically by using a high-resolution imaging systems, such as laser confocal scanning microscopy and light sheet microscopy. However, these techniques require the synthetic cell to be labelled with fluorescent tags, and have performance limits such as being restricted to volumes less than (approximately) $200 \mu\text{m}^3$. Here, we present the label-free, 3D imaging of soft, free-standing, multicompartment synthetic cell using optical coherence tomography (OCT). The volumes of sub-cellular compartments within individual synthetic cells can be obtained via OCT imaging measurement. The spatial arrangements of the compartments and their contact angle information can be illustrated and measured, respectively. This approach provides a new method to evaluate multiphase soft materials spanning the range of micrometres to millimetres, towards the optimisation of synthetic cell construction for novel biomimetic material development.

Keywords:

Optical coherence tomography, synthetic cells, soft materials, volumetric imaging, contact angle measurement.

Corresponding author:

lij40@cardiff.ac.uk



P. Dimitriou, O. Castell, J. Birchall, and J. Li, 'Label-free Volumetric Imaging of Synthetic Cell Chassis using Optical Coherence Tomography', *Cardiff University School of Engineering Research Conference*, Cardiff, UK, 2023, pp. 15-18.

doi.org/10.18573/conf1.e

INTRODUCTION

One goal of synthetic biology is to apply engineering principles to devise new biological devices and artificial biological systems [1]. Bottom-up synthetic cells can be formed from water-in-oil emulsion templates and fabricated as soft microcapsules using microfluidic approaches [2,3]. Such constructs can encapsulate cellular metabolic reactions and biological processes, to mimic natural cell functionalities, controlled with well-organised, fluidic, cellular compartments [4–6]. This paves the way to develop next-generation biotechnology tools and novel biomimetic materials, for new pharmaceutical and healthcare applications [7,8].

The imaging of synthetic cells and other droplet-based materials are typically undertaken using a fluorescent imaging system, such as laser confocal scanning microscopy, total internal reflection fluorescence microscopy and light sheet microscopy [9,10]. These are widely applied in biophysics studies to determine artificial membrane properties, identify intercellular communications through reconstituted protein channels, and monitor the process of cell-free synthesis in droplet networks. Optical coherence tomography (OCT) provides a non-invasive, label free, and rapid imaging method for soft tissues, affording spatial resolution of 10 μm or less in three dimensions and has been widely applied in medicine, including ophthalmology, dermatology and dentistry [11–13]. In OCT, a light source is directed onto samples, and the time delay and intensity of the reflected light are used to construct a high-resolution image of the specimen. Here, we report the use of an OCT system to measure emulsion-based synthetic cells (Fig. 1) for the first time. The structural information of individual synthetic cells can be acquired efficiently without using additional water, or lipid soluble fluorescent dyes or fluorescently tagged biomolecules, such as proteins, peptides or oligonucleotides. It is also possible to use OCT systems for mapping tissue-like architectures made from synthetic cells, hence providing a cost-effective imaging tool for engineered compartmentalised soft structures.

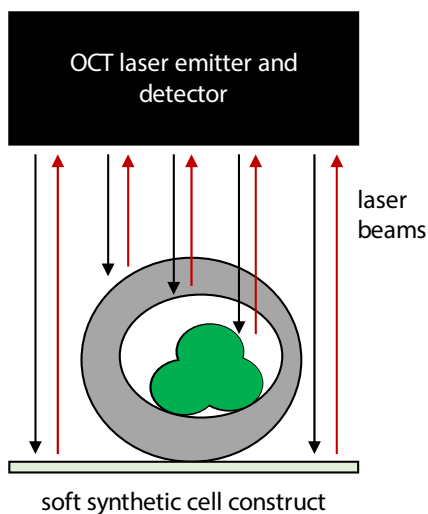


Fig. 1. Schematic of using optical coherence tomography (OCT) system to image a soft synthetic cell construct. The time delay and intensity of the reflected light are used to construct 3D images.

MATERIALS AND METHODS

OCT (VivoSight System, Michelson Diagnostics, UK) system was used to take axial images of synthetic cells. Synthetic cells were produced using 3D-printed microfluidic devices. Microfluidic device fabrication, chemical protocols and experiment setup can be found in our previous publications [6,14]. An example of multicompartment synthetic cell is shown in Fig. 2, which fluorescent image was taken using a EVOS M7000 microscope (Invitrogen). During the OCT imaging, synthetic cells were transferred onto a microscope glass slide, which was in turn placed on the imaging platform. The moving platform was adjusted to focus the microscope objective on the samples by tuning its z-axis dial. An area of 6 mm² was scanned at 500 FPS with a 4 μm step size. Image processing was carried out using ImageJ Fiji, for the visualisation of orthogonal views and 3D image reconstruction of the synthetic cells.

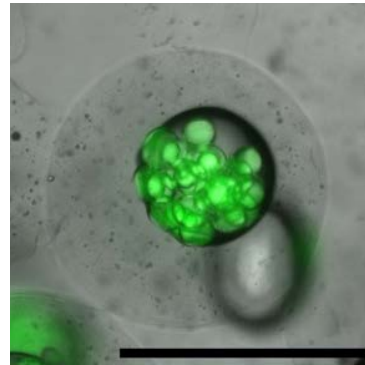


Fig. 2. Example of water (green)-in-oil-in-hydrogel synthetic cell. Scale bar = 500 μm .

RESULTS AND DISCUSSION

Free-standing, multicompartment synthetic cell capsules were made from water-in-oil-in-hydrogel-in oil complex emulsions (Fig. 2). The alginate shell hosts the fragile lipid-segregated droplet interface bilayer network inside [4], and provides the mechanical stability by virtue of which the synthetic cells can be manipulated and transported. The orthogonal views and z-projected image of an example synthetic cell is shown in Fig. 3. These orthogonal views can be used to extract data like the diameter of different compartments, and the contact angles of the droplet interface bilayers, informing on membrane forces. As shown in Fig. 4, 12 contact angle measurement can be implemented from a synthetic cell with a droplet network containing three compartments from a single OCT image, while with conventional 2D fluorescent imaging, this would be limited to 2 to 4 contact angle measurements, depending on the imaging orientation. These contact angle measurements can be used for non-destructive investigation of the artificial membrane properties inside synthetic cells. Regulation of membrane contact angle can be used to determine packing order [15], and therefore droplet network connectivity and function [16].

The volume of the three aqueous cores was calculated to be approximately 6, 7 and 8 nL, by utilizing the high contrast axial images, as shown in Fig. 5. This was achieved by measuring the area of each core at every axial scan and multiplying the sum of the area with the step resolution (4 μm). The thickest and the thinnest regions of the hydrogel shell layer can also be evaluated. The average hydrogel shell thickness (measured from all orthogonal views) of an individual artificial cell was estimated to be 340 $\mu\text{m} \pm 31 \mu\text{m}$ for the thickest, and 37 $\mu\text{m} \pm 3 \mu\text{m}$ for the thinnest in Fig. 5.

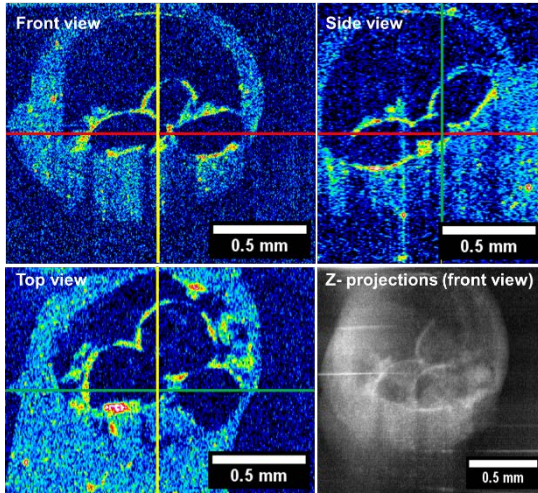


Fig. 3. Orthogonal views and z-projection of a synthetic cell imaged by OCT (with false 16-colour LUT).

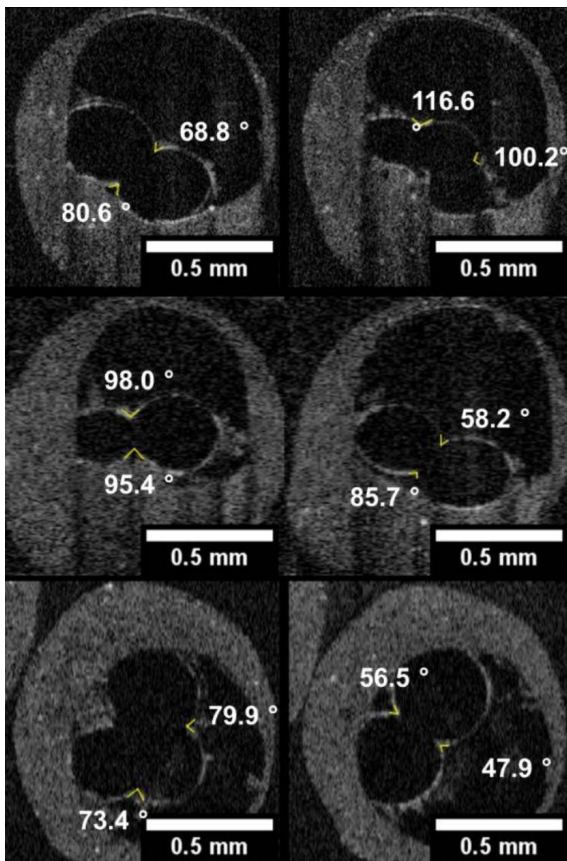


Fig. 4. OCT orthogonal views of a 3-core synthetic cell with 12 annotated contact angle values.

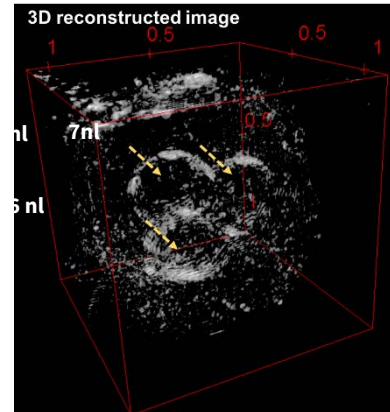


Fig. 5. 3D volumetric measurements of synthetic cell compartments of Fig. 4. The volumes of the three water compartments, highlighted by orange arrows, were calculated as 6, 7 and 8 nL.

Moreover, the capsule diameters can be measured from each orthogonal view (or from any desired angle of view) to identify the exact location of the compartment in three dimensions (3D). For example, the 3D central position (p_{3D}) of the oil core (within which the aqueous droplet network in Fig. 5 is contained) was expressed as $P_{3D}(\text{centre}) = 0.62x + 0.66y + 0.42z$, by measuring the diameter of the synthetic cell outer shell in every axis ($\sigma_x = 1.135$ mm, $\sigma_y = 1.150$ mm, $\sigma_z = 1.045$ mm), considering the bottom left corner as the origin $(x,y,z) = (0,0,0)$ (Fig. 6). Therefore, the approximate 3D structure of the synthetic cell can be mathematically reconstructed, providing numerical models for structural optimisation [17], and behavioural simulations [18], using COMSOL Multiphysics software.

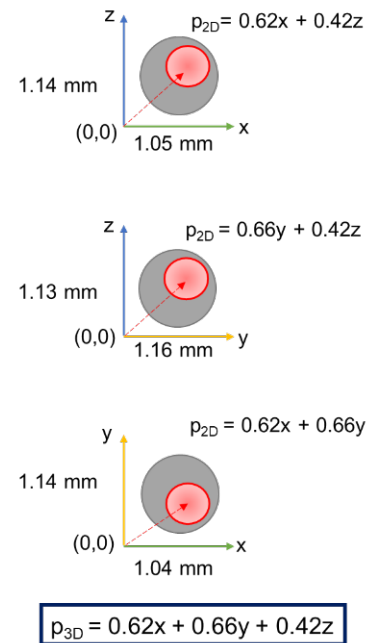


Fig. 6. Three-dimensional positions of sub-cellular oil compartment within the synthetic cell can be calculated as P_{3D} , from the OCT imaging data of (i) front, (ii) side, and (iii) bottom.

In addition, the total imaging volume of the OCT system is sufficient to image large, tissue-like structures comprised of multiple artificial cells, that are not easily amenable to confocal microscopy imaging. As such, OCT is a suitable tool for the rapid scanning and mapping of 3D-printed superstructures of hybrid materials [19], for our research in the development and programming of functional synthetic tissues.

CONCLUSIONS

Optical coherence tomography can be utilised for label-free imaging of 3D architectures of bottom-up synthetic cells, and droplet-based soft materials. Volumetric information, spatial arrangements, and contact angles between sub-cellular compartments can be obtained from the OCT imaging data to assist the optimisation of synthetic cell fabrication.

Acknowledgments

This work was primarily supported and funded by the European Horizon 2020 project ACDC (Artificial Cells with Distributed Cores) under project award number 824060.

Conflicts of interest

The authors declare no conflict of interest.

REFERENCES

- [1] W. Jiang *et al.*, 'Artificial Cells: Past, Present and Future', *ACS Nano*, 2022, 16, 15705-15733. doi.org/10.1021/acsnano.2c06104
- [2] E.C. Freeman, A.B. Farimani, N.R. Aluru, and M.K. Philen, 'Multiscale modeling of droplet interface bilayer membrane networks', *Biomicrofluidics*, 2015, 9, 064101. doi.org/10.1063/1.4935382
- [3] T. Trantidou, M.S. Friddin, A. Salehi-Reyhani, O. Ces, and Y. Elani, 'Droplet microfluidics for the construction of compartmentalised model membranes'. *Lab Chip*, 2018, 18, 2488-2509. doi.org/10.1039/C8LC00028J
- [4] D.K. Baxani *et al.*, 'Bilayer Networks within a Hydrogel Shell: A Robust Chassis for Artificial Cells and a Platform for Membrane Studies', *Angewandte Chemie International Edition*, 2016, 55, 14240-14245. doi.org/10.1002/anie.201607571
- [5] Y. Elani, 'Construction of membrane-bound artificial cells using microfluidics: a new frontier in bottom-up synthetic biology', *Biochemical Society Transactions*, 2016, 44, 723-730. doi.org/10.1042/BST20160052
- [6] Li, J. *et al.*, 'Formation of Polarized, Functional Artificial Cells from Compartmentalized Droplet Networks and Nanomaterials, Using One-Step, Dual-Material 3D-Printed Microfluidics', *Adv Sci (Weinh)*, 2019, 7, 1901719. doi.org/10.1002/advs.201901719
- [7] P. Dimitriou, J. Li, G. Tornillo, T. McCloy, and D. Barrow, 'Droplet Microfluidics for Tumor Drug-Related Studies and Programmable Artificial Cells', *Global Challenges*, 2021, 5, 2000123. doi.org/10.1002/gch2.202000123
- [8] R. Strutt *et al.*, 'UV-DIB: label-free permeability determination using droplet interface bilayers', *Lab on a Chip*, 2022, 22, 972-985. doi.org/10.1039/D1LC01155C
- [9] S. Berhanu, T. Ueda, and Y. Kuruma, 'Artificial photosynthetic cell producing energy for protein synthesis', *Nat Commun*, 2019, 10, 1325. doi.org/10.1038/s41467-019-09147-4
- [10] C. Xu, N. Martin, M. Li, and S. Mann, 'Living material assembly of bacteriogenic protocells', *Nature*, 2022, 609, 1029-1037. doi.org/10.1038/s41586-022-05223-w
- [11] S.A. Coulman *et al.*, 'In vivo, in situ imaging of microneedle insertion into the skin of human volunteers using optical coherence tomography', *Pharm Res*, 2011, 28, 66-81. doi.org/10.1007/s11095-010-0167-x
- [12] T. Rattanapak *et al.*, 'Transcutaneous immunization using microneedles and cubosomes: Mechanistic investigations using Optical Coherence Tomography and Two-Photon Microscopy', *Journal of Controlled Release*, 2013, 172, 894-903. doi.org/10.1016/j.jconrel.2013.08.018
- [13] S. Parker, S. Coulman, and J. Birchall, 'Characterising the wall thickness of Quali-V®-I capsules', 2021, 6.
- [14] J. Li, P. Dimitriou, O. Castell, and D. Barrow, 'Generation of complex emulsions using monolithic, dual material 3D-printed microfluidic devices' in *MicroTAS 2020 proceedings 2020*.
- [15] A. Alcinesio *et al.*, 'Controlled packing and single-droplet resolution of 3D-printed functional synthetic tissues', *Nat Commun*, 2020, 11, 2105. doi.org/10.1038/s41467-020-15953-y
- [16] J. Li *et al.*, 'Building programmable multicompartment artificial cells incorporating remotely activated protein channels using microfluidics and acoustic levitation', *Nat Commun*, 2022, 13, 4125. doi.org/10.1038/s41467-022-31898-w
- [17] X.-F. Han, H. Laga, and M. Bennamoun, 'Image-Based 3D Object Reconstruction: State-of-the-Art and Trends in the Deep Learning Era', *IEEE Transactions on Pattern Analysis and Machine Intelligence*, 2021, 43, 1578-1604. doi.org/10.1109/TPAMI.2019.2954885
- [18] O. Gryshkov *et al.*, 'Coaxial Alginate Hydrogels: From Self-Assembled 3D Cellular Constructs to Long-Term Storage', *International Journal of Molecular Sciences*, 2021, 22, 3096. doi.org/10.3390/ijms22063096
- [19] L. Zhou *et al.*, 'Lipid-Bilayer-Supported 3D Printing of Human Cerebral Cortex Cells Reveals Developmental Interactions', *Advanced Materials*, 2020, 32, 2002183. doi.org/10.1002/adma.202002183.

Duman A

*Cardiff University
School of Engineering*

Thomas S

*Velindre NHS Trust,
Department of Oncology, Cardiff*

Powell J

*Velindre NHS Trust,
Department of Oncology, Cardiff*

Spezi E

*Cardiff University
School of Engineering*

ENGINEERING FOR HEALTH

Evaluation of Radiomic Analysis over the Comparison of Machine Learning Approach and Radiomic Risk Score on Glioblastoma

Accurate patient prognosis is important to provide an effective treatment plan for Glioblastoma (GBM) patients. Radiomics analysis extracts quantitative features from medical images. Such features can be used to build models to support medical decisions for diagnosis, prognosis, and therapeutic response. The progress of radiomics analysis is continuously improving. The aim of this research is to extract standardised radiomic features from MRI scans of GBM patients, perform feature selection, and compare radiomic-based risk score (RRS) and machine learning (ML) approaches for the risk stratification of GBM patients. We have also tested the generalisability of these models which is crucial for clinical implementation. Our work demonstrates that a stratification model based on logistic regression generalised better than the RRS method when applied to new unseen datasets.

Keywords:

Glioblastoma, radiomics, brain tumour, overall survival.

Corresponding author:

DumanA@cardiff.ac.uk



A. Duman, J. Powell, S. Thomas, and E. Spezi, 'Evaluation of Radiomic Analysis over the Comparison of Machine Learning Approach and Radiomic Risk Score on Glioblastoma', *Cardiff University School of Engineering Research Conference 2023*, Cardiff, UK, 2023, pp. 19-22.

doi.org/10.18573/conf1.f

INTRODUCTION

Glioblastoma (GBM) is a malignant and lethal brain tumour [1]. Grade IV gliomas exhibit the highest level of aggression and rapid progression. After initial diagnosis, the median survival time for GBM patients is 15 months [2]. The poor prognosis for GBM can be related to genetic heterogeneity between patients and at intratumor level [3].

In clinical practice, brain tumours are evaluated for their diagnosis and prognosis by utilising magnetic resonance imaging (MRI) techniques. The location of tumours is detected in three dimensions via non-invasive MRI technology. In contrast to X-ray and CT imaging, MRI gives high resolution with better soft tissue contrast without the use of ionising radiation [4].

Biopsies are an invasive procedure to diagnose, grade and characterise brain tumours [5]. Due to having genetic differences in sub-regions of a tumour, biopsies can provide only limited information with a sample of small section from tumour tissue [6]. Other assessment methods including quantitative image analysis, which is non-invasive and evaluate the entire tumour tissue, can support biopsy as additional assessment. Image analysis utilising radiomics features has the potential to replace biopsies when they are infeasible or risky [7].

Radiomics analysis is a rapidly growing field of medical imaging involving the extraction of large amounts of quantitative data from medical images [8], [9]. This approach seeks to reveal hidden patterns and features that are imperceptible by the naked eye in order to provide patients with more personalised and precise care. To extract radiomic features from medical images, radiomics analysis employs advanced image processing techniques that can characterise tumour heterogeneity [10] and microenvironment [11]. Radiomic imaging features can be then used to train a model to stratify patients in different risk groups. This is achieved using statistical methods and machine learning (ML) techniques as outlined in the literature [9].

N. Beig et al. proposed a Radiomics-based Risk Score (RRS) for GBM tumour habitat [12]. However, a comparison with alternative methods including machine learning (ML) approaches was not performed. In this work, we investigate the best model to risk-stratify GBM patients including RRS, and a range of ML approaches applied to a large dataset of clinical MRI images and clinically defined contours.

MATERIALS AND METHODS

In this research we used two GBM datasets: (1) the publicly available BraTS 2020 including 236 cases [13]–[15] and (2) a local dataset STORM_GLIO including 53 eligible cases. Both datasets included overall survival (OS) information. The MRI sequences included in the datasets were: T1-weighted (T1), T1-weighted contrast-enhanced (T1ce), T2 weighted (T2), and T2 Fluid attenuated inversion recovery (T2-FLAIR). All scans included in the STORM_GLIO dataset were acquired between April 2014 - April 2018 in Wales.

Sixty six percent of the BraTS dataset was used as training cohort with the remaining 33% used in the testing cohorts together with the STORM_GLIO dataset. Image pre-processing techniques similar to those used for the curation of the BraTS2020 dataset were implemented in this work. They included the following steps: (1) skull stripping, which was carried using HD-BET algorithm [16] (2) rigid

registration of all sequences was applied to the dataset based on T1ce modality (3) an intensity normalisation algorithm implementing Z-score normalisation was applied to all datasets.

The BraTS2020 challenge [17], included three annotated regions: enhancing tumour (ET), tumour core (TC; enhancing tumour and necrotic) and whole tumour (WT; enhancing tumour, necrotic and edema). On the other hand, the STORM_GLIO dataset included Gross Tumour Volume (GTV) segmentation which is defined as the gross palpable or visible/demonstrable extent and location of malignant growth [18]. For the purpose of this study, we considered GTV and TC equivalent volumes where to perform radiomics analysis in Fig.1. We have demonstrated the equivalence of these two volumes in previous work [19].

For each patient, 143 imaging features were extracted from each scan. The radiomics analysis was performed using SPAARC Pipeline for Automated Analysis and Radiomics Computing (SPAARC) [20], [21] which is an IBSI compliant software package [22] written in MATLAB (The MathWorks, Natick USA).

The study was designed to investigate the ability of radiomics features based on MRI scans to risk-stratify on GBM patients. The integration of radiomics-based risk stratification within the oncology landscape carries profound implications for transforming clinical decision-making and achieving significant advancements in patient outcomes. Radiomic feature selection was carried out using the LASSO Cox regression method. Selected features were then used on the training cohort to build a stratification model. An RRS, was constructed by linearly combining the features chosen with LASSO technique within the training cohort and multiplying them with their corresponding coefficients [12]. The median value of the RRS was used as a fixed cut-off for stratifying low-risk and high-risk groups. Additionally, we used a range of machine learning (ML) techniques to build alternative risk stratification models and compared their performance with the RSS model. The ML techniques used in this work were: Logistic Regression, Support Vector Machine, Decision Tree, Random Forest and Neural Networks. For both ML approach and RSS method, the precise evaluation of the expected overall survival was tested by implementing the Kaplan–Meier (KM) survival analysis and log-rank test. The KM curve is a graphical representation of the estimated probability of survival over time, and it is frequently used in survival analysis to evaluate the results of medical research. KM plots were used to compare survival times across low-risk and high-risk groups on both training and testing cohorts for T1, T1ce, T2 and T2-FLAIR modalities. P-values < 0.05 were accepted as significant. For ML models, the low-risk and high-risk stratification was based on grid search to determine a cut-off on overall survival (OS). This method searches the optimum cut-off which is OS in month by trying to reach the minimum P-value.

RESULTS

In Table 1, the performance of the RRS method for all available modalities in the datasets is reported. The table includes the P-value for tests carried out with both BraTS and STORM_GLIO datasets. The data indicate that the model based on the T2 modality provides significantly higher performance for risk stratification while its application generalises well an unseen dataset (STORM_GLIO).

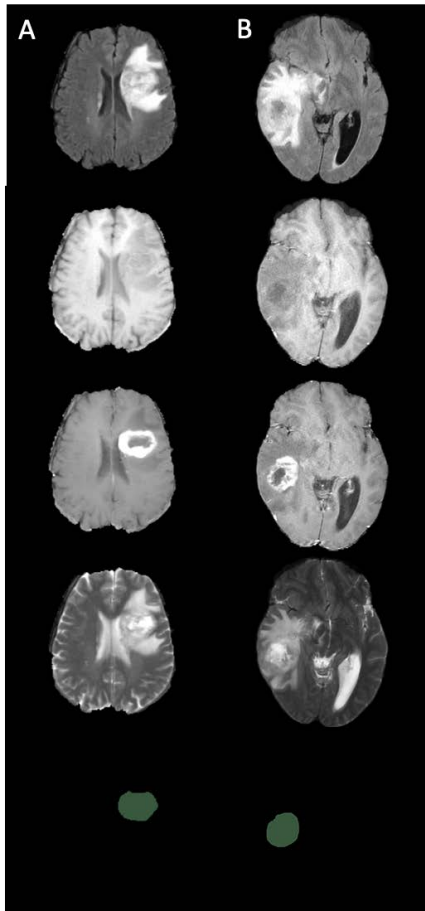


Fig. 1. Example of A) TC delineation from the BraTS dataset and B) GTV delineations from the STORM_GLIO dataset. From top to bottom modalities; T1, T1ce, T2 and T2-FLAIR and Reference contour.

Modality	BraTS Testing	STORM_GLIO
T1	0.01	0.22
T1ce	0.14	0.86
T2	0.0007	0.001
T2-FLAIR	0.003	0.94

Table 1. Performance of the RSS method for BraTS and STORM_GLIO dataset (P-value < 0.05 is significant).

Method	BraTS Testing	STORM_GLIO Testing
RRS	0.0007	0.001
Logistic Regression	0.01	5.75x10-5
Decision Tree	0.26	0.91
Random Forest	0.046	0.002
Support Vector Machine	0.01	0.0016
Neural Networks	0.007	0.75

Table 2. Performance of RRS and ML models for T2 modality (P-value < 0.05 is significant)

Fig. 2 shows KM curves of Logistic Regression and RRS method for STORM_GLIO dataset. The survival probability of RRS remained constant along the X-axis at a value of 0.2 from 5-month of OS to over 15-month of OS. On the other hand, that of Logistic Regression in the same figure remained constant at a less value than 0.2 which resulted in a significantly better P-value in Table 2.

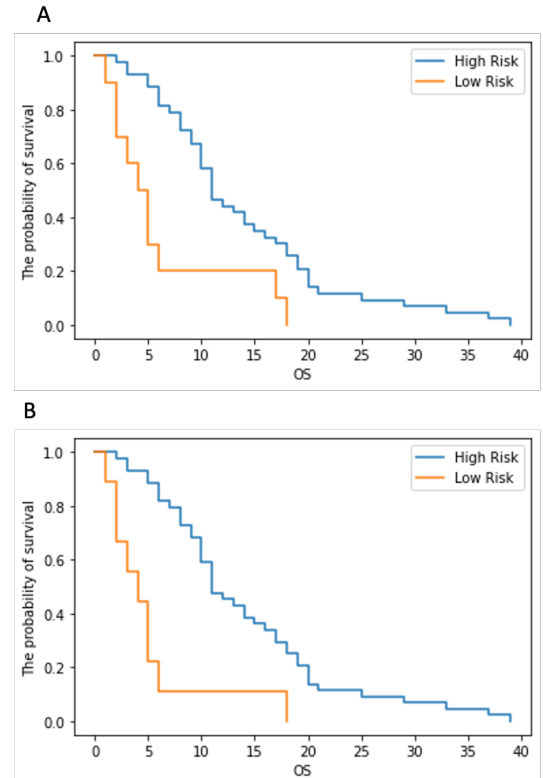


Fig. 2. The KM curve of T2 modality for A) RRS score with a median cut-off and B) Logistic Regression (The blue line represents high-risk group and the orange line represents low-risk group).

DISCUSSION

To the best of our knowledge, this is the first time that RRS and ML approaches are compared in their ability to risk-stratify on GBM patients. Although the performance of ML approaches used in the BraTS dataset was inferior to RRS, our results suggest that they can be considered as an alternative method for risk stratification based on overall survival information. The generalisability of stratification models is an important factor for clinical implementations and the logistic regression model performed well when tested on local MRI scans of GBM.

Acknowledgments

This work was sponsored by the Turkish Ministry of National Education..

Conflicts of interest

The authors declare no conflict of interest.

REFERENCES

- [1] L. M. DeAngelis, 'Brain Tumors', *New England Journal of Medicine*, vol. 344, no. 2, pp. 114-123, Jan. 2001. doi.org/10.1056/NEJM200101113440207
- [2] [2] K. Chang *et al.*, 'Multimodal imaging patterns predict survival in recurrent glioblastoma patients treated with bevacizumab', *Neuro Oncol*, vol. 18, no. 12, pp. 1680-1687, 2016 doi.org/10.1093/neuonc/now086
- [3] M. A. Qazi *et al.*, 'Intratumoral heterogeneity: pathways to treatment resistance and relapse in human glioblastoma', *Annals of Oncology*, vol. 28, no. 7, pp. 1448-1456, 2017. doi.org/10.1093/annonc/mdx169
- [4] S. Banerjee, H. S. Arora, and S. Mitra, 'Ensemble of CNNs for Segmentation of Glioma Sub-regions with Survival Prediction', in *Brainlesion: Glioma, Multiple Sclerosis, Stroke and Traumatic Brain Injuries*, 2020, pp. 37-49. doi.org/10.1007/978-3-030-46643-5_4
- [5] J. Müller Bark, A. Kulasinghe, B. Chua, B. W. Day, and C. Punyadeera, 'Circulating biomarkers in patients with glioblastoma', *Br J Cancer*, vol. 122, no. 3, pp. 295-305, 2020. doi.org/10.1038/s41416-019-0603-6
- [6] I. Dagogo-Jack and A. T. Shaw, 'Tumour heterogeneity and resistance to cancer therapies', *Nat Rev Clin Oncol*, vol. 15, no. 2, pp. 81-94, 2018. doi.org/10.1038/nrclinonc.2017.166
- [7] N. Beig, K. Bera, and P. Tiwari, 'Introduction to radiomics and radiogenomics in neuro-oncology: implications and challenges', *Neurooncol Adv*, vol. 2, no. Supplement_4, pp. iv3-iv14, Dec. 2020. doi.org/10.1093/nojnl/vdaa148
- [8] A. Shaheen, S. T. Bukhari, M. Nadeem, S. Burigat, U. Bagci, and H. Mohy-ud-Din, 'Overall Survival Prediction of Glioma Patients With Multiregional Radiomics', *Front Neurosci*, vol. 16, 2022. doi.org/10.3389/fnins.2022.911065
- [9] R. J. Gillies, P. E. Kinahan, and H. Hricak, 'Radiomics: Images Are More than Pictures, They Are Data', *Radiology*, vol. 278, no. 2, pp. 563-577, Nov. 2015, doi: 10.1148/radiol.2015151169. doi.org/10.1148/radiol.2015151169
- [10] X. Wang, T. Xie, J. Luo, Z. Zhou, X. Yu, and X. Guo, 'Radiomics predicts the prognosis of patients with locally advanced breast cancer by reflecting the heterogeneity of tumor cells and the tumor microenvironment', *Breast Cancer Research*, vol. 24, no. 1, p. 20, 2022, doi.org/10.1186/s13058-022-01516-0
- [11] X. Han, W. Cao, L. Wu, and C. Liang, 'Radiomics assessment of the tumor immune microenvironment to predict outcomes in breast cancer', *Front Immunol*, vol. 12, p. 5356, 2022. doi.org/10.3389/fimmu.2021.773581
- [12] N. Beig *et al.*, 'Radiogenomic-Based Survival Risk Stratification of Tumor Habitat on Gd-T1w MRI Is Associated with Biological Processes in Glioblastoma', *Clin Cancer Res*, vol. 26, no. 8, pp. 1866-1876, Apr. 2020. doi.org/10.1158/1078-0432.CCR-19-2556
- [13] B. H. Menze *et al.*, 'The Multimodal Brain Tumor Image Segmentation Benchmark (BRATS)', *IEEE Trans Med Imaging*, vol. 34, no. 10, pp. 1993-2024, 2015. doi.org/10.1109/TMI.2014.2377694
- [14] S. Bakas *et al.*, 'Advancing the cancer genome atlas glioma MRI collections with expert segmentation labels and radiomic features', *Sci Data*, vol. 4, no. 1, pp. 1-13, 2017. doi.org/10.1038/sdata.2017.117
- [15] S. Bakas *et al.*, 'Identifying the best machine learning algorithms for brain tumor segmentation, progression assessment, and overall survival prediction in the BRATS challenge', *arXiv preprint arXiv:1811.02629*, 2018.
- [16] F. Isensee *et al.*, 'Automated brain extraction of multisequence MRI using artificial neural networks', *Hum Brain Mapp*, vol. 40, no. 17, pp. 4952-4964, Dec. 2019. doi.org/10.1002/hbm.24750
- [17] B. H. Menze *et al.*, 'The Multimodal Brain Tumor Image Segmentation Benchmark (BRATS)', *IEEE Trans Med Imaging*, vol. 34, no. 10, pp. 1993-2024, 2015. doi: 10.1109/TMI.2014.2377694
- [18] D. Jones, 'ICRU Report 50-Prescribing, Recording and Reporting Photon Beam Therapy', *Med Phys*, vol. 21, no. 6, pp. 833-834, Jun. 1994. doi.org/10.1118/1.597396
- [19] A. Duman, P. Whybra, J. Powell, S. Thomas, X. Sun, and E. Spezi, 'Transferability of deep learning models to the segmentation of gross tumour volume in brain cancer', in *Estro 2023 Conference (Accepted)*, 2023. doi.org/10.1016/S0167-8140(23)66535-1
- [20] P. Whybra, C. Parkinson, K. Foley, J. Staffurth, and E. Spezi, 'Assessing radiomic feature robustness to interpolation in 18F-FDG PET imaging', *Sci Rep*, vol. 9, no. 1, p. 9649, 2019. doi.org/10.1038/s41598-019-46030-0.
- [21] C. Piazzese, K. Foley, P. Whybra, C. Hurt, T. Crosby, and E. Spezi, 'Discovery of stable and prognostic CT-based radiomic features independent of contrast administration and dimensionality in oesophageal cancer', *PLoS One*, vol. 14, no. 11, p. e0225550, 2019. doi.org/10.1371/journal.pone.0225550
- [22] A. Zwanenburg *et al.*, 'The image biomarker standardization initiative: standardized quantitative radiomics for high-throughput image-based phenotyping', *Radiology*, vol. 295, no. 2, pp. 328-338, 2020. doi.org/10.1148/radiol.2020191145

Foster I

*Cardiff University
School of Engineering*

Spezi E

*Cardiff University
School of Engineering*

Wheeler P

*Velindre NHS Trust
Velindre Cancer Centre, Cardiff*

ENGINEERING FOR HEALTH

Inter-planner Variability in Expert Driven Pareto-guided Automated Planning Solutions

An intra-planner study has been carried out to compare planning choices among qualified professionals when utilising Pareto-guided automated planning (PGAP) navigation. PGAP was used to calibrate planning goal weights of a protocol-based automatic iterative optimisation automated planning system. Four qualified professionals (Participant A-D) navigated solutions for eight prostate seminal vesicle (PSV) patient cases using PGAP. Plans were based on an existing clinically approved planning protocol containing seven planning goals (PGs). Three PG weights were navigated per plan (rectum Dmean, bladder Dmean and PTV conformality) with all other weights held constant at a value assigned in the original clinically approved protocol. Statistically significant differences were observed between participants for all PG groups except bladder Dmean. However, dosimetrically the PGAP system mitigated the majority of discrepancies in deviations at the calibration stage with few statistically significant dose-volume metric differences observed, none of which were clinically significant.

Keywords:

Pareto optimisation, radiotherapy planning, prostate cancer, inter-observer variability.

Corresponding author:

FosterID@cardiff.ac.uk



I. Foster, E. Spezi, and P. Wheeler, 'Inter-planner Variability in Expert Driven Pareto-guided Automated Planning Solutions', *Cardiff University School of Engineering Research Conference 2023*, Cardiff, UK, 2023, pp. 23-26.

doi.org/10.18573/conf1.g

INTRODUCTION

Automated planning (AP) is fast becoming the state-of-the-art in radiotherapy planning for intensity-modulated radiotherapy (IMRT) and volumetric-modulated radiotherapy (VMAT) [1, 2, 3] and can be classified into one of two categories: knowledge-based planning (KBP) or rules-based planning (RBP). KBP uses statistical techniques [4, 2, 5, 6] and is trained on historical clinical datasets to inform planning for novel cases through prediction of optimisation objectives [7], dose-volume histograms [8, 9] or voxel-level dose [2]. RBP employs logic to converge on a solution. For example, a lexicographic ordering that optimises planning goals (PGs) in strict sequential order [10, 11, 12] and protocol-based automatic iterative optimisation (PBAIO) that uses algorithms to automatically adapt planning parameters during optimisation.

Protocol based automatic iterative optimisation (PBAIO) uses common protocols for patients within a cancer site. This leads to improved quality compared to manual planning although may not result in individualised planning. The most clinically desirable plans are “Pareto optimal” meaning no dosimetric improvements can be made to anyone planning goal except at the detriment of another. “Pareto guided automated planning” (PGAP) refers to any branch of AP that incorporates Pareto navigation as part of its functionality and studies suggest such methods have may have congruence with oncological preference leading to clinically desirable solutions [13, 14, 15]. However, even in highly regulated fields such as radiotherapy planning where qualified practitioner adhere to strict local and universal practices, it is not unreasonable to expect some variance in performance.

This study aims to explore discrepancies in choices made by different qualified practitioners when using PGAP built on a PBAIO framework known as the Experience Driven Plan Generation Engine by Velindre Cancer Centre or EdgeVcc. Given a PGAP system is used, it is hypothesised the interactive and intuitive nature of this approach enables observer-relative interpretations of oncological preference. Hence, findings of this work will help to determine the clinically relevant region of the Pareto front as defined by a range of qualified individuals.

MATERIALS AND METHODS

All sessions took place between 1 December 2019 and 28 February 2020 and 4 participants were selected to take part:

- medical physicist (Participant A)
- two oncologists (Participant B and D).
- professional planner (Participant C)

Participants were fully qualified, highly familiar with the prostate seminal vesicles (PSV) treatment site and had multiple years of experience. Plan generation with EdgeVcc is dependent upon a base site-specific “AutoPlan protocol” containing a set of prioritised planning goals (PGs). The PGs are prioritised according to assigned weight values defined using the Pareto navigation functionality in EdgeVcc. Figure 1 shows a CT scan of a typical patient including delineated regions used during planning.

The base AutoPlan protocol contains seven PGs and had been designed for clinical use and validated prior to this study. The weights for PGs 1-3 were navigated by participants in this study with all other PG weights held constant. PG 1-3 were as following: (1) rectum D_{mean} , (2)

bladder D_{mean} and (3) PTV conformality. Navigated PGs were chosen for this study based on preliminary research of PGs showing the most significant trade-off relationships.

Eight PSV patients were randomly chosen for this retrospective study. This number of patients was chosen because Pareto plan generation is computationally expensive and in addition, navigation of large numbers of patients can become a time-consuming task for participants outside of their clinical duties. This set of patients was therefore chosen such that the number of cases was considered large enough to observe a sufficient range of anatomies but small enough not to become unnecessarily time-consuming for participants.

Observers completed the task in an environment fit for clinical planning and had access to the clinical goals defined by an oncologist and could interact with the TPS however they desired. However, given not all participants were familiar with the PGAP system, they were all required to complete a practice case before completing the eight study cases. The results of the practice case were not considered in this study. Resulting plans were compared for difference in terms of relative weighting factors and dosimetric features and were tested using ANOVA when appropriate and a Friedman test otherwise. Sørensen–Dice coefficients (DiceC) were also used to describe similarity between participant choices.



Fig. 1. An example sagittal plane indicating delineated regions-of-interest used during planning. Shown are the external contour (purple), bladder (yellow), rectum (brown), high dose PTV (red), low dose PTV (orange).

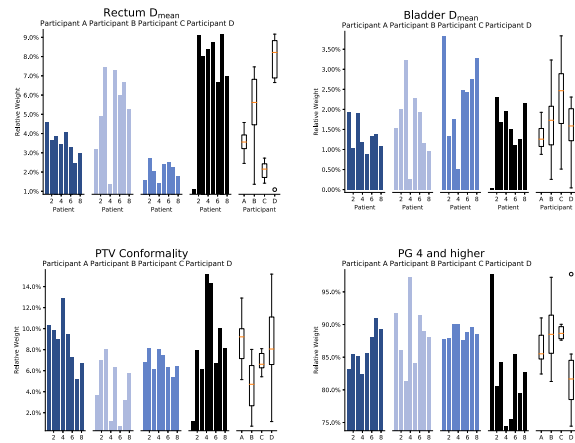


Fig. 2. Relative weights of the three navigated planning goals (rectum D_{mean} , bladder D_{mean} and PTV conformality) and non-navigated planning goals (PG 4 and higher).

RESULTS

Weights

Differences were observed between participants for all PG groups except bladder D_{mean} (Figure 2). For rectum D_{mean} , the highest degree of similarity was observed between B and D with a DiceC values 0.884. The PG with the highest degree of agreement between participants was bladder D_{mean} . The DiceC metric indicates A&C prioritised PTV conformality similarly with a values of 0.950. All DiceC values are higher than 0.99 for the PG 4 and higher group.

Dosimetry

DVH Statistic		Participant A	Participant C	Participant B	Participant D
PTV60	$D_{98\%}$ (Gy)	57.6 ± 0.3	57.7 ± 0.2	57.6 ± 0.3	57.5 ± 0.3
	$D_{2\%}$ (Gy)	61.7 ± 0.1	61.6 ± 0.1	61.7 ± 0.1	61.7 ± 0.1
	CI	0.85 ± 0.0	0.82 ± 0.02	0.845 ± 0.01	0.84 ± 0.02
PTV48	$D_{98\%}$ (Gy)	46.2 ± 0.2	46.4 ± 0.5	46.4 ± 0.24	46 ± 0.64
	$D_{2\%}$ (Gy)	59.2 ± 0.2	59.4 ± 0.3	59.2 ± 0.1	59.3 ± 0.3
	CI	0.82 ± 0.02	0.72 ± 0.06	0.81 ± 0.02	0.77 ± 0.04
Rectum	$V_{24.3Gy}$ (%)	27.2% ± 5.8%	25.3% ± 5.2%	28.6% ± 5.9%	24.8% ± 4.7%
	$V_{56.8Gy}$ (%)	5.25% ± 1.4%	5.16% ± 1.5%	5.32% ± 1.5%	4.78% ± 1.1%
	D_{mean} (Gy)	17.9 ± 2.8	17.0 ± 2.8	18.7 ± 2.8	16.7 ± 2.3
Bladder	$V_{40.5Gy}$ (%)	12.6% ± 6.3%	12.9% ± 6.7%	12.5% ± 6.4%	12.8% ± 6.3%
	$V_{56.8Gy}$ (%)	4.8% ± 2.7%	5.1% ± 3.0%	4.8% ± 2.7%	4.9% ± 2.8%
	D_{mean} (Gy)	15.9 ± 6.4	15.2 ± 6.2	15.5 ± 6.7	15.7 ± 6.3

Table 1. Summary of key dose metrics. Values shown are mean ± 1 standard deviation and statistical difference at the 95% level of significance indicated in boldface.

As reported in Table 1, differences were observed between participant C&D for PTV60 $D_{98\%}$ (Gy). Higher doses were observed for C than D with a mean difference of 0.155 Gy. PTV48 differences were observed for $D_{50\%}$ (Gy) related to participants A&B only. Observed dose was lower for A than B with a mean difference of 0.832 Gy. For CI60 observed difference relate to participant A&B with observed indices low for A on average given a mean difference of 0.0315 units. CI48 saw participant B observe lower indices than all other participants with deviations of 0.0973, 0.0899 and 0.0546 units for A, C and D respectively. All observed difference were considered clinically small indicating differences in planning decisions may be clinically negligible with this PGAP system.

DISCUSSION

There still exists a gap in the literature for further inter-planner studies, but of those that do exist, there is evidence showing inconsistencies in participant choices [16, 17, 18, 19]. Given this expectation, the aim of applying PGAP to mitigate discrepancies was explored here with a view of observing clinically significant differences. It was observed that oncologists (participant B and D) applied a higher priority to sparing the rectum than do planners or physicists. Following interviews with the participants, participant B stated a preference to push dose in the anterior direction to help spare the rectum even at some cost to conformality or even increasing dose to the bladder. This participant considered the rectum a notably

higher clinical priority over the bladder and would increase sparing of the rectum given a suitable dose distribution to PTVs was still achieved and all clinical goals were being met.

A key difference between the oncologists in this study was the tendency for participant D to use a higher range of the navigation scale than participant B. The tendency of participant D to use the higher end of the scale resulted in a generally higher priority to the navigated PGs over the other PGs than is seen for any other participant. However, interviews with participant D revealed simple preferences. Participant D wanted to ensure the achievement of the clinical goals but had fewer concerns about the planning details than some of the other participants. Although traditional IMRT planning methods have been criticised for being tedious and lacking an intuitive approach that facilitates interaction of physicians [13], this work suggests clinical preference can at times be broad. The number of clinically applicable choices can be overwhelming for physicians even with the use of intuitive techniques such PGAP.

The physicist (participant A) and the planner (participant C) performed the most similarly by default with participant A in particular showing notably greater levels of consistency in planning choices between patients. Nevertheless, the PBAIO system was valuable in mitigated the majority of discrepancies in deviations at the calibration stage with few statistically significant dosimetric differences observed none of which were clinically significant.

CONCLUSION

There is evidence that expert-driven PGAP can be used to deliver consistent dosimetric planning with the clinically relevant region of the Pareto front defined comparably by any expert.

Conflicts of interest

The authors declare no conflict of interest.

REFERENCES

- [1] M. Hussein, B.J.M. Heijmen, D. Verellen, and A. Nisbet, 'Automation in intensity modulated radiotherapy treatment planning-a review of recent innovations', *British Journal of Radiology*, vol. 91, no. 1092, p. 20180270, 2018.
doi.org/10.1259/bjr.20180270
- [2] Y. Ge and Q.J. Wu, 'Knowledge-based planning for intensity-modulated radiation therapy: A review of data-driven approaches', *Medical Physics*, vol. 46, no. 6, pp. 2760-2775, 2019.
doi.org/10.1002/mp.13526
- [3] C. Parkinson, C. Matthams, K. Foley, and E. Spezi, 'Artificial intelligence in radiation oncology: A review of its current status and potential application for the radiotherapy workforce', *Radiography*, vol. 27, pp. S63-S68, 2021.
doi.org/10.1016/j.radi.2021.07.012
- [4] S. Momin, Y. Fu, Y. Lei, J. Roper, J.D. Bradley, W.J. Curran, T. Liu, and X. Yang, 'Knowledge-based radiation treatment planning: A data-driven method survey', *Medical Physics*, vol. 22, no. 8, pp. 16-44, 2021.
doi.org/10.1002/acm2.13337
- [5] M. Zarepisheh, T. Long, N. Li, Z. Tian, H.E. Romeijn, X. Jia, and S.B. Jiang, 'A DVH-guided IMRT optimization algorithm for automatic treatment planning and adaptive radiotherapy replanning', *Medical Physics*, vol. 41, no. 6Part1, p. 061711, 2014.
doi.org/10.1118/1.4875700
- [6] L. Yuan, Y. Ge, W.R. Lee, F.F. Yin, J.P. Kirkpatrick, and Q.J. Wu, 'Quantitative analysis of the factors which affect the interpatient organ-at-risk dose sparing variation in IMRT plans', *Medical Physics*, vol. 39, no. 11, pp. 6868-78, 2012.
doi.org/10.1118/1.4757927
- [7] J.J. Boutilier, T. Lee, T. Craig, M.B. Sharpe, and T.C.Y. Chan, 'Models for predicting objective function weights in prostate cancer IMRT', *Medical Physics*, vol. 42, no. 4, pp. 1586-1595, 2015.
doi.org/10.1118/1.4914140
- [8] J. Ma, D. Nguyen, T. Bai, M. Folkerts, X. Jia, W. Lu, L. Zhou, and S. Jiang, 'A Feasibility Study on Deep Learning--Based Individualized 3D Dose Distribution Prediction', *Medical Physics*, vol. 48, no. 8, pp. 4438-4447, 2021.
doi.org/10.1002/mp.15025
- [9] E. Cagni, A. Botti, A. Chendi, M. Iori, and E. Spezi, 'Use of knowledge based DVH predictions to enhance automated re-planning strategies in head and neck adaptive radiotherapy', *Physics in Medicine & Biology*, vol. 66, no. 13, 2021.
doi.org/10.1088/1361-6560/ac08b0
- [10] A.C. Spalding, K.-W. Jee, K. Vineberg, M. Jablonowski, B.A. Fraass, C.C. Pan, T.S. Lawrence, R.K. Ten Haken, and E. Ben-Josef, 'Potential for dose-escalation and reduction of risk in pancreatic cancer using IMRT optimization with lexicographic ordering and gEUD-based cost functions', *Medical Physics*, vol. 34, no. 2, pp. 521-529, 2007.
doi.org/10.1118/1.2426403
- [11] S. Breedveld, P.R. Storchi, M. Keijzer, A.W. Heemink, and B. J. Heijmen, 'A novel approach to multi-criteria inverse planning for IMRT', *Physics in Medicine & Biology*, vol. 52, no. 20, p. 6339, 2007.
doi.org/10.1088/0031-9155/52/20/016
- [12] M.-C. Biston, M. Costea, F. Gassa, A.-A. Serre, P. Voet, R. Larson, and V. Gregoire, 'Evaluation of fully automated a priori MCO treatment planning in VMAT for head-and-neck cancer', *Physica Medica*, vol. 87, pp. 31-38, 2021.
doi.org/10.1016/j.ejmp.2021.05.037
- [13] D.L. Craft, T.S. Hong, H.A. Shih, and T.R. Bortfeld, 'Improved planning time and plan quality through multicriteria optimization for intensity-modulated radiotherapy', *International Journal of Radiation Oncology-Biology-Physics*, vol. 82, no. 1, p. e83-e90, 2012.
doi.org/10.1016/j.ijrobp.2010.12.007
- [14] P.A. Wheeler, M. Chu, R. Holmes, O.W. Woodley, C.S. Jones, R. Maggs, J. Staffurth, N. Palaniappan, E. Spezi, D.G. Lewis, S. Campbell, J. Fitzgibbon, and A.E. Millin, 'Evaluating the application of Pareto navigation guided automated radiotherapy treatment planning to prostate cancer', *Radiotherapy & Oncology*, pp. 220-226, 2019.
doi.org/10.1016/j.radonc.2019.08.001
- [15] P.A. Wheeler, M. Chu, R. Holmes, M. Smyth, R. Maggs, E. Spezi, J. Staffurth, D.G. Lewis, and A.E. Millin, 'Utilisation of Pareto navigation techniques to calibrate a fully automated radiotherapy treatment planning solution', *Physics and Imaging in Radiation Oncology*, pp. 41-48, 2019.
doi.org/10.1016/j.phro.2019.04.005
- [16] I. Das, K. Cashion, K. Chopra, K. Khadivi, H. Malhotra, and C. Mayo, 'WE-E-T-617-06: Intra- and inter-planner dosimetric variations in inverse planning of IMRT', *Medical Physics*, vol. 32, no. 6Part20, pp. 2147-2147, 2005.
doi.org/10.1118/1.1998607
- [17] S. Srivastava, O. Nohadani, C. Medawar, C. Cheng and I. Das, 'Su-e-t-604: Inter planner dosimetric variations in imrt', *Medical Physics*, vol. 39, no. 6, Part 19, p. 3845, 2012.
doi.org/10.1118/1.4735693
- [18] Y.E. Erkal, A. Karabey, M.C. Sahin, A. Karayel, B. Tirpanci and H.Ş. Erkal, 'Intensity- modulated radiotherapy planning for prostate cancer: The evaluation of inter-observer variability and treatment delivery efficiency', *International Journal of Radiation Research*, vol. 20, no. 1, pp. 49-53, 2022.
doi.org/10.52547/ijrr.20.1.8
- [19] M. Esposito, G. Maggi, C. Marino, L. Bottalico, E. Cagni, C. Carbonini, M. Casale, S. Clemente, V. D'Alesio, D. Fedele, F. R. Giglioli, V. Landoni, and A. Martinotti, 'Multicentre treatment planning inter- comparison in a national context: the liver stereotactic ablative radiotherapy case', *Physica Medica*, vol. 32, no. 1, pp. 277-283, 2016.
doi.org/10.1016/j.ejmp.2015.09.009

Civil Infrastructure



Civil Infrastructure

- 29 A 3D Coupled Finite Element Model for Self-Healing Quasi-Brittle Materials
- 34 Pinball Tendons Crack Closure Technology
- 39 Smart Activation System for the Hybrid Tendons Crack Closure Technology
- 44 3D-Printed Mini-vascular Networks for Self-healing Lime-based Mortars
- 48 Agricultural Waste as a Cementitious Material – Rice Husk Ash
- 52 Waste Foundry Sand (WFS) as Aggregate Replacement for Green Concrete
- 55 Biomimetic Materials in Construction Industry: the Necessity of Simulation
- 58 Characterisation of Innovative Mortar Formulations for the Restoration of Roman Mosaics
- 62 Modelling Buildings During Flood Inundation Using TELEMAC-2D
- 66 Shrinkage Potential and Water Transport Properties of Self-compacting Concrete at Different Temperatures
- 70 Determining Surface Velocity Coefficients in Headwater Streams for Natural Flood Management
- 75 Simulating Flood Hazard in Wye Valley during Storm Dennis using Hec-Ras
- 80 Influence of Healing Agents and Concrete Environment on PLA 3D Printed Mini-vascular Networks for Self-healing Concrete Structures

Freeman B

*Cardiff University
School of Engineering*

Jefferson A

*Cardiff University
School of Engineering*

CIVIL INFRASTRUCTURE

A 3D Coupled Finite Element Model for Self-Healing Quasi-Brittle Materials

This study presents an overview of a 3D coupled finite element model for self-healing quasi-brittle materials. The model was developed alongside a linked experimental programme such that model components were formulated based on observed material behaviour and physical processes. The mechanical model comprises an embedded strong discontinuity element for representing discrete macro-cracks and a linked damage-healing cohesive-zone model. This is coupled to a transport model that simulates the reactive transport of healing agents in both discrete macro-cracks and the surrounding matrix material. For the simulation of the healing reaction that governs crack sealing and mechanical regain, a generalised healing front model is employed. The performance of the model is demonstrated through the consideration of the healing of a cementitious specimen. The results show that the model can accurately reproduce the crack filling predicted by a cement hydration model, and naturally accounts for the effect of healing period and crack width.

Keywords:
*Self-healing, numerical modelling,
finite element method, concrete,
quasi-brittle materials.*

Corresponding author:
FreemanBL@cardiff.ac.uk



B. Freeman and A. Jefferson, 'A 3D Coupled Finite Element Model for Self-Healing Quasi-Brittle Materials', *Cardiff University School of Engineering Research Conference 2023*, Cardiff, UK, 2023, pp. 29-33.

doi.org/10.18573/conf1.h

INTRODUCTION

Self-healing materials offer great potential for increased durability, leading to reduced maintenance costs (in terms of both time and money) and increased service life. As a result of this, the development of self-healing quasi-brittle materials such as concrete has been subject to a great deal of interest [1]. Alongside this work, the development of numerical models for simulating the self-healing response has received increasing attention. Whilst initial works focused principally on the mechanical behaviour [2-4], more recent developments have included coupled models that simulate the physical processes governing the healing response [5,6]. It is noted however, that to date no unified model framework for self-healing materials, nor a complete experimental dataset to provide the necessary properties, exists [7].

This study describes a model developed as part of a combined experimental-numerical programme of work. The aim of the work was to develop model components based on an understanding of the physical processes, and to obtain a complete dataset for a particular self-healing system. The experimental work is reported in [8,9], whilst the model components are reported in [10-13]. The work initially focused on a self-healing concrete system with embedded vascular networks and a cyanoacrylate healing agent, though has since been extended to alternative healing systems and agents [13].

This study presents an overview of the model and its extension to healing due to further hydration where multiple healing phases are precipitated within the crack. Model predictions are compared to the results of a cement hydration model (CemPP, a version of CEMHYD3D [14,15]), before an illustrative example concerning a direct tension test, with varying healing crack width and healing periods, is presented.

THEORETICAL BASIS

Model Overview

This study presents an overview 3D coupled chemo-mechanical finite element model developed to simulate the physical processes governing the self-healing behaviour of quasi-brittle materials such as concrete. The various components of the model include:

- An embedded strong discontinuity element for representing discrete macro-cracks [10],
- A cohesive zone damage-healing model that allows for simultaneous and an arbitrary number of cycles of damage and healing [12],
- An unfitted finite element for representing the healing agent spread in 2D discrete cracks [13],
- A healing agent transport model for flow through the discrete cracks, the surrounding continuum matrix material, and, if present, embedded vascular networks [11,13,16],
- A healing front model for simulating the build-up of healed material, emanating from the crack faces [11,12].

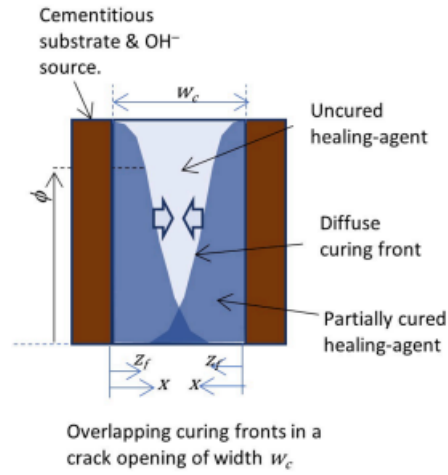


Fig. 1. Conceptual diagram of healing front model that governs crack sealing and mechanical regain (reproduced from [12] with permission)

A conceptual diagram of the healing front model component (that is a key focus of the present work), can be seen in Figure 1.

In the present work, the example problem considered is under saturated conditions and healing and damage occur independently. As such, for brevity, the presentation is focused on the cohesive zone model and healing front model, which herein is extended to the case of multiple healing phases. For further details on the other model components, the interested reader is referred to the papers cited above.

Cohesive Zone Model

The cohesive zone model relates the crack-plane traction vector ($\boldsymbol{\tau}_c$) to the relative displacement vector (\mathbf{u}) as follows:

$$\boldsymbol{\tau}_c = (1 - \omega) \cdot \mathbf{K} : \mathbf{u} + h \cdot \mathbf{K} : (\mathbf{u} - \mathbf{u}_h) \quad (1)$$

where $\omega \in [0,1]$ is the damage variable, \mathbf{K} is the elastic stiffness, h is the degree of healing and \mathbf{u}_h is the relative displacement at the time of healing. Damage evolution is governed by an exponential softening function [12]:

$$\omega = 1 - \frac{u_t}{\delta} e^{-c \frac{\delta - u_t}{u_m - u_t}} \quad (2)$$

in which $u_t = f_t/K$, where f_t is the tensile strength of the material, $c = 5$ is a softening constant, u_m is the relative displacement at the end of the softening curve and δ is the damage evolution parameter that depends on the maximum value of the inelastic relative displacements.

Mechanical healing is observed once healed material bridges the crack, and -in the absence of re-damage- is given by the total relative area of healed material (φ_{tot}) at the centre of the crack [12]:

$$h(w, t) = \varphi_{tot} \left(\frac{w}{2}, t \right) \quad (3)$$

Healing with Multiple Phases

The healing reaction concerns the precipitation of healed material in the crack, emanating from the crack faces. This process can be simulated as the propagation of a diffuse reaction front, and can be described by the following, derived from an analytical solution of the advection-diffusion equation [11]:

$$\varphi_{ph}(x, t) = \frac{\varphi_{ph}^{max}}{2} \left(1 - \tanh \left(\left(\frac{2}{\sqrt{\pi}} \right) \left(\frac{x - z(t) - z_{c2}}{z_{c2} + \sqrt{\frac{z(t)}{z_{c1}}}} \right) \right) \right) \quad (4)$$

It is noted that in the present work, we have employed Equation (4) to directly describe the propagation (or build-up) of a diffuse front of healed material, as opposed to considering an advection-diffusion-reaction system. This approach is equivalent to an advection-diffusion-reaction system in which the reaction is sufficiently fast relative to the rates of transport. In this case, the profile of healed material (reaction products) is directly proportional to the concentrations of the reactants. The concentration of the reactants is governed by an advection-diffusion equation with a retardation factor and therefore, the profile of healed material can be described by an advection-diffusion equation.

An illustration of the behaviour of Equation (4) (and Equation (6)) can be seen in Fig. 2.

In (4), x denotes the position measured from the crack face and $z(t)$ is the position of the reaction front given by [11]:

$$z(t) = z_{c0} \left(1 - e^{-\frac{t}{\tau}} \right) \quad (5)$$

where z_{c0} is the critical reaction front depth and τ is the curing time parameter. Finally, z_{c2} is a wall factor and z_{c1} is a diffusion-like coefficient.

In previous works one phase of healed material was considered and the total profile of the relative area of healed material was given by Equation (4) (where $\varphi_{ph}^{max} = 1$). In the present work however, the example considered features multiple phases of healed material and as such, the total profile of the relative area of healed material becomes a summation given by:

$$\varphi_{tot}(x, t) = \sum_{ph=1}^{nph} \varphi_{ph}(x, t) \quad (6)$$

where φ_{ph} is the relative area of healed material of phase ph and nph is the number of healed phases. In addition, φ_{ph}^{max} is the maximum relative area of healed material for phase ph , and it is noted that the condition $\sum_{ph=1}^{nph} \varphi_{ph}^{max} \leq 1$ must be satisfied.

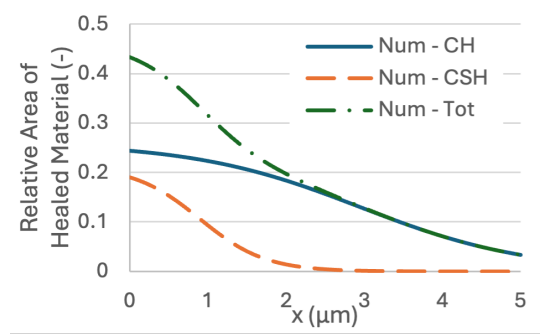


Fig. 2. Illustrative profiles of relative area of healed material as predicted by (4) and (6) (where CH denotes calcium hydroxide, CSH is calcium silicate hydrate and Tot is the total, i.e. CH+CSH).

NUMERICAL IMPLEMENTATION

In the present work the model is implemented in a finite element framework.

For the mechanical behaviour, embedded strong discontinuity elements are employed for the representation of discrete cracks, whilst the nonlinearity is dealt with using a Newton-Raphson procedure [13].

For the transport behaviour, an embedded discrete fracture method is used to describe the coupling between the flow in the porous matrix and the discrete cracks [11], an unfitted finite element method is used to describe the strong discontinuity at the healing agent interface within discrete cracks [13] and the nonlinearity is dealt with using a Picard procedure.

For further details on the numerical implementation, the interested reader is referred to [10-13]. The source code for a 2D version of the model is given in [12].

EXAMPLE PROBLEM

To demonstrate the performance of the model we consider the healing of a cementitious specimen due to further hydration, based on the results presented in [14]. In this example, further hydration leads to precipitation of Calcium hydroxide (CH) and calcium silicate hydrate (CSH) in the crack, with healing observed once the precipitates bridge the crack. In [14], the authors employ the cement hydration model CemPP (CEMHYD3D) to simulate further hydration in a 10 μ m crack, giving a prediction of the degree of healing as a function of healing time. In the present work, we first employ the healing front model to simulate the healing reaction. Following this, a direct tension test of a double-notched cementitious cube is simulated to illustrate the stress-crack mouth opening displacement (CMOD) response of the model with varying healing periods and CMOD at which healing begins.

The model parameters employed can be seen in Table 1, whilst a schematic of the direct tension test set up is shown in Fig. 3. In [14], the authors found that the degree of mechanical healing was approximately double the degree of healing at the centre of the crack. To reflect this, the mechanical parameters of the healed material were set to double that of the cementitious matrix.

Parameter	Value	Parameter	Value
E (GPa)	30	$z_{c1,CSH}$ (mm)	100
E_h (GPa)	60	τ_{CSH} (days)	42
ν, ν_h (-)	0.3	$z_{c0,CH}$ (mm)	0.03
f_t (MPa)	1.5	$z_{c1,CH}$ (mm)	100
f_{th} (MPa)	3	τ_{CH} (days)	1167
u_m (mm)	0.02	z_{c2} (mm)	0.0001
u_{mh} (mm)	0.0075	ϕ_{CSH}^{max} (-)	0.25
$z_{c0,CSH}$ (mm)	0.025	ϕ_{CH}^{max} (-)	0.324

Table 1. Model parameters.



Specimen dimensions = 100x100x100mm³
Notch depth = 25mm

Fig. 3. Schematic of direct tension test.

A comparison between the predictions of the healing front model and the results of [14] can be seen in Fig. 4.

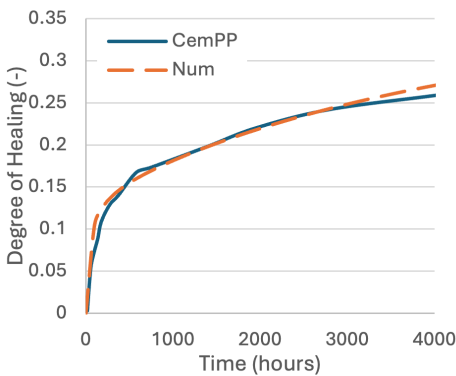


Fig. 4. Degree of healing of 10µm crack as predicted by CemPP [14] and present model.

The results of the direct tension test can be seen in Fig. 5.

DISCUSSION

The examples presented show that the multi-phase healing front model can accurately reproduce the results of the cement hydration model, CemPP (see Fig. 4). In addition, the direct tension test demonstrates that the model can account for both the effects of varying healing period and CMOD at the time of healing (see Fig. 5).

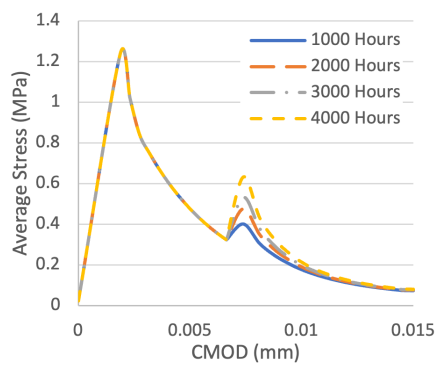
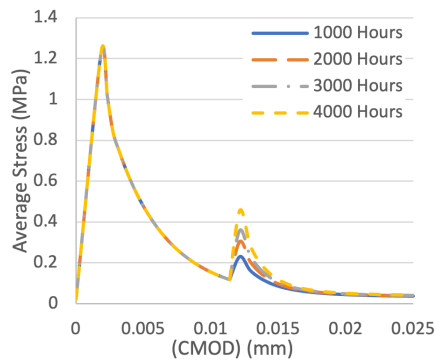


Fig. 5. Predicted Stress-CMOD response different healing periods and at CMODs of a) 0.011mm and b) 0.007mm respectively.

CONCLUSIONS

This study has provided an overview of a couple finite element model, developed as part of a combined experimental-numerical programme, for simulating self-healing quasi-brittle materials. The model features various components for simulating each of the physical processes that govern the healing response. The healing front model for simulating the build-up of healed material in discrete cracks has been extended to the case of multiple healing phases. The performance of the model has been demonstrated through the consideration of an example problem concerning the healing due to further hydration of a cementitious specimen, and its mechanical response in a direct tension test. The results of the example problem show that the extended healing front model can accurately reproduce the predictions of a cement hydration model, and that the coupled model naturally captures the effects of both the healing period and crack opening at the onset of healing.

Future work will investigate the extension of the model to further healing systems and agents.

Acknowledgements

Financial support from the UKRI-EPSC Grant EP/P02081X/1 "Resilient Materials for Life (RM4L)" is gratefully acknowledged.

Conflicts of interest

The authors declare no conflict of interest.

REFERENCES

- [1] N. De Belie *et al.*, 'A review on self-healing concrete for damage management of structures', *Adv Mater Interfaces*, 2018, 5:1-28.
doi.org/10.1002/admi.201800074
- [2] E.J. Barbero, F. Greco, and P. Lonetti, 'Continuum damage-healing mechanics with application to self-healing composites', *Int J Damage Mech*, 2005, 14:51-81.
doi.org/10.1177/1056789505045928
- [3] E.C. Schimmel and J.J.C. Remmers, 'Development of a constitutive model for self-healing materials', *Delft Aerospace Computational Science*, 2006, Report DACS-06-003.
- [4] S. Granger, G. Pijaudier-Cabot, and A. Loukili, 'Mechanical behaviour of self-healed ultra-high performance concrete: from experimental evidence to modeling', *Proceedings of the 6th International Conference on Fracture Mechanics of Concrete and Concrete Structures*, 2007, 3:1827-1834.
- [5] C. Romero Rodriguez *et al.*, 'Numerical investigation of crack self-sealing in cement-based composites with superabsorbent polymers'. *Cem Concr Compos*, 2019, 104:103395.
doi.org/10.1016/j.cemconcomp.2019.103395
- [6] A. Cibelli *et al.*, 'A discrete numerical model for the effects of crack healing on the behaviour of ordinary plain concrete: implementation, calibration and validation', *Eng Fract Mech*, 2022, 263:108266.
doi.org/10.1016/j.engfracmech.2022.108266
- [7] A.D. Jefferson *et al.*, 'Research progress on numerical models for self-healing cementitious materials', *Adv Mater Interfaces*, 2018, 5(17).
doi.org/10.1002/admi.201701378
- [8] T. Selvarajoo *et al.*, 'Mechanical response of a vascular self-healing cementitious material system under varying load conditions', *Const Build Mater*, 2020, 254:119245.
doi.org/10.1016/j.conbuildmat.2020.119245
- [9] T. Selvarajoo *et al.*, 'Characterisation of a vascular self-healing cementitious material system: flow and curing properties', *Const Build Mater*, 2020, 245:118332.
doi.org/10.1016/j.conbuildmat.2020.118332
- [10] B.L. Freeman *et al.*, 'A specialised finite element for simulating self-healing quasi-brittle materials', *Adv Model and Simul Engl Sci*, 2020, 7(32).
doi.org/10.1186/s40323-020-00171-4
- [11] B.L. Freeman and A.D. Jefferson, 'The simulation of transport processes in cementitious materials with embedded healing systems', *Int J Numer Anal Methods Geomech*, 2020, 44:293-326.
doi.org/10.1002/nag.3017
- [12] A.D. Jefferson and B.L. Freeman, 'A crack-opening-dependent numerical model for self-healing cementitious materials', *Int J Solids Struct*, 2022. 244-245:111601.
doi.org/10.1016/j.ijsolstr.2022.111601
- [13] B.L. Freeman and A.D. Jefferson, 'A 3D coupled finite element model for simulating mechanical regain in self-healing cementitious materials' *J Eng Mech*, 2023, 149(7):04023038.
doi.org/10.1061/JENMDT.EMENG-6944
- [14] B. Hilloulin *et al.*, 'Mechanical regains due to self-healing in cementitious materials: experimental measurements and micro-mechanical model', *Cem Concr Res*, 2016, 80:21-32.
doi.org/10.1016/j.cemconres.2015.11.005
- [15] D.P. Bentz, 'Three-dimensional computer simulation of Portland cement hydration and microstructure development', *J Am Ceram Soc*, 1997, 80:3-21.
doi.org/10.1111/j.1151-2916.1997.tb02785.x
- [16] B.L. Freeman and A.D. Jefferson, 'A 3D coupled chemo-mechanical model for simulating transient damage-healing processes in self-healing cementitious materials', *Proceedings of EuroC-2022 Computational Modelling of Concrete and Concrete Structures – Meschke, Pichler and Rots*, 2022, 117-121.
doi.org/10.1201/9781003316404-14

Sharifi S

*Cardiff University
School of Engineering*

Balzano B

*Cardiff University
School of Engineering*

CIVIL INFRASTRUCTURE

Pinball Tendons Crack Closure Technology

Concrete is a popular construction material due to its unyielding nature. Although concrete is resistant to erosion, rotting, and rusting, due to its low tensile strength, reinforced concrete is prone to cracking. Also, because the cracks expand and become bigger over time, they can be a potential risk for concrete elements and lead to the failure of structures. Consequently, effective and early crack-closing and concrete healing can greatly enhance and improve concrete structures' lifespan. Mechanical closing of the cracks by tendons has been one of the successful solutions. These tendons act based on a stored force in a balanced system. The new generation of tendons being investigated on a laboratory scale is Pinball Tendons (PBT). In addition to the simple activation phase, these tendons can store much more force due to their sleeve being made from steel. The significant feature of PBTs is that they do not need to receive any energy or recharge after the casting in concrete, so their service life lasts until they are activated to close the crack and release the prestressed force. According to the recorded CMOD data in this study, the tendons managed to close more than 65% of the crack aperture. The speed of the crack closure is another positive aspect of PBTs, 90% of crack closure has been done within the first 8 seconds. Because of this performance, in addition to the self-healing during the life span of structures, tendons can be a helpful alternative for repairing and enhancing concrete in sudden events like earthquakes and explosions.

*Keywords:
Self-Healing, crack closure,
durability, concrete.*

*Corresponding author:
SharifiS@cardiff.ac.uk*



S. Sharifi and B. Balzano, 'Pinball Tendons Crack Closure Technology', *Cardiff University School of Engineering Research Conference 2023*, Cardiff, UK, 2023, pp. 34-38.

doi.org/10.18573/conf1.i

INTRODUCTION

Concrete is the most frequently used engineering material in the modern world due to its high performance and low cost. It is regarded as one of the global consumption's most valuable construction materials [1,2]. However, despite concrete's many advantages, such as good strength and durability, cracks can easily damage it. Cracks can threaten concrete elements and decrease their toughness and life span [3]. Cracks allow moisture and corrosive chemicals to access the steel reinforcement, speeding up the deterioration process [4]. This has led to high maintenance and repair costs for concrete, which comprise a significant portion of the overall cost of concrete structures [5].

Self-healing concrete is an effective solution for reducing concrete degradation by automatically repairing cracks [6]. One of the most recent concrete self-healing methods presenting acceptable results is using tendons to close cracks [7]. Initially, these tendons could close the crack based on the generated force by the shrinkage of a particular type of polymer known as a shape memory polymer (SMP)[8]. But later, with changes in the design of the tendons, the new tendons (Hybrid SMP) were able to close the crack with a prestressed force as the main force, which was a significant improvement in the ability to close cracks [9].

In the Hybrid SMP, a core of aramid fibres (made from Kevlar) is put into the Polyethylene terephthalate (PET) tube, then the Kevlar is tensioned, which causes the compression on orientated PET tube. Anchors are used to holding the aramid fibres in this position. So, this tendon will be in an equilibrium condition until the activation. The Pre-stressed aramid fibre (Kevlar) offers the needed force to close the concrete crack. The Hybrid SMP employed the prestressed force in the core for closing cracks which depended on the PET's strength; despite initial success, the prestresses in the tendon were relatively limited because the compressive strength of the PET sleeve was low and limited [9].

This paper describes the preliminary research on a new tendon with the aim of increasing the prestressed capacity by removing the PET and trying to make a more accessible activation phase. The new system is made of three parts; the first is a stainless steel tube, the second is a hybrid prestressed element (Kevlar) and another stainless steel tube that forms the core of the tendon, and the third is a metal ball that holds the system in equilibrium and acts as an activator. The tendon is in equilibrium until the activation phase. The prestressed force is released at this point, and the load is applied as a compressive force to cracks.

The initial findings demonstrate an ability to increase the prestressed load, which improves crack-closure ability significantly.

GENERAL CONCEPT

Heide and Schlangen demonstrated in 2007 that they could minimise the size of cracks in concrete by applying compressive forces to the samples. By emerging the shape memory alloys (SMAs), this finding took concrete self-healing systems in a new direction[10]. Due to the high cost of using the SMAs, Jefferson et al. (2010) suggested using Shape Memory Polymers (SMPs). The polyethylene terephthalate (PET) was considered a good shape memory polymer for the manufacturing of crack-closure technology. PET has the characteristic of shortening when heated.

When constrained, its shape memory action develops stress which can be used to close cracks within the concrete element. Balzano et al. (2021) suggested an improved design for the SMP Tendons. The improved Hybrid Tendons were characterized by a pre-stressed Kevlar inner core constrained by an outer PET sleeve. When activated, the PET would shrink hence releasing the pre-stress stored in the inner core [9,7].

Although Jefferson et al. (2010) demonstrated and proved the general concept of crack closure, the ability to close cracks was limited to the force generated by PET shortening [7]. Also, Hybrid SMP tendons had some limitations because their ability remained limited to the strength of the PET sleeve [9].

This work aims to maximise the prestressed force by designing a new tendon, namely Pin-Ball Tendon (PBT). Figure 1 illustrates the concept of the new crack-closure system created for this study.

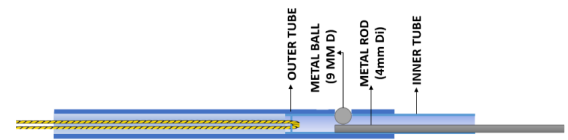


Fig. 1. Assembly of the tendon and locking of the components before the tension.

The PBT tendon is composed of three main parts:

- The inner component core (which is initially in tension),
- A steel tube (which is initially in compression),
- A metal ball that will tolerate shear force (it is the result of tension and compression forces).

The metal ball was placed into the holes in tubes by a metal rod in the first stage, and then the system was locked (Fig. 1). The second stage involved pre-tensioning the core elements (Fig. 2a), which is elastically tensioned. The entire system was "sealed" when the core achieved the desired prestress T . The system is now in an equilibrium state, and the external force has been released on the inner core. The outer element is now being compressed while the core elements are in tension. (Fig. 2b).

The prestressed PBT tendon will then be embedded into the structural element. When cracking occurs, the tendon becomes active (Fig. 3a). The ball will release upon activation, and the prestressed load in the inner core will close the crack (Fig. 3b). They do not need to receive any energy or recharge after the casting in concrete, so their service life lasts until they are activated to close the crack and release the prestressed force.

MATERIALS

The external element is a steel tube with an outer diameter of 16 MM, a wall thickness of 1.5 MM, and a drilled hole. The geometrical properties of the Outer element are illustrated in Fig. 4a.

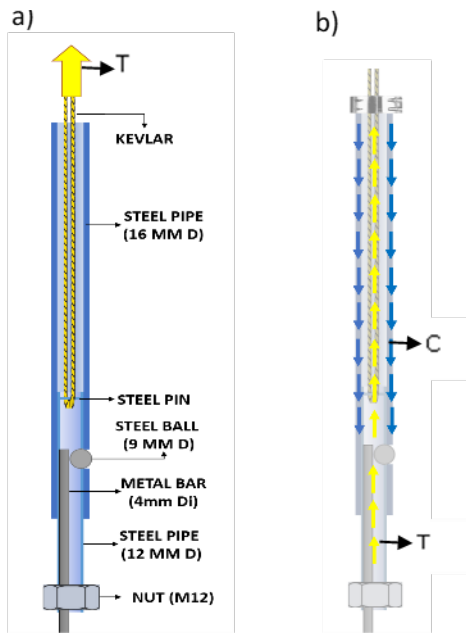


Fig. 2. General concept of PBT tendon.

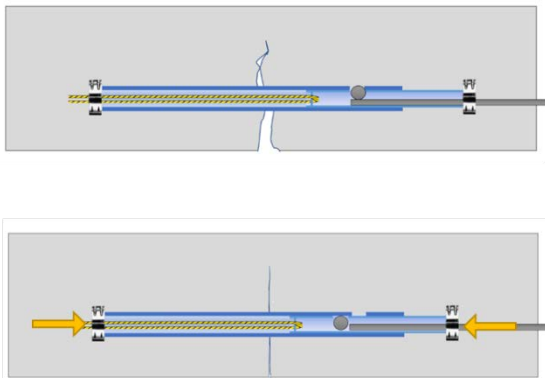


Fig. 3. Activation phase and closing cracks: the appearance of cracks in concrete (top) and closing crack by activating the tendon and releasing the prestressed force (bottom)

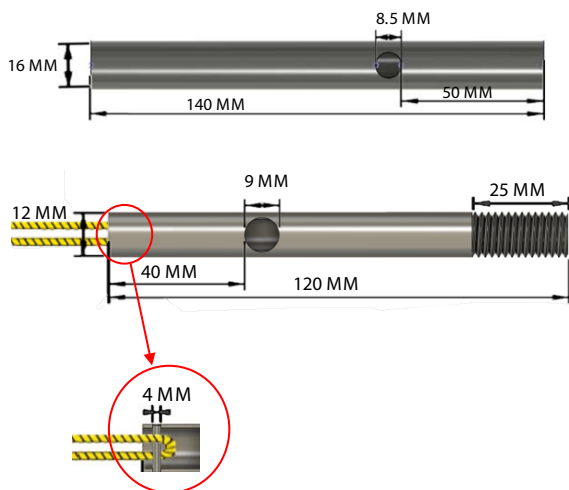


Fig. 4. The geometrical properties of the tendon: outer element (top) and inner element (bottom).

The inner element comprises a 12 MM steel tube with a 1 MM wall thickness and an aramid fibre called Kevlar, which is engaged with the 12 MM tube by a pin (Fig. 4a). A 9 MM hole has also been drilled in the inner tube. Once the Kevlar is tensioned, since the Kevlar is already engaged with the tube, the tensile stress will be distributed at the tube as well.

The inner and outer elements will be held together by a 9 MM steel ball. The steel ball was placed at the drilled hole in both elements, and then the tendons were sealed with a clamp (the total length of the tendons was 170 MM). The tubes are made of 304 stainless steel, and a 2.33 MM diameter Kevlar rope was used. Table 1 shows the mechanical properties of Kevlar.

Tensile Strength MPa	Young Modulus MPa	Density KG/M3
600	5-7 x103	1440

Table 1. Kevlar rope mechanical properties.

When the tendons are stretched, the force distribution in the tendon leads the steel ball to move towards the inside of the tubes. This situation will continue until the tubes slide on each other, and the force will be released. A piece of the iron rod was placed inside the tube to control the activation phase and prevent the ball movement. This rod will be displaced during the activation phase until it no longer obstructs the ball, and at that point, the tendon will be activated.

The tendon is hung on a load cell from the ropes side to begin the prestressing process. The inner element was then prestressed and sealed with commercially available clamps. Afterwards, the inner part was stressed to achieve a prestress of 2000 N stored in each tendon.

LABORATORY EXPERIMENTS

Preparation of the specimens

Two mortar beams with dimensions of 75x75x255 MM were tested for this preliminary study. Figure 5 depicts a typical cross-section of a mortar specimen with embedded prestressed PBTs. A tendon was embedded in the mortar beams at a distance of 15 MM from the bottom and an equal distance from the lateral sides.

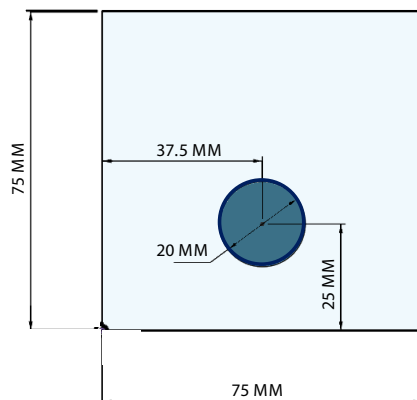


Fig. 5. Cross section of the mortar beam with embedded tendon.

The mortar paste was made using a 3:1 sand-to-cement ratio and a 0.6 water-to-cement ratio. The moulds were cast in three layers. In order to aid in the mortar's compaction, a slight vibration was imposed between each layer.

After 24 hours, the mortar beams were removed from the moulds, covered in wet hessian, and wrapped in plastic. The specimens were cured for seven days.

TESTING

A three-point bending test was carried out on the mortar beams after curing to form a crack. The bottom surface of the specimens was notched to 3 MM depth, and then the knife-edge plates adhered to the notch's sides for the purpose of attaching a monitoring gadget for recording the Crack Mouth Opening Displacement (CMOD) during the experiment.

The size of the generated crack was controlled by managing the applied force via feedback from a machine stroke displacement transducer and monitoring the CMOD.

Figure 6 depicts the relationship between the force and the CMOD and shows how the force initially rose until the first crack appeared in the samples. Then, as the deformation increased, the force reduced (due to decreasing the needed force for extending the crack). The unloading process began when the CMOD reached above 0.3 MM (Balzano et al. 2021). The final created CMOD was recorded at the end (when there was no force on the samples).

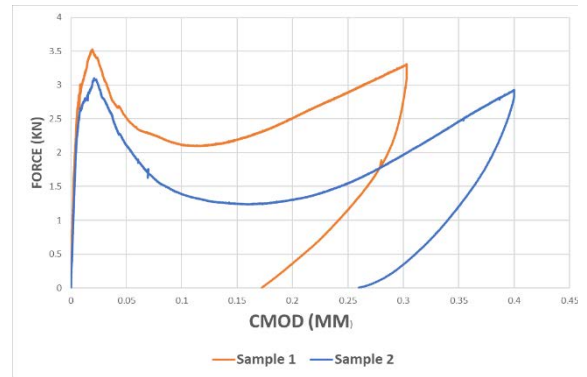


Fig. 6. Force-CMOD diagram recorded during the 3-point bending test for the mortar specimen.

RESULTS AND DISCUSSION

For a more precise presentation of the results, the CMOD data were recorded before and after activation, and the crack width was measured using a magnifying camera and CAD software. Figure 7 shows the outcome of crack closure by tendons.

According to the recorded CMOD data, the tendons were correctly activated and functioning properly. In the first sample, the tendon managed to close 67.47% of the crack aperture, and in the second tendon, the crack closing rate was 64.94%, which are both significant results. The speed tendon crack's closure is another aspect to take into consideration. 90% of crack closure has been done within the first 8 seconds. Because of this performance, tendons are a helpful alternative for repairing and enhancing concrete in sudden events like earthquakes and explosions.

Pictures by the magnifying camera from before and after the activation phase confirm the monitoring device's outcomes and the effectiveness of the tendons (Fig.8).

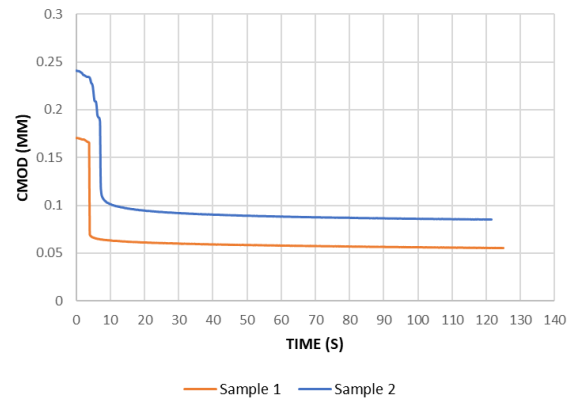


Fig. 7. The CMOD at the samples before and after the activation.

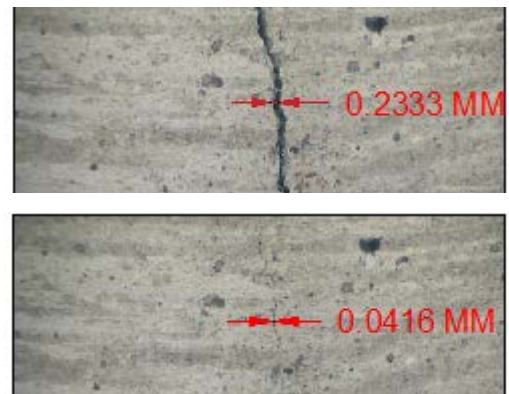


Fig. 8. Comparison of crack width before (top) and after (bottom) activation at sample 2.

CONCLUSION

The proposed PBT tendon has the capacity to store high stresses to close cracks in mortar beams successfully. In addition to showing an acceptable result in closing the cracks and providing an encouraging solution for the durability of concrete structures, the system also has the advantage of acting quickly, hence offering a potential repair mechanism in sudden accidents.

The study is still in its early stages, but the investigation into this prestressed system is ongoing.

Conflicts of interest

The authors declare no conflict of interest.

REFERENCES

- [1] W. Zhang, Q. Zheng, A. Ashour, and B. Han, 'Self-healing cement concrete composites for resilient infrastructures: A review', *Compos Part B: Eng*, vol. 189, p. 107892, May 2020.
doi.org/10.1016/j.compositesb.2020.107892
- [2] C.R. Gagg, 'Cement and concrete as an engineering material: An historic appraisal and case study analysis', *Eng Fail Anal*, vol. 40, pp. 114140, May 2014.
doi.org/10.1016/j.engfailanal.2014.02.004
- [3] T. Qureshi and A. Al-Tabbaa, *Advanced Functional Materials*, 2020.
- [4] A. Sinha, Q. Wang, and J. Wei, 'Feasibility and Compatibility of a Biomass Capsule System in Self-Healing Concrete', *Mater*, vol.14, no. 4, p.958, Feb. 2021.
doi.org/10.3390/ma14040958
- [5] D. Gardner, R. Lark, A. Jefferson, and R. Davies, 'A survey on problems encountered in current concrete construction and the potential benefits of self-healing cementitious materials', *Case Stud Constr Mater*, vol. 8, pp. 238-247, June. 2018.
doi.org/10.1016/j.cscm.2018.02.002
- [6] S. Sangadji, 'Can Self-healing Mechanism Helps Concrete Structures Sustainable?', *Procedia Eng*, vol. 171, pp. 238-249, 2017.
doi.org/10.1016/j.proeng.2017.01.331
- [7] A. Jefferson, C. Joseph, R. Lark, B. Isaacs, S. Dunn, and B. Weager, 'A new system for crack closure of cementitious materials using shrinkable polymers', *Cem Concr Res*, vol. 40, pp. 795-801, May 2010.
doi.org/10.1016/j.cemconres.2010.01.004
- [8] O. Teall, M. Pilegis, R. Davies, J.Sweeney, T. Jefferson, R. Lark, D. Gardner, 'A shape memory polymer concrete crack closure system activated by electrical current', *Smart Mater Struct*, vol. 27, no. 7, p. 075016, Jul. 2018.
doi.org/10.1088/1361-665X/aac28a
- [9] B. Balzano, J. Sweeney, G. Thompson, C.-L. Tuinea-Bobe, and A. Jefferson, 'Enhanced concrete crack closure with hybrid shape memory polymer tendons', *Eng Struct*, vol. 226, p. 111330, Jan. 2021.
doi.org/10.1016/j.engstruct.2020.111330
- [10] Y. Yang, X. Ding, and M. W. Urban, 'Chemical and physical aspects of self-healing materials', *Prog Polym Sci*, vol. 49-50, pp.34-59, Oct. 2015.
doi.org/10.1016/j.progpolymsci.2015.06.001

Balzano B

*Cardiff University
School of Engineering*

Sharifi S

*Cardiff University
School of Engineering*

Tsang CY

*Cardiff University
School of Engineering*

CIVIL INFRASTRUCTURE

Smart Activation System for the Hybrid Tendons Crack Closure Technology

Cracks are a typical characteristic of a concrete structure, formed as a direct consequence of the concrete's low tensile strength. They represent a risk to the longevity of a concrete structure; over time, under the effects of loads and environmental factors, cracks tend to grow and coalesce. It is widely known that cracks reduce the mechanical properties of, and significantly increase the diffusion of deleterious materials through a concrete structure, thus shortening its service-life. The need for enhanced structural longevity and reduced maintenance costs have driven an increased demand for self-healing technologies. Smart crack-closure technologies can lead to the production of more adaptable structural elements, with reduced associated waste and CO2 emissions. The work will cover the developments of a digitally controlled system that uses smart hybrid tendons (HTs) embedded in concrete to detect and close cracks. In particular the work will focus on the digital activation system for the HTs. This technology comprises a shape memory polymer tubular sleeve hosting a pre-stressed strong core which act together to provide an effective crack-closing action and offer flexural reinforcement to the concrete element. The HTs have been the object of a lab-scale study and the digital activation system will complete their design, paving the way for their use in the real world.

Keywords:

Concrete, self-healing, smart structures, resilience, reinforcement.

Corresponding author:

BalzanoB@cardiff.ac.uk



B. Balzano, S. Sharifi, and C.Y Tang, 'Smart Activation System for the Hybrid Tendons Crack Closure Technology', *Cardiff University School of Engineering Research Conference 2023*, Cardiff, UK, 2023, pp. 39-43.

doi.org/10.18573/conf1.j

INTRODUCTION

Concrete is the most used building material and its use is irreplaceable for countless large infrastructure developments [1]. However concrete-based buildings and infrastructure are susceptible to cracking due to the limited tensile strength of the concrete itself [2], [3].

Micro cracks are an unavoidable phenomenon in ordinary concrete[4]. Fractures in concrete structures may form as a result of temperature variations, structural difficulties, and freeze-thaw cycles. In time micro-cracks will generate macro-cracks, which facilitate the penetration of harmful ions such as chloride into concrete. These cracks may eventually cause serious challenges for concrete structures and shorten their lifespan [5].

As a solution to the challenge of cracking in concrete, self-healing concrete has been widely explored by many researchers [6]–[10].

In particular a possible solution would be to embed engineered (autonomic) self-repair mechanisms into concrete structural elements, which are able to heal cracks as they form. [11], [12].

Balzano et al 2021[12] presented a new healing system that uses pre-tensioned hybrid tendons to close cracks in cementitious structural elements. The tendons comprise an inner core, formed from aramid fibre ropes, and an outer sleeve made from a shape memory PET. During the manufacturing process, the inner core of a tendon is put into tension and the outer sleeve into compression, such that the tendon is in equilibrium. A set of tendons are then cast in a cementitious structural element and heat activated once cracking occurs. This triggers the shrinkage potential of the PET sleeve, which in turn releases the stored strain energy in the inner core. The tensile force thereby released applies a compressive force to the cementitious element, in which the tendons are embedded, that acts to close any cracks that have formed perpendicular to the axis of the tendons.

This system was proven to successfully close 0.3 mm cracks in mortar beams. Moreover, the hybrid tendons can act as effective reinforcement both before and after activation.

Although proven effective, the Hybrid tendons are still far from being ready to be used in a working infrastructure. In particular a proper activation system was still needed. Previously the tendons would be activated by placing the samples in the oven but this is not an optimal procedure especially in view of a possible use on a structure. An activation system is needed that would be embedded within the structural element and be triggered by the crack detection.

This paper describes the initial experimental work carried out to explore the use of electric heating wires as activation system for the Hybrid Tendons on structural concrete beams.

GENERAL CONCEPT

Balzano et al. (2021) introduced a novel crack-closure technology namely hybrid tendons which proved to successfully close cracks in mortar beams. The present work follows up on the progress of this past research by applying the hybrid tendon on concrete beams of a relevant scale and exploring the viability of an activation via a heating system embedded in the beam together with the tendons.

The Hybrid tendons were activated via a system of electric wires wrapped around each tendon and externally connected to a power supply. The whole system was then connected to a computer for data collection and to control the activation.

The general scheme of the experiment setting is represented in Fig.1.

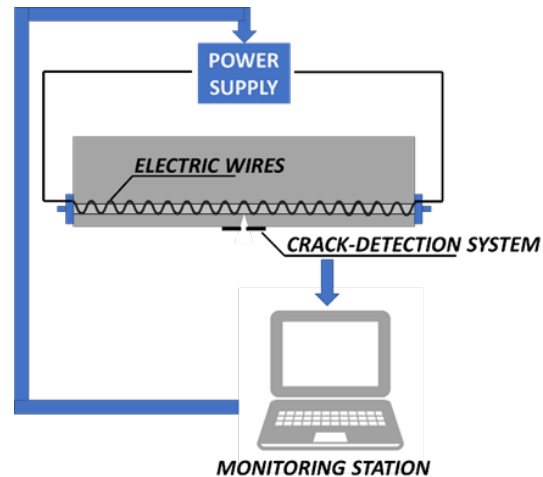


Fig. 1. General concept.

MATERIALS

PET

A commercial grade of polyethylene terephthalate (PET) material (Dow Lighter C93) was used. This is an amorphous polymer, and so its shape memory behaviour is controlled by its glass transition temperature T_g ; orientation must be imposed at around this temperature, and shape recovery is also achieved near T_g . For this material, $T_g=78^\circ\text{C}$ according to manufacturer's figures. This makes the triggering temperature compatible with the setting concrete environment.

Kevlar

Kevlar® is an organic fibres belonging to the family of the aramid fibres and is characterized by a relatively high tensile strength (ca 700 MPa).

Electrical Equipment

The electrical activation system is designed using high resistivity wires with excellent oxidation resistance, making it suitable to work in concrete.

The wire was wrapped around each tendon to make a coil resistance able to generate the heat for activation.

The finished tendon plus activation system is reported in Figure 2.

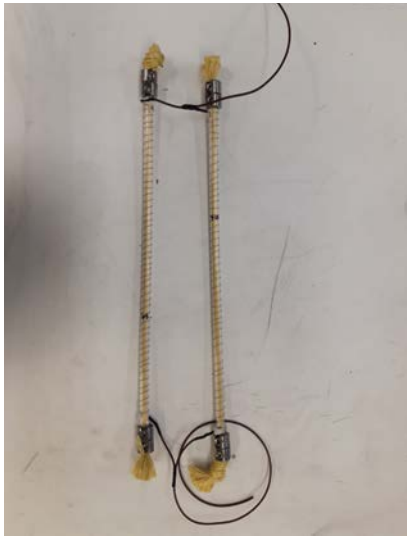


Fig. 2. Hybrid Tendons with electric wires.

Concrete

The concrete for the beam specimens was prepared using Portland cement CEM II A/L 32.5 R (CAS number 65997-15-1), standard quartz sand (CAS number 14808-100 60-7) as fine aggregate, 10mm aggregates and tap water. Cement (c), sand (s) and aggregates were mixed in a ratio of 1:1.55:2.1 by mass, and water (w) was added at a w/c ratio of 0.55 by mass.

Three 100x100x100mm cubes and three 100x200mm cylinders were produced in order to perform compression and splitting tests in accordance with BS EN 12350-1:2000 and BS EN 12390-6:2009 respectively, with the aim of determining the compressive cube strength (fcu) and tensile splitting strength (fcyl) of the mortar paste. All the specimens were cured for 7 days prior to being tested. The compressive and splitting test results are given below in Table 1, noting that CV denotes the coefficient of variation.

	fcu (7days) MPa	fcyl (7days) MPa
Mean	29.2	3.48
CV	0.02	0.08

Table 1. Mechanical Properties of the concrete mix.

LABORATORY EXPERIMENTS

Preparation of the specimens

For the purpose of this preliminary study, four concrete beams with dimensions 100x100x500mm were tested. Figure 3 shows the typical cross section of the concrete specimens with the embedded hybrid tendons.

Following the stressing procedure described in Balzano et al 2021, each tendon would store an average pre-stress of 1.2kN. A number of four tendons have then been embedded in each concrete beam.

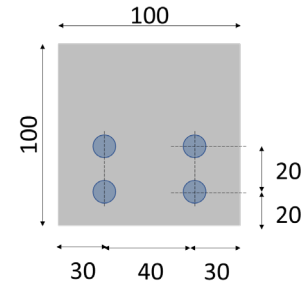


Fig. 3. Geometry of the concrete beam cross section with embedded tendons.

After 24 hours the concrete beams were then removed from the mould and covered in wet hessian and wrapped in cling film. The specimens were cured for 7 days (Figure 4).



Fig. 4. Concrete beam specimens

Testing

After curing, each specimen was tested in three-point bending (Fig. 5). Prior the test, the specimen was notched in order to accommodate the knife edge plates glued to the underside of the beam. A lightweight clip gauge was located between the plates to monitor the Crack Mouth Opening Displacement (CMOD) during the experiment. The load was controlled via feedback from a machine stroke displacement transducer which allows the softening behaviour to be captured. Once the crack aperture reached the desired value the loading was stopped and the test was switched to displacement control. At this point the power supply was activated, gradually heating the embedded tendons. Two Thermocouples type K were installed in each specimen to monitor the temperature raise, hence confirming the system was capable of rising the temperature of the PET up to the activation.



Fig. 5. Three-point bending test apparatus.

RESULTS

Figure 6 shows the Force-CMOD graph recorded during the test. This shows that the specimen exhibited a quasi-linear behaviour until a peak (which corresponds to the point where the concrete began cracking), after which the load decayed with increasing deformation.

The test was stopped at a CMOD value ranging from 0.25 and 0.3 mm. The tendons were then activated and the crack closure was monitored. Figure 6a shows how the CMOD reduces after activation and this process took approximately 20 minutes. However being the machine set on Displacement-control, the load shows a rise as the crack closes.

Figure 6b shows the data from the thermocouples embedded in the concrete beam. Unfortunately the thermocouple in B1 stopped working during the experiment. However the other three show how the CMOD decrease when the temperature raises, proving the closing action of the Tendons.

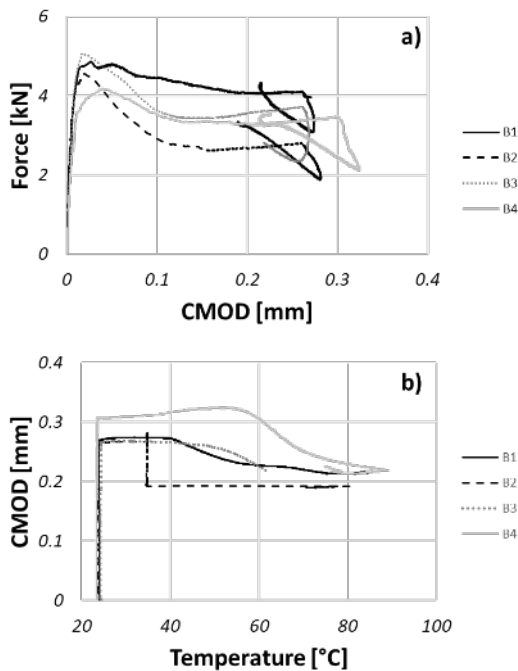


Fig. 6. Load-CMOD results.

CONCLUSIONS

This paper presented the design of an embedded activation system for the crack-closure technology of the hybrid tendons.

The activation system consisted in electric wires wrapped around each tendon and connected to a power supply, which would activate once the crack forms.

The results of the preliminary experimental campaign are very promising, showing the potential of this system to successfully heat and activate the tendons, hence releasing the stored stress.

REFERENCES

- [1] R.J. Flatt, N. Roussel, and C.R. Cheeseman, 'Concrete: An eco material that needs to be improved', *J Eur Ceram Soc*, vol. 32, no. 11, pp. 2787–2798, Aug. 2012. doi.org/10.1016/J.JEURCERAMSOC.2011.11.012
- [2] L. Dai, H. Bian, L. Wang, M. Potier-Ferry, and J. Zhang, 'Prestress Loss Diagnostics in Pretensioned Concrete Structures with Corrosive Cracking', *Journal of Structural Engineering*, vol. 146, no. 3, Mar. 2020. doi.org/10.1061/(asce)st.1943-541x.0002554
- [3] Y. Shen, H. Yang, J. Xi, Y. Yang, Y. Wang, and X. Wei, 'A novel shearing fracture morphology method to assess the influence of freeze–thaw actions on concrete–granite interface', *Cold Reg Sci Technol*, vol. 169, p. 102900, Jan. 2020. doi.org/10.1016/J.COLDREGIONS.2019.102900.
- [4] V. Wiktor and H.M. Jonkers, 'Quantification of crack-healing in novel bacteria-based self-healing concrete', *Cem Concr Compos*, vol. 33, no. 7, pp. 763–770, Aug. 2011. doi.org/10.1016/j.cemconcomp.2011.03.012
- [5] F. Althoey *et al.*, 'Machine learning based computational approach for crack width detection of self-healing concrete', *Case Studies in Construction Materials*, vol. 17, Dec. 2022. doi.org/10.1016/j.cscm.2022.e01610
- [6] D.G. Bekas, K. Tsirka, D. Baltzis, and A.S. Paipetis, 'Self-healing materials: A review of advances in materials, evaluation, characterization and monitoring techniques', *Compos B Eng*, vol. 87, pp. 92–119, Feb. 2016. doi.org/10.1016/J.COMPOSITESB.2015.09.057
- [7] A. Danish, M.A. Mosaberpanah, and M.U. Salim, 'Past and present techniques of self-healing in cementitious materials: A critical review on efficiency of implemented treatments', *Journal of Materials Research and Technology*, vol. 9, no. 3, pp. 6883–6899, May 2020. doi.org/10.1016/J.JMRT.2020.04.053
- [8] S. Gupta, H.W. Kua, and S.D. Pang, 'Healing cement mortar by immobilization of bacteria in biochar: An integrated approach of self-healing and carbon sequestration', *Cem Concr Compos*, vol. 86, pp. 238–254, Feb. 2018. doi.org/10.1016/J.CEMCONCOMP.2017.11.015
- [9] P. Kumar Jogi and T.V.S. Vara Lakshmi, 'Self healing concrete based on different bacteria: A review', *Mater Today Proc*, vol. 43, pp. 1246–1252, Jan. 2021. doi.org/10.1016/J.MATPR.2020.08.765
- [10] M.R. Hossain, R. Sultana, M.M. Patwary, N. Khunga, P. Sharma, and S.J. Shaker, 'Self-healing concrete for sustainable buildings. A review', *Environmental Chemistry Letters*, vol. 20, no. 2. Springer Science and Business Media Deutschland GmbH, pp. 1265–1273, Apr. 01, 2022. doi.org/10.1007/s10311-021-01375-9
- [11] B. Han *et al.*, 'Smart concretes and structures: A review', *Journal of Intelligent Material Systems and Structures*, vol. 26, no. 11. SAGE Publications Ltd, pp. 1303–1345, Jul. 03, 2015. doi.org/10.1177/1045389X15586452
- [12] B. Balzano, J. Sweeney, G. Thompson, C.L. Tuinea-Bobe, and A. Jefferson, 'Enhanced concrete crack closure with hybrid shape memory polymer tendons', *Eng Struct*, vol. 226, p. 111330, Jan. 2021. doi.org/10.1016/J.ENGSTRUCT.2020.111330

De Nardi C

*Cardiff University
School of Engineering*

Gardner D

*Cardiff University
School of Engineering*

Jefferson A

*Cardiff University
School of Engineering*

CIVIL INFRASTRUCTURE

3D-Printed Mini-vascular Networks for Self-healing Lime-based Mortars

Climate change is exposing our built heritage to greater and more extreme hazards. Historic masonry repair technologies must evolve in response to these, promoting a new, long-term resilient preservation strategy. Drawing inspiration from the study of mini-vascular networks to develop self-healing in concrete structures, this work proposes the use of biomimetic mini-vascular networks (m-MVNs) for repairing cracks in lime-based mortars. The m-MVNs are 3D printed units formed by interconnected channels capable of storing and protecting healing agents that are released when threshold damage is exceeded. In the case where patching is required for restoration of historic masonry wall, m-MVNs are designed to fit completely within the mortar joint. Initial results demonstrated that m-MVNs printed from clear PLA, have a promising design capable of storing healing agents without leaking or premature curing. Future experiments will investigate the appropriateness of this design of m-MVNs to enclose suspensions of bacteria and deliver them to cracks.

Keywords:

3D printing, self-healing, built heritage, lime-based mortars.

Corresponding author:

DeNardiC@cardiff.ac.uk



C.De Nardi, D. Gardner, and A. Jefferson, '3D-Printed Mini-vascular Networks for Self-healing Lime-based Mortars', *Cardiff University School of Engineering Research Conference 2023*, Cardiff, UK, 2023, pp. 44-47.

doi.org/10.18573/conf1.k

INTRODUCTION

Recent changes in weather patterns expose our built heritage to greater and more aggressive hazards, significantly reducing the service-life of historical structures. A range of traditional intervention strategies are available to address damage in masonry structures (e.g repointing, bed joint reinforcement) [1], although these have not always been successful [2]. A more resilient and durable solution to these problems is urgently needed.

Mini-vascular networks (MVNs) were recently proposed by Cardiff University researchers as a form of biomimetic self-repair system for concrete [3]. The use of MVNs was proposed as an alternative to conventional vascular networks [4] maintenance and replacement of civil engineering infrastructure attracts significant expenditure in the UK. Anecdotal evidence suggests that a significant number of existing and new concrete structures suffer from repair and maintenance problems, but a lack of objective construction industry supported data concerning these problems makes it difficult to establish, with any certainty, the actual problems encountered in current concrete construction in the UK. To address this lack of data, a market research exercise was commissioned by the Materials for Life (M4L, which might cause delays to the concrete casting process caused by their in-situ placement.

As illustrated in Figure 1, 3D PLA-printed regular shaped tetrahedral units (termed TETs hereafter) can be easily introduced to wet concrete during the mixing process. The TET design has been improved to provide good bond properties with the concrete matrix and the ability to store either single (TETs) or bi-components healing agents (d-TETs). Their efficiency to rupture and release sufficient healing agents at a designed crack width has recently been shown by De Nardi et al [5] which employs 3D-printed tetrahedral mini-vascular networks (MVNs). Several healing agents have been tested, such as sodium silicate (SS) solutions, stored individually or in combination with nanosilica (Nsilica) and nanolime (Nlime) solutions.

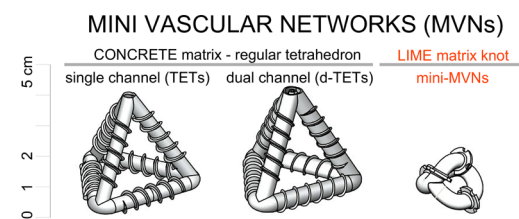


Figure 1. MVNs and m-MVNs design

In particular, TETs filled with SS can produce strength and stiffness recoveries of 20% and 75-80% respectively in prismatic concrete beams. d-TETs filled simultaneously with SS and either Nlime or Nsilica showed representative increase of strength and stiffness recovery indices of ~10% in comparison to samples containing only SS as healing agent [6].

Recently, the MVN design has been revised and optimised enabling technology transfer from newly constructed concrete structures to historical masonry walls.

Traditionally, if significant sections of masonry have deteriorated to such a degree that mortar joints have lost their function, then patching techniques can be used to restore structural continuity while preserving the original blocks [7] and in some cases were still being, repaired

and strengthened. The size and shape of previous MVNs were totally revised allowing mini-mini vascular networks (m-MVNs) to lie entirely within the mortar joint thickness. As with concrete MVNs, m-MVNs are meant to host and protect healing agents that are released when threshold damage is exceeded.

As represented in Figure 2, the concept design was drawn from the idea to manufacture the unit by turning an extruded tube around a spherical shape. The advantages of the proposed new-shaped m-MVNs are that i) they are (almost) directionally invariant with respect to their mechanical behaviour and, (ii) the ribs anchor the unit within the lime matrix, which limits the degree of sliding between the channels and the matrix and means that a channel is likely to fracture when crossed by a crack.

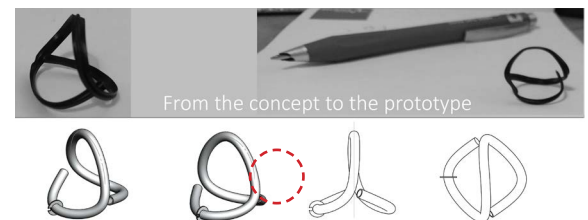


Figure 2. m-MVNs from the concept to the prototype

Regarding the healing agents, much attention will be paid to compatibility criteria, so that the active healing agents are designed to fulfil conservation requirements i.e. be physically, chemically, and mechanically compatible with the host material. In this context, the ability to store healing agents, mainly in the form of aqueous solution have been studied.

MATERIALS AND METHODS

To meet the requirements of the proposed application, m-MVNs were originally created by modifying standard MVN units.

The aim of this first stage was to optimize the design as well as the printing process to satisfy the requirements, namely i) 3D printability of units with reduced geometry and wall-thickness; ii) the ability to be fully watertight when inserted into a lime-based matrix; iii) the ability to prevent any chemical interactions with the healing agent components.

Several variants of m-MVNs were printed from clear PLA, purchased from Verbatim®, using an Ultimaker2+® printer (Utrecht, The Netherlands) with a 0.25 mm nozzle.

In the initial stages of m-MVN development, watertightness tests were conducted to evaluate the ability of thin-wall units to store low-viscosity healing agents over time without premature curing of evident polymer degradation (through longevity tests). m-MVNs were filled with healing agents; either ink, sodium silicate (Na₂O3Si) solution - Sigma Aldrich, nanolime (CaOH₂) solution, marked as Nanoretore by the Company CTS Europe produced by CSGI - University of Florence and lithium silicate (Li₂O3Si, referred to as LIS herein) marked as Acquacons by CIR Chimica Italiana Restauri.

The longevity tests spanned 4 weeks and consisted of 36 m-MVNs being prepared and filled with SS, Nlime and Nsilica solutions. Three m-MVNs from each solution were opened and examined at 1-7-21-28 days.

The main printing parameters are summarized in Table 1.

Printing parameters	
nozzle	0.25 mm
layer height	0.06 mm
support type	buildplate
bottom_layers	5
cool_fan_speed	80
infill_sparse_density	100
support_infill_rate	2
support_z_distance	0.25
top_bottom_pattern	grid
top_bottom_thickness	0.06 mm
top_layers	5
wall_line_count	16
wall_thickness	0.25 mm
xy_offset	0

Table 1. 3D Printing parameters.

RESULTS AND DISCUSSION

A prototype was successfully 3D printed: the shape was well defined with homogenous surfaces and excellent adhesion between layers. The accuracy and repeatability of printing were also checked, assuring the quality standards in terms of form and dimensional accuracy and stability over printing in separate batches, as can be seen in Figure 3.

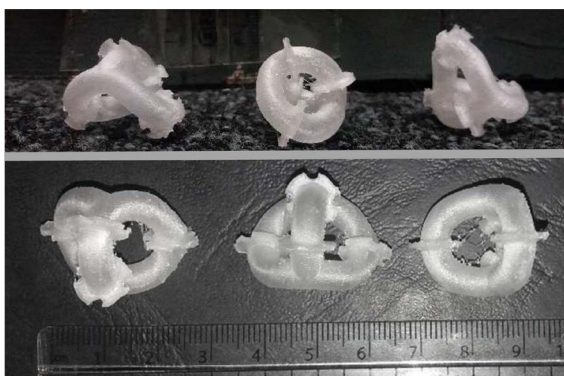


Figure 3. 3D printed m-MVNs from clear PLA.

Following 24 hours of watertightness testing, small quantities of ink were observed. Therefore, in order to ensure complete impermeability, a thin wax coating was externally applied to the m-MVNs. The same coating will provide protection from the alkaline environment to m-MVN units in lime matrices.

The results of longevity tests are summarized in Table 2.

It should be noted that changes in both viscosity of healing agents and PLA polymer were determined through visual inspection and so only provide a qualitative approximation

of any change can be reported. The letters l, g, s denote the following: Liquid (l) – no discernible change; Gel (g) – beginning to behave solidly; and Solid (s). The consistency of the polymer was approximately checked by breaking the units and observing if the rupture was brittle (B=brittle) or ductile (D=ductile). The latter was taken as an indication of the initial degradation of the polymer.

clear PLA m-MVNs	Test durations			
	1 day	7 days	21 days	28 days
SS	l/B	l/B	l/B	g/B
Nlime	l/B	l/B	l/D	l/D
Nsilica	l/B	l/B	l/B	l/D
LiS	l/B	l/B	l/B	l/B

Table 2. Longevity tests results.

From the results, it can be seen that SS solution remained liquid for 21 days. After that period the SS appeared similar to transform into a colloidal gel. No changes to the polymer were observed for the SS.

Contrary to this, both Nlime and Nsilica solutions remained liquid throughout the 28 days, without showing any change in viscosity. However, they both caused softening of the PLA. The latter phenomenon was observed in samples ruptured at 21 days in m-MVNs filled with Nlime, and at 28 days in m-MVNs filled with Nsilica. m-MVNs’ original mechanical properties are likely to be altered by chemical interactions between the PLA polymer and both Nlime and Nsilica solutions.

CONCLUSIONS

From the analyses of the results presented in the paper, the following main conclusions can be drawn:

- 3D printed MVNs provide a flexible system enabling technology transfer from newly constructed concrete structures to historical masonry walls.
- m-MVNs form the basis of a viable self-healing system for lime-based matrices.
- The 3D printing parameters for m-MVNs need improvement to achieved full watertightness. However, a thin wax coating was able to prevent any leakage and protect the units from the alkalinity of lime.
- SS solution can be stored within m-MVNs with no discernible change in viscosity up to 21 days, after which it forms a gel like substance. No visual changes to the PLA polymer were observed throughout the 28 days.
- Nlime solution remained liquid up to 28 days, but softening effects on the PLA polymer were observed after 21 days. A similar behaviour was observed in m-MVNs filled with Nsilica.

Acknowledgments

This research was funded by the Engineering and Physical Sciences Research Council (EPSRC), grant number EP/P02081X/1 and the Leverhulme Trust ECF-2022-235.

The authors would also like to acknowledge the considerable help and expertise of Samuel Moeller for his technical support on 3D printing.

Conflicts of interest

The authors declare no conflict of interest.

REFERENCES

- [1] M. R. Valluzzi, F. Casarin, E. Garbin, F. Da Porto, and C. Modena, 'Long-term damage on masonry towers case studies and intervention strategies', in *11th International Conference on Fracture 2005*, ICF11, vol. 5, pp. 3253–3256, 2005.
- [2] P. Harding, 'The Limits of Lime, Repointing a damp church tower in the Hebrides', *Historic Churches*, 2010.
- [3] C. De Nardi, D. Gardner, A. Jefferson, T. Selvarajoo, and G. Evans, 'The Development of Mini-Vascular Networks for Self-Healing Concrete', in *Durable Concrete for Infrastructure under Severe Conditions*, pp. 19–23, Sept. 2019.
- [4] D. Gardner, R. Lark, T. Jefferson, and R. Davies, 'A survey on problems encountered in current concrete construction and the potential benefits of self-healing cementitious materials', *Case Stud Constr Mater*, vol. 8, pp. 238–247, 2018.
doi.org/10.1016/j.cscm.2018.02.002
- [5] C. De Nardi, D. Gardner, and A. D. Jefferson, 'Development of 3D Printed Networks in Self-Healing Concrete', *Materials (Basel)*, vol. 13, no. 6, p. 1328, Mar. 2020.
doi: 10.3390/ma13061328
- [6] C. De Nardi, D. Gardner, D. Cristofori, L. Ronchin, A. Vavasori, and T. and Jefferson, 'Advanced 3D printed mini-vascular network for self-healing concrete', *Manuscr. Submitt. Publ.*
- [7] D. Penazzi, M. R. Valluzzi, A. Saisi, L. Binda, and C. Modena, 'Repair and strengthening of historic masonry', *Atti del Congr. Internazionale "More than two thousand years Hist. Archit. safeguarding Struct. our Archit. heritage"*. Bethlehem, Palest., vol. 2, pp. 1–6, 2001.

Neghabat Shirazi B

*Cardiff University
School of Engineering*

Balzano B

*Cardiff University
School of Engineering*

Almutlaqah A

*Cardiff University
School of Engineering*

Maddalena R

*Cardiff University
School of Engineering*

CIVIL INFRASTRUCTURE

Agricultural Waste as a Cementitious Material — Rice Husk Ash

To reduce global CO₂ emissions, researchers have been exploring various materials to replace Portland cement. Rice husk ash has been considered a promising alternative due to its widespread availability and increased production. However, the current process of using rice husk ash in construction involves burning the husks at high temperatures (700-900 °C), which is energy-intensive and generates CO₂ emissions. In this study, we investigated the use of unprocessed rice husk ash, burnt at 400°C, as a replacement for Portland cement in concrete. We used rice husk ash at 10%, 20%, and 30% by mass and conducted tests to measure its reactivity, mechanical strength, and durability. Preliminary results indicate that the pozzolanic reactivity of unprocessed rice husk ash is similar to that of fly ash and other supplementary cementitious materials. However, the main peak of hydration is delayed compared to that of Portland cement. Mechanical strength and durability were found to be influenced by curing age, with samples cured for 90 days showing improved tensile strength. Furthermore, higher rice husk ash content at 90 days of curing resulted in lower chloride penetration, a parameter often used to describe the corrosion potential of cementitious matrices. Overall, our findings suggest that unprocessed rice husk ash can be a promising replacement for Portland cement in concrete, as it offers similar reactivity to other supplementary materials and has the potential to improve the durability of the resulting cementitious matrix.

Keywords:

Agricultural waste, concrete, strength, durability.

Corresponding author:

MaddalenaR@cardiff.ac.uk



B. Neghabat Shirazi, A. Almutlaqah, B. Balzano and R. Maddalena, 'Agricultural Waste as a Cementitious Material — Rice Husk Ash', *Cardiff University School of Engineering Research Conference 2023*, Cardiff, UK, 2023, pp. 48-51.

doi.org/10.18573/conf1.1

INTRODUCTION

Concrete is one of the most used materials in the world and its production accounts for significant environmental issues (i.e. transportation, fuels used calcination, carbon footprint). Typical constituents of concrete are aggregate (crushed stones and sand) and Portland cement. The latter is responsible for over 8% of the anthropogenic CO₂ emissions [1].

One way of mitigating greenhouse gas emissions associated to the production of concrete is by replacing Portland cement with waste materials and by-products with similar chemical composition, and capable of providing structural resilience and mechanical performance. Such materials, known as supplementary cementitious materials (SCMs), have been proposed in construction since 1970's. The most common SCMs are pulverized fuel ash (PFA), a waste material generated from the coal industry, ground granulated blast furnace slags (GGBS), a by-product of the steel industry, and silica fume, or micro-silica (SF), associated with the production of silicon and ferro-silicon [2]. Such materials have a mineralogical composition that satisfy the requirements to improve fresh and hardened properties of conventional concrete.

However, forthcoming shortages in fly ash availability, and global projected increase of cement production of 4.38 Gt by 2050 [3], has led researchers to investigate other pozzolanic materials, such as rice husk ash.

Rice husk ash (RHA), a by-product of the agriculture industry can be used as a filler or binder to produce sustainable concrete [4], [5]. RHA exhibits a high pozzolanic index when burnt at around 700 °C, where most of the organic carbon is removed. However, such high calcination temperatures make the RHA an energy-intensive material. Zerbino et al. (2010) studied the effect of RHA without further processing (grinding), showing that natural RHA concrete achieved similar mechanical performance of natural RHA [6].

The effect of RHA grinding on the concrete strength resulted in refined particle size and subsequent pozzolanic activity [4], [7].

RHA as a binder replacement influences the mechanical performance of the hardened concrete. Increasing the RHA content to up to 30% by mass resulted in a loss of compressive, flexural and tensile strength [8]. However, due to its pozzolanic index, RHA develops strength beyond the nominal 28 days, typical for conventional Portland cement concrete [9].

Whilst structural performance and physical properties of RHA concrete have been extensively investigated, durability properties of un-processed RHA in concrete have not yet been fully investigated.

This work present preliminary studies on unprocessed RHA, produced at a calcination temperature of 400 °C to minimise their energy demand. The effect of increasing cement replacement with RHA at 10, 20 and 30% was investigated by measuring the concrete tensile strength and surface electrical resistivity at different curing ages.

MATERIALS AND METHODS

Concrete specimens were prepared by mixing Portland cement (CEM II, A-L, class 32.5 MPa) with a content of 400 kg/m³, fine and coarse aggregate, respectively river sand (680 kg/m³) and crushed limestone (920 kg/m³), at a water to binder (w/b) ratio in the range of 0.42 – 0.62. Portland cement was replaced (by mass) with rice husk ash (RHA) supplied by E-COCO Products UK Ltd and sourced from Malaysia. To produce RHA, rice husk was burnt at 400 °C, and no further refinement (grinding) was conducted. The mix design at varying cement replacement levels is reported in Table 1.

Series	Cem	RHA	f/b	c/b	w/b
Control	100%	0%	1.7	2.3	0.42
RHA10	90%	10%			0.50
RHA20	80%	20%			0.62
RHA30	70%	30%			0.62

Table 1. Mix design details with mass content (%) of Portland Cement (Cem), rice husk ash (RHA), sand to binder (f/b) ratio, coarse aggregate to binder (c/b) ratio and water to binder (w/b) ratio.

Samples were cast into cylindrical (100 mm in diameter and 200 mm in height) moulds, following the standard BS EN 12390-2:2019 [10]. After 24 hours, specimens were demoulded and cured in water at 20 °C for either 28 days or 90 days. After mixing, 300 g of fresh concrete was sampled from the mixer and the heat of hydration was measured by using an isothermal calorimeter (Calmetrix, I-Cal 8000 HPC, USA) at a constant temperature of 20 °C for 168 hours. After curing, specimens were first tested for surface electrical resistivity by using a Wenner probe (SURF, Giatec, Canada) [11], [12] the surface resistance and the uniaxial resistance measurements provide equivalent measures of resistivity once geometry is appropriately taken into account. However, cementitious systems are not always homogenous. This article compares bulk and surface resistance measurements in cementitious materials intentionally composed of layered materials (i.e., layers with different resistivities followed by tensile strength measurements. Physical and mechanical properties were measured on three samples at each curing age (28 and 90 days), and the average value was recorded.

RESULTS AND DISCUSSIONS

The heat of hydration of representative samples with 10, 20 and 30% of RHA replacement is shown in Fig. 1, and compared to the hydration of concrete made with 100% Portland cement (Control). For all mixes, the first peak appears at around 10 – 20 hours from mixing, in line with previous studies [13], [14]. However, when compared to the control sample, the RHA series exhibit a delay in hydration, due to the high carbon content and subsequent dissolution, resulting in a lower hydration degree [4].

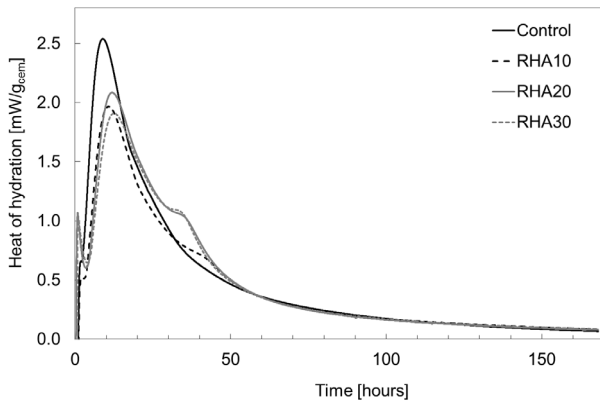


Fig. 1. Heat of hydration of selected samples at 10, 20 and 30% RHA content and compared to the control series.

The tensile strength measurements showed that an increase in RHA content resulted in decrease in mechanical strength, as reported in Fig. 2; samples cured for 28 days showed a reduction of approximately 50% in tensile strength (RHA30).

However, longer curing ages (90 days) resulted in an improved strength on samples with the lower RHA content (RHA10), an average of 3.1 MPa, approximately 32% less than the control samples. The tensile strength values are lower than those reported in literature for the same RHA content [14], [15]. This is due to the nature of RHA used in this work; as previously stated, refinement processes of RHA such as grinding and calcination temperature influence the overall mechanical performance of concrete. However, whilst the tensile strength values suggest that RHA cannot be used for structural applications, other civil engineering applications (pre-cast concrete, pavement elements, cladding material) are deemed suitable.

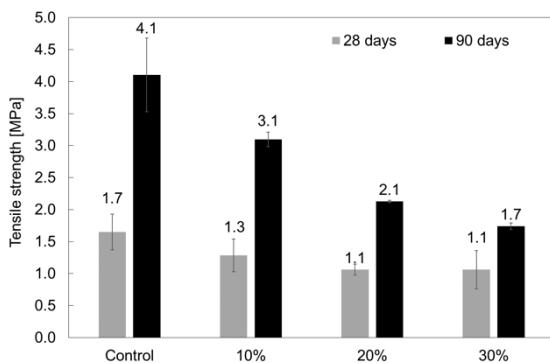


Fig. 2. Tensile strength at 28 days and 90 days. Error bars represent the standard deviation.

In concrete, one of the most studied durability parameter is the corrosion potential, as a result of chloride ingress [16]. Factors such as porosity, permeability and pore size distribution affect the chloride diffusivity of the cementitious matrix, often measured by rapid chloride penetration tests or indirect investigation, such as electrical resistivity measurements [11]. In this study the surface electrical resistivity of cylindrical specimens was measured and compared to the 56-day chloride ingress potential. The highest the surface resistivity, the lowest the chloride diffusivity. Values of surface resistivity in < 10 kΩcm indicate a high chloride penetration, whilst values in the range of 10 – 15 kΩcm indicate a moderate chloride diffusivity.

Results presented in Fig. 3 show that an increase in RHA resulted in a lower chloride penetration when samples were cured for 90 days. RHA content at 20% (RHA20) and 30% (RHA30) improved the chloride penetration by 32% and 35% respectively when compared to the control mix (RHA 0%).

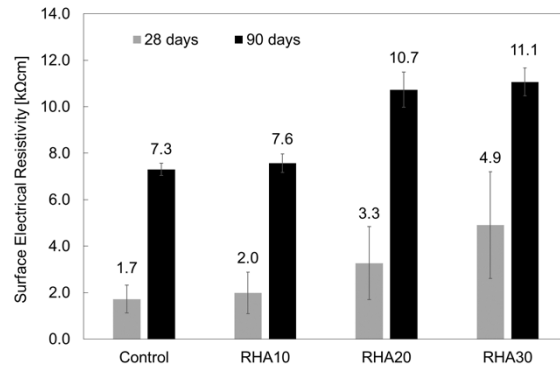


Fig. 3. Surface electrical resistivity of concrete samples at 28 days and 90 days of curing. Error bars represent the standard deviation.

According to Eurocodes, the choice of concrete grade must ensure durability requirements in different environments. Hence, with their varying grades, different concrete mixes can be utilised for various civil engineering applications such as paving or small walls (RHA30) and foundations or flooring (RHA20). Although the initial results indicate minor differences in surface electrical resistivity among the various mixes, it suggests that the proposed concretes can maintain their resistance to chloride ingress. This indicates a similar corrosion risk, which is a crucial aspect of Eurocodes recommendations. Therefore, it is believed that these mixes can be employed in a broader range of applications once their corrosion potential is better explored.

CONCLUSIONS

This work presents a preliminary investigation into the use of unprocessed rice husk ash as a replacement for cement in concrete. Rice husk ash produced at 400 °C is less energy-intensive than conventional rice husk ash, resulting in a minimized carbon footprint. The mechanical strength values of concrete with rice husk ash content up to 30% by mass suggest that it can be used in construction as a non-structural material. However, increasing the rice husk ash content results in decreased chloride penetration, which is often used to quantify the corrosion potential.

Future work will include investigating the water transport properties and conducting a detailed life cycle assessment to evaluate the environmental benefits of unprocessed rice husk ash in construction.

Funding

This research was funded by the Cardiff University ENGIN COVID-19 Early Career Academic Fund (grant reference: Thermo-crete, 2021), and the ENGIN Research Boost Fund (grant reference: Concrete MOT, 2022).

Conflicts of interest

The authors declare no conflict of interest.

REFERENCES

- [1] L. Proaño, A. T. Sarmiento, M. Figueredo, and M. Cobo, 'Techno-economic evaluation of indirect carbonation for CO₂ emissions capture in cement industry: A system dynamics approach', *J Clean Prod*, vol. 263, p. 121457, Aug. 2020. doi.org/10.1016/j.jclepro.2020.121457
- [2] R. Siddique and M. I. Khan, *Supplementary Cementing Materials*, vol. 37. in *Engineering Materials*, vol. 37. Berlin, Heidelberg: Springer Berlin Heidelberg, 2011. doi.org/10.1007/978-3-642-17866-5
- [3] M. Schneider, M. Romer, M. Tschudin, and H. Bolio, 'Sustainable cement production-present and future', *Cem Concr Res*, vol. 41, no. 7, pp. 642–650, Jul. 2011. doi.org/10.1016/j.cemconres.2011.03.019
- [4] S.K. Antiohos, V.G. Papadakis, and S. Tsimas, 'Rice husk ash (RHA) effectiveness in cement and concrete as a function of reactive silica and fineness', *Cem Concr Res*, vol. 61–62, pp. 20–27, July 2014. doi.org/10.1016/j.cemconres.2014.04.001
- [5] M.F.M. Zain, M.N. Islam, F. Mahmud, and M. Jamil, 'Production of rice husk ash for use in concrete as a supplementary cementitious material', *Constr Build Mater*, vol. 25, no. 2, pp. 798–805, Feb. 2011. doi.org/10.1016/j.conbuildmat.2010.07.003
- [6] R. Zerbino, G. Giaccio, and G. C. Isaia, 'Concrete incorporating rice-husk ash without processing', *Constr Build Mater*, vol. 25, no. 1, pp. 371–378, Jan. 2011. doi.org/10.1016/j.conbuildmat.2010.06.016
- [7] J. Alex, J. Dhanalakshmi, and B. Ambedkar, 'Experimental investigation on rice husk ash as cement replacement on concrete production', *Constr Build Mater*, vol. 127, pp. 353–362, Nov. 2016. doi.org/10.1016/j.conbuildmat.2016.09.150
- [8] H. Huang, X. Gao, H. Wang, and H. Ye, 'Influence of rice husk ash on strength and permeability of ultra-high performance concrete', *Constr Build Mater*, vol. 149, pp. 621–628, Sep. 2017. doi.org/10.1016/j.conbuildmat.2017.05.155
- [9] H. Chao-Lung, B. Le Anh-Tuan, and C. Chun-Tsun, 'Effect of rice husk ash on the strength and durability characteristics of concrete', *Constr Build Mater*, vol. 25, no. 9, pp. 3768–3772, Sep. 2011. doi.org/10.1016/j.conbuildmat.2011.04.009
- [10] British Standards Institution, 'BS EB 12390-2:2019 Testing hardened concrete Making and curing specimens for strength tests', 2019.
- [11] H. Layssi, P. Ghods, A.R. Alizadeh, and M. Salehi, 'Electrical resistivity of concrete.', *Concr Int*, vol. 37, no. 5, pp. 41–46, 2015.
- [12] R. P. Spragg *et al.*, 'Surface and uniaxial electrical measurements on layered cementitious composites having cylindrical and prismatic geometries', in *Proc 4th Int Conf Durab Concr Struct ICDCS 2014*, July 2014, pp. 317–326. doi.org/10.5703/1288284315417
- [13] S.-H. Kang, S.-G. Hong, and J. Moon, 'The use of rice husk ash as reactive filler in ultra-high performance concrete', *Cement and Concrete Research*, vol. 115, pp. 389–400, Jan. 2019. doi.org/10.1016/j.cemconres.2018.09.004
- [14] M.A. Mosaberpanah and S.A. Umar, 'Utilizing Rice Husk Ash as Supplement to Cementitious Materials on Performance of Ultra High Performance Concrete: – A review', *Mater Today Sustain*, vol. 7–8, Mar. 2020. doi.org/10.1016/j.mtsust.2019.100030
- [15] S.A. Zareei, F. Ameri, F. Dorostkar, and M. Ahmadi, 'Rice husk ash as a partial replacement of cement in high strength concrete containing micro silica: Evaluating durability and mechanical properties', *Case Stud Constr Mater*, vol. 7, pp. 73–81, Dec. 2017. doi.org/10.1016/j.cscm.2017.05.001
- [16] V. Marcos-Meson, A. Michel, A. Solgaard, G. Fischer, C. Edvardsen, and T.L. Skovhus, 'Corrosion resistance of steel fibre reinforced concrete - A literature review', *Cem Concr Res*, vol. 103, pp. 1–20, Jan. 2018. doi.org/10.1016/j.cemconres.2017.05.016

Binti Q

*Cardiff University
School of Engineering*

Jin F

*Cardiff University
School of Engineering*

Rudge J

*Cardiff University
School of Engineering*

Maddalena R

*Cardiff University
School of Engineering*

CIVIL INFRASTRUCTURE

Waste Foundry Sand (WFS) as Aggregate Replacement for Green Concrete

Globally, 113 million tonnes (Mt)/year of cast metal are produced, generating 10-20 Mt/year of waste foundry sand (WFS). In the UK alone, 200,000 tonnes of WFS are disposed via landfilling, challenging current efforts in tackling climate change and sustainable development (CO₂ emissions due to transportation, extraction of natural resources, increase in landfill inputs). Concrete uses up to 90% of natural aggregate per tonne of concrete produced, including sand. The latter is the most extracted material in the world today. Approximately 40-50 billion tons of sands are mined around the globe for construction each year (UNEP2016).

This work examines the use of waste foundry sand (WFS) as a replacement for fine aggregate (sand) in concrete. Two types of WFS supplied by Weir UK were used: quartz and chromite sand. After initial chemical and physical characterization, both types of sand were deemed suitable for use in construction. We compared the physical and chemical properties of both WFS types to river sand used for concrete production. Quartz and chromite WFS were finer and contained less silicon than conventional sand but richer in metallic ions. Leaching tests showed that WFS released metals, but their chloride, fluoride and sulphate content was less than river sand. WFS was then used in concrete at different fine aggregate replacement levels (30%, 50% and 100%). We investigated the mechanical performance at 28 days of curing, water transport and durability properties. Whilst the overall compressive strength decreased with increasing the WFS content, samples subjected to freeze/thaw cycles exhibited outstanding durability performance with respect to their water absorption capability. Preliminary results suggest that WFS is an environmentally sustainable solution both for the cast metal industry and the construction sector, as it repurposes a material otherwise disposed of into a raw material for durable concrete production.

Keywords:

Agricultural waste, concrete, strength, durability.

Corresponding author:

MaddalenaR@cardiff.ac.uk



Q. Binti, J. Rudge, F. Jin, and R. Maddalena, 'Waste Foundry Sand (WFS) as Aggregate Replacement for Green Concrete', *Cardiff University School of Engineering Research Conference 2023*, Cardiff, UK, 2023, pp. 52-54.

doi.org/10.18573/conf1.m

INTRODUCTION

WFS is mainly made of siliceous sand (up to 95%) and additives (binders, clays, etc...). In the past decade, research has been carried out worldwide to evaluate the effect of WFS in aggregate replacement in concrete [1]. It has been found that replacement of river sand with WFS up to 30% in concrete resulted an increase of compressive strength [2]. On the other hand, replacement up to 60% resulted in a decrease in strength, however acceptable within certain limits for non structural applications (<35 MPa) [3], [4]. WFS was also studied as a fine aggregates replacement (up to 40%) in self-compacting concrete, resulting in increased mix segregation, albeit with a 40% improvement in strength [5].

Although WFS is classified in the EU as a non-hazardous waste and its replacement up to 60-100% in concrete has been proposed at lab-scale, current standards in the construction sector allow only up to 30% by weight [6] [7]. One obvious reason to this limitation is the variability of the WFS physico-chemical properties, not only on an international level, but also within the same foundry activities. In fact, the composition of WFS depends on the foundry location, on the type of casting activity and binders used. Another factor of influence is the presence of organic and inorganic contaminants in the WFS that might migrate from the hardened concrete with time [8].

This work seeks to i) assess the variability of WFS stream composition from the Weir Minerals Europe Ltd Todmorden foundry to determine its physical properties (specific surface area and particle size) and chemical composition (sulphates, phosphates, phenols, chromium, etc.), and ii) incorporate WFS into concrete as a partial (but >30% current limit) or total replacement of fine aggregates.

MATERIALS AND METHODS

The study used various methods to analyse the physical and chemical properties of river sand and two waste foundry sands (WFS), quartz and chromite (as shown in Fig. 1). Particle size analysis showed that the WFS were finer than the river sand. XRF and XRD analysis revealed differences in elemental and mineral compositions among the sands, with the WFS containing more iron and heavy metals. Loss on ignition and total carbon analyses showed that the organic content and carbonaceous material were lower in the WFS compared to the river sand. Finally, pH and electroconductivity measurements of leachate from the sands suggested that the WFS would behave similarly to the river sand when used in concrete.

Concrete specimens were prepared by mixing Portland cement (CEM II, A-L, class 32.5 MPa) with a content of 400 kg/m³, fine and coarse aggregate, respectively river sand (680 kg/m³) and crushed limestone (920 kg/m³), at a water to binder (w/b) ratio in the range of 0.42 – 0.62. Fine aggregate was replaced chromite and quartz waste foundry sand at level of up to 100%.

Several tests were carried out to determine the properties of the concrete. The bulk density was determined using ASTM C138 by measuring the dry and saturated unit weight along with its Archimedes weight. Compressive and splitting tensile strength tests were conducted by crushing and splitting the cubes and cylinders, respectively. Rapid chloride ion penetration was tested by sandwiching the samples between two chambers in a test cell and exposing them to NaOH and NaCl solutions with a current of 60V applied for 6 hours. Thermal conductivity was measured

using a 50 mm probe, portable sensor, and computer application software. Lastly, the water absorption was determined by immersing samples in a water tank and recording their mass at regular square intervals of time. Freezing and thawing were tested by placing oven-dried samples in a water bath for 8 hours and freezing them overnight for 20 cycles.

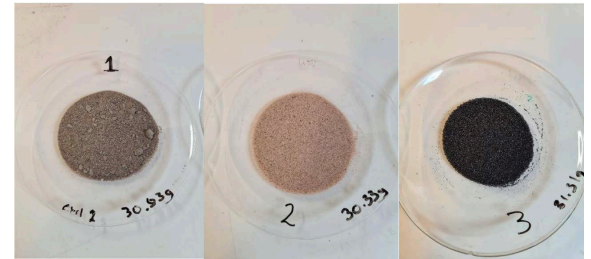


Fig. 1. River sand (1), Quartz WFS (2) and Chromite WFS (3).

RESULTS AND DISCUSSION

Initial studies on the chemical analysis of the WFS incorporated in concrete showed that Barium concentration increases with age in the samples, as it is present in Portland Cement, but this poses an environmental issue since the WHO drinking standards set a limit of 0.7 ppm for heavy metals in drinking water. Control samples and samples with high percentages of Chromite and Quartz show barium levels three times higher than the safety limit. Samples with Selenium also exceeded the WHO drinking standard limit of 0.01ppm, but the concentration reduces with curing age and can be reduced by increasing WFS. Although the trace amount of Chromium detected cannot be relied on due to LOD, the results suggest that concrete can sequester harmful contaminants, with curing age playing a role in containment.

Tests on the mechanical properties showed that compressive strength (Fig. 2) and splitting tensile strength decreased as the substitution level increased due to the high-water content and fineness of the sands. Thermal conductivity decreased with increasing substitution levels, but water absorption decreased at all substitution levels. Lowering the amount of water added to the mixtures containing WFS could increase strength, but excessive water added to 100% chromite sand led to total collapse.

Waste foundry sands as a substitute for natural sands in concrete can improve its properties. The study found that a full substitution rate is possible, and the resulting concrete is more durable and resistant to water and harsh chemicals. The concrete with waste foundry sands also performed better under stress and showed less internal degradation due to its higher density and less porous structure. The study also conducted tests on the concrete's ability to withstand freezing and thawing cycles, which further boosted its mechanical properties.

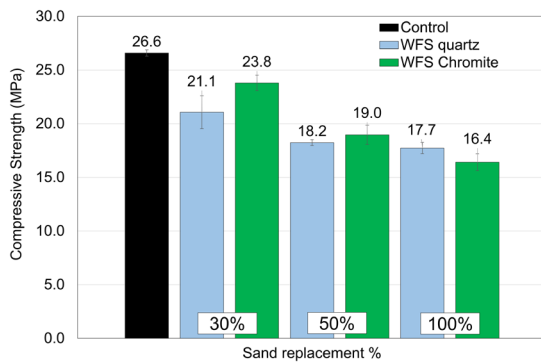


Fig. 2. Compressive strength of specimens at different levels of fine aggregate replacement.

CONCLUSIONS

Overall, using waste foundry sands in concrete can be a viable and beneficial alternative to using natural sands. This work suggests that WFS is an environmentally sustainable solution for both the cast metal industry and the construction sector, as it repurposes a material that would otherwise be disposed of into a raw material for durable concrete production. Future work will include:

investigating the water transport properties and conducting a detailed life cycle assessment to evaluate the environmental benefits of unprocessed rice husk ash in construction.

Mechanical and durability testing (simulated harsh environment) to evaluate the full extent of 100% WFS substitution and re-grading by combining different WFS types and/or standard sand.

Life cycle assessment to target infrastructure applications (retaining wall, pavement).

Acknowledgements

This research was carried out by undergraduate students with the supervision of Dr Riccardo Maddalena and Dr Fei Jin; further work was possible thanks to Cardiff University summer placements.

Conflicts of interest

The authors declare no conflict of interest.

REFERENCES

- [1] D. Kumar and S. Kumar, 'Robustness of self-compacting concrete containing waste foundry sand and metakaolin: A sustainable approach', *J Hazard Mater*, vol. 401, no. April 2020, p. 123329, 2021. doi.org/10.1016/j.jhazmat.2020.123329
- [2] N. Thamaraiselvi, N. Sakthieswaran, and O. G. Babu, 'Materials Today: Proceedings Improving the performance of mortar containing industrial wastes', *Mater Today Proc*, vol. 37, pp. 1062–1065, 2021. doi.org/10.1016/j.matpr.2020.06.294
- [3] F. Friol Guedes de Paiva, J. R. Tamashiro, L. H. Pereira Silva, and A. Kinoshita, 'Utilization of inorganic solid wastes in cementitious materials – A systematic literature review', *Constr Build Mater*, vol. 285, 2021. doi.org/10.1016/j.conbuildmat.2021.122833
- [4] M. A. de B. Martins, R. M. Barros, G. Silva, and I. F. S. dos Santos, 'Study on waste foundry exhaust sand, WFES, as a partial substitute of fine aggregates in conventional concrete', *Sustain Cities Soc*, vol. 45, no. November 2018, pp. 187–196, 2019. doi.org/10.1016/j.scs.2018.11.017
- [5] P. R. de Matos, R. Pilar, L. H. Bromerchenkel, R. A. Schankoski, P. J. P. Gleize, and J. de Brito, 'Self-compacting mortars produced with fine fraction of calcined waste foundry sand (WFS) as alternative filler: Fresh-state, hydration and hardened-state properties', *J Clean Prod*, vol. 252, p. 119871, 2020. doi: 10.1016/j.jclepro.2019.119871
- [6] British Standard Institution, 'BS EN 206:2013+A2:2021 - Concrete. Specification, performance, production and conformity', London, UK, 2021.
- [7] British Standard Institution, 'BS EN 12620:2002+A1:2008 - Aggregates for Concrete', London, UK, 2002.
- [8] M. F. Iqbal *et al.*, 'Prediction of mechanical properties of green concrete incorporating waste foundry sand based on gene expression programming', *J Hazard Mater*, vol. 384, no. June 2019, p. 121322, 2020. doi.org/10.1016/j.jhazmat.2019.121322

Sayadi S

*Cardiff University
School of Engineering*

Mihai I

*Cardiff University
School of Engineering*

Jefferson A

*Cardiff University
School of Engineering*

CIVIL INFRASTRUCTURE

Biomimetic Materials in Construction Industry: the Necessity of Simulation

Biomimetic materials are a possible solution to tackle the environmental and sustainability concerns of the construction industry. Automation in repairing and self-healing features can increase the durability of brittle materials which are susceptible to cracking. A number of different self-healing technologies have been introduced over the past two decades; however, further research is needed to simulate their behaviour and study their performance. Mathematical models are needed for design and assessment purposes. In this paper the formulation as well as the application of a micromechanical model is presented. This model can capture simultaneous fracture and healing processes. The results from this constitutive formulation can be implemented in finite element framework for simulating the boundary value, and multiscale problems. The model is tested for an encapsulated self-healing cementitious mortar and the results show that it can capture the stiffness recovery with an acceptable accuracy

Keywords:

Biomimetic materials, numerical modelling, micromechanics.

Corresponding author:

SayadiMoghadamS@cardiff.ac.uk



S. Sayadi, I. Mihai, and A. Jefferson, 'Biomimetic Materials in Construction Industry: the Necessity of Simulation', *Cardiff University School of Engineering Research Conference 2023*, Cardiff, UK, 2023, pp. 55-57.

doi.org/10.18573/conf1.n

INTRODUCTION

The materials used for construction are required to be produced in a large volume. Despite their low environmental impact per unit, the overall impact on environment is enormous [1], due to the high-volumes of these materials used by the construction industry. In addition to the impact of producing new materials for buildings, the economical and environmental cost because of repair and maintenance are other concerns that motivate researchers to look for much more sustainable solutions [2]. Cementitious materials, lime mortar and geomaterials are the most frequent materials used in buildings [3]. These materials are brittle which means they are prone to cracking under tensile loading. Structural durability is significantly affected by cracking. Inspired by nature, researchers have introduced some new biomimetic techniques to enhance the performance of conventional materials employed in construction industry [4]. In particular,

self-healing and crack closure systems have been developed for enhancing durability. The behaviour of these materials is governed by a set of coupled chemo-physical processes. Employing autonomous self-healing techniques such as micro and microencapsulation, embedding vascular network and using bacteria can provide the self-healing features for these materials in case of damage [5]. Using microfibres or shape memory tendons can control and close the crack which aids autogenous healing (i.e., inherent self-healing that naturally occurs in cementitious materials, e.g., hydration of unhydrated particles) [6]. Fig. 1 shows schematically the different methods employed for developing biomimetic materials.

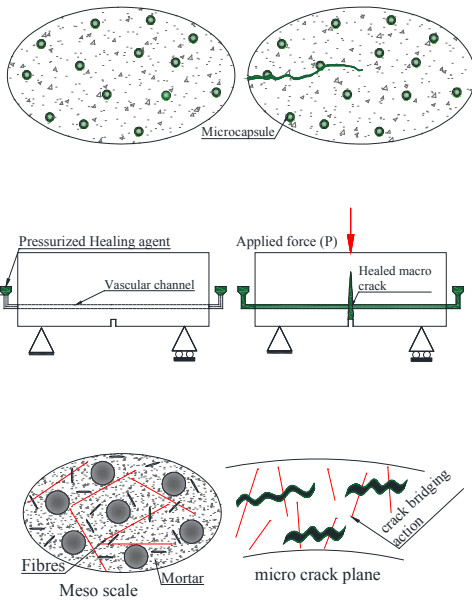


Fig. 1. Different self-healing practice, a) encapsulation (top), b) vascular network (middle) and c) fibre-reinforcing (bottom).

Some experimental research has been undertaken to evaluate the performance of these materials [5-6]. However, a little research has been devoted to determining the mechanisms observed in these experiments [7]. Finding a reliable model which can capture the essential behaviour of self-healing materials is essential for assessment and design.

In the reminder of this paper the newly developed methodology for simulating mechanical properties of biomimetic material is explained. The numerical results for encapsulated system briefly presented in the Results section.

MATERIALS AND METHODS

The biomimetic materials used in construction industry are composite multiphase systems. The chemo-mechanical actions within these materials occur at different length scales. To capture the behaviour of these materials, a multiscale method is required that can bridge between the different length scales. For these purposes, the micromechanical formulation is adopted to simulate the complex behaviour of this materials. The overall mechanical properties are obtained through homogenization techniques. A hierarchical multiscale averaging method is employed to upscale each phase properties to the higher scale. Fig.2 Shows schematic procedure for projecting each scale properties to the desired length scale.

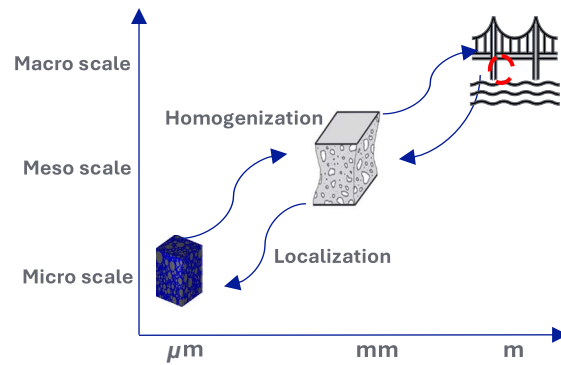


Fig. 2. Schematic procedure for hierarchy homogenization and multiscale analysis

The microcracking effect on the mechanical response is considered by assuming the formation of randomly distributed penny shaped microcracks inside the considered medium. Equation (1) shows how the effect of cracks is represented mathematically:

$$\mathbf{s}_L(\theta, \phi) = (1 - \omega(\theta, \phi)) \mathbf{D}_L \boldsymbol{\varepsilon}_L(\theta, \phi) \quad (1)$$

where \mathbf{s}_L and $\boldsymbol{\varepsilon}_L$ are the stress and strain local vector on a crack plane respectively. ω is the matrix damage parameter and \mathbf{D}_L is the local crack plane stiffness matrix. The healing contribution is added to the above equation as follows:

$$\mathbf{s}_{Lh} = (1 - \omega) \mathbf{D}_L \boldsymbol{\varepsilon}_L + h_v \mathbf{D}_{Lh} (1 - \omega_h) (\boldsymbol{\varepsilon}_L - \boldsymbol{\varepsilon}_h) \quad (2)$$

where the subscript h is for declaring the healing materials. h_v is the amount of the cracks that healed and $\boldsymbol{\varepsilon}_h$ is healing offset strain for thermodynamic consistency condition. These equations represent 1D crack-healing constitutive behaviour. The overall 3D response is derived through the micromechanical integration proposed by Budiansky & O'Connell's method [8]. The full formulation derivation is explained in detail in forthcoming paper.

The performance of the proposed model is tested for a distributed crack-healing scenario. A concrete cylinder with embedded encapsulated healing agent was tested

under compressive loading [9]. the degree of healing was measured by the stiffness recovery. The experimental sample details are presented in Table.1

Material/Properties	v_f %	E (GPa)	f_t (MPa)
Concrete	99.0	32	2
Microcapsules	1	0.3	0.24
Healing agent	-	16	4.5

Table.1. material properties

RESULTS

The stress-strain response under compression load is depicted in Fig.3. The stiffness recovery and its comparison with the experimental data is plotted in Fig.3. Figure 3a shows how the stiffness is derived before and after healing for the sample with 0.5% microcapsules.

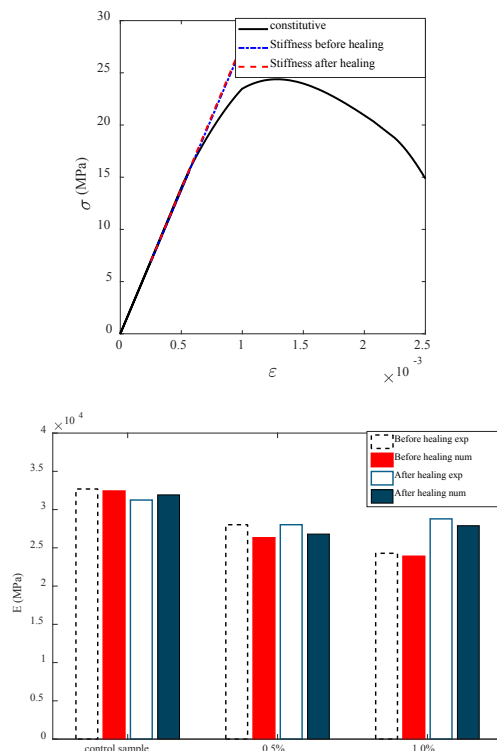


Fig. 3. Numerical results; a) compressive stress-strain relation (top), and b) stiffness recovery comparison (bottom).

DISCUSSION

The results show that the overall main mechanical characteristics of the composite system can be captured through the proposed closed form formulation. Furthermore, the comparison between elastic moduli of the encapsulated systems with the different volume fractions indicates that microcapsules can reduce the initial mechanical properties of cementitious composite systems. Using a high-volume fraction of microcapsules can increase the probability of triggering and following that the healing. This shows the importance of simulation in finding the optimum dosage of microcapsules in design applications.

Acknowledgments

This project has received funding from the European Union's Horizon 2020 research and innovation programme under the Marie Skłodowska-Curie grant agreement No 860006.

Conflicts of interest

The authors declare no conflict of interest.

REFERENCES

- [1] C. R. Gagg, 'Cement and concrete as an engineering material: An historic appraisal and case study analysis', *Engineering Failure Analysis*, vol. 40, pp. 114–140, May 2014. doi.org/10.1016/j.engfailanal.2014.02.004.
- [2] R.J. Woodward et al., 'Deliverable D14 Final report BRIME Contract no. RO-97-SC.2220'. EC 4th framework programme.
- [3] J.M. Crow, 'The concrete conundrum', *Chem World*, 2008: 62–66. Archived.
- [4] V. Cappellesso et al., 'A review of the efficiency of self-healing concrete technologies for durable and sustainable concrete under realistic conditions', *Int Mater Reviews*, vol. 68, no. 5, pp. 556–603, Jul. 2023. doi.org/10.1080/09506608.2022.2145747
- [5] N. De Belie et al., 'A Review of Self-Healing Concrete for Damage Management of Structures', *Adv Mater Interfaces*, vol. 5, no. 17, p. 1800074, Sep. 2018. doi.org/10.1002/admi.201800074
- [6] K. Van Tittelboom and N. De Belie, 'Self-Healing in Cementitious Materials—A Review', *Materials*, vol. 6, no. 6, pp. 2182–2217, Jun. 2013. doi.org/10.3390/ma6062182
- [7] T. Jefferson, E. Javierre, B. Freeman, A. Zaoui, E. Koenders, and L. Ferrara, 'Research Progress on Numerical Models for Self-Healing Cementitious Materials', *Adv Materials Inter*, vol. 5, no. 17, p. 1701378, Sep. 2018,. doi.org/10.1002/admi.201701378
- [8] A. D. Jefferson and T. Bennett, 'Micro-mechanical damage and rough crack closure in cementitious composite materials', *Int J Num Anal Meth Geomechanics*, vol. 31, no. 2, pp. 133–146, Feb. 2007. doi.org/10.1002/nag.551
- [9] J. Gilford, M. M. Hassan, T. Rupnow, M. Barbato, A. Okeil, and S. Asadi, 'Dicyclopentadiene and Sodium Silicate Microencapsulation for Self-Healing of Concrete', *J Mater Civ Eng*, vol. 26, no. 5, pp. 886–896, May 2014. doi.org/10.1061/(ASCE)MT.1943-5533.0000892

Stucchi NME

*Università Ca' Foscari Venezia
Dept. Molecular Science and Nanosystem*

Ronchin L

*Università Ca' Foscari Venezia
Dept. Molecular Science and Nanosystem*

De Nardi C

*Cardiff University
School of Engineering*

Vavasori A

*Università Ca' Foscari Venezia
Dept. Molecular Science and Nanosystem*

Franceschin G

*Istituto Italiano di Tecnologia
Center for Cultural Heritage Technology*

Traviglia A

*Istituto Italiano di Tecnologia
Center for Cultural Heritage Technology*

CIVIL INFRASTRUCTURE

Characterisation of Innovative Mortar Formulations for the Restoration of Roman Mosaics

This contribution is focused on the study of the workability and mechanical properties of innovative mortars previously developed for preservation of ancient mosaics. The new formulations are based on the study of the Vitruvian recipe for Roman mortars, respecting the compatibility criteria with the original material. Different additives in different concentrations have been added to the previous formulations with the aim of studying their role in improving the durability, physicochemical, and rheological properties of the consolidating formulations. Preliminary slump tests were carried out to evaluate the effect of the additives on the workability of designed lime-based mortars. The achieved results highlighted the benefits of the use of plant-derived gel and inorganic nanoparticles in mortar mixtures, when added in suitable concentration. Considering these results, the best mortars formulations have been selected to examine in depth their mechanical properties.

Keywords:
*Mosaic, consolidation, mortars,
workability, durability.*

Corresponding author:
Neva.Stucchi@iit.it



N.M.E. Stucchi, C.De Nardi, G. Franceschin, L. Ronchin, A. Vavasori, and A. Traviglia, 'Characterisation of Innovative Mortar Formulations for the Restoration of Roman Mosaics', *Cardiff University School of Engineering Research Conference 2023*, Cardiff, UK, 2023, pp. 58-61.

doi.org/10.18573/conf1.o

INTRODUCTION

Composition of roman mosaic stratifications were reported already in ancient literature. Vitruvius [1] indicates a system made of 5 different strata: (i) tesserae; (ii) supranucleus, a strata of putty lime; (iii) nucleus, a thin layer made of fine pozzolana, sand, air lime mortar and water; (iv) rudus, composed by fine and great pozzolana, putty lime and water; (v) statumen, a strata of rough big stone and bricks. In Figure 1 the scheme of the typical mosaic floor stratification is reported. This system has been discovered in several archeological sites, including Aquileia [2, 3], which has been well documented and recognised.

Due to the inherent heterogeneity of the materials used to construct each stratum, restorers encounter several challenges when conserving mosaics [4]. The interaction of each layer with the environment causes several degradations, including fractures and swelling of mortar. This results in the loss of tesserae and, therefore, the loss of mosaic decoration integrity. A range of traditional interventions are available to address damage in mosaics systems, including the consolidation of different strata, namely (i) application of consolidants in grouting process; (ii) filling of cracks with injection mortars; (iii) repointing of lost tesserae with pastes [5-6]; and if needed (iv) detachment of mosaics from the original site and their collocation on new supports [7].

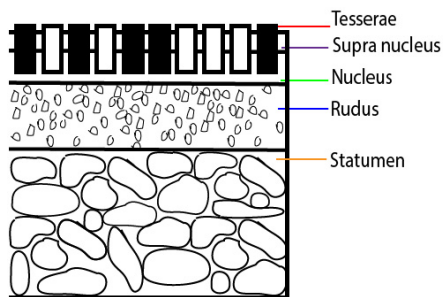


Fig. 1. Structure of mosaic with indication of all the superficial strata.

Operations as described in i-iii involve the use of either hydraulic or non-hydraulic lime mortars mixed with acrylic emulsions [8]. It is good practice, that the compounds employed for preservation are selected to be compatible with and sympathetic to conservation requirements, i.e. be physically, chemically and mechanically compatible with the host material [9]. So, the mortar mix design used for restoration is the reproduction of ancient compositions with modern materials, selected among which have chemical compositions similar to the original ones [10].

Fluidity is one of the most important parameters to take into account when dealing with the development of mortar pastes. The water/binder ratio is the key factor to consider in order to change the viscosity and workability properties of the formulation [11]. As early as ancient literature, the addition of natural organic compounds such as figs or fats to mortar mixtures was a practice in use [12] in order to change mechanical and physical characteristics.

Nowadays, the trend towards producing greener and more sustainable compounds is bringing about a renewal of the use of plant products as additives for admixtures of building materials. For example, the practice of adding *Opuntia mucilage* to construction mixtures is traditional and currently in use among the Mexican population [13, 14] to improve durability and mechanical properties [15] several Thermogravimetric Analysis (TGA), inhibit quick drying and

prevent cracking on renders [16]. Generally nanotechnology is used to increase or vary properties of materials [17]. In the last decades, several researchers tested the use of nanoparticles in order to change the mechanical properties of cements and mortar mixtures. The addition of inorganic nanoparticles increases the compressive strength of cement paste and mortar thanks to pozzolanic reactions [18]. More recently, self-healing materials have been developed in many fields of material science, including restoration of built heritage, as an alternative to the traditional damage prevention methods [19], [20].

In this research the mechanical behavior of innovative mortar formulations has been investigated. Taking in consideration Vitruvian recipes for the production of both nucleus and rudus, hydraulic mortars produced in order to have compatible hydraulic compounds for both the strata have been mixed with natural gel and inorganic nanoparticles. The effect on workability of the mixtures containing different proportions of additives have been evaluated through slump test and the results were used to select the best set of concentration and composition of additives to be studied from a mechanical point of view.

MATERIALS AND METHODS

Table 1 summarises the composition of the investigated mortars. Mix design for producing the studied mortars is drawn following Vitruvius' description, with binder to aggregate volume ratio kept constant at 1:3. Mortar A was based on "Nucleus" recipe, with 100%v of cocchiopesto as aggregate. Mortars B and C were based on "Rudus" composition, containing respectively 25%v and 50%v of sand to cocchiopesto ratio.

Mortars designation	B v/v	A v/v		W w%	N w%	S w%
		S	C			
A	1	-	3	0.04	-	-
AN_1	1	-	3	0.04	1	-
AN_2.5	1	-	3	0.04	2.5	-
AS_1	1	-	3	0.04	-	1
B	1	3		0.025	-	-
		1	4			
BN_1	1	1	4	0.025	1	-
BN_2.5	1	1	4	0.025	2.5	-
BS_1	1	1	4	0.025	-	1
BS_2.5	1	1	4	0.025	-	2.5
C	1	3		0.025	-	-
		1	2			
CN_1	1	1	2	0.025	1	-
CN_2.5	1	1	2	0.025	2.5	-
CS_1	1	1	2	0.025	-	1
CS_2.5	1	1	2	0.025	-	2.5
		1				

Table 1. Composition of investigated mortars. Designation conforms to the following: Binder (B), Aggregate (A); Fine Cocchiopesto (C); Fine Quartz Sand (S). Content of Water (W%); natural gel (N%) and inorganic nanoparticles (S%).

For mortars B and C are reported the ratio of sand and cocciopesto used for the composition of the aggregate, expressed in the ratio of volume of sand on total volume of cocciopesto. Two types of aggregates were used, fine cocciopesto (granulometry < 0,4 mm) and fine quartz sand (grain size of 0,1-0,3 mm). Water addition was scaled proportionally to parity of different aggregates for the preparation of mixes A and C. Binder and aggregates used for mortar production are purchased by C.T.S.

Mortars containing the addition of either natural gel or inorganic nanoparticles to A, B, and C at two concentrations (i.e. 1% and 2.5% by weight of mortar) were also studied. The nature of the inorganic nanoparticles and the plant-derived gel (properties and pre-treatment) cannot be disclosed as subject to evaluation for patent protection. The concentrations of additives and water are expressed in % on total weight.

Mini slump tests were performed on all mortar mixtures in order to evaluate the change in viscosity induced by the different compositions. The size of the cone normally used for testing concrete was proportionally scaled to analyse small quantity of mortars in laboratory, while respecting the normalised procedure [21].

RESULTS

Results of the first mini slump test indicated how additives affected viscosity and fluidity.

In Table 2 and Table 3 mini slump test results respectively of mortars A, B, C and of additivated mortars (AN, BN, CN, AS, BS, CS) are reported.

Mortars designations	r ² (cm)
A	4,2
B	5,1
C	4,3

Table 2. Results of slump test of mortar mixtures (M) A, B, C; values of the diameter of slump of the mortars.

Mortars designations	r ² (cm)	
	1 %	2,5%
AN	5,2	5,4
BN	5	5,2
CN	4,9	5,1
AS	4,1	4
BS	4,1	4,1
CS	4,2	4,1

Table 3. Evaluation of the diameter of slump of mortar mixtures with additives natural gel (AN, BN, CN) and inorganic nanoparticles (AS, BS, CS) in different concentrations 1%, 2,5%.

Mixture A and C showed similar results with a slump diameter of ~4,2 cm. It was found that the two mortars had similar workability being stiff enough to maintain the shape of the cone. Differently, mortar B resulted to be more fluid and is characterized by a greater diameter of 5,1 cm.

Greater addition of natural gel (confidential) had increased the slump of mortars A and more significantly of mortar C. Mortar B exhibited similar slump parameters regardless of the amount of natural gel added.

In all mortars, the addition of inorganic nanoparticles (confidential) seemed to have a negligible influence on the workability, i.e. slump diameter equal to $4,1 \pm 0,1$ cm.

DISCUSSION

Fluidity and viscosity are the main important characteristics to take in consideration for the design of mortars. Slump test is a first step to evaluate these characteristics. Mortar A and C show an equal slump parameter. Increment of fluidity was achieved for paste B, with respect to mortar C and A. To parity different ratios of sand and cocciopesto, the same amount of water is added for mix B and C, demonstrating the need to scale water content to parity with a reduction in sand ratio.

For mixtures A and C, the increase of slump test diameter is proportional to the increase of natural gel, demonstrating that paste fluidity increases with gel addition (confidential). Results suggested that the addition of plant-derived gel might result in a lower amount of water, further research will be carried out to assess the retention of water by the use of gel. The slump tests for mortar mixtures B were the same regardless of the addition of 1% gel concentration ($5 \text{ cm} \pm 0,2$) and results increase of $\pm 0,2$ with the addition of 2.5 % of gel. No relevant changes in viscosity have been seen in mortars containing inorganic nanoparticles (confidential) additions. All mortar mixtures with this additive showed similar slump test values of $4,2 \text{ cm} \pm 1$ and conserved the cone shape of the slump test, as shown also for mixtures A and C.

Based on the results presented in this work, the best mortar-additive formulations are selected to be studied by the application of mechanical test and multiple characterization techniques, for the definition of their physical and chemical characteristics. Furthermore, in the future the rheological properties of mortars containing natural gel as a fluidifier will be intensively investigated as well as the effect of inorganic nanoparticles addition. Tailored self-healing materials will be also added with the purpose to improve durability of the injection mortar once used for conservation process of mosaic system.

Acknowledgements

This research was funded by the Leverhulme Trust 59 ECF-2022-235. The authors thank NopalVet s.r.l for the furniture of cladodes of Opuntia Ficus d'India.

Conflicts of interest

The authors declare no conflict of interest.

REFERENCES

- [1] Vitruvio. *De Architectura*. vol. I.
- [2] B. Portulano *et al.*, 'Caratteri stratigrafici dei mosaici di Aquileia', *Scienza e beni culturali*, XVIII, pp.637–646, 2002.
- [3] C. Boschetti *et al.*, 'Making Roman Mosaics in Aquileia (I BC – IV AD): Technology, Materials, Style and Workshop Practices. Two Case Studies from the insula della Casa delle Bestie Ferite', in *Local Styles or Common Pattern Books in Roman Wall*, pp.91–111, 2021.
- [4] P. Pasqualucci, 'Da un riesame delle fonti e dall'analisi dei mosaici di Privernum una nuova lettura della tecnica di esecuzione pavimentale romana', *Atti X Coll AISCOM*, pp. 527–538, 2004.
- [5] T. Roby, 'The conservation of mosaics in situ: preserving context and integrity', in *Stories in stone: conserving mosaics of roman Africa*, pp. 101–114, 2011.
- [6] R. Albini and C. Zizola, 'Zippori. In situ conservation of a floor mosaic in polychrome stones and glass paste', in *Vith International Conference of the International Committee for the Conservation of Mosaics*, pp. 235–247, 1996.
- [7] E. Madrigali, 'Esperienze di restauro e valorizzazione di Aquileia: L'esempio dei fondi ex Cossar', in *L'architettura privata ad Aquileia in età romana*, 2011.
- [8] M. Macchiarola, 'Conservazione musiva in Italia: luci ed ombre', in *I mosaici dell'alto adriatico*, pp. 37–44, 2010.
- [9] S. Botas, R. Veiga, and A. Velosa, 'Air lime mortars for conservation of historic tiles: Bond strength of new mortars to old tiles', *Construction and Building Materials* vol. 145, pp. 426–434, Aug. 2017. doi.org/10.1016/j.conbuildmat.2017.04.027
- [10] A. Moropoulou, A. Bakolas, M. Karoglou, E. T. Delegou, K. C. Labropoulos, and N. S. Katsiotis, 'Diagnostics and protection of Hagia Sophia mosaics', *Journal of Cultural Heritage*, vol. 14, no. 3, pp. e133–e139, Jun. 2013. doi.org/10.1016/j.culher.2013.01.006
- [11] G. Artioli, M. Secco, and A. Addis, 'The Vitruvian legacy: Mortars and binders before and after the Roman world', in *The Contribution of Mineralogy to Cultural Heritage, Mineralogical Society of Great Britain and Ireland*, 2019, pp. 151–202. doi.org/10.1180/EMU-notes.20.4
- [12] Pliny the Elder. *Naturalis Historia*, Liber XXXVI.
- [13] C. Alisi *et al.*, 'Mucilages from Different Plant Species Affect the Characteristics of Bio-Mortars for Restoration', *Coatings*, vol. 11, no. 1, p. 75, Jan. 2021. doi.org/10.3390/coatings11010075
- [14] A. R. Sprocati, C. Alisi, G. Migliore, P. Marconi, and F. Tasso, 'Sustainable Restoration Through Biotechnological Processes: A Proof of Concept', in *Microorganisms in the Deterioration and Preservation of Cultural Heritage*, E. Joseph, Ed., Cham: Springer International Publishing, 2021, pp. 235–261. doi.org/10.1007/978-3-030-69411-1_11
- [15] C. G. H. Carrillo, J. A. Gómez-Cuaspad, and C. E. M. Suarez, 'Compositional, thermal and microstructural characterization of the Nopal (*opuntia ficus indica*), for addition in commercial cement mixtures', *J Phys: Conf Ser*, vol. 935, no. 1, p. 012045, Dec. 2017. doi.org/10.1088/1742-6596/935/1/012045
- [16] Y. Kita, 'The functions of vegetable mucilage in lime and earth mortars. A Review', in *Proceedings of the 3rd Historic Mortars Conference*, Glasgow, UK, 9–14 September 2013.
- [17] A. Sierra-Fernandez, L. S. Gomez-Villalba, M. E. Rabanal, and R. Fort, 'New nanomaterials for applications in conservation and restoration of stony materials: A review', *Materiales de Construcción*, vol. 67, no. 325, pp. e107–e107, Mar. 2017 doi.org/10.3989/mc.2017.07616
- [18] M. Secco, S. Dilaria, A. Addis, J. Bonetto, G. Artioli, and M. Salvadori, 'The Evolution of the Vitruvian Recipes over 500 Years of Floor-Making Techniques: The Case Studies of the Domus delle Bestie Ferite and the Domus di Tito Macro (Aquileia, Italy)', *Archaeometry*, vol. 60, no. 2, pp. 185–206, Apr. 2018 doi.org/10.1111/arcim.12305
- [19] W. Zhang, Q. Zheng, A. Ashour, and B. Han, 'Self-healing cement concrete composites for resilient infrastructures: A review', *Composites Part B: Engineering*, vol. 189, p. 107892, May 2020. doi.org/10.1016/j.compositesb.2020.107892
- [20] C. De Nardi, A. Cecchi, L. Ferrara, A. Benedetti, and D. Cristofori, 'Effect of age and level of damage on the autogenous healing of lime mortars', *Composites Part B: Engineering*, vol. 124, pp. 144–157, Sep. 2017. doi.org/10.1016/j.compositesb.2017.05.041
- [21] Z. Tan, S. A. Bernal, and J. L. Provis, 'Reproducible mini-slump test procedure for measuring the yield stress of cementitious pastes', *Mater Struct*, vol. 50, no. 6, p. 235, Oct. 2017. doi.org/10.1617/s11527-017-1103-x

Rowley SJ

*Cardiff University
School of Engineering*

Pan S

*Cardiff University
School of Engineering*

CIVIL INFRASTRUCTURE

Modelling Buildings During Flood Inundation Using TELEMAC-2D

Global climate change significantly increases flood risk. Inundation around buildings in both urban and rural areas can pose significant risk to life and property. Accurate and precise modelling is the key to a better understanding and quantification of flood risk. This study applies three different methods for modelling buildings within TELEMAC-2D from a dyke breach scenario: a) buildings excluded from the mesh; b) buildings modelled as elevated bathymetry; and c) buildings modelled as vegetation friction. The maximum flood hazard rating for each method is then calculated from the hydrodynamics generated by the model and compared. The results show that using vegetation friction to represent the buildings in the model is the most effective and accurate approach in evaluating the flood risk.

Keywords:

*Flooding, buildings, modelling,
TELEMAC, River Severn.*

Corresponding author:

RowleySJ@cardiff.ac.uk



S.J. Rowley and S. Pan, 'Modelling Buildings During Flood Inundation Using TELEMAC-2D', *Cardiff University School of Engineering Research Conference 2023*, Cardiff, UK, 2023, pp. 62-65.

doi.org/10.18573/conf1.p

INTRODUCTION

Climate change and increasing urbanisation have left communities globally more exposed to flooding. Flooding affected 54.86 million people worldwide in 2022, directly causing 7,398 deaths [1]. The estimated cost of flooding in 2019 was approximately 52 billion US dollars [2].

Buildings, particularly housing and commercial premises, are one of the primary assets at risk from flooding. When floodwater surrounds a structure there is a significant risk to life, and there can be considerable financial losses. The way that water flows around structures influences local inundation depths, flow velocities, as well as pollutant and debris transport. These in turn all influence the risks to life and property. To better understand the increasing risk, flooding needs to be accurately modelled. It is important to evaluate various modelling methods in comparison to one another and where possible verify them with empirical evidence.

Research has focused on models with uniform buildings in a simplified urban district [3], porosity modelling of bulk areas [4] and modelling buildings with Manning's roughness coefficient, reflection boundaries and raised beds [5]. The contrasts between bare earth models against raised buildings have been examined but not using a resistance method or exclusion for buildings [6]. Comparisons between similar methods as those proposed in this study have been made previously, but they did not use the same resistance formulation [7].

Bewdley is a village on the River Severn in Worcestershire, England, and is known for its frequent flooding [8]. The village has erectable temporary flood defences operated by the UK Environment Agency (EA), as well as some permanent embankment defences. This paper introduces three different approaches for modelling buildings in TELEMAC-2D, examining a group of buildings near the River Severn in Bewdley. Flood Hazard Ratings are generated for the different methods and comparison made between them.

MATERIALS AND METHODS

TELEMAC-2D is a modelling framework that simulates free surface flows in a two-dimensional space by solving the Saint-Venant depth averaged shallow water equations with the finite-element or finite volume methods, using an unstructured, irregular triangular mesh.

In this study, the finite element method is used and the building zone at Bewdley adjacent to the River Seven as highlighted in Fig. 1 is selected for model application.



Fig. 1. Satellite image (Google Maps) of the River Severn and part of Bewdley, with building outlines used in this study highlighted in red.

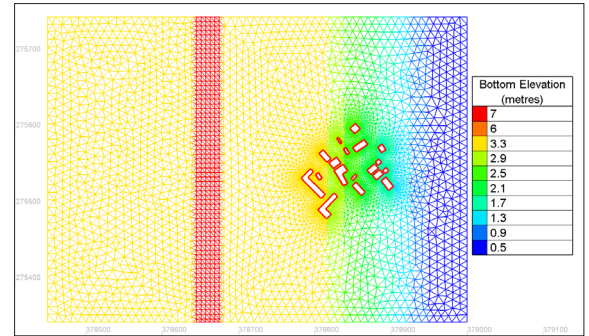


Fig. 2. Computational mesh for the domain with bottom elevation.

The computational domain is idealised from the study site shown in Fig. 1. The bathymetry is assumed to incline from the edge of the dyke, moving across the buildings zone to the rightmost edge of the modelled area. The drop over the incline is 5m, a gradient of 1:64. This allows the model to drain once the dyke is breached and the inundation has peaked.

Three methods are examined here for modelling buildings:

- 1) **BH Method:** Buildings are excluded in the computational mesh, meaning that no hydrodynamic computations are carried out within the boundaries, as shown in Fig. 2.
- 2) **BR Method:** Raising of the bed level at building locations is used. The mesh is raised to uniform levels of 5.8m and 3.2m, depending on whether the building is 1 or 2 stories high.
- 3) **BV Method:** Buildings are represented by the vegetation friction in TELEMAC-2D with a specific built-in module. It simulates the buildings as ultra-high friction zones with near zero velocity fields. Vegetation friction can be modelled as a linear superposition with the bed roughness [9], in this case Manning's roughness coefficient.

$$\lambda = \lambda' + \lambda'' \quad (1)$$

where, λ is total roughness, λ' is bed roughness and λ'' is vegetation resistance per unit area. With the method proposed by [10], it simulates vegetation as a drag coefficient, by considering the vegetation diameter, treated as a cylinder, and vegetation density as:

$$\lambda'' = \begin{cases} 4C_D \cdot \frac{Dh}{\Delta^2} & \text{for } h \leq h_p \\ 4 \cdot \left(\frac{1}{\sqrt{C_D} \frac{Dh_p}{\Delta^2}} + \frac{1}{\sqrt{2}\kappa} \ln \frac{h}{h_p} \right)^{-2} & \text{for } h > h_p \end{cases} \quad (2)$$

where C_D is the drag coefficient, D is the plant diameter, h is the flow depth, Δ is the element spacing, κ is von Kármán constant and h_p is the vegetation height. It also has two layer flow for submerged and non-submerged vegetation.

A dyke breach scenario simulates the rapid inundation of buildings as may occur during a fluvial flood. The water level behind the dyke rises in accordance with the symmetrical storm design used in ReFH2 [11]. Near the peak water level, the dyke breach begins over a given width and period via the TELEMAC-2D user function by lowering the dyke by 2 m over 15 minutes. This causes water to rapidly flow through the dyke to the building zone and the surrounding area.

The EA provides guidance on assessing the risk to life from flood waters [12]. It combines the effects of water depth and velocity as Flood Hazard Risk (FHR) as:

$$FHR = D(V + 0.5) + DF \tag{3}$$

where D is water depth (m), V is velocity (m/s), and DF is a debris coefficient varying from 0-1 depending on local conditions. The output can then be graded with a numerically stepped risk classifier, shown in Table 1.

FHR	Level	Description
<0.75	L	Flood zone with shallow flowing water or deep standing water.
0.75 - 1.25	M	Moderate Danger for some (i.e. children). <i>Danger: Flood zone with deep or fast flowing water.</i>
1.25 - 2.50	H	Significant Danger for most people. <i>Danger: flood zone with deep fast flowing water.</i>
>2.50	E	Extreme Danger for everyone. <i>Extreme danger: flood zone with deep fast flowing water.</i>

Table 1. Classifications of Flood Hazard Risk

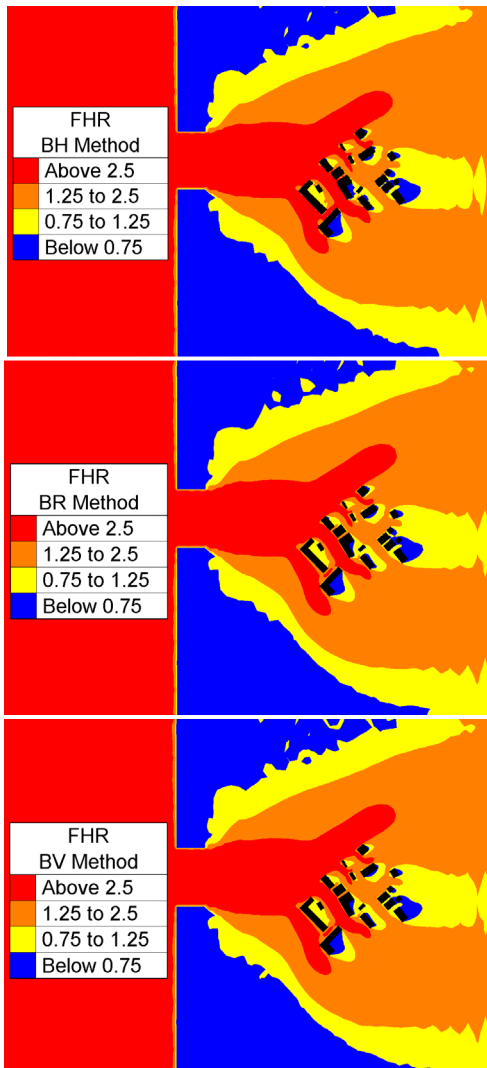


Fig. 3. Maximum FHR with: (a) BH method (top), (b) BR method (middle), and (c) BV method (bottom).

RESULTS

FHR Maps

FHR maps were produced from the model results, which are shown below. Figure 3. shows the maximum FHR from the three methods proposed for simulating buildings. In general, the FHRs for the 3 methods are similar, with the shape and size of the extreme danger zones (>2.5) being nearly identical for all methods, and the other danger zones having the similar distributions. There are small discrepancies in the spaces between the buildings and in-between the low and medium risk zones further out from the buildings.

Comparison of FHR Maps

A direct comparison of the results took the differences between the maximum FHR outputs, highlighting any significant changes in risk profiles between methods.

The scale used for comparisons shows minimal changes between ± 0.1 as white space.

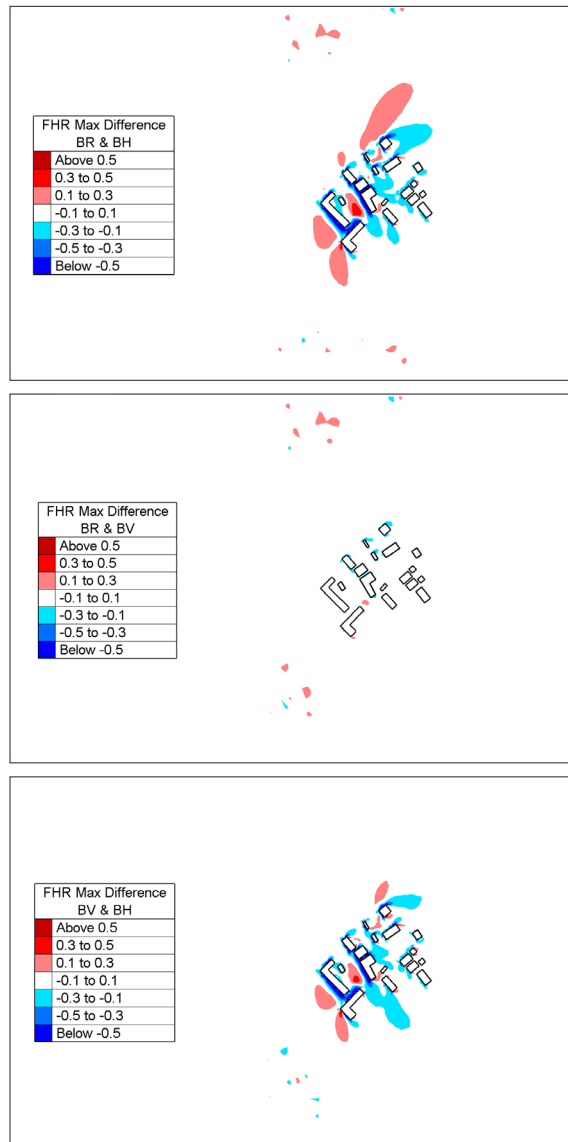


Fig. 4. The difference of the maximum FHR values between: (a) BR and BH (top), (b) BR and BV (middle), and (c) BV and BH (bottom).

DISCUSSION

The three methods examined in this study have broadly the same output when considering the general shape, size, and FHR classification of structures within the flow.

The BR and BV methods are in good agreement in their FHR results. There are a few zones of change (Fig. 4. Part b) near to the buildings, but these are small, and nearly all within the range of 0.1 to 0.3 or -0.3 to -0.1 range.

There are some discrepancies between the BR and BV methods and the output of the BH method. The BH method predicts significantly higher (Dark blue, -0.5 or below) FHR values near the front of buildings. This is accompanied by a zone of lower risk (Red, 0.3 to 0.5) between buildings in the centre of the study area. The area of the change is smaller for the BV method (Fig. 4. Part c) than for the BR method (Fig. 4. Part a). These discrepancies require further analysis, especially to determine which of the methods, if any, is the most physically realistic.

Excluding the buildings from the mesh prevents any water from entering. However, buildings are not impenetrable structures, but are often porous to some degree. The exclusion method (BH) makes any porosity or overtopping impossible and therefore may be the less representative of the three methods.

The vegetation friction method can capture building infiltration and storage and is simple to apply to any model. These advantages along with its broad agreement with the raised bedforms method make it potentially useful and applicable in modelling floodwaters.

CONCLUSIONS

This paper outlines three methods to model buildings on a flood plain during a dyke break scenario in TELEMAC-2D.

The methods have general agreement in terms of maximum FHR but there are discrepancies between the BH method and the BV and BR methods.

The use of vegetation friction is to the authors knowledge a novel method. It has acceptable model outputs and so could be a valid option to choose to model buildings during a flood event.

Future work is needed concentrating on the discrepancies between methods, as well as validation cases. Models need to account for additional floodplain obstructions, and a mesh density sensitivity analysis should be completed.

Acknowledgments

The authors would like to acknowledge the EPSRC funded WISE-CDT (Grant No: EP/L016214/1) for providing funding for this research.

Conflicts of interest

The authors declare no conflict of interest.

REFERENCES

- [1] D. Guha-Sapir, 2023. *EM-DAT The International Disaster Database*. [Online] Available at: www.emdat.be [Accessed 10 03 2023].
- [2] The World Bank Group, 2023, *The World Bank*, 2023. [Online]. Available: <https://data.worldbank.org/indicator/NY.GDP.MKTP.CD>. [Accessed 10 03 2023].
- [3] Z. Li, J. Liu, C. Mei, W. Shao, H. Wang, and D. Yan, 'Comparative Analysis of Building Representations in TELEMAC-2D for Flood Inundation in Idealized Urban Districts', *Water*, vol. 11, no. 9, p. 1840, Sep. 2019. doi.org/10.3390/w11091840
- [4] J. Hervouet, R. Samie, and B. Moreau, 'Modelling urban areas in dam-break flood-wave numerical simulations', *Developments in Water Science*, vol. 47, pp. 1613-1620, 2022.
- [5] V. Bellos and G. Tsakiris, 'Comparing Various Methods of Building Representation for 2D Flood Modelling In Built-Up Areas', *Water Resources Management*, vol. 29, no. 2, pp. 379-397, Jan. 2015. doi.org/10.1007/s11269-014-0702-3
- [6] R. Reshma and S. N. Kuiry, 'Significance of Representing Buildings in Urban Flood Simulations', in *Recent Trends in River Corridor Management*, V. Chembolu and S. Dutta, Eds., in Lecture Notes in Civil Engineering. Singapore: Springer Nature, 2022, pp. 141-151. doi.org/10.1007/978-981-16-9933-7_9
- [7] J.E. Schubert, and B.F. Sanders Sanders, 'Building treatments for urban flood inundation models and implications for predictive skill and modeling efficiency', *Advances in Water Resources*, vol. 41, pp. 49-64, 2012. doi.org/10.1016/j.advwatres.2012.02.012
- [8] Environment Agency, 2023. *Environment Agency welcomes approval of its planning application to protect Beales Corner in Bewdley, Worcestershire from flooding*. [Online] Available at: <https://www.gov.uk/government/news/environment-agency-welcomes-approval-of-its-planning-application-to-protect-beales-corner-in-bewdley-worcestershire-from-flooding>
- [9] F. Folke, R. Kopmann, G. Dalledone, and M. Attieh, 'Comparison of different vegetation models using TELEMAC-2D', *Telemac User Conference 2019*, Toulouse (TUC2019).
- [10] M.J. Baptist et al., 'On inducing equations for vegetation resistance', *Journal of Hydraulic Research*, 45(4), pp. 435-450, 2006. doi.org/10.1080/00221686.2007.9521778
- [11] Wallingford Hydro Solutions, 2023 *ReFH Technical Guide* [Online] Available: <https://refhdocs.hydrosolutions.co.uk/Design-DDF-Rainfall-Hyetographs/Design-Storm-Profiles/>. [Accessed 10 03 2023].
- [12] Environment Agency, 2008. *Defra Flood and Coastal Defence Appraisal Guidance - Social Appraisal - Supplementary Note to Operating Authorities - Assessing and Valuing the Risk to Life from Flooding for Use in Appraisal of Risk Management Measures*, s.l.: DEFRA.

Degani I

*Cardiff University
School of Engineering*

Maddalena R

*Cardiff University
School of Engineering*

Kulasegaram S

*Cardiff University
School of Engineering*

CIVIL INFRASTRUCTURE

Shrinkage Potential and Water Transport Properties of Self-compacting Concrete at Different Temperatures

In recent years, self-compacting concrete (SCC) has gained popularity due to its numerous advantages. While the fresh properties of SCC have been extensively discussed, there is a need for further research on its durability properties, particularly with respect to SCC cured at different temperatures. The present study aims to investigate the shrinkage, water absorption rate, and chloride permeability of high-strength SCC cured under water at four different temperatures i.e., 10 °C, 20 °C, 35 °C, and 50 °C.

The results showed that the samples which were cured at temperature 50 °C gained the largest shrinkage, while the samples cured at 10 °C temperature resulted in low shrinkage value, low sorptivity and electrical resistivity after 90 days of curing.

Keywords:

Self-compacting concrete, shrinkage, sorptivity, curing temperature, electrical resistivity.

Corresponding author:

DeganilM@cardiff.ac.uk



I. Degani, R. Maddalena, and S. Kulasegaram, 'Shrinkage Potential and Water Transport Properties of Self-compacting Concrete at Different Temperatures', *Cardiff University School of Engineering Research Conference 2023*, Cardiff, UK, 2023, pp. 66-69.

doi.org/10.18573/conf1.q

INTRODUCTION

Self-compacting concrete (SCC) is a new type of high-performance concrete, where the concrete has a high flow rate and can spread into place by itself, achieving good consolidation without vibration and minimising segregation and bleeding. The SCC mix is designed to ensure that the mix has both fluidity and resistance to water dilution and segregation [1]. The SCC has excellent deformability and passing ability, as well as high segregation resistance that allows it to be used in heavily reinforced applications and compacted under its own weight. In addition to improving construction productivity and decreasing the total cost of the structure, SCC enhances the work environment, by achieving sustainable characteristics, increasing the practically allowable reinforcement rate, and increasing the construction rate and total quality of the casting structures [2][3]

The fresh properties of self-compacting concrete have been widely researched in the last decades. However, the durability properties of SCC need more investigations. Durable concrete is concrete that has mechanical characteristics, protective properties, and visual appearance which are not adversely influenced by harsh environmental conditions after prolonged exposure [4]the studies that have addressed the use of the recycled aggregate in concrete subjected to freeze-thaw cycles are divergent. Thus, the present work suggests the use of recycled coarse aggregate (RCA). There are many factors that influence the durability of concrete and these factors can lead to concrete structure damage or deterioration including shrinkage, water absorption, and chloride permeability.

According to [5-[6] and [7], there is a direct correlation between autogenous shrinkage and temperature; autogenous shrinkage increases with increased temperature where high temperatures at early ages lead to cement hydration which accelerate and result in a non-uniform distribution of calcium silicate hydrate. This results in increased porosity and a higher risk of shrinkage and cracks formation.

The temperature, microstructure and porosity of concrete are some of the main factors contributing moisture transport in concrete. Concrete may experience a reduction in pH value due to the inevitable ingress of moisture with harmful ions [8]. In addition, the temperature plays a critical role in the rate of moisture transfer in concrete due to the fact that it can alter the pore pressure at a critical level to leading concrete spalling. It is reported in [9]-10] that concrete cured at 50 °C had a greater penetration, higher absorption, and higher moisture diffusivity than concrete cured at 20 °C.

The objective of this study is to investigate the effects of curing under water at different temperatures (i.e., 10 °C, 20 °C, 35 °C and 50 °C) on high strength self-compacting concrete and study its shrinkage potential and water transport properties.

MATERIALS AND METHODS

Materials

Portland cement CEM I 52.5 N was used as binder in accordance with [11]. A superplasticiser of Poly-Aryl-Ether based type [12], with a specific gravity of 1.07 was used. In this study, crushed limestone coarse aggregate with a specific gravity of 2.65 and a maximum size of 10 mm was used. River sand, sieved to a diameter of 2.0 mm and

specific gravity of 2.55 was used as the fine aggregate. The fine aggregate was substituted by a percentage of (30%) limestone dust with a specific gravity of 2.6 and size between 0.125 mm and 2 mm.

Test methods

The fresh properties were investigated according to [11]. Three SCC samples were prepared for each test, the samples were wrapped with plastic sheet and cured in water directly after casting. Cubes with size of mm³ were prepared for the compressive strength test. Prismatic moulds sized (width 280 mm and cross-section 75×75 mm²) were used to measure the shrinkage potential by using a length comparator device, as outline in the methodology BS EN 12390-16:2019 [20]. Measurements of rate of water absorption were conducted according to ASTM C1585[21].

In this investigation the samples were cured at 10 °C, 20 °C, 35 °C and 50 °C. Total of 12 beams were prepared for the shrinkage potential test, 3 beams for each curing temperature, and the samples were cured for 90 days. For the water absorption rate, 24-cylinder samples with 100 mm diameter and 50 mm height were prepared in which 6 samples were used for each curing temperature and the tests were done at 3 days and 90 days. For electrical resistivity test 12 cylinders with 100 mm diameter and 200 mm height were used, and these samples were cured for 90 days.

RESULTS AND DISCUSSIONS

Fresh and hardened properties

Table 1 shows the results of fresh properties test and compressive strength at 28 days. The slump flow, J-ring, and compressive strength tests have been conducted as quality control to ensure this mix achieved the predicted strength.

Slump flow diameter	Slump flow diameter – slump flow in J-ring	Compressive strength at 28 days
670 mm	18 mm	71.2 MPa

Table 1. Fresh and compressive strength results.

Length change

Fig. 1 shows the results of shrinkage potential measurements for all samples cured at different temperatures. All samples showed autogenous shrinkage due to the hydration process in the concrete. The largest shrinkage value at all ages was recorded for the samples cured at 50 °C in which case the shrinkage was measured in the range between -623.1 µm/m to -653 µm/m. The second largest shrinkage value obtained was for the sample that cured at 35 °C for which shrinkage value for all ages was in the range of -250.7 µm/m to -452 µm/m. When the temperature increases the shrinkage increases as noted in [6]. The lowest shrinkage value for all ages was for the sample that cured at 10 °C where the measurement was within the range of (-160.8 µm/m to -291.5 µm/m. Curing the samples at low temperatures led to slowing of hydration reaction in the concrete which reduced the risk of shrinkage [15].

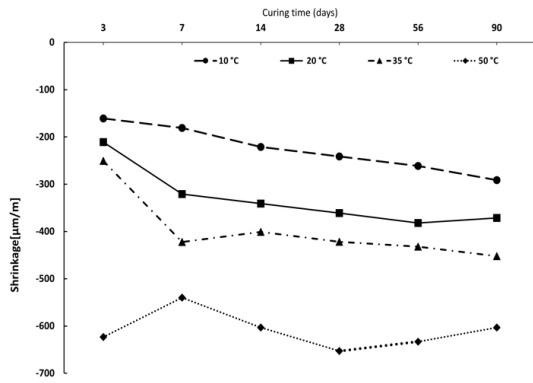


Fig. 1. Result of shrinkage for samples cured at 10°C, 20°C, 35°C and 50°C.

Sorptivity

The calculated sorptivity values for the samples cured at different temperatures are shown in Fig. 2. It can be observed that the sorptivity values after 3 days were within the range of 0.113 to 0.147, while the values after 90 days test were between 0.053 and 0.135. The lowest sorptivity value after 3 days was 0.113 for the curing temperature 50 °C, while after 90 days the highest sorptivity value was recorded for 50 °C with the 19% increase in the rate. This may be attributed to the fact that high curing temperatures accelerate the hydration reaction at the early ages, leading to a denser microstructure and lower absorption properties initially; while, at later ages, the accelerated hydration can result in a more porous microstructure, allowing for higher water absorption and higher sorptivity values [16]. The highest value of sorptivity at 3 days was noted for samples cured at 10 °C, which was 0.147, whereas the lowest value of sorptivity was recorded at 90 days, which was 0.053, where the sorptivity value decreased about 63% from the early age. This may be due to the fact that lower curing temperatures result in slower hydration, leading to less hydration, increased porosity, and higher sorptivity values at early ages. However, over time, continued hydration fills voids, reduces porosity, and creates a denser microstructure, resulting in lower water absorption rates [17].

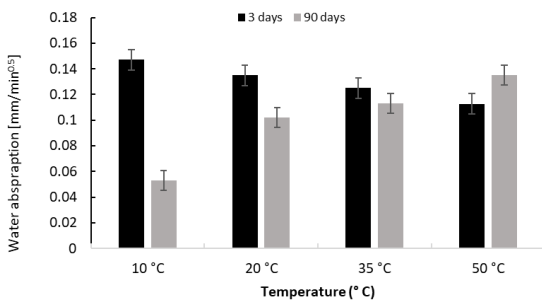


Fig. 2. Result of Sorptivity test for 3 days and 90 days.

Surface Electrical Resistivity

Fig. 3 shows the results of the surface electrical resistivity test. This test is generally performed to determine chloride permeability within the concrete samples. It can be noted from Fig. 3 that the best electrical resistivity after day 1 was for the samples cured at 35 °C and 50 °C (2.3 kΩ.cm), which was approximately 17% higher compared to the samples cured at 20 °C. This is due to the hydration process at an early age which was much faster at higher temperatures and made the hydration products fill the microstructure [18].

Nevertheless, at 90 days, the samples cured at 35 °C and 50 °C exhibited the lowest resistance values of 4.03 kΩ.cm and 3.13 kΩ.cm, respectively. These values were approximately 52.8% and 96.8% lower than the resistance value observed for the samples cured at 20 °C, where the high curing temperature led to change in pore structure, which allowed water and aggressive materials to penetrate the concrete [9]-[19].

At the early age, the samples cured at 10 °C and 20 °C exhibited the lowest electrical resistivity values of 1.33 kΩ.cm and 1.96 kΩ.cm, respectively. However, after 90 days, higher electrical resistivity values of 6.06 kΩ.cm and 6.16 kΩ.cm were observed for the samples cured at 10 °C and 20 °C, respectively. This represents a growth rate of approximately 78% for the 10 °C sample and 68% for the 20 °C sample. At the early age, the hydration reaction proceeds slowly at lower temperatures of 10 °C and 20 °C. As a result, only a limited number of hydration products are formed, leading to increased penetration and higher porosity. However, as the curing period reaches 90 days, the ongoing hydration process results in the filling of more voids and a significant reduction in porosity [18].

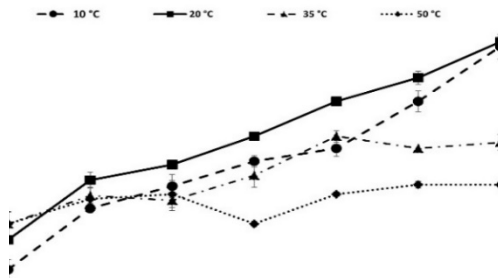


Fig. 3. Result of electrical resistivity.

CONCLUSION

In this study shrinkage, sorptivity and chloride permeability of self-compacting concrete cured at temperatures 10 °C, 20 °C, 35 °C and 50 °C have been evaluated:

Curing at 35 °C and 50 °C temperature led to increase shrinkage values, while, curing at 10 °C temperature resulted in the lowest shrinkage value.

At early age of sorptivity test samples cured at low temperatures revealed the highest sorptivity values. However, at 90 days most of the samples showed lower sorptivity.

Curing at temperatures 10 °C and 20 °C resulted in high electrical resistivity at later ages. However, curing at higher temperatures produced lower electrical resistivity.

REFERENCES

- [1] K.H. Khayat, 'Workability, Testing, and Performance of Self-Consolidating Concrete', *Materials Journal*, vol. 96, no. 3, pp. 346-353, 1999. doi.org/10.14359/632
- [2] W. Zhu and P.J.M. Bartos, 'Permeation properties of self-compacting concrete', *Cem Concr Res*, vol. 33, no. 6, pp. 921-926, Jun. 2003. doi.org/10.1016/S0008-8846(02)01090-6
- [3] M. Okamura and H. Ouchi, 'Self Compacting Concrete - research paper', *Journal of Advanced Concrete Technology*, vol. 1, no. 1. pp. 5-15, 2003. doi.org/10.3151/jact.1.5
- [4] N. S. Amorim Júnior, G.A.O. Silva, and D.V. Ribeiro, 'Effects of the incorporation of recycled aggregate in the durability of the concrete submitted to freeze-thaw cycles', *Constr Build Mater*, vol. 161, pp. 723-730, Feb. 2018. doi.org/10.1016/j.conbuildmat.2017.12.076
- [5] Z. Zhang, Q. Wang, and H. Chen, 'Properties of high-volume limestone powder concrete under standard curing and steam-curing conditions', *Powder Technol*, vol. 301, pp. 16-25, 2016. doi.org/10.1016/j.powtec.2016.05.054
- [6] [6] A. Loukili, D. Chopin, A. Khelidj, and J. Y. Le Touzo, 'New approach to determine autogenous shrinkage of mortar at an early age considering temperature history', *Cem Concr Res*, vol. 30, no. 6, pp. 915-922, 2000. doi.org/10.1016/S0008-8846(00)00241-6
- [7] N. Lahmar *et al.*, 'Experimental and finite element analysis of shrinkage of concrete made with recycled coarse aggregates subjected to thermal loading', *Constr Build Mater*, vol. 247, p. 118564, 2020. doi.org/10.1016/j.conbuildmat.2020.118564
- [8] K. Wang, J. Guo, X. Liu, L. Yang, and P. Zhang, 'Effect of dry-wet ratio on pore-structure characteristics of fly ash concrete under sulfate attack', *Mater Struct Constr*, vol. 54, no. 3, pp. 1-13, 2021. doi.org/10.1617/s11527-021-01700-2
- [9] V.K.R. Kodur and L. Phan, 'Critical factors governing the fire performance of high strength concrete systems', *Fire Saf J*, vol. 42, no. 6-7, pp. 482-488, 2007. doi.org/10.1016/j.firesaf.2006.10.006
- [10] F. de J. Cano Barrita, T.W. Bremner, and B.J. Balcom, 'Effects of curing temperature on moisture distribution, drying and water absorption in self-compacting concrete', *Magr Concr Res*, vol. 55, no. 6, pp. 517-524, 2003. doi.org/10.1680/macr.2003.55.6.517
- [11] EFNARC, 'Specification and Guidelines for Self-Compacting Concrete,' *Rep. from EFNARC*, vol. 44, no. February, p. 32, 2002, [Online]. Available: <http://scholar.google.com/scholar?hl=en&btnG=Search&q=intitle:Specification+and+Guidelines+for+Self-Compacting+Concrete#0>
- [12] F.O.F. Application, 'MasterGlenium ACE 474 MasterGlenium ACE 474,' no. 3, pp. 2-5, 2016.
- [13] A. El Mir and S.G. Nehme, 'Utilization of industrial waste perlite powder in self-compacting concrete', *J Clean Prod*, vol. 156, pp. 507-517, Jul. 2017. doi.org/10.1016/j.jclepro.2017.04.103
- [14] C09 Committee, 'Standard Test Method for Measurement of Rate of Absorption of Water by Hydraulic-Cement Concretes', ASTM C1585-5, vol. 41, no. 147, pp. 1-6, 2018. doi.org/10.1520/C1585-13
- [15] Z. Liu, W. Jiao, A. Sha, J. Gao, Z. Han, and W. Xu, 'Portland Cement Hydration Behavior at Low Temperatures: Views from Calculation and Experimental Study', *Adv Mater Sci Eng*, vol. 2017, 2017. doi.org/10.1155/2017/3927106
- [16] Q. Wang, M. Shi, and D. Wang, 'Influence of elevated curing temperature on the properties of cement paste and concrete at the same hydration degree', *J Wuhan Univ Technol Mater Sci Ed*, vol. 32, no. 6, pp. 1344-1351, 2017. doi.org/10.1007/s11595-017-1751-2
- [17] D. J. Naus and H. L. Graves, 'A review of the effects of elevated temperature on concrete materials and structures', *Int Conf Nucl Eng Proceedings, ICONE*, vol. 2006, no. 1886, 2006. doi.org/10.1115/ICONE14-89631.
- [18] E. Gallucci, X. Zhang, and K. L. Scrivener, 'Effect of temperature on the microstructure of calcium silicate hydrate (C-S-H)', *Cem Concr Res*, vol. 53, pp. 185-195, 2013. doi.org/10.1016/j.cemconres.2013.06.008
- [19] K. O. Kjellsen, R. J. Detwiler, and O. E. Gjrv, 'Pore structure of plain cement pastes hydrated at different temperatures', *Cem Concr Res*, vol. 20, no. 6, pp. 927-933, 1990. doi.org/10.1016/0008-8846(90)90055-3

Little J

*Cardiff University
School of Engineering*

Pan S

*Cardiff University
School of Engineering*

Follett E

*Liverpool University
School of Engineering*

CIVIL INFRASTRUCTURE

Determining Surface Velocity Coefficients in Headwater Streams for Natural Flood Management

With concerns about climate change, nature-based solutions for flood risk management have been increasing in popularity across Europe, and targeting headwater streams can be an effective approach by increasing forest floodplains through inundation of surrounding areas. However, accurately measuring stream discharge remains a challenge. One promising method is to measure the surface velocity and apply a surface velocity coefficient. This study investigates the determination of surface velocity coefficient in headwater streams using the float and current meter methods. The relationship between surface velocity coefficient and relative submergence (ratio of water depth to roughness height) is analysed. The results support prior modelling results that the surface velocity coefficient decreases with relative submergence and extend the range of prior work for very small relative submergence, using experimental and field observations. The surface velocity coefficient was observed to decrease from 0.85 to 0.53 as relative submergence decreased from 270000 in a smooth glass laboratory channel to 0.093 in a field setting. Field discharge measurements upstream of a channel-spanning engineered logjam were used to show used to predict local inundation and the uncertainty is reported.

Keywords:
Natural flood management, hydrometrics, surface velocity coefficient, relative submergence, engineered log jam.

Corresponding author:
LittleJA1@cardiff.ac.uk



J. Little, S. Pan, and E. Follett, 'Determining Surface Velocity Coefficients in Headwater Streams for Natural Flood Management', *Cardiff University School of Engineering Research Conference 2023*, Cardiff, UK, 2023, pp. 70-73.

doi.org/10.18573/conf1.r

INTRODUCTION

Nature based solutions to flood risk management have been gaining significant traction across Europe over the last decade and a half with the Flood and Water Management ACT (2010) including a recommendation to better “work with natural processes” [1] due to concerns relating to the impacts of climate change [2].

Targeting headwater streams (which are often found in mountainous, forested regions), can result in increased forest floodplains by forcing inundation in areas surrounding these streams [3]. This approach holds significant promise for the deployment of Engineered Log Jams (ELJs) as a solution to reduce adverse catchment flooding [3], [4].

Characterising the physical properties of small water bodies, specifically headwater streams, is necessary for the design and assessment of natural flood management projects and of significant broader interest as headwater streams represent 73.4% of the UK river network [5].

A key metric is stream discharge. Calculating discharge of small streams remains an open issue due to the prevalence of shallow flows, variable bed roughness, and remote site location that complicates implementation of traditional measurement methods [6]–[8].

The most popular method of measuring discharge is the velocity-area method [6]–[11], specifically the midsection method [7] in which discharge is calculated by measuring the spatial average velocity (U) and cross-sectional area (A) of a section within a uniform stretch, and then summing the product of the two values together as follows:

$$Q = \sum_{i=1}^n A_i U_i = \sum_{i=1}^n q_i \quad (1)$$

Existing methods for measuring spatial average velocity include current meters, Acoustic Doppler Velocimetry, dilution gauging, remote sensing and surface Particle Image Velocimetry (PIV). Due to the shallow and remote nature of headwater streams, many of these methods are impractical [6]. One relatively simple method for obtaining spatial average velocity in headwater streams is by measuring surface velocity and applying a Surface Velocity Coefficient (λ) [7]. Surface velocity can be measured using the float method. Ideally, an object that lies below the surface (such as an orange) is preferred as it has a similar specific gravity to water and thus is resistant to air disturbances [8].

Previous studies have indicated that λ is highly variable and dependent on the conditions of the specific location being measured such as aspect ratio, depth, relative submergence, local vegetation, and Reynolds number [9]. Prior literature has suggested λ ranges from as low as 0.552 [10] in wide shallow streams to 0.85 in smooth uniform prismatic channels.

This study presents new measurements of surface velocity coefficients found in a headwater stream used for a natural flood management project at Nant Drysiog, Wales, UK (as shown in Fig. 1) and explores the range of variation of λ with relative submergence through lab measurements and comparison to prior results. Study results will inform use of the float method in headwater streams typical of natural flood management projects, filling a research gap for channels that are wide (aspect ratio > 5) but shallow (relative submergence close to or of the order of flow depth).



Fig. 1. Example of channel-spanning ELJ in a headwater stream (Nant Drysiog, Wales, UK, 16th February 2022).

In this study, the float method and current meter method were used to determine surface velocity and spatial average velocity (U) respectively across a range of aspect ratios, stream velocities, and relative submergences. The float method was chosen to measure surface velocity as it required no heavy or expensive equipment making it ideal for headwater streams which are typically situated in remote locations or as part of monitoring programmes led by volunteer groups.

Lab experiments were conducted to validate the methods with a built-in flow meter in a smooth rectangular channel. The float method was repeated multiple times with the aim of identifying the number of repeats necessary to reduce uncertainty of the method in laboratory and field conditions. The standard deviation was computed for all measurements. The discharge was then computed and subsequently used to calculate a dimensionless metric representing jam physical structure (C_A) to predict local inundation during high flow conditions and characterise structural change over time.

METHODS

Laboratory experiments were conducted in a smooth glass, 1.7m long, 1.2m wide, and 1m deep bi-directional recirculating tilting flume at the Hydraulics Lab at the Cardiff University School of Engineering. The current meter (OTT MF PRO) [12] midsection method and float method were used to measure spatial average velocity and surface velocity respectively [12]. The current meter was attached to a wading rod and was validated using a Controlotron 1020 Clamp-On Transit-Time Flow meter. Its software was used to calculate partial discharge in each section from the spatial average velocity and the area of the section, thus giving the total discharge. Since the flume is a smooth rectangular channel, current meter measurements were taken every 0.05m laterally across the cross section ($b = 1.20m$) resulting in 24 stations in total. A series of time averaged measurements were taken along each vertical from the bed to the surface at 0.2h intervals using a wading rod. Data was collected for ten seconds at 50Hz and then time averaged via the current meter software.

In field observations, an orange was predominantly used for the float method. However, during low flow conditions (such as 8 July 2022), a stick was used instead due the orange diameter exceeding the depth of flow. As the site at Nant

Dyrsiog is well-protected by forest cover it is assumed that there is little wind as no surface ripples were observed [13] and therefore it is assumed that use of a stick did not bias the measurement.

Relative Submergence (RS) was determined using the following relationship [14]:

$$RS = \frac{h}{k_s'} \quad (2)$$

where h is the depth of flow at the point of measurement and k_s' is the equivalent Nikuradse sand grain roughness height as: $k_s' = 6.8D_{50}$. D_{50} is the median sediment size. This was measured downstream of the ELJ by taking 1m x 1m samples and calculating the average diameter in three dimensions. The upstream was measured by taking a sample roughly 60mm deep and performing a sieve analysis.

RESULTS

Float method measurements were conducted to measure surface velocity and compute the surface velocity coefficient. The number of float method repeats required to obtain a value within $\pm 2.5\%$ of the moving average was explored in a field setting. To reduce error and obtain a more accurate mean float velocity, multiple repetitions of the measurement were conducted. On average, it took between 10 and 20 repeats for the cumulative average to drop within of the set average. Fig. 2 demonstrates the number of repeats it took to achieve this average velocity, where a total of 36, 30, 30, and 30 measurements were recorded at field visits (Nant Drysiog, Wales, UK) on 8 July 22, 16 February 23, 23 February 23, and 7 March 23 respectively. Dashed lines indicate $\pm 2.5\%$ of the set average.

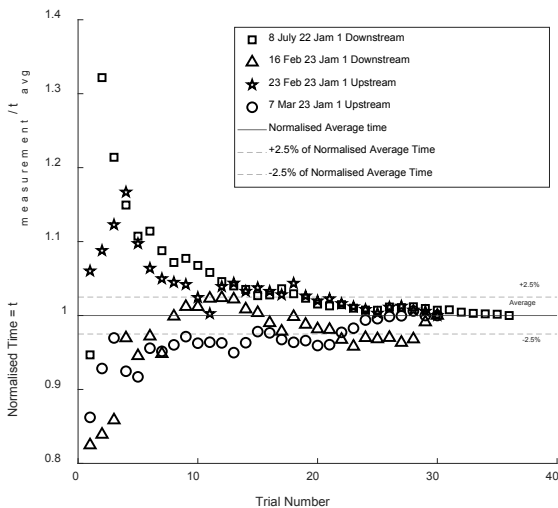


Fig. 2. Normalised time for float to cross measurement section relative to trial average.

To provide surface velocity coefficients for headwater streams in order to support use of surface velocity measurements for discharge calculation at natural flood management sites, the following relationship is defined to relate spatial average velocity (U) over the channel cross-section to surface velocity (u_{Surf}):

$$\lambda = U / u_{Surf} \quad (3)$$

where λ is the surface velocity coefficient.

The lateral average flow depth ranged from 0.2m to 0.4m for lab observations and 0.041m to 0.365m for field observations. The shallowest flow depths approached the range of operability of the OTT MFPro current meter (0.04 m, [12]). In the lab the standard deviation of λ ranged from 0.05 to 0.13; and in the field it ranged from 0.10 to 0.24 upstream of the ELJ and from 0.05 to 0.19 downstream of the ELJ.

Figure 3 below shows the values of λ for a range of relative submergences. λ was observed to remain relatively constant $\lambda_{lab} = 0.84$ with relative submergence in flume experiments whilst decreasing with relative submergence for field conditions; with λ decreasing from 0.70 to 0.53 over relative submergence 26.8 to 0.093.

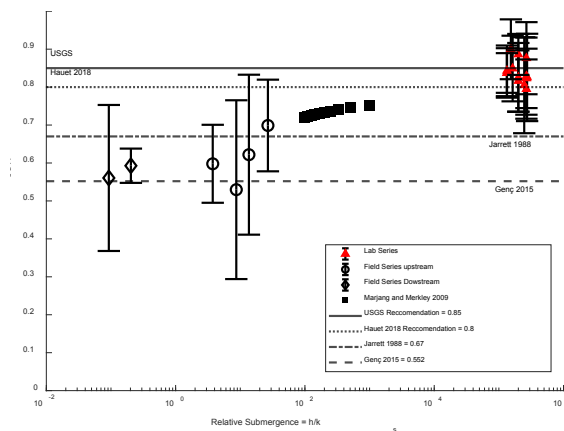


Fig. 3. Comparison of surface velocity coefficient against relative submergence observed in lab and field settings.

DISCUSSION

Field observations extend numerical modelling results from [15] (black squares Fig. 3), demonstrating a decrease in λ as Relative Submergence (RS) decreases. In their study, it was observed that changes in surface roughness height have no significant effect on the surface velocity but do slow the flow near the boundary, thereby reducing spatial average velocity.

The observed range of λ in this study supports this hypothesis and is in agreement with prior literature, with values spanning from 0.552 in shallow but wide streams [10] to 0.85 in smooth uniform prismatic channels [7], [8]. Although a direct relationship between λ and RS isn't explicitly documented in previous literature, the present results were connected to prior work by examining experimental conditions under which the studies were conducted.

Measurements from [10] (dashed line Fig. 3) show consistency with our findings that shallow and wide streams result in a reduced λ . Further support comes from the study by [11] (dotted line Fig. 3), which recommends using $\lambda = 0.8$ for water depths less than 2 meters and observes a decrease in λ with hydraulic radius. This is consistent with the hypothesis that λ reduces with RS, however, it is insufficient to describe the effects of very low RS as the study was conducted in relatively larger streams.

Lastly, [16]'s (dash-dotted line Fig. 3) estimation of $\lambda = 0.67$ in mountainous streams also concurs with our hypothesis. This estimation stems from the observation of S-shaped and nonlogarithmic flow profiles in such streams. This lowers

the measurable depth of U from 0.6d to 0.5d and is due to the high velocity flow and exceptional drag from the cobble and boulder bed material impacting the flow surface.

In addition to examination of λ , field observations were used to record the logjam structural metric linking discharge to jam-generated backwater rise, C_A [17]:

$$H_2 = \sqrt{3} * \sqrt[3]{\frac{C_A q^2}{2g}} \quad (4)$$

Where H_2 is the backwater rise and $q = Q/B$ the discharge per unit channel width.

Discharge readings obtained in July 2022 using the float method and λ were used to calculate C_A as 15.8 ± 4.5 , which was then used to predict the extent of backwater rise in February 2022 based on the discharge readings for that month, predicting $= 0.393\text{m} \pm 0.03\text{m}$ compared to the measured $= 0.365\text{m} \pm 0.0005\text{m}$ giving an absolute percentage error of only 7.56%. The cubic and square terms in (4) mean that whilst the error for C_A seems large, when used to predict, the measurement is fairly accurate.

The resulting values indicated that the ELJ site would experience localized flooding, which was observed during that visit and recorded in photographs.

Bedforms were not observed in the field and thus the effect of bedforms such as ripples and dunes due to the presence of a moveable boundary is to be further explored.

CONCLUSIONS

Surface velocity measurements present a method for determining discharge in headwater streams for effective implementation of natural flood management techniques. To use surface velocity, an accurate relationship to U must be made using an appropriate surface velocity coefficient.

In field and laboratory experiments, between 10 and 20 repetitions of the float method were necessary to reduce uncertainty caused by human error and flow profile variations. The results of field observations suggest that for small streams with water depths less than 0.365m, the surface velocity coefficient decreases with relative submergence, ranging from 0.72 to 0.53 for to 0.093. For a smooth rectangular laboratory channel, $\lambda = 0.84 \pm 0.084$ (σ). No trend was observed with varying relative submergence in the laboratory tests.

Further analysis into the relationship between relative submergence and λ will be conducted, in addition to investigation of alternative methods to compute discharge including rhodamine dye dilution gauging and a forced weir constriction method to improve accuracy of results.

Acknowledgments

We would like to express our gratitude to Cardiff University School of Engineering Hydro-environmental Research Centre. We would also like to thank the members of our research team for their contributions and efforts, and to Natural Resources Wales for giving access to the site at Nant Drysiog. The third author has received funding from the Royal Academy of Engineering's Research Fellowships programme. The first author has received funding from Cardiff University.

Conflicts of interest

The authors declare no conflict of interest.

REFERENCES

- [1] P. Metcalfe *et al.*, K. Beven, B. Hankin, and R. Lamb, 'A modelling framework for evaluation of the hydrological impacts of nature-based approaches to flood risk management, with application to in-channel interventions across a 29-km² scale catchment in the United Kingdom', *Hydrol Process*, vol. 31, no. 9, pp. 1734–1748, 2017. doi.org/10.1002/hyp.11140
- [2] A. Black *et al.*, 'Natural flood management, lag time and catchment scale: Results from an empirical nested catchment study', *J Flood Risk Manag*, vol. 14, no. 3, p. e12717, 2021. doi.org/10.1111/jfr3.12717
- [3] S.J. Dixon, D.A. Sear, N.A. Odoni, T. Sykes, and S.N. Lane, 'The effects of river restoration on catchment scale flood risk and flood hydrology', *Earth Surf Process Landf*, vol. 41, no. 7, pp. 997–1008, Jun. 2016. doi.org/10.1002/esp.3919
- [4] C. Linstead and A.M. Gurnell, *Large Woody Debris in British Headwater Rivers - Physical Habitat Role and Management Guidelines*, Research and Development Technical Report W185, Environment Agency, 1999.
- [5] W.D. Riley *et al.*, 'Small Water Bodies in Great Britain and Ireland: Ecosystem function, human-generated degradation, and options for restorative action', *Science of the Total Environment*, vol. 645. Elsevier B.V., pp. 1598–1616, Dec. 15, 2018. doi.org/10.1016/j.scitotenv.2018.07.243
- [6] D.W. Clow and A.C. Fleming, 'Tracer gauge: An automated dye dilution gauging system for ice-affected streams', *Water Resource Res*, vol. 44, no. 12, 2008. doi.org/10.1029/2008WR007090
- [7] D.P. Turnipseed, V.B. Sauer, and USGS, *Discharge measurements at gaging stations*, Reston, VA, 2010. doi.org/10.3133/tm3A8
- [8] N.D. Gordon, T.A. McMahon, B.L. Finlayson, C.J. Gippel, and R.J. Nathan, *Stream hydrology: an introduction for ecologists*. John Wiley and Sons, 2004.

- [9] F. Bandini *et al.*, 'A drone-borne method to jointly estimate discharge and Manning's roughness of natural streams', *Water Resource Res.*, vol. 57, no. 2, p. e2020WR028266, 2021.
doi.org/10.1029/2020WR028266
- [10] O. Genç, M. Ardiçlioğlu, and N. Ağırlioğlu, 'Calculation of mean velocity and discharge using water surface velocity in small streams', *Flow Measurement and Instrumentation*, vol. 41, pp. 115–120, 2015.
doi.org/10.1016/j.flowmeasinst.2014.10.013
- [11] A. Hauet, T. Morlot, and L. Daubagnan, 'Velocity profile and depth-averaged to surface velocity in natural streams: A review over a large sample of rivers', in *E3s web of conferences*, 2018, vol. 40, p. 06015.
doi.org/10.1051/e3sconf/20184006015
- [12] OTT Hydromet, *Flow and Discharge Measurement with the OTT MF pro*, 2015. Accessed: Mar. 03, 2022. [Online]. Available: <https://www.ott.com/download/ott-mf-pro-white-paper/>
- [13] G. Dolcetti, B. Hortobágyi, M. Perks, S. J. Tait, and N. Dervilis, 'Using noncontact measurement of water surface dynamics to estimate river discharge', *Water Resour. Res.*, vol. 58, no. 9, p. e2022WR032829, 2022.
doi.org/10.1029/2022WR032829
- [14] P.Y. Julien, *Erosion and Sedimentation*, 2nd ed. Cambridge University Press, 2010.
doi.org/10.1017/CBO9780511806049
- [15] N. Marjang and G.P. Merkley, 'Surface velocity coefficients for application of the float method in rectangular and compound open channels', *Irrig. Sci.*, vol. 27, no. 6, pp. 457–470, 2009.
doi.org/10.1007/s00271-009-0162-3
- [16] R.D. Jarrett, 'Hydrologic and hydraulic research in mountain rivers', *IAHS-AISH publication*, vol. 190, pp. 107–117, 1989.
- [17] E. Follett, I. Schalko, and H. Nepf, 'Momentum and Energy Predict the Backwater Rise Generated by a Large Wood Jam', *Geophys. Res. Lett.*, vol. 47, no. 17, Sep. 2020.
doi.org/10.1029/2020GL089346

Andrews E

*Cardiff University
School of Engineering*

Pan S

*Cardiff University
School of Engineering*

CIVIL INFRASTRUCTURE

Simulating Flood Hazard in Wye Valley during Storm Dennis using Hec-Ras

A 2D Hec-Ras flood model is established at the middle reach of the River Wye, from Ross-on-Wye to Monmouth, along the English-Wales border. The flow conditions during Storm Dennis, which occurred on 15-16 Feb 2020 are used to simulate the flood extents in the study area. The flood hazard rate, suggested by EA, is analysed to assess the risk level of flooding in the area. The results show the extensive flood extents at the study site. The flood hazard rate map shows that large part of Wye Valley is at high risk of flooding.

Keywords:
*River Wye, flooding dynamics,
hazard rate, Hec-Ras, Wye Valley,
Ross-on-Wye.*

Corresponding author:
PanS2@cardiff.ac.uk



E. Andrews and S. Pan, 'Simulating Flood Hazard in Wye Valley during Storm Dennis using Hec-Ras' *Cardiff University School of Engineering Research Conference 2023*, Cardiff, UK, 2023, pp. 75-79.

doi.org/10.18573/conf1.s

INTRODUCTION

In recent years, the UK has been met with some of the most severe flooding since records began. For example, February 2020 was recorded as the highest peak flow[1], exceeding the previous record by a significant margin, with 3.5-4 times the average long-term flow. The recent records in 2021 and 2022 also suggested that the events previously considered as extreme, are now the new normal. Over the past decades, the River Wye catchment, particularly in the middle reach (from Hereford to Monmouth), has been subjected to frequent and severe flooding. The flood extents in Ross-on-Wye during Storm Dennis in Feb 2020 were devastating to the local community. This study is to use an advanced 2D flood model – Hec-Ras to simulate that flood event in the area between Ross-on-Wye and Monmouth, as shown in Fig. 1 under the storm conditions.

MATERIALS AND METHODS

The River Wye (Welsh: Afon Gwy) is one of Britain's most scenic and un-spoilt rivers, flowing 157 miles (251 km) through Hay-on-Wye, Hereford and Ross-on-Wye and continues on through Symonds Yat, Monmouth and Tintern, and reaches Chepstow where it joins the Severn Estuary. It is the fifth longest river in the UK. The river changes from a spring at its source on Mount Plynlimon to a fast flowing upland stream to a wide meandering river towards the mouth of the river at Beachley, on the edge of the Forest of Dean.

In this study, the middle reach of the River Wye between Ross-on-Wye and Monmouth as shown in Fig.1 is selected as the study site.

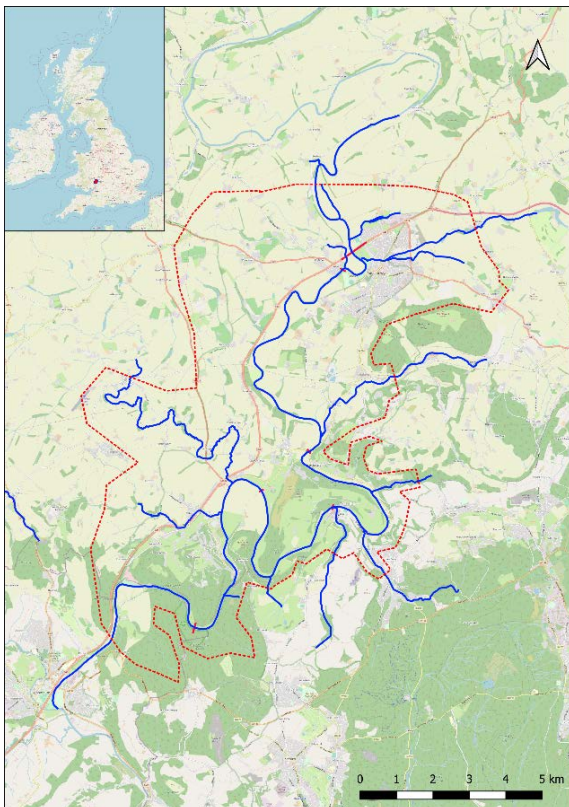


Fig. 1. Study site: Middle reach of River Wye (blue lines, including connecting waterways) and the 2D computational domain (dotted line).

To simulate the flood events, a 2D model based on the Hec-Ras software is created in the study area.

Hec-Ras is an open source software, primarily designed to aid channel flow analysis with an emphasis on floodplain determination, initially developed by the United States Army Corps of Engineers for use within the public sector, following its release to the public in 1995. It has the capability of modelling both one- and two-dimensional unsteady open channel flows, containing many continents particularly to understand and alleviate flooding[2]. It has been continually developed and updated, to include features such as dam break analysis[3] and flood analysis[4], and widely used in industry and for research. In this study, the version (6.3.1) of the software released in 2022, is used.

To set up the computer model for the study site, lidar data with resolution of 2 m by 2 m, obtained from EA, are used as the bathymetry, as shown in Fig. 2.

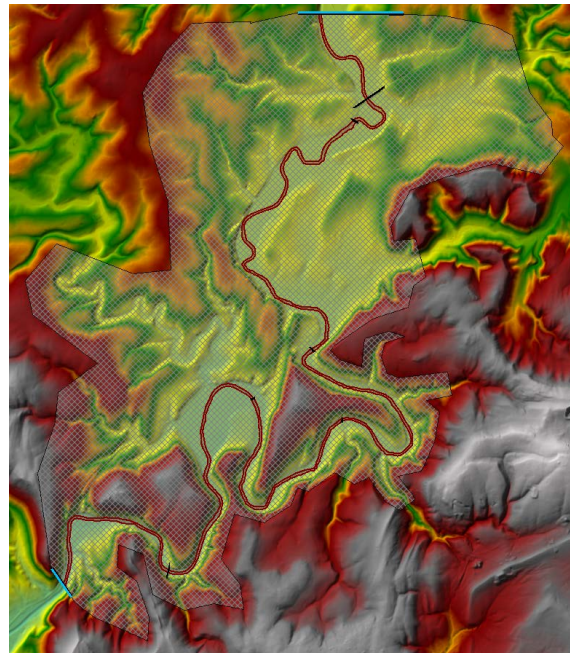


Fig. 2. Terrain of the study site derived from 2m Lidar data (EA) with computational mesh, bridges and upstream and downstream boundaries.

Within the study site, there are 6 bridges across the River Wye, including 2 foot bridges (Fig. 2), which are fully implemented in the model. Fig. 3 shows the implementation of the longest, Bristow Bridge, along the A40 and Huntsham Bridge off B4229 in the model. A number of break lines are defined in the domain, such as that for A40, to achieve a better quality of the computational mesh. The mesh contains in total 35,193 cells, with the largest cell being 5,560 m² and smallest cell being 306 m².

The flow boundary condition is set at the upstream boundary, using the daily measurements from the National River Flow Archive (nrfa.ceh.ac.uk). Since there is no measuring station at the upstream boundary (near Bristow Bridge), a combination of the daily flows at Belmont (NRFA Station ID: 55002), Lugwardine (55003), Yarkhill (55018) and Three-Elms (55032) is assumed to contribute to the total flow discharge in River Wye into the study site. Fig. 4 shows the hydrograph used at the upstream boundary

for the period of Storm Dennis (20220212 00:00 UTC-20220220 00:00UTC). Normal water depth is adopted for the downstream boundary.

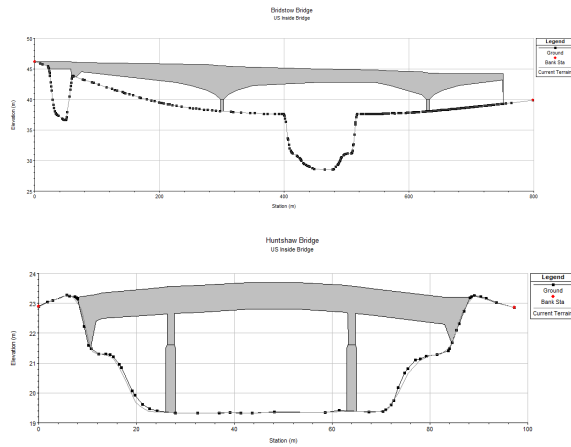


Fig. 3. 2D and Storage Area (SA) connections for bridges: (a) Bristow Bridge (top) and (b) Huntsham Bridge (bottom).

Uniform Manning’s coefficient (n) of 0.035 is used in the model simulations. The time step is set to 5 mins and output interval is set 15 mins.

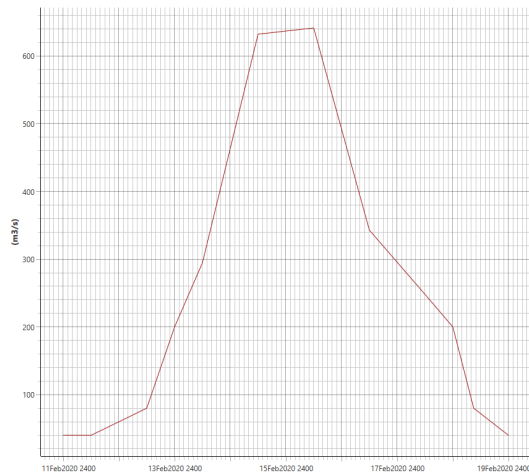


Fig. 4. Hydrograph for the upstream boundary for Storm Dennis (8 days from 20220212 00:00UTC).

RESULTS

The duration of the computation is set to 192 hrs (8 days), with a leading period of 36 hrs at the averaged discharge to establish initial flow conditions in the domain. Fig. 5(a) shows the maximum water depth at the study site. During Storm Dennis, the water depth in the upstream section (near Ross-on-Wye) is found to be around 5 m in the river, and 3 m in the flood plain. Almost all flood plain is flooded during the storm. In the downstream end of the domain, the water depth is found to be deeper, in a range of 8-10 m. The areas around Huntsham Farm and Saint Dubricius Church are severely flooded. The highest water level at Huntsham Bridge from the model is 23.09 mAOD, which exceeds the low dock level and overtops part of the bridge, as shown in Fig. 6.

The maximum flow velocity, as shown in Fig 5(b), is generally lower than 1 m/s, due to the river overflowing. However, the velocity in the downstream channel can exceed 3.0 m/s.

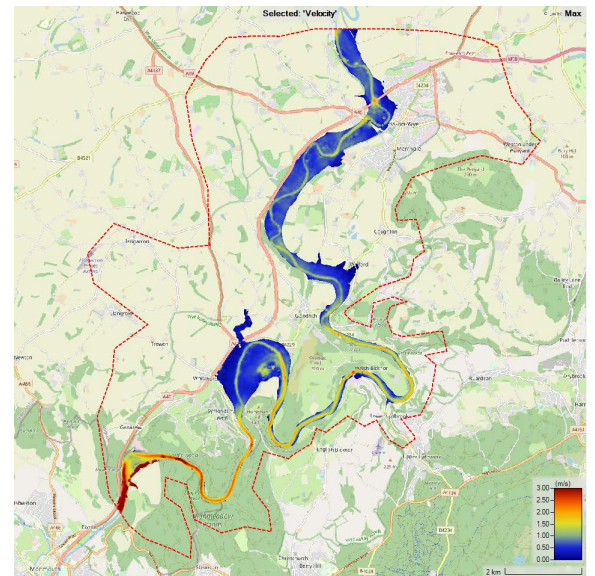
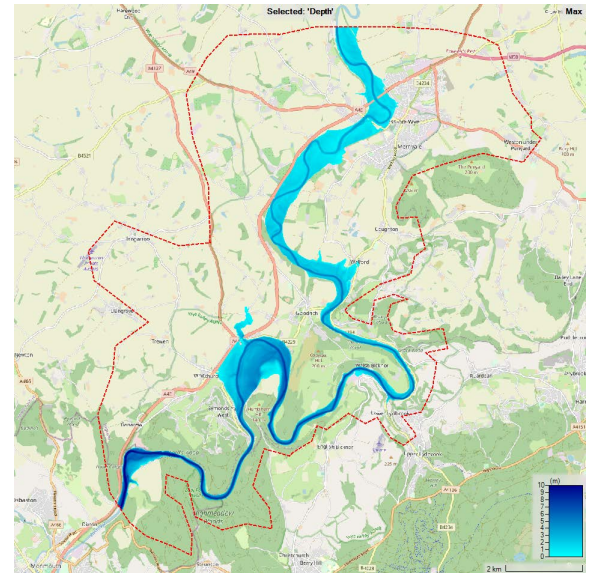


Fig. 5. (Top) max water depth (m) and (bottom) max velocity (m/s) during Storm Dennis

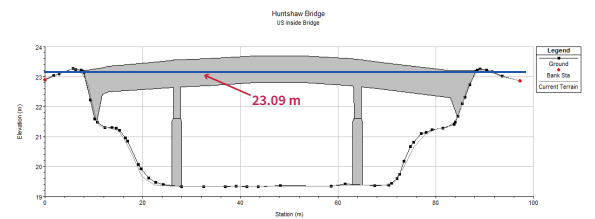


Fig. 6. The highest water level at Huntsham Bridge from the model (23.09 mAOD).

In order to study the flood dynamics[5], the Flood Hazard Rate (FHR) suggested by the EA is used in this study as:

$$FHR = d(v + 0.5) + F_{Deb} \tag{1}$$

where, d is water depth (m); v is velocity (m/s); and F_{Deb} is a debris coefficient varying from 0~1 depending on local conditions. The flood hazard can be generally categorised into 4 groups, based on the FHR values as listed in Table 1.

FHR	Level	Description
<0.75	L	Flood zone with shallow flowing water or deep standing water
0.75 – 1.25	M	Moderate Danger for some (i.e. children). <i>Danger: Flood zone with deep or fast flowing water.</i>
1.25 - 2.50	H	Significant Danger for most people. <i>Danger: flood zone with deep fast flowing water.</i>
>2.50	E	Extreme Danger for everyone. <i>Extreme danger: flood zone with deep fast flowing water.</i>

Table 1. Classifications of Flood Hazard Risk

A FHR layer is created within HEC-RAS taking the time series of water depth and velocity from the model with a user script based on Eq. 1 during the event. The effect of the debris coefficient has been discounted i.e. $F_{deb} = 0.0$ across the area as the required details, (e.g. soil structure, flora density and presence of paving/ subsurface drainage) are unknown. As a result of this, the inclusion of an F_{deb} coefficient would likely be fictitious thereby reduce the accuracy of results.

DISCUSSION

Fig. 7(a) shows the FHR before the peak river discharge (20200215 00:00) and Fig. 7(b) shows the FHR at the maximum river discharge (20200216 00:00). The results indicate that before the peak flow discharge, where the inflow is at ~500 m³/s, representing a typical flood event, the FHR ranges predominately from low to moderate, with a small area being high as shown in Fig. 7(a). However, as shown Fig. 7(b), it is clear that the FHR increases considerably at the peak river discharge (~640 m³/s), which represents a severe flood event in the area. The FHR in the majority of the study site is at high risk level, whilst the area of moderate risk is noticeably reduced.

To further examine the details of the flood risk level locally, two areas, as indicated in Fig. 7(b) as “A” and “B”, are selected. Area A is centred in the surrounding area of Ross-on-Wye, a historically flood prone area, while Area B is centred in Wye valley.

For Area A, as shown in Fig. 8(a), it is clear that most of the area is at high risk of flooding, but most residential areas are at low risk or safe due to the relative high ground, but access to these areas is restricted, as Wilton Bridge is likely to be flooded. In Area B, Fig. 8(b) shows a high risk level of flooding in most of the area. The Huntsham farm land near St Dubricius Church is inundated, but the residential area along the west bank near the church is at low risk.

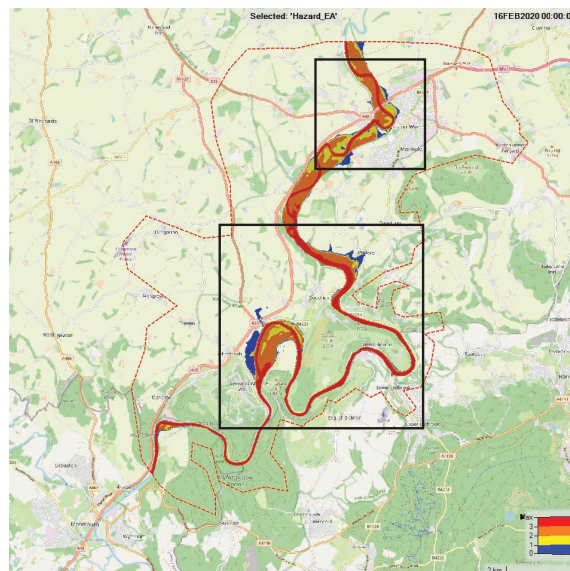
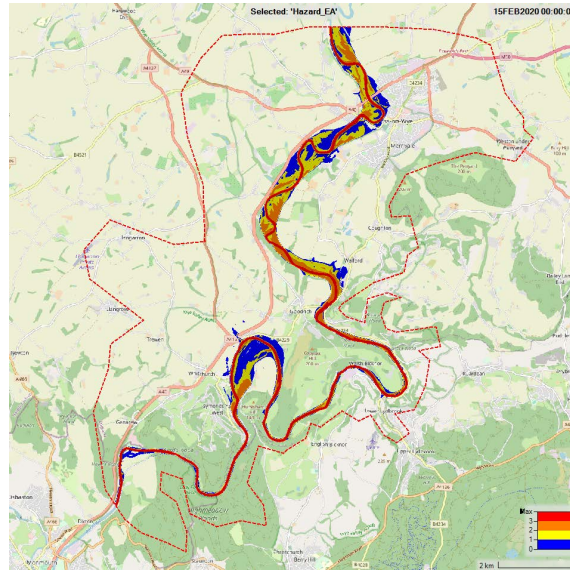


Fig. 7. FHR during Storm Dennis: (a) before peak discharge (top); (b) at the peak discharge (bottom).

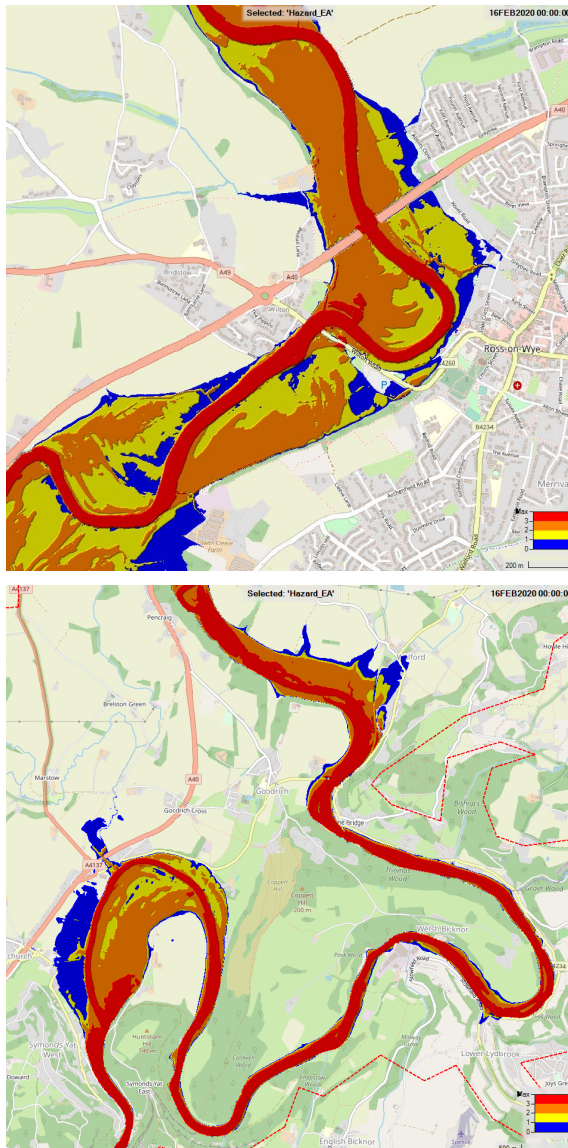


Fig. 8. FHR during Storm Dennis at the peak discharge in: (a) Area A; (b) Area B (see Fig. 7(b)).

CONCLUSIONS

A 2D Hec-Ras flood model is established at the middle reach of River Wye from Ross-on-Wye to Monmouth along the English-Wales border. The flow conditions during Storm Dennis occurred on 15-16 Feb 2020 are used to simulate the flood extents at the study site. The FHR as suggested by EA is analysed to assess the risk level of flooding in the study site.

The results indicate that under the severe flow conditions such as those during Storm Dennis, a large area close to the river course and flood plain at the river study site is inundated. Bridges and highways are likely to be flooded. The FHR which combines the water depth and flow velocity indicates that the most area at the study site is at high risk from flooding. This is particularly severe in the Wye Valley, where the vast agricultural lands could be affected.

Conflicts of interest

The authors declare no conflict of interest.

REFERENCES

- [1] M.G. Parry *et al.*, 'Risk stratification for prostate cancer management: value of the Cambridge Prognostic Group classification for assessing treatment allocation', *BMC Medicine*, vol.18, no. 1, p. 114, May 2020. doi.org/10.1186/s12916-020-01588-9
- [2] D. J. Mehta, S. Eslamian, and K. Prajapati, 'Flood modelling for a data-scare semi-arid region using 1-D hydrodynamic model: a case study of Navsari Region', *Model Earth Syst Environ*, vol. 8, no. 2, pp. 2675–2685, Jun. 2022 doi.org/10.1007/s40808-021-01259-5
- [3] Y. Xiong, 'A Dam Break Analysis Using HEC-RAS', *Journal of Water Resource and Protection*, vol. 3, no. 6, pp. 370–379, Jun. 2011. doi.org/10.4236/jwarp.2011.36047
- [4] V. M. Quiroga, S. Kurea, K. Udoa, and A. Manoa, 'Application of 2D numerical simulation for the analysis of the February 2014 Bolivian Amazonia flood: Application of the new HEC-RAS version 5', *Ribagua*, vol. 3, no. 1, pp. 25–33, Jan. 2016. doi.org/10.1016/j.riba.2015.12.001
- [5] A. Khatrush and S. Pan, 'Mapping of Flood Dynamics due to Sea Level Rise in Dyfi Estuary', in *24th Telemac-Mascaret User Conference*, Graz, Austria, 2017.

Cazzador G

*Università Ca' Foscari Venezia
Dept. Molecular Science and Nanosystem*

Ronchin L

*Università Ca' Foscari Venezia
Dept. Molecular Science and Nanosystem*

De Nardi C

*Cardiff University
School of Engineering*

Vavasori A

*Università Ca' Foscari Venezia
Dept. Molecular Science and Nanosystem*

CIVIL INFRASTRUCTURE

Influence of Healing Agents and Concrete Environment on PLA 3D Printed Mini-vascular Networks for Self-healing Concrete Structures

The aim of this study is to investigate the effect of alkaline environment and healing agents on 3D-printed Poly Lactic Acid (PLA) mini vascular networks (MVNs) for self-healing concrete structures. PLA is an interesting thermoplastic polymer for 3D printing MVNs, due to its good mechanical property and its sustainability. Studies conducted recently on single channel MVNs also known as TETs, and dual channel MVNs, or d-TETs, have indicated that they can effectively store either a single or two-component healing agents to promote the self-healing process in concrete structures. Solubility tests and Differential Scanning Calorimetry (DSC) analysis were conducted in this study to assess the degradation of PLA polymer resulting from various factors, including the printing process, embedment of MVNs in concrete matrices, and prolonged contact with healing agents such as sodium silicate and nanolime solutions.

Keywords:
Self-healing, concrete, 3D-printing, PLA degradation, mini-vascular networks.

Corresponding author:
Giulia.Cazzador@unive.it



G. Cazzador, C. De Nardi, L. Ronchin, and A. Vavasori, 'Influence of Healing Agents and Concrete Environment on PLA 3D Printed Mini-vascular Networks for Self-healing Concrete Structures', *Cardiff University School of Engineering Research Conference 2023*, Cardiff, UK, 2023, pp. 80-83.

doi.org/10.18573/conf1.t

INTRODUCTION

Biomimicry is among the innovative methods being utilized in civil engineering to address the increasing need for construction materials that offer better and longer service-life performance [1-2]. This approach enhances the durability of materials by enabling them to detect and respond to damage, thus reducing or eliminating the need for constant repair or replacement of the material.

Recent studies on mini-vascular networks (MVNs) with single channels, also known as TETs, and MVNs with dual channels, or d-TETs, have shown that they can effectively hold one or two-component healing agents to facilitate self-healing in concrete structures [3-4].

TETs and d-TETs, which comprise hollow ligaments that interconnect to form a network with a characteristic dimension, specifically a maximum ligament length that is approximately twice the size of the largest aggregate particle found in the cement composite, are printed from Poly Lactic Acid (PLA) [5].

The broad spectrum of potential applications of PLA, including in building materials, makes it an attractive biopolymer at present [6-8]. Furthermore, the continuous growth of polymers for fuse deposition model (FDM) printing has been reported widely in recent years. [9-10].

PLA is a thermoplastic polymer, completely based on renewable resources and its degradation can be entrusted to microorganisms which would reconvert it to its monomer, lactic acid (LA), and carbon dioxide [11]. The durability of 3D printed parts is largely determined by the conditions in which they are used and operated. As a result, these conditions can impact the mechanical and chemical properties of the parts when subjected to static or dynamic contact [11].

In this study, Solubility tests and Differential Scanning Calorimetry (DSC) analysis were carried out to evaluate the deterioration of PLA polymer caused by different factors, such as the printing process, embedding of MVNs in concrete matrices, and extended exposure to healing agents like sodium silicate (SS) and nanolime (NL) solutions.

MATERIALS AND METHODS

TETs and d-TETs were printed from clear PLA Ultimaker²® printer (Utrecht, The Netherlands) with a 0.25 mm nozzle, as represented in Fig. 1.

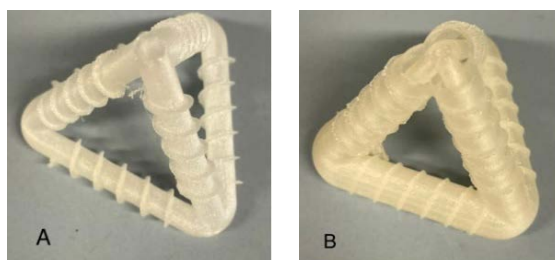


Fig. 1. 3D printed single channel TET (A) and double channel d-TETs (B).

Evaluation of PLA degradation are carried out by Infrared spectroscopy measurement (IR Brucker vector 2), solubility and swelling tests and Differential Scanning Calorimetry (DSC). DSC was performed using a Linseis PTA ST1000 using an amount of polymer of about 40 mg, placed in an open aluminium, under nitrogen flow of 80 ml min⁻¹, with a

temperature ramp of 10°C min⁻¹ from 30 to 250°C, depending on the type of measurement and polymer.

DSC measurements were carried out on samples collected directly from: i) the filament roll (wire); ii) a single channel TETs ligament after being printing; iii) d-TET ligaments; i.e. internal or external channel, before and after the contact with nanolime (NL) and sodium silicate (SS) (and after the healing period).

The solubility tests of fragments of TETs PLA were conducted using various solvents at room temperature, with a treatment duration of 48 hours.

Some solvents, such as chloroform and styrene used for solubility test are widely recognized as a mutagen and thus potentially carcinogenic, as such its inclusion in the formulations is not recommended, although it has been included here for completeness. Indeed, the solubility tests use solvents both polar and non-polar, in order to take into account a wide range of environments from polar to non-polar.

The swelling tests were conducted at room temperature after solubility tests, comparing the fragment before solubility treatment and observing the volumetric change.

RESULTS

In Figure 2 are reported the thermogram of the PLA samples. Solubility tests results are reported in Table 1.

As can be seen in Table 2, although some solvents did not solubilize the PLA, a certain degree of swelling was observed, except for neat water.

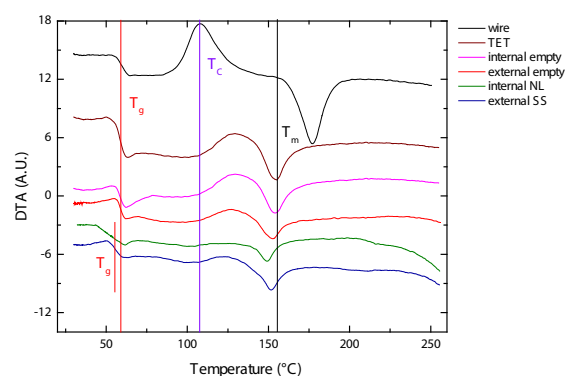


Fig. 2. DSC measurements of various PLA samples obtained from TETs in different conditions. Run conditions: open aluminium crucible, sample 40 mg, ramp 10°C/min to 250°C, nitrogen flow 80ml/min.

Solvents	Poly lactide acid (PLA)
Dichloromethane	Y
Chloroform	Y
Diethyl ether	N
Styrene	N
Acrylic Acid	N
Ethyl Acrylate	N
Acetic Acid	N
Trifluoroacetic acid	Y
Aqueous Na(OH)	Y
Aqueous Ca(OH) ₂	Y
Methyl alcohol	N
Ethyl alcohol	N
Water	N

Table 1. PLA Solubility tests degradation of PLA in organic solvents, water and alkaline condition; Y= soluble, N=insoluble.

Solvents	Poly lactide acid (PLA)
Diethyl ether	Y
Styrene	Y
Acrylic Acid	Y
Ethyl Acrylate	Y
Acetic Acid	Y
Methyl alcohol	Y
Ethyl alcohol	Y
Water	N

Table 2. Swelling tests of degradation of PLA in organic solvents and water; Y= swelling, N= no swelling.

DISCUSSION

It appears in Fig 2, the pure PLA wire shows the typical thermogram (curve 1) of the polymer suggesting the absence of significant amount of additives and co-polymers, whose presence may interfere with the typical behaviour of the PLA. Thermogram curves (curves 2) obtained from TETs' ligament showed a displacement of the peak of crystallization at higher temperature (from 108°C to 128-130°). Furthermore, the measurements show an even more evident displacement of the melting point from 177°C to 153-154°C for PLA wire and worked ones, respectively. It appears there are practically no effect due to the permanence inside the concrete (compare curve 2 with 3 and 4). Regardless, the enthalpies of both crystallization and melting seem to be reduced once the PLA has been processed by the printer. It should be noted that precise enthalpy values were not measured as they were beyond the scope of this study and no calibration was conducted.

This reduction in enthalpies indicates a modification in the polymer's crystallinity. This behaviour is even more evident when the TETs are filled with sodium silicate, nano-silica and nano-lime (curves 5-6) suggesting the presence of these compounds reduce further the crystallinity of the polymer. No clear variations of the glass transition temperature are evidenced by the thermogram (curves 1-4, T_g=58-59°C), thus suggesting no relevant modification of the polymer

structure is occurred. On the contrary, curves 5-6 showed a displacement in range the T_g to 52-55°C suggesting a certain modification of the polymer structure induced by the presence of solvent whose adsorption may modify substantially such a physical property.

According to Table 1, degradation of the material occurred in both an alkaline environment and in the presence of organic substances. To prevent this issue, a future research study will explore a strategy aimed at reducing the degradation of PLA, which will involve investigating both healing materials and PLA surface treatments.

Table 2 shows that the polymer experiences swelling in the presence of all organic solvents except for water, which does not cause significant swelling of the PLA. This is in agreement with the results of DSC where modification of the thermal properties of the PLA are more evident when alkali and solvent are present together.

To assess their compatibility with PLA, we tested all of these solvents since they are potentially used in healing polymer formulations. Our findings indicate that an aqueous solvent with mildly basic or acidic conditions would be the most appropriate choice. In future studies, surface treatments could be incorporated to safeguard the polymer bulk and prevent any internal modifications.

Funding

Funding was provided by Ca' Foscari University of Venice ADIR 2021 and Leverhulme Trust ECF-2022-235.

Acknowledgments


The authors thank Samuel Moeller (Cardiff University) for his technical support on 3D printing.

Conflicts of interest

The authors declare no conflict of interest.

REFERENCES

- [1] Z. Li, L. R. De Souza, C. Litina, A. E. Markaki, and A. Al-Tabbaa, 'A novel biomimetic design of a 3D vascular structure for self-healing in cementitious materials using Murray's law', *Mater Des*, vol. 190, pp. 1–14, May 2020.
doi.org/10.1016/j.matdes.2020.108572
- [2] Y. Shields, N. De Belie, A. Jefferson, and K. Van Tittelboom, 'A review of vascular networks for self-healing applications', *Smart Mater Struct*, vol. 30, no. 6, p.63001, Jun. 2021.
doi.org/10.1088/1361-665X/abf41d
- [3] C. De Nardi, D. Gardner, and A. D. Jefferson, 'Development of 3D Printed Networks in Self-Healing Concrete', *Materials* (Basel), vol. 13, no. 6, p. 1328, Jan. 2020.
doi.org/10.3390/ma13061328
- [4] C. De Nardi, D. Gardner, D. Cristofori, L. Ronchin, A. Vavasori, and T. Jefferson, 'Advanced 3D printed mini-vascular network for self-healing concrete', *Materials & Design*, vol. 230, p. 111939, Jun. 2023.
doi.org/10.1016/j.matdes.2023.111939
- [5] C. De Nardi, D. Gardner, A. Jefferson, T. Selvarajoo, and G. Evans, 'The Development of Mini-Vascular Networks for Self-Healing Concrete', in *Durable Concrete for Infrastructure under Severe Conditions Durable Concrete for Infrastructure under Severe Conditions*, no. September, pp. 19–23, 2019.
- [6] A. Sayadi, T.R. Neitzert, and G. Charles Clifton, 'Influence of poly-lactic acid on the properties of perlite concrete', *Constr Build Mater*, vol. 189, pp. 660–675, Nov. 2018
doi.org/10.1016/j.conbuildmat.2018.09.029
- [7] A.E. Abd-Elmoaty, 'Self-healing of polymer modified concrete', *Alexandria Eng J*, vol. 50, no. 2, pp. 171–178, Jun. 2011.
doi.org/10.1016/j.aej.2011.03.002
- [8] A.Y. Patil, N.R. Banapurmath, and U.S. Shivangi, 'Feasibility study of epoxy coated Poly Lactic Acid as a sustainable replacement for river sand', *J Clean Prod*, vol. 267, p. 121750, Sep. 2020.
doi.org/10.1016/j.jclepro.2020.121750.
- [9] R. Arrigo, A. Frache, 'FDM Printability of PLA Based-Materials: The Key Role of the Rheological Behavior', *Polymers* (Basel), vol. 14, no. 9, p.1754, Jan. 2022.
doi.org/10.3390/polym14091754
- [10] S. Wang, 'Lifting the quality of fused filament fabrication of polylactic acid based composites', *Compos Part B Eng*, vol. 210, p. 2021, pp. 1–10, Apr. 2021.
doi.org/10.1016/j.compositesb.2021.108613
- [11] E.R. Rezvani Ghomi, F. Khosravi, A. Saedi Ardahaei, Y. Dai, R.E. Neisiany, F. Foroughi, M. Wu, O. Das, S. Ramakrishna, 'The Life Cycle Assessment for Polylactic Acid (PLA) to Make It a Low-Carbon Material', *Polymers*, vol. 13, no. 11, p. 1854, Jun. 2021.
doi.org/10.3390/polym13111854



Advanced Manufacturing

Advanced Manufacturing

- 86 Accelerating Multi-step Sparse Reward Reinforcement Learning
- 91 Safety for Human-Robot Interaction with a Shared Autonomy
- 95 A Novel Hybrid Bees Regression Convolutional Neural Network (BA-RCNN) Applied to Porosity Prediction in Selective Laser Melting Parts
- 100 The Research on Mechanical Properties and Compressive Behavior of Graphene Foam with Multi-scale Model
- 105 Developing Antibacterial Nanocomposites
- 109 Microwave Resonator-based Microfluidic Sensors Fabricated Using 3D-Printing Technology
- 113 Using DCGAN and WGAN-GP to Generate Artificial Thermal RGB Images for Induction Motors
- 118 Altering the Tribological Properties of Laser Powder Bed Fusion Materials through Various Methods: A Review
- 123 Development of a Net Zero Route for the Circular Production of Additive Manufacturing Powders
- 128 A Study on the Surface Chemistry of Laser Textured Parts

Yang X

Cardiff University
School of Engineering

Ji Z

Cardiff University
School of Engineering

ADVANCED MANUFACTURING

Accelerating Multi-step Sparse Reward Reinforcement Learning

After the great successes of deep reinforcement learning (DRL) in recent years, developing methods to speed up DRL algorithms for more complex tasks closer to those in the real world has become increasingly important. In particular, there is a lack of research on long-horizon tasks that contain multiple subtasks or intermediate steps and can only provide sparse rewards at task completion point. This paper suggests to 1) use human priors to decompose a task and provide abstract demonstrations – the correct sequences of steps to guide exploration and learning, and 2) adjust the exploration parameters adaptively according to the online performances of the policy. The proposed ideas are implemented on three popular DRL algorithms, and experimental results on gridworld and manipulation tasks prove the concept and effectiveness of the proposed techniques.

Keywords:

Deep reinforcement learning, abstract demonstration, adaptive exploration, sparse reward, long-horizon manipulation.

Corresponding author:

JiZ1@cardiff.ac.uk



X. Yann and Z. Ji, 'Accelerating Multi-step Sparse Reward Reinforcement Learning', *Cardiff University School of Engineering Research Conference 2023*, Cardiff, UK, 2023, pp. 86-90.

doi.org/10.18573/conf1.u

INTRODUCTION

Deep reinforcement learning (DRL) has achieved important progresses in the field of recommendation systems, computer games, navigation, economics, etc. [1]. However, DRL algorithms still struggle to learn tasks with long horizon, multiple intermediate steps, and sparse task completion rewards. In the real world, many robotic manipulation tasks exhibit such characteristics. For example, for the block-pushing task shown in Fig. 1, the robot needs to learn to open the chest before it can learn to push the block into the chest. With only a sparse reward signal based on task completion, such a task is hopeless for state-of-the-art continuous control DRL algorithms. This paper seeks to improve the performances of DRL in such tasks.



Fig. 1. Visualisation of a multi-step pushing task.

For such long horizon tasks, classic methods have provided successful examples of adopting manual task decomposition. For example, the popular task and motion planning (TAMP) methods employ domain languages to describe subtasks and skills, and search in the hybrid space of discrete subtasks and continuous manipulator motions for a solution for a long-horizon manipulation problem [2]. These methods, however, require the access to an accurate dynamic model of the world, which is one of the bottlenecks that limits their applications. On the other hand, this paper focuses on model-free DRL methods [1], which is freed from the assumption of having an accurate system dynamic model. The downside, however, is the difficulty of training DRL agents with a long task horizon and a sparse reward function.

In previous research, human demonstrations, in the forms of kinesthetic motion trajectories, have been one of the important options to help DRL in such difficult scenarios [3,4]. However, these methods are not scalable due to the difficulty of collecting them. In response, this paper adopts an abstract form of demonstrations that consist of the correct sequences of the task steps to be learnt and achieved, given the access to a task decomposition scheme. Specifically, abstract demonstrations 1) do not encode human biases into the robot motions and 2) are much easier to collect compared to kinesthetic teaching. The idea is plausible because the short motion trajectories in between two subtasks can be learnt efficiently with hindsight experience replay (HER) even in the face of sparse reward signals [5].

Another issue that slows down learning is related to the design of the exploration strategy of DRL agents. In particular, most exploration strategies of DRL agents at the current stage is task-agnostic [6]. They are therefore not exactly suitable for multi-step tasks, in which the later task steps depend heavily on the former ones. For example, stacking the fourth block would require the previous blocks to be stacked well. As a result, the default setting of using a strategy that explores constantly or decays the randomness in a task-agnostic way [6] will have difficulty dealing with multi-step tasks.

In response to this limitation, this work suggests to adapt the exploration parameters of a DRL agent in accordance with its online performances of each task step. The main idea of this adaptive exploration strategy is to reduce unnecessary exploration when the target subtask has been well-learnt.

MATERIALS AND METHODS

This research employs the recent framework of goal-conditioned reinforcement learning (GRL) [5], in which a universal policy $\pi(a|s, g)$ or universal q function $Q^\pi(s, g, a)$ is optimised towards the expected maximum discounted cumulated future goal-based rewards $\mathbb{E}_\pi[G] = [\sum_{t=0} \gamma^t R_t(s, g, a)]$, where $\gamma \in [0,1]$ is the discount factor that determines the importance of future rewards. The term *universal* implies that the policy or q function make decisions for a set of goals, instead of a single goal as in standard RL paradigm [7].

The following will introduce 1) the experiment tasks and the implementation of the goal-conditioned Markov decision processes (GMDPs), 2) the main learning algorithms, 3) the abstract demonstration method, and 4) the adaptive exploration method.

Tasks and the GMDP

To examine the effectiveness of the proposed methods, three robotic manipulation tasks developed in simulation are used in the experiments, including the ChestPush, the ChestPick and the BlockStack tasks from the Pybullet Multigoal (PMG) simulation software [8], as shown in Fig. 2. From left to right in Fig. 2, the robot needs to 1) open the chest and push the block into it, 2) open the chest, grasp the block and drop it into the chest, and 3) pick and stack the blocks as indicated by the transparent spheres.

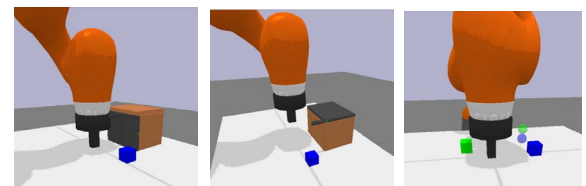


Fig. 2. The experimented tasks.

The GMDP descriptions of the tasks are exactly the same as that presented by in the simulation package [8], except that the representation of the goals is extended. The state of the system consists of the absolute positions and Euler orientations of the blocks, the relative positions and Euler orientations of the blocks w.r.t. the gripper tip, the relative linear and angular velocities of the blocks w.r.t. the gripper tip, the absolute position and velocity of the gripper tip and the finger width. At the beginning of an episode, the algorithm is given a final goal that specifies the desired positions of the blocks and the gripper and the desired width between the fingers. The algorithm gives actions based on the state and goal to move the gripper in the Cartesian space and control its finger width. It is given a reward of 0 when the final goal is achieved, and a reward of -1 otherwise. A desired goal is said to be achieved when its Euclidean distance to the actually achieved goal is less than a threshold .

Reinforcement Learning Algorithms

Two RL algorithms for continuous action space tasks: deep deterministic policy gradient (DDPG) [9] and soft actor critic (SAC) [10] are employed as the base algorithms. A short description of the two algorithms is given below, and the readers are referred to the original papers for further details. Also, as one shall see, the proposed acceleration techniques described in the following subsections are not limited to these two algorithms.

DDPG and SAC are both actor-critic algorithms [9,10]. DDPG seeks to learn a critic network, q_{ω}^{μ} , that predicts the expected return for a pair of state and action, and a deterministic actor network, μ_{θ} , that takes into the state and predicts the action that maximise the output of the critic network. For the goal-conditioned version, it simply takes the goal as an extra input to the policy and critic. Implementation-wise, the goal vector is concatenated into the input vector. As a deterministic policy agent, DDPG needs a behavioural policy to collect exploration data. In this work, the base exploration used by DDPG is the epsilon-Gaussian (EGa) strategy [5]:

$$\mu_b(a|s, g) = \begin{cases} \mathcal{N}(\mu(s), \sigma), & z \geq \epsilon \\ \mathcal{U}(A), & z < \epsilon \end{cases} \quad (1)$$

where, \mathcal{N} stands for a normal distribution, \mathcal{U} stands for a uniform distribution, $z \sim \mathcal{U}(0,1)$ and $\epsilon \in [0,1]$. In short, the EGa strategy takes a random action with probability ϵ , and take the action output by the learnt policy with zero-mean Gaussian noise with a probability of $1 - \epsilon$. The algorithm optimises the following objectives for the critic and the actor networks, respectively:

$$J_{DDPG}(\theta') \approx \mathbb{E}_{(s,g) \sim D, a \sim \mu_{\theta'}(s,g)} [q_{\omega}^{\mu}(s, g, a)] \quad (2)$$

$$J_{DDPG}(\omega') \approx \mathbb{E}_{(s,g,a,r,s') \sim D} \left[\frac{1}{2} (y - q_{\omega'}^{\mu}(s, g, a))^2 \right] \quad (3)$$

where, $y = r + \gamma \cdot q_{\omega}^{\pi} - (s', g, a' |_{a' = \pi_{\theta'}(s', g)})$ is the target Q value computed by the target critic network with weights, and are the parameters of the main policy and Q networks, stands for the replay buffer.

The SAC algorithm is also an actor-critic algorithm, but instead employs a stochastic actor [10]. In short, SAC uses a neural network to predict the mean and deviations of a Gaussian actor policy. The main difference with DDPG is twofold.

First, the SAC optimises the critic and actor not only towards the maximum return direction, but also the maximum policy entropy:

$$J_{SAC}(\theta'') \approx \mathbb{E}_{(s,g) \sim D, a \sim \pi_{\theta''}(s,g)} [\alpha \log \pi_{\theta''} - q_{\omega''}^{\pi}(s, g, a)] \quad (4)$$

$$J_{SAC}(\omega'') \approx \mathbb{E}_{(s,g,a,r,s') \sim D} \left[\frac{1}{2} (y - q_{\omega''}^{\pi}(s, g, a))^2 \right] \quad (5)$$

where, $y = r + \gamma \cdot q_{\omega''}^{\pi} - (s', g, a' |_{a' = \pi_{\theta''}(s', g)}) - \alpha \log \pi_{\theta''}$ is the soft target Q value, θ'' and ω'' are the parameters of the main policy and Q networks, and α is the temperature parameter.

Secondly, the SAC algorithm conducts exploration by sampling from its own policy, whose randomness is determined by the output of the neural network. As the objective partly maximises the entropy of the policy, it can retain a certain degree of exploration without collapsing into a deterministic policy.

These two algorithms are selected because they are well-known representatives of recent model-free DRL algorithms. Also, they both retain the state-of-the-art performances of popular continuous control benchmarks [9,10]. However, they are not tailored for the kind of long-horizon and multi-step tasks considered in this paper, and the following will then introduce the two techniques that can speed up these two agents.

Abstract demonstrations

The idea of abstract demonstrations (AD) is very similar to the human practices of learning to build a Lego house or assemble a furniture using a user manual that specifies a series of key task steps.

AD assumes the access to a task decomposition scheme that produces a set of task steps, each corresponds to a subset of goals in the GRL framework. In this work, the decomposition scheme comes from human priors, but it is certainly interesting to develop automated task decomposition methods in the future. Specifically, the given tasks are decomposed as follows:

- ChestPush: push the door open reach the blue block push the block into the chest.
- ChestPick: push the door open grasp the blue block move to the top of the chest drop the block.
- BlockStack: grasp the first block move to the target position grasp the second block put it on top of the first one.

Instead of providing only the final goal at the start of training, the agent is given the subgoals associated with the subtasks in the correct order. When a subgoal is achieved, the next one according to the demonstrations will be given, until the final goal is reached or the episode runs out of time. A parameter, $\eta = 0.75$ is used to control in how many episodes during training that the agent is demonstrated.

Adaptive exploration

To adapt the exploration parameters, the adaptive exploration (AE) method first keeps a record of the online performances on each subtask, and then uses the performance to scale the exploration parameters. The following will explain the implementations on the DDPG and SAC agents.

For convenient usage, the average success rates of the agent over 30 testing episodes on each subtask are used as the performance metric, denoted as a n -dimensional vector, \mathcal{S} , where N is the number of subtasks. This evaluation run is performed after every training epoch (800 episodes). To ensure a smoothly changing behaviour of the performance record, the Polyak average of the success rate is used instead of the arithmetic mean:

$$\mathcal{S}^- \leftarrow (1 - \tau_S) \cdot \mathcal{S}^- + \tau_S \cdot \mathcal{S} \quad (6)$$

where \mathcal{S}^- is the Polyak averaged success rate vector and $\tau_S = 0.3$ is the update ratio.

To update the DDPG exploration strategy, Eq.1 is used with an individual ϵ^n and σ^n for the n -th step. All of them starts with $\epsilon_0 = 0.2$ and $\sigma_0 = 0.05$. After each evaluation run, these two parameters are updated as follows:

$$\epsilon \leftarrow \epsilon_0 \cdot (1 - S^-), \sigma \leftarrow \sigma_0 \cdot (1 - S^-) \quad (7)$$

For the SAC agent, the evaluation success rates are used to scale the deviations predicted by the actor neural network for each subtask after an evaluation run:

$$\sigma^{SAC} \leftarrow \hat{\sigma}^{SAC} \cdot (1 - S^-) \quad (8)$$

where $\hat{\sigma}^{SAC}$ is predicted by the actor network.

RESULTS

To examine the effectiveness of the proposed ideas, ablative experiments are conducted with the three robotic manipulation tasks. All codes are available on GitHub: <https://github.com/IanYangChina/A-2-paper-code>.

As shown in Fig. 3, the DDPG and SAC agents are both run on the three tasks in their original forms (Vanilla), aided with abstract demonstrations (AD), and aided with both methods (ADAE). The first row is the performances of the DDPG agents, and the second row is for the SAC agents. For each row, the success rates correspond to the three tasks from left to right: ChestPush, ChestPick and BlockStack.

In Fig. 3, both agents have substantial improvements on the three tasks with the help of the abstract demonstrations (compare the blue and green lines). As the task becomes more difficult (from left to right), the improvements over the vanilla algorithms become more obvious. This suggests that providing abstract demonstrations can substantially accelerate multi-step sparse reward reinforcement learning.

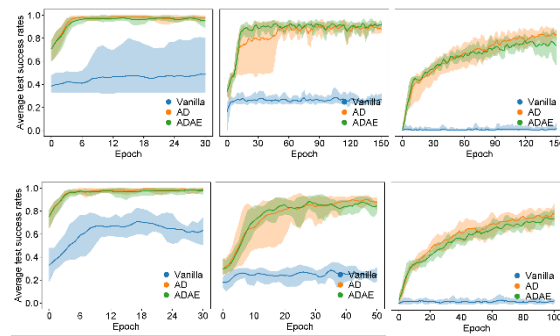


Fig. 3. Test success rates.

Secondly, the adaptive exploration has gained less obvious performance improvements in addition to the abstract demonstrations (compare the orange and green lines). However, it does reduce the variances of the success rates, indicating a more stable training processes.

DISCUSSION

The proposed abstract demonstrations and adaptive exploration methods have been proved in the result section to improve the performance of two popular DRL algorithms in long-horizon, multi-step and sparse reward continuous control tasks.

Compared to previous studies which use motion-level trajectories as demonstrations [3,4], abstract demonstrations are much easier to collect and implement. However, there is no free lunch. It requires a given task decomposition scheme. In the future, developing automated task decomposition and subgoal discovery methods are promising directions. Also, abstraction demonstrations can be used along with kinesthetic demonstrations, when the motions in between subtasks are still too hard to learn by pure exploration.

There is not much research that paid attention to task-oriented exploration strategy design [6]. In fact, the idea is compatible to use with many task-agnostic exploration strategies, as shown by the DDPG and SAC implementations in this work. For example, one can use a success rate to scale the noise injection rate in [11] or the random action probability of the popular epsilon-greedy method [7].

In addition to what were mentioned, more efforts are demanded to implement and evaluate the proposed methods on more realistic tasks, especially tasks with complex and noisy observations. For example, the representation and generation of subtasks and high-dimensional goals [12]. Such studies will also empower techniques in other areas of robotic research.

Acknowledgments

Xintong thanks the China Scholarship Council for the financial support during his PhD career (No. 201908440400).

Conflicts of interest

The authors declare no conflict of interest.

REFERENCES

- [1] A. Lazaridis, A. Fachantidis, and I. Vlahavas, 'Deep Reinforcement Learning: A State-of-the-Art Walkthrough', *jair*, vol. 69, pp. 1421–1471, Dec. 2020. doi.org/10.1613/jair.1.12412
- [2] C. R. Garrett *et al.*, 'Integrated Task and Motion Planning', *Annu Rev Control Robot Auton Syst*, vol. 4, no. 1, pp. 265–293, May 2021. doi.org/10.1146/annurev-control-091420-084139
- [3] H. Ravichandar, A. S. Polydoros, S. Chernova, and A. Billard, 'Recent Advances in Robot Learning from Demonstration', *Annu Rev Control Robot Auton Syst*, vol. 3, no. 1, pp. 297–330, May 2020. doi.org/10.1146/annurev-control-100819-063206
- [4] A. Nair, B. McGrew, M. Andrychowicz, W. Zaremba, and P. Abbeel, 'Overcoming Exploration in Reinforcement Learning with Demonstrations', in *2018 IEEE International Conference on Robotics and Automation (ICRA)*, Brisbane, QLD: IEEE, May 2018, pp. 6292–6299. doi.org/10.1109/ICRA.2018.8463162
- [5] M. Andrychowicz *et al.*, 'Hindsight experience replay [C]', *NeurIPS*, Long Beach, UK, 4–9 Dec. 2017. doi.org/10.48550/arxiv.1707.01495
- [6] P. Ladosz, L. Weng, M. Kim, and H. Oh, 'Exploration in deep reinforcement learning: A survey', *Information Fusion*, vol. 85, pp. 1–22, Sep. 2022. doi.org/10.1016/j.inffus.2022.03.003
- [7] R. S. Sutton and A. G. Barto, *Reinforcement learning: an introduction*, Second edition. in Adaptive computation and machine learning series. Cambridge, Massachusetts: The MIT Press, 2018.
- [8] X. Yang, Z. Ji, J. Wu, and Y.-K. Lai, 'An open-source multi-goal reinforcement learning environment for robotic manipulation with pybullet [C]', *Towards Autonomous Robotic Systems*. Springer, Cham, Lincoln, UK, 8–10 Sep. 2021. doi.org/10.1007/978-3-030-89177-0_2
- [9] T.P. Lillicrap *et al.*, 'Continuous control with deep reinforcement learning' [C] *ICLR*, San Juan, Puerto Rico, 2–4 May 2016. doi.org/10.48550/arXiv.1509.02971
- [10] T. Haarnoja *et al.*, 'Soft actor-critic: Off-policy maximum entropy deep reinforcement learning with a stochastic actor', [C] *ICML*, Stockholm, Sweden, 10–15 Jul. 2018. doi.org/10.48550/arXiv.1801.01290
- [11] M. Fortunato *et al.*, 'Noisy networks for exploration' [C] *ICLR*, Vancouver, Canada, 30 Apr.–3 May 2018. doi.org/10.48550/arXiv.1706.10295
- [12] S. Pateria, B. Subagdja, A.-H. Tan, and C. Quek, 'End-to-End Hierarchical Reinforcement Learning With Integrated Subgoal Discovery', *IEEE Trans Neural Netw Learning Syst*, vol. 33, no. 12, pp. 7778–7790, Dec. 2022. doi.org/10.1109/TNNLS.2021.3087733

Tafrishi SA

*Cardiff University
School of Engineering*

Ravankar AA

*Tohoku University
Robotics Department*

Hirata Y

*Tohoku University
Robotics Department*

ADVANCED MANUFACTURING

Safety for Human-Robot Interaction with a Shared Autonomy

Robots were placed under fixed safeguards in the early stages of robotics development. Safety and real-time risk assessment are not easy, especially when robots are in places that co-exist with humans. However, robot and human interaction have essential applications in human physical assistance, human-robot task coordination and cooperation. This paper presents our proposed new approach to developing shared autonomy under safety. We derive the shared autonomy policies and explain how safety is quantified. After demonstrating an experiment result, the paper describes open problems that will be investigated in future research activities. It also covers how it can have potential applications in industry, welfare, and rescue.

Keywords:

Robotics, safety, human-robot interaction, compliant actuators.

Corresponding author:

TafrishiSA@cardiff.ac.uk



S.A. Tafrishi, A.A. Ravankar, and Y.Hirata, 'Safety for Human-Robot Interaction with a Shared Autonomy', *Cardiff University School of Engineering Research Conference 2023*, Cardiff, UK, 2023, pp. 91-94.

doi.org/10.18573/conf1.v

INTRODUCTION

Robots are getting into every aspect of life. In particular, assistive robots are the next great innovation leap that will be included in the different tasks, such as the physical assistance of humans. Human-robot interaction has a significant challenge. The human model is mainly assumed to be a BlackBox without a clear understanding of whether human motion is safe and stable. And there must be real-time feed from the environment and humans about their stability and normal motion behaviour. This problem gets more challenging when the situation requires the human and robot to work in cooperation.

Ignoring the human model has certain limitations for assistive robots [1-2]. This issue from the human aspect stops robots from getting into human's nearby workspace. The main challenge is finding the human intention and doing risk assessment in real-time while assisting the person with a robot. For example, Vianello et al. [3] did studies for predicting the posture of human body limbs, but this study could have constraints due to developed leader-following motion controls. In addition, the heavy computations make these strategies challenging for real-time human-robot interactions [3-4].

The next challenge is developing a shared autonomy between humans and assisting robots. There have been some attempts to develop shared autonomy between inputs from human counterparts and manipulator robots' controllers [5-6]. For instance, Javdani et al. [6] proposed a partially observable Markov decision process (POMDP) to guess the object the user wants to pick. In this problem, it was assumed automated robot does not know the priori goal (without desired configuration). The study shed light on controller design with no desired states, but there are remaining open problems. In this regard, the arm robot mainly ran with an internal controller and did not consider any complex trajectory that the person/patient wanted to control the joystick. However, assistive mobile robots may follow highly complex paths, spontaneously changing decisions for the desired goals.

Based on the motivations mentioned earlier, we were able to quantify the safety of human upper body motion by using a spring-damper predictive model in our previous study [9]. Also, we proposed an assistive controller based on differential geometry that created corrected velocity inputs based on user joystick inputs and mobile wheelchair robot's states [10]. In this paper, we propose a new shared autonomy policy that combines the predictive safety model that gets human conditions by IMU with our assistive controller and an onboard motion planner. Additionally, our problem is more challenging since there is an assistive walker robot that, with an onboard navigation system, tries to correct its assistance to the user (see Fig. 1) based on inputs from the user, assistive controller and motion planner.

First, we describe the shared autonomy concept under safety. Next, we find out the policies for the shared autonomy. Next section, we explain the predictive safety model and its sensory design. Finally, the experiment results are shown for an example case.

SHARED AUTONOMY POLICIES

This section explains how shared autonomy is derived with respect to the safety and assistive controller. Next, the formulation is explained between robots and humans.

Fig. 1 presents an example scenario where the patient uses an assistive mobile robot. In this problem, the person's information is captured with inertia measurement sensors (IMU). The whole concept of multi-robot cooperation for human assistance is given in our previous study [7]. Similarly, a wireless IMU sensor is attached to a person's chest. Also, an assistive walker robot can autonomously navigate through the environment using the LiDAR sensor. The walker robot has a differential wheel model, and users with joystick inputs can get assistance. To simplify the problem the robot is underactuated; hence the information from user directly corresponds to the velocity and orientation of the walker but actuators work as breaks to support the patient during the move from one place to another.

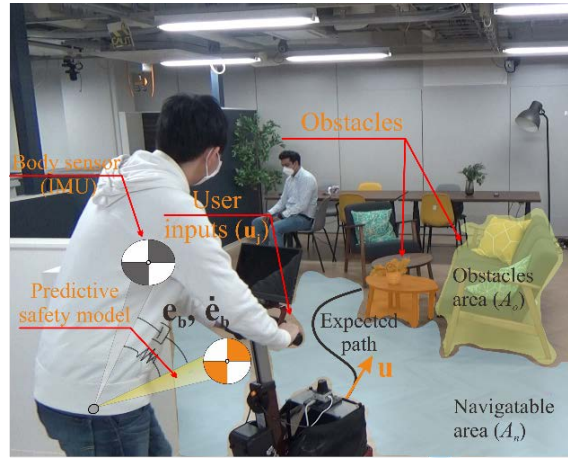


Fig. 1. Shared autonomy scenario.

The principal inputs formula with shared autonomy policy is proposed as follows:

$$\mathbf{u}(t) = \frac{1}{\sum_{i=1}^k \lambda_i} (\sum_{i=1}^k \lambda_i \mathbf{u}_i) \quad (1)$$

where $\lambda_i \in [0 - 1]$, \mathbf{u}_i and k are the trust ratio, arbitrary velocity vector and maximum number of inputs. In this problem, the inputs are planner, assistive controller and walker joystick, $k=3$. The inputs and trust factors for each system are defined as motion planner (\mathbf{u}_p, λ_p), assistive controller (\mathbf{u}_a, λ_a) and human push (\mathbf{u}_j, λ_j). Then, we have proposed two shared autonomy policy as follows:

$$\mathbf{u}_t = \lambda_s \left(\frac{\lambda_j \mathbf{u}_j + \lambda_a \mathbf{u}_a}{2} \right) + (1 - \lambda_s) \left(\frac{\lambda_a \mathbf{u}_a + \lambda_p \mathbf{u}_p}{2} \right) \quad (2)$$

$$\mathbf{u}_t = \lambda_o \left(\frac{\lambda_a \mathbf{u}_a + \lambda_p \mathbf{u}_p + \lambda_j \mathbf{u}_j}{3} \right) + (1 - \lambda_o) \lambda_p \mathbf{u}_p$$

where λ_s and λ_o are safety quantifier ratio and obstacle inclusion ratio on the scene, respectively. To give better understanding of how inputs are decided based on the level of risk and environment information, we can show their extreme conditions as follows:

$$\text{Policy 1} = \begin{cases} \mathbf{u}_t = \frac{\lambda_j \mathbf{u}_j + \lambda_a \mathbf{u}_a}{2}, & \lambda_s \rightarrow 1 \\ \mathbf{u}_t = \frac{\lambda_a \mathbf{u}_a + \lambda_p \mathbf{u}_p}{2}, & \lambda_s \rightarrow 0 \end{cases} \quad (3)$$

$$\text{Policy 2} = \begin{cases} \mathbf{u}_t = \frac{\lambda_a \mathbf{u}_a + \lambda_p \mathbf{u}_p + \lambda_j \mathbf{u}_j}{3}, & \lambda_o \rightarrow 1 \\ \mathbf{u}_t = \lambda_p \mathbf{u}_p, & \lambda_o \rightarrow 0 \end{cases}$$

It is clear from Eq.3 that when the trust λ_s is not high in human condition (safety input gives high error in human upper body motion), the input of robot actuators mainly relies on the assistive controller and motion planner.

This helps to avoid unstable behaviour of the user inputs e.g., this can be direct force/moment to the walker by the user. However, when the trust is near one, the control input consists of human and assistive control input. In the second policy, the problem is a little different since the risk-assessment happens with the number of seeable obstacles in the scene where we have simply defined it by $\lambda_o = (A_n / A_o)$ where A_n and A_o are areas that can be navigated and obstacles. Thus, when the risk is low due to existing low number of obstacles, the human input is followed with correction through the assistive controller with motion planner. And the planner is mainly considered with existing high levels of obstacles.

We can easily develop the shared autonomy by solving the equations (2) for two trust ratio variables of lambda sub p planner and lambda sub o human inputs. Since the computation might be highly complicated, we leave the details of the stability and boundedness to another study.

QUANTIFYING THE SAFETY IN HUMAN MOTION AND ASSISTIVE CONTROLLER

Quantifying the safety concerning human motion is important since the real-time risk assessment help assistive robots be more agile and dynamic in environments with humans. Therefore, considering human body motion stability and normal motion realisation rather than as Blackbox would be highly crucial in different scenarios.

Our previous work [8] defined safety as human tenancy to have an unstable or abnormal motion concerning standard/ natural motions. To include the safety of the problem of navigation and human-robot interaction, we have used the chest (onboard IMU) information. A predictive safety model is utilised where the system is based on a spring-damper safety model with a reduced-dimension dataset [8]. This model quantifies and tracks how much human posture (upper body) deviates in orientation and velocity (e_b, \dot{e}_b) as shown in Fig. 2 based on probability dataset shown in Fig.3. Because the ultimate goal is to feed the information of safety for share autonomy, we have defined a trust ratio $n_s \in [0 - 1]$ (smaller better) as follows:

$$\lambda_s = k_p \frac{\|e_b\|}{e_m} + k_d \frac{\|\dot{e}_b\|}{\dot{e}_m} \quad (4)$$

where k_p and k_d are the constant gains and (e_m, \dot{e}_m) is the maximum error value for orientation and velocity.

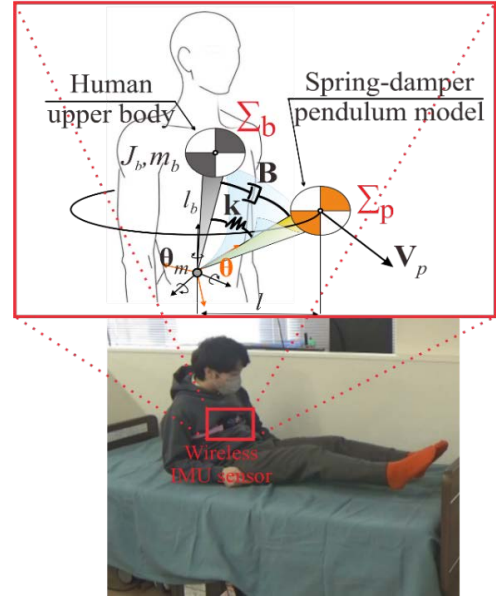


Fig. 2. Predictive safety model (PSM) using IMU on patient chest.

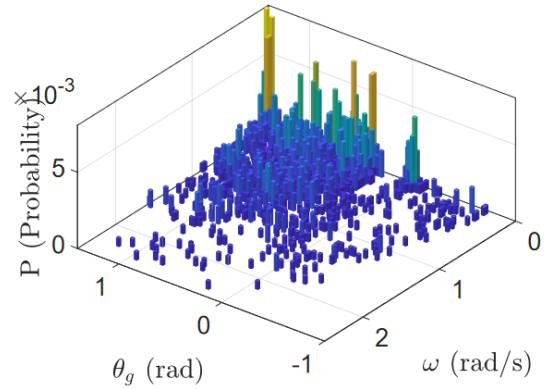
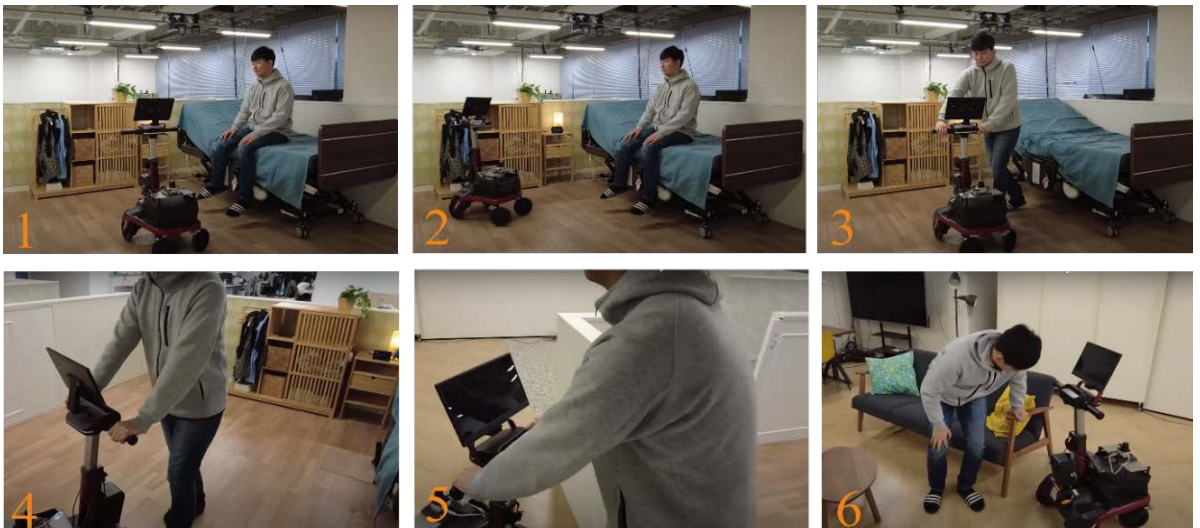


Fig. 3. Probability distribution for analyzing safety model of human upper body where θ_g and ω are the angular direction of gravity and norm of angular velocity [8].

Fig. 4 (below). Captured frames for the user that uses assistive walker with our proposed shared autonomy.



The motion planner that was targeted for this problem was considered is the time elastic band (TEB) planner. The motion planner not only gives the desired control inputs \mathbf{u}_p for reaching the robot based on local and global maps with avoiding obstacles in the scene but also feed the obstacle information (A_n, A_o) to calculate λ_o . The assistive controller that is utilized is from our previously proposed model [9] based on differential geometry where it takes the vehicle velocity and user inputs and tries to give a corrected smooth velocity inputs \mathbf{u}_a as follows:

$$\mathbf{u}_a(t) = \begin{bmatrix} u_{v,a} \\ u_{\omega,a} \end{bmatrix} = \delta \begin{bmatrix} 1 + R_v \gamma_s \\ \alpha_s \end{bmatrix} \quad (5)$$

where $[u_{v,a}, u_{\omega,a}]$ is the linear and angular velocity inputs and $\{\gamma_s, \alpha_s, \delta\}$ are the geometric functions [9] for creating the assistive input with respect to user inputs \mathbf{u} . However, we have here improved the controller by dynamically changing its values of trust τ_a with proportional to user disability and characteristics.

RESULTS AND DISCUSSION

To study the proposed shared autonomy behaviour, we have tested the concept at an example scenario.

Fig. 4 presents the results, the scenario at the Tohoku University Living lab. At first, the patient is standing up from the bed as the sensors are tracking the patient's safety level. Next, he requests to go out and a walker-supporting robot is sent. While the walker robot tries to navigate to the patient, using onboard sensors, it scans the environment for obstacles. After successfully stopping in the proper location, the user stands up and grabs the walker robot. Next, the assistive controller tries to react to the person's inputs from grippers by giving the assist through the motion planner. In this part, the shared autonomy policy gets more into the picture. Finally, the video shows how the user navigates safely to the desired location, and the person sits on the couch. This confirms that the strategy of shared autonomy works properly.

Although the strategy is promising, there are still open problems to research. For instance, if the user suddenly stops giving input, the shared autonomy policy might saturate and could not create a proper response based on the nature of equations (1)-(2). This confirms that the strategy has certain singular points and more careful design requires for real-world practical applications. Additionally, the delay in sensor communication and lack of high-level understanding of a person's intention requires further study; hence, the assistive robot can be more responsive with considering self-efficacy.

CONCLUSIONS

In this paper, we propose a new shared autonomy policy considering human safety. We confirmed our studies with a simple experiment scenario. Also, the potential open problems in this field are discussed.

Conflicts of interest

The authors declare no conflict of interest.

REFERENCES

- [1] N. Pedrocchi, F. Vicentini, M. Matteo, and L. M. Tosatti, 'Safe Human-Robot Cooperation in an Industrial Environment', *International Journal of Advanced Robotic Systems*, vol. 10, no. 1, p. 27, Jan. 2013. doi.org/10.5772/53939
- [2] A. Kanazawa, J. Kinugawa, and K. Kosuge, 'Adaptive Motion Planning for a Collaborative Robot Based on Prediction Uncertainty to Enhance Human Safety and Work Efficiency', *IEEE Transactions on Robotics*, vol. 35, no. 4, pp. 817–832, Aug. 2019. doi.org/10.1109/TRO.2019.2911800
- [3] L. Vianello, J.-B. Mouret, E. Dalin, A. Aubry, and S. Ivaldi, 'Human Posture Prediction During Physical Human-Robot Interaction', *IEEE Robotics and Automation Letters*, vol. 6, no. 3, pp. 6046–6053, Jul. 2021. doi.org/10.1109/LRA.2021.3086666
- [4] A. Shafti, A. Ataka, B. U. Lazpita, A. Shiva, H. A. Wurdemann, and K. Althoefer, 'Real-time Robot-assisted Ergonomics', in *2019 International Conference on Robotics and Automation (ICRA)*, May 2019, pp. 1975–1981. doi.org/10.1109/ICRA.2019.8793739
- [5] A. D. Dragan and S. S. Srinivasa, 'A policy-blending formalism for shared control', *The International Journal of Robotics Research*, vol. 32, no. 7, pp. 790–805, Jun. 2013. doi.org/10.1177/0278364913490324
- [6] S. Javdani, H. Admoni, S. Pellegrinelli, S. S. Srinivasa, and J. A. Bagnell, 'Shared autonomy via hindsight optimization for teleoperation and teaming', *The International Journal of Robotics Research*, vol. 37, no. 7, pp. 717–742, Jun. 2018. doi.org/10.1177/0278364918776060
- [7] A. A. Ravankar, S. A. Tafrishi, J. V. Salazar Lucas, F. Seto, and Y. Hirata, 'CARE: Cooperation of ai Robot Enablers to Create a Vibrant Society', *IEEE Robotics & Automation Magazine*, vol. 30, no. 1, pp. 8–23, Mar. 2023. doi.org/10.1109/MRA.2022.3223256
- [8] S. A. Tafrishi, A. A. Ravankar, and Y. Hirata, 'PSM: A Predictive Safety Model for Body Motion Based On the Spring-Damper Pendulum', in *2022 IEEE/RSJ International Conference on Intelligent Robots and Systems (IROS)*, Kyoto, Japan: IEEE, Oct. 2022, pp. 6657–6664. doi.org/10.1109/IROS47612.2022.9981274
- [9] S. A. Tafrishi, A. A. Ravankar, J. V. S. Lucas, and Y. Hirata, 'A Novel Assistive Controller Based on Differential Geometry for Users of the Differential-Drive Wheeled Mobile Robots', in *2022 International Conference on Robotics and Automation (ICRA)*, Philadelphia, PA, USA: IEEE, May 2022, pp. 5755–5761. doi.org/10.1109/ICRA46639.2022.9811593

Alamri NMH

*Cardiff University
School of Engineering*

Packianather MS

*Cardiff University
School of Engineering*

Bigot S

*Cardiff University
School of Engineering*

ADVANCED MANUFACTURING

A Novel Hybrid Bees Regression Convolutional Neural Network (BA-RCNN) Applied to Porosity Prediction in Selective Laser Melting Parts

Convolutional Neural Network (CNN) is a Deep Learning (DL) technique used for image analysis. CNN can be used in manufacturing, for predicting the percentage of porosity in the finished Selective Laser Melting (SLM) parts. This paper presents a new approach based on Regression Convolutional Neural Network (RCNN) for assessing the porosity which was better than the existing image binarization method. The algorithms were applied to artificial porosity images that were similar to the real images with a 0.9976 similarity index. The RCNN yielded a prediction accuracy of 75.50% compared to 68.60% for image binarization. After the RCNN parameters were optimized using the Bees Algorithm (BA), the application of the novel Bees Regression Convolutional Neural Network (BA-RCNN) improved the porosity prediction accuracy further to 85.33%. When three noise levels were used to examine its sensitivity to noise, the novel hybrid BA-RCNN was found to be less sensitive to noise.

Keywords:

Deep learning (DL), convolutional neural network (CNN), bees regression convolutional neural network (BA-RCNN), porosity prediction, selective laser melting (SLM).

Corresponding author:

AlamriNM@cardiff.ac.uk



N.M.H. Alamri, M.S. Packianather, and M.S. Bigot, 'A Novel Hybrid Bees Regression Convolutional Neural Network (BA-RCNN) Applied to Porosity Prediction in Selective Laser Melting Parts', *Cardiff University School of Engineering Research Conference 2023*, Cardiff, UK, 2023, pp. 95-99.

doi.org/10.18573/conf1.w

INTRODUCTION

Artificial Intelligence (AI) allows machines to perform tasks that require human intelligence [1]. Deep Learning (DL) is one of the most popular AI techniques that can model high-dimensional data and investigate complex patterns [2,3]. It has the advantage of automatic feature extraction which makes DL better than normal artificial neural networks [4]. One of the most popular DL algorithms is Convolutional Neural Network (CNN) which is used mainly for image analysis whether for classification or prediction [4]. CNN can be used in different contexts such as in the manufacturing field, particularly to predict the percentage of porosity in the parts manufactured by the Selective Laser Melting (SLM) process.

This paper presents a new approach based on the use of a Regression Convolutional Neural Network (RCNN) and Bees Regression Convolutional Neural Network (BA-RCNN) for assessing porosity better than the existing image binarization method. The drawback of the existing image binarization method is in determining the proper threshold to binarize the CT scan slices of the finished parts in order to highlight the porosity as a foreground. This method is sensitive to the noise created in the image background due to the mutual influence of CT setup and radiodensity variation [5]. If higher greyscale is selected, then the noise will be shown as foreground which overestimates the percentage of porosity. However, selecting low greyscale would lead to altering the morphological features which underestimates the percentage of porosity. So, it is difficult to compensate for these variations with a unique greyscale [5]. The authors in [5] estimated the porosity in the finished parts manufactured by the SLM process using a naturalized threshold in order to evaluate the greyscale issue. They found that the trend of the predicted percentage of porosity using image binarization is similar to the trend of the predicted values using the Archimedes method. They concluded that a naturalized greyscale method is not the best approach to assessing the porosity in the finished parts manufactured by the SLM process because it is sensitive to the noise created in the image background. Such limitation is present in one of the two main methods used for porosity assessment [6]. So, the contribution of the paper is proposing a new approach based on the CNN which is less sensitive to the noise created in the CT scan slices providing a more accurate prediction for the percentage of porosity in the finished SLM parts. The structure of the paper consists of the methods section describing the BA-RCNN algorithm used for porosity assessment, then the results and discussion section showing the results of applying the image binarization method, RCNN, and BA-RCNN algorithms to predict the percentage of porosity in the finished SLM parts and discussing the comparative results in terms of sensitivity toward the noise in the artificial porosity images. Finally, the conclusion section concludes the paper and recommends future work.

METHODS

This section shows the architecture of the hybrid BA-RCNN algorithm used to predict the percentage of porosity in the finished SLM parts without the difficult thresholding step used in the existing image binarization method. The CNN architecture starts with an input layer which is a matrix of pixel brightness values with a size based on the height, width, and number of channels of the images. Then, the feature learning layers come with five convolutional layers that allow for learning the image features using the convolutional filters which are matrices of weights

multiplied by the input matrix yielding the feature map matrix [7], the convolutional layers are followed by rectified linear unit layers to increase the training speed [8] and batch normalization layers to mitigate the overfitting issue [9] with four average pooling layers in between to reduce the output dimensions which minimizes the computational cost [10], the average pooling type is selected because the image background is lighter than the foreground [11]. Finally, the fully connected layer and regression layer are used for the prediction task providing the predicted values, so the total number of layers is 22 layers.

Stochastic Gradient Descent with Momentum (SGDM) is used to train the BA-RCNN algorithm [9] along with the Bees Algorithm (BA) which is used to optimize the CNN four parameters namely Section Depth (SD) that controls the network depth, the Initial Learning Rate (ILR) that allows for features learning, the Momentum (M) that updates the parameters, and the Regularization (R) that prevents overfitting [12]. The advantage of using BA is in the global, local, and intense searches applied in the algorithm to find the optimal solutions [13,14]. The values for the BA parameters are selected based on computer capability and equations shown in [15] as shown in the following Table 1:

Parameter	Equation	Value
Iteration	-	1
Scout Bees	-	4
Selected Bees	$0.5 * \text{Scout Bees}$	2
Elite Sites	-	1
Bess for Elite Sites	$2 * \text{Selected Bees}$	4
Bees for Other Sites	$0.5 * \text{Scout Bees}$	2
	$0.1 * (\text{Max} - \text{Min})$	
	$SD = 0.1 * (3 - 1)$	0.2
Neighbourhood Size	$ILR = 0.1 * (1 - 1e-2)$	0.099
	$M = 0.1 * (0.98 - 0.8)$	0.018
	$R = 0.1 * (1e-2 - 1e-10)$	0.001

Table 1. BA Parameters Values.

Figure 1 shows the steps for the novel BA-RCNN:

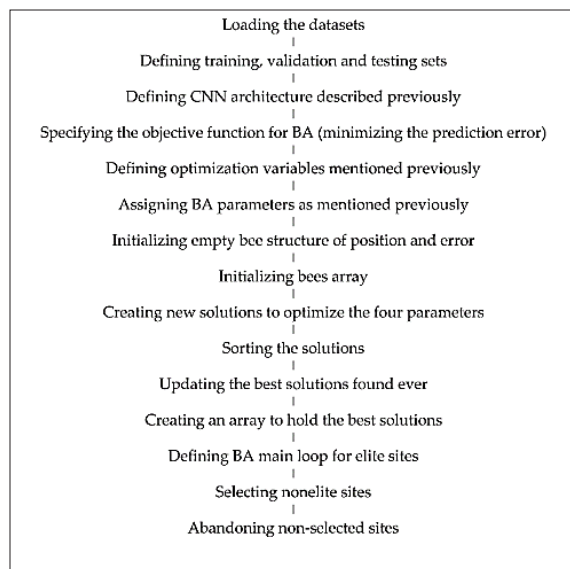


Fig. 1. The steps for the BA-RCNN [16].

Testing the BA-RCNN algorithm requires a large amount of experimental data which is not cost-effective, so the 3000 artificial porosity images created in [16] are used to predict the percentage of porosity. Different pores numbers and pores diameters were generated based on laser power and scanning speed and then the pores were positioned in 30 cubes, the images were created by slicing the 30 cubes into 100 slices each resulting in 3000 slices of pores mimicking the CT scans of the finished SLM parts with a similarity index of 0.9976. The artificial porosity images were overlaid with the noisy background of real images. So, the noise is determined based on the degree of overlaying which is a factor with a value between 0 and 1 [17]. Thus, with a factor of 1, the pore image is shown without noisy background and with a factor of 0, the noisy background is shown without pores. A factor of 0.125 was selected in [16] to visually be the best value that combined both pore and noisy background. In order to test the sensitivity toward the noise, two more factors are arbitrarily selected which are 0.2 and 0.25 resulting in more noisy images.

The following figure 2 shows an illustrative example of the noisy slices highlighting the pores within the circles along with the binarized image:

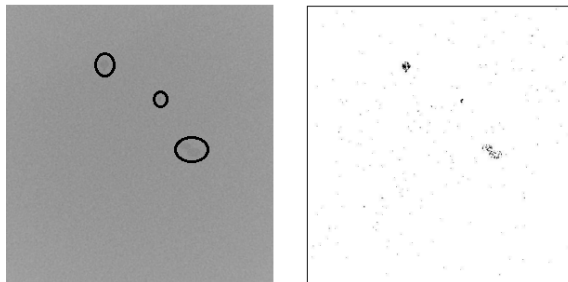


Fig. 2. The Artificial Image with Noise of 0.2 (Left - Pores are Inside the Rings) Vs The Binarized Artificial Image (Right - Pores are Visible).

The MATLAB platform is used to design the CNN architecture and apply BA to optimize its parameters. A single GBU with 256 GB is used to analyse 3000 images with a size of $(650 * 630 * 3)$. The images are shuffled at every epoch of the 20 epochs [18] and the training, validation and testing sets are selected randomly after each shuffle in order to minimize the data biases and improve the validity of the experiments [19]. The 3000 slices are divided into 1800 images used for training, 600 images for validation, and the same for the testing set.

RESULTS AND DISCUSSION

This section shows the results of applying the image binarization method, RCNN, and BA-RCNN algorithms to predict the percentage of porosity in the finished SLM parts. The following table 2 shows the prediction accuracy for the three methods with a 0.125 level of noise [16] and within the acceptable threshold of 0.02:

Method	Prediction Accuracy
Image Binarization	68.60%
RCNN	75.50%
BA-RCNN	85.33%

Table 2. Porosity Prediction Accuracy.

Applying the RCNN on 3000 slices of the artificial porosity images, improved porosity prediction accuracy from 68.60% for the image binarization method to 75.50% for the RCNN, while integrating BA produced the best prediction accuracy with a value of 85.33% which is approximately 17% better than existing image binarization method.

Applying the image binarization method to 3000 slices with three different levels of noise (0.125, 0.2 and 0.25) results in the following table 3 which shows the prediction accuracy for the percentage of porosity:

Level of Noise	Prediction Accuracy
0.125	68.60%
0.2	40.73%
0.25	26.60%

Table 3. Porosity Prediction Accuracy using Image Binarization Method with Different Levels of Noise.

Similarly, the hybrid BA-RCNN algorithm is applied to artificial porosity images with the same three levels of noise. The following table 4 shows the testing accuracy for predicting the percentage of porosity:

Level of Noise	Prediction Accuracy
0.125	85.33%
0.2	79.21%
0.25	77.33%

Table 4. Porosity Prediction Accuracy using BA-RCNN algorithm with Different Levels of Noise.

To clearly investigate the variations in the prediction accuracy, the following figure 3 is created which presents the accuracies at different levels of noise:

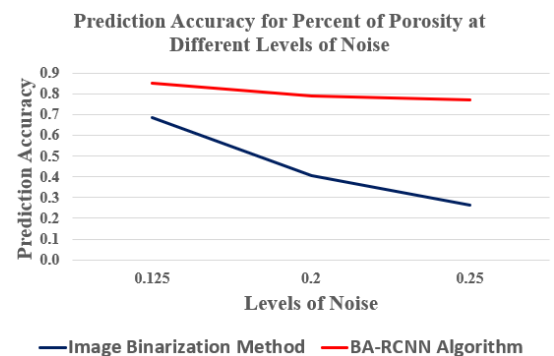


Fig. 3. Porosity Prediction Accuracy with Different Levels of Noise.

As can be seen from the figure, the difference between the minimum and maximum accuracy in the BA-RCNN algorithm is less than the range of accuracies in the image binarization method, so it is concluded that the BA-RCNN algorithm is less sensitive to noise. The convolutional filters in CNN that slide along the pixel brightness input matrix can deal with the level of noise in the artificial porosity images so that the creation of the feature map matrix is not affected [7]. On the other hand, the image binarization method is affected by the level of noise as increasing the sensitivity factors [20] to binarize the images reduces the black spots resulting from the noisy background, but it alters the pores' morphological

feature dramatically resulting in underestimating the percentage of porosity. If the sensitivity factor is decreased, the black spots appear more in the binarized images which overestimate the percentage of porosity. So, these thresholds would result in significantly different predictions of porosity levels.

CONCLUSIONS

In this paper, a novel hybrid Bees Regression Convolutional Neural Network (BA-RCNN) applied to porosity percentage prediction in SLM parts has been presented. Applying the RCNN algorithm yielded a prediction accuracy of 75.50% compared to 68.60% for the image binarization method. After the RCNN parameters were optimized using the BA, the application of the novel BA-RCNN has been found to improve the prediction accuracy further to 85.33%. Three different noise levels were used to examine its sensitivity to noise, and the results showed that the novel BA-RCNN to be less sensitive to noise compared to the image binarization method. Future work will consider applying the novel BA-RCNN to real porosity images.

Acknowledgments

Our thanks are due to Cardiff University and the Saudi Arabian Cultural Bureau for their support, and the H2020 project partners of Additive Manufacturing using Metal Pilot Line (MANUELA) project (grant agreement No. 820774) for their collaboration.

Conflicts of interest

The authors declare no conflict of interest.

REFERENCES

- [1] B. Li, B. Hou, W. Yu, X. Lu, and C. Yang, 'Applications of artificial intelligence in intelligent manufacturing: a review', *Frontiers of Information Technology & Electronic Engineering*, vol. 18, no. 1, pp. 86–96, Jan. 2017. doi.org/10.1631/FITEE.1601885
- [2] L. A. C. D. Filippis, L. M. Serio, and F. Facchini, and G. Mummolo, 'ANN Modelling to Optimize Manufacturing Process', in *Advanced Applications for Artificial Neural Networks*, IntechOpen, 2017. doi.org/10.5772/intechopen.71237
- [3] T. Wuest, D. Weimer, C. Irgens, and K.-D. Thoben, 'Machine learning in manufacturing: advantages, challenges, and applications', *Production & Manufacturing Research*, vol. 4, no. 1, pp. 23–45, Jan. 2016. doi.org/10.1080/21693277.2016.1192517
- [4] A. K. Singh, B. Ganapathysubramanian, S. Sarkar, and A. Singh, 'Deep Learning for Plant Stress Phenotyping: Trends and Future Perspectives', *Trends in Plant Science*, vol. 23, no. 10, pp. 883–898, Oct. 2018. doi.org/10.1016/j.tplants.2018.07.004
- [5] H. Gong, V. K. Nadimpalli, K. Rafi, T. Starr, and B. Stucker, 'Micro-CT Evaluation of Defects in Ti-6Al-4V Parts Fabricated by Metal Additive Manufacturing', *Technologies*, vol. 7, no. 2, p. 44, Jun. 2019. doi.org/10.3390/technologies7020044
- [6] C. Arvieu, C. Galy, E. Le Guen, and E. Lacoste, 'Relative Density of SLM-Produced Aluminum Alloy Parts: Interpretation of Results', *Journal of Manufacturing and Materials Processing*, vol. 4, no. 3, p. 83, Aug. 2020. doi.org/10.3390/jmmp4030083
- [7] J. Hui, *Convolutional neural networks (CNN) tutorial, 2017* [online]. Available at <https://jhui.github.io/2017/03/16/CNN-Convolutional-neural-network> [Accessed: 15 November 2021].
- [8] (MathWorks-1), *Convolutional Neural Network* [Online]. Available at <https://uk.mathworks.com/solutions/deep-learning/convolutional-neural-network.html> [Accessed: 7 October 2019].
- [9] R. Yamashita, M. Nishio, R. K. G. Do, and K. Togashi, 'Convolutional neural networks: an overview and application in radiology', *Insights Imaging*, vol. 9, no. 4, pp. 611–629, Aug. 2018. doi.org/10.1007/s13244-018-0639-9
- [10] J. McDermott, *Convolutional Neural Networks – Image Classification w. Keras* [online], 2021. Available at <https://www.larndatasci.com/tutorials/convolutionalneural-networks-image-classification> [Accessed: 15 November 2021].
- [11] H. Ouf, *Maxpooling vs minpooling vs average pooling* [online], 2017. Available at <https://hany-ouf.blogspot.com/2020/08/maxpooling-vs-minpooling-vs-average.html> [Accessed: 15 November 2021].

A Novel Hybrid Bees Regression Convolutional Neural Network (BA-RCNN) Applied to Porosity Prediction in Selective Laser Melting Parts

- [12] (MathWorks-2), *Deep Learning Using Bayesian Optimization* [online]. Available at <https://www.mathworks.com/help/deeplearning/ug/deep-learning-usingbayesian-optimization.html> [Accessed: 4 April 2020].
- [13] A. Al-Musawi, *The development of new artificial intelligence based hybrid techniques combining bees algorithm, data mining and genetic algorithm for detection, classification and prediction of faults in induction motors*, doctoral dissertation, Cardiff University, 2019.
- [14] Ebubekir, *The Bees Algorithm Theory, Improvements and Applications*, Manufacturing Engineering Centre, University of Wales, Cardiff, United Kingdom, 2010.
- [15] (MathWorks-3), *Bees Algorithm (BeA) in MATLAB* [online]. Available at <https://uk.mathworks.com/matlabcentral/fileexchange/52967-bees-algorithm-bea-in-matlab> [Accessed: 9 April 2020].
- [16] N. M. H. Alamri, M. Packianather, and S. Bigot, 'Predicting the Porosity in Selective Laser Melting Parts Using Hybrid Regression Convolutional Neural Network', *Applied Sciences*, vol. 12, no. 24, p. 12571, Jan. 2022.
doi.org/10.3390/app122412571
- [17] (MathWorks-4), *Overlay image on top of image* [online]. Available at <https://www.mathworks.com/matlabcentral/answers/414351-overlay-image-ontop-of-image> [Accessed: 4 October 2022].
- [18] (MathWorks-5), *TrainingOptionsSGDM* [online]. Available at <https://uk.mathworks.com/help/deeplearning/ref/nnet.cnn.trainingoptionssgdm.html> [Accessed: 15 November 2021].
- [19] S. Joshi, D. K. Verma, G. Saxena, and A. Paraye, 'Issues in Training a Convolutional Neural Network Model for Image Classification', in *Advances in Computing and Data Sciences*, M. Singh, P. K. Gupta, V. Tyagi, J. Flusser, T. Ören, and R. Kashyap, Eds., in Communications in Computer and Information Science. Singapore: Springer, 2019, pp. 282–293.
doi.org/10.1007/978-981-13-9942-8_27
- [20] (MathWorks-6), *adaptthresh* [online]. Available at <https://uk.mathworks.com/help/images/ref/adaptthresh.html>. [Accessed: 2 September 2022].

Qi P

Cardiff University
School of Engineering

Zhu H

Cardiff University
School of Engineering

ADVANCED MANUFACTURING

The Research on Mechanical Properties and Compressive Behavior of Graphene Foam with Multi-scale Model

Computational simulation is an effective method to study the deformation mechanism and mechanical behaviour of graphene-based porous materials. However, due to limitations in computational methods and costs, existing research model deviate significantly from the real material in terms of the scale of structure. Therefore, building a highly accurate computational model and maintaining an appropriate cost is both necessary and challenging. This paper proposed a multi-scale modelling approach for finite element (FE) analysis based on the concept of structural hierarchy. The stochastic feature of the microstructure of porous materials are also considered. The simulation results of the regular structure model and the Voronoi tessellation model are compared to investigate the effect of regularity on the material properties. Despite some shortcomings, other microstructural features of porous graphene materials can be gradually introduced to improve the material model step by step. Thus the developed multiscale model has great potential to simulate the properties of materials with mesoscopic size structure such as graphene foam (GF).

Keywords:

Computational simulation, graphene-based, porous materials, multi-scale, finite element.

Corresponding author:

QiP@cardiff.ac.uk



P. Qi and H. Zhu, 'The Research on Mechanical Properties and Compressive Behavior of Graphene Foam with Multi-scale Model', *Cardiff University School of Engineering Research Conference 2023*, Cardiff, UK, 2023, pp. 100-104.

doi.org/10.18573/conf1.x

INTRODUCTION

Graphene foam (GF) is a promising multifunctional material for military, energy, and aerospace industry. The materials have excellent mechanical, thermal, and electrical properties due to the combination of the two-dimensional characteristics of graphene with the three-dimensional (3D) structural features of porous materials. However, the conflicting demands of different properties on structural parameters, such as varying requirements of mechanical and electrical properties for material density, result in multifunctional applications of GF remaining a challenge. In the past few years, several molecular dynamics (MD) models have been developed to investigate the relationship between the meso-structural characteristics of graphene porous materials and their mechanical properties.

Qin et al. [1] constructed an all-atom molecular dynamics (AAMD) GF model by mimicking the process of GF synthesis by CVD. Based on the model, they calculated the basic mechanical properties of GF, such as young's modulus, buckling modulus, tensile strength, and compressive strength, under different density. To explore relationship between the density and tensile response of GF, Patil et al. [2] investigated the deformation behaviour of GF under uniaxial tension by using a MD model. They proposed a power law dependence on the density for the tensile strength of this material. To expand the simulation domain of the MD method, the coarse-grained molecular dynamics (CGMD) method has also been developed by some scientists. Wang et al. [3] developed a CGMD model based on the CG model of graphene in the work of Cranford and Buehler [4]. Using their MD model, Wang's team studied the elastic deformation behaviour of GF by observing the evolution of microstructure of the material under uniaxial compression. In another two works, they also discussed the energy dissipative mechanism [5] and the characteristics of high elasticity of GF [6]. Their works are useful for understanding GF elasticity behaviour.

Similarly, Pan et al. [7] used the CGMD model to analyse the compression and recovery behaviour of GF with hole wall under large strain. The mesoscopic evolution of structure and the deformation trends of the graphene walls in GF were also studied. They revealed that the multilevel residual deformation is distributed to the mechanical interlocking behaviour among the hole-flakes. It should be noted, however, that due to the modelling mechanism and approach of MD models, even the CGMD models differ in scale from the real GF material by two to four orders of magnitude. Hence, the simulation results do not match the real material properties, which makes it difficult to provide effective guidance for the study of macroscopic materials properties.

The mechanical properties of graphene foams (GF) are intricately linked to both the microstructure and the macrostructural design of the material. On a microscopic scale, GF exhibits a multitude of irregular unit cells, and the non-uniformity in their structure significantly impacts the material's properties. However, it's worth noting that the individual unit cells tend to have nearly tetrahedral shapes, and the size distribution of these cells remains relatively constrained. Consequently, the morphological disparities and microstructural heterogeneity among GF cells exert only a minimal influence on the material's macroscopic behaviour. Building upon insights and research from prior studies, this paper introduces a cell model that closely mimics the microstructure of GF. This model is constructed and simulated using the finite element method. Furthermore, by applying periodic boundary conditions,

the cell model is scaled up to represent a structure with macroscopic dimensions. This approach allows for the modelling and analysis of GF's multi-scale structure. The impact of cell regularity is also investigated using various cell models. Through these models, it becomes possible to effectively predict and calculate the properties of macroscopic-scale materials structured in the manner of graphene foam. This research facilitates a deeper understanding of the mechanical behaviour of GF and contributes to the ability to make accurate predictions and assessments of graphene foam-structured materials on a macroscopic level.

METHODOLOGY

The key aspect of this study is the modelling of the geometrical features (GF), with a particular focus on the cell model. In this paper, the Kelvin cell structure, which is the most used regular cell structure in porous modelling, is introduced to create a fully regular finite element model. The Kelvin cell structure, recognized for its typical Body-Centred Cubic (BCC) configuration, is composed of a four-open decahedron consisting of eight hexagonal and six square faces.

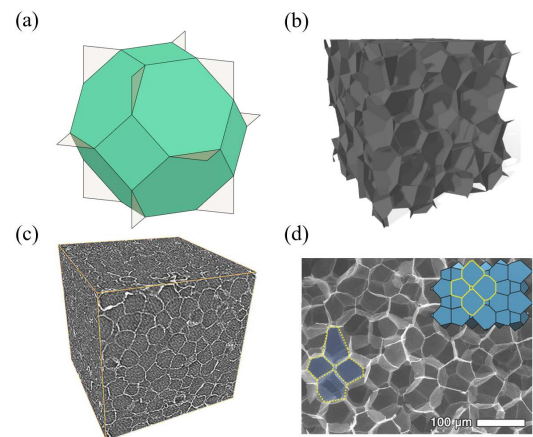


Fig. 1. (a) The schematic of Voronoi foam model and (b) inclusion packaging code; (c) 3D reconstructed X-ray microtomography image; (d) SEM image of GF [8].

Additionally, 12 triangular plates are included in the model to create a cell model with a periodic boundary structure. This structure is widely adopted as a simplified regular structure for foams due to its excellent resemblance to actual foam shapes.

Periodic boundary conditions are imposed on the unitary model according to the methodology given in a previous paper [9]. Here, the relative density is used as a parameter to calculate the elastic properties of the models with different structural dimensions. The relative density ρ can be obtained according to the following equation:

$$\rho = 1.185 \frac{t}{L} - 0.4622 \left(\frac{t}{L} \right)^2 \quad (1)$$

Where t is the thickness of wall of model, L is the edge length of Kelvin model.

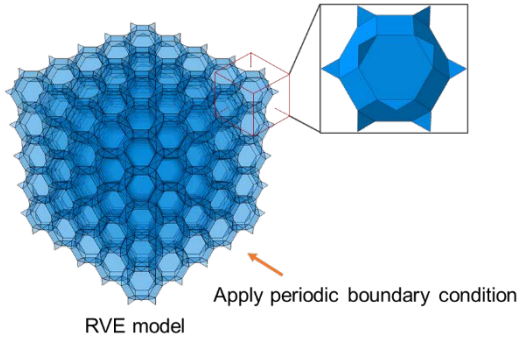


Fig.2. The schematic of GF multiscale model.

Furthermore, the study explores the possibility of constructing an irregular 3D foam structure model based on the Voronoi tessellation algorithm. This algorithm divides the simulation domain around each randomly generated seed into regions closest to the respective seed. The model generated through this algorithm is more in line with the way real foams naturally form and exhibits a desirable level of randomness. To construct the irregular cell model using the Voronoi tessellation algorithm, a minimum allowable distance denoted as δ is introduced to regulate the separation between the points used as seeds for the tessellation process. The value of δ can be employed to control the extent of irregularity in the resulting foam structure. For the creation of a regular lattice containing n identical tetrakaidehedral cells within the volume V_0 a minimum distance denoted as a_0 between any two adjacent points is determined using equation below [10]:

$$d_0 = \frac{\sqrt{6}}{2} \left(\frac{V_0}{n\sqrt{2}} \right)^{1/3} \quad (2)$$

This minimum distance calculation likely ensures that the tessellation process yields a structured and consistent irregular foam model. To obtain n cells by tessellating a space of volume V_0 with Voronoi tessellation, the maximum δ should be less than a_0 ; otherwise, it will result in a lack of cells. In this cubic RVE case, to construct a random Voronoi tessellation with n cells in an $L \times L \times L$ cubic RVE space, the maximum δ should be:

$$\delta_{max} = \frac{\sqrt{6}}{2} \frac{L}{2^{1/6} n^{1/3}} \quad (3)$$

When δ is equal to 1, the three-dimensional Voronoi lattice is completely regular and is a cubic lattice with closed-hole Kelvin cells. Here four unitary models with different degrees of regularity (0.2,0.4,0.6,0.8) are constructed to compare with the fully regular model.

Based on these cell models, representative volume element (RVE) models with different microstructures are constructed. Simulation analysis of the macroscopic model of the GF can be achieved by imposing periodic boundary conditions on the RVE model. The focus here is to calculate the elastic properties of the GF multiscale model through six loading cases (three pure shear cases and three uniaxial compression cases), as shown in Fig 3.

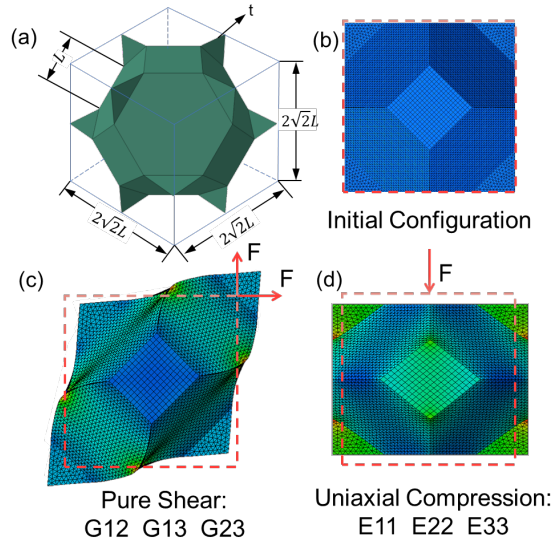


Fig. 3. The schematic of configuration and load case of GF model.

RESULTS AND DISCUSSION

As the BCC cell model is symmetrical about three orthogonal planes, material properties based on this model can be obtained directly from the simulation results of the individual cell model.

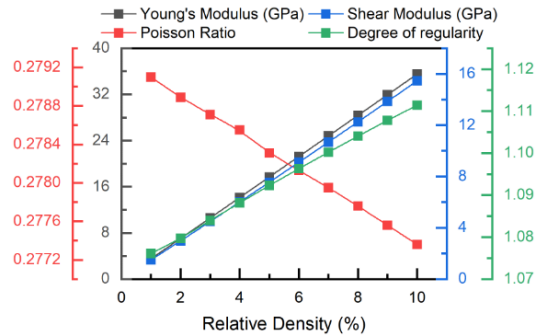


Fig. 4. Elastic properties of GF model with different relative densities.

In ABAQUS, the elastic parameters of the perfect RVE model are calculated under 6 loading conditions (3 uniaxial compression and 3 pure shear conditions). The elastic properties of GA are calculated to be approximately linearly related to the relative density of the material. The fitting polynomial functions of the elastic properties are shown as below :

$$\frac{E_{GA}}{E_g} = 0.3435 \left(\frac{\rho_{GA}}{\rho_g} \right) + 0.1803 \left(\frac{\rho_{GA}}{\rho_g} \right)^2 \quad (4)$$

$$\frac{G_{GA}}{G_g} = 0.1438 \left(\frac{\rho_{GA}}{\rho_g} \right) + 0.1308 \left(\frac{\rho_{GA}}{\rho_g} \right)^2 \quad (5)$$

$E_{GA}, \rho_{GA}, G_{GA}(E_g, \rho_g, G_g)$ is elastic modulus, density, and shear modulus of GF (graphene materials), respectively.

For irregular models, models with different degrees of regularity were constructed as shown in the following Fig 5.

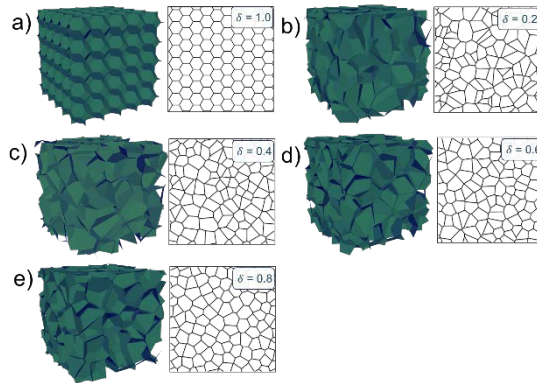


Fig. 5. RVE GF model with different regularity δ . a) $\delta=1$; b) $\delta=0.2$; c) $\delta=0.4$; d) $\delta=0.6$; e) $\delta=0.8$.

The properties of the GF models with respect to the degree of regularity are shown in Fig 6. It can be seen that, the kelvin cell model, on the other hand, has an overall higher performance than the irregular model due to the regular symmetry of the structure. Whereas, influenced by the degree of irregularity, there is some fluctuation in the material properties of the irregular model when evaluating the calculated properties, but the deviation is generally around 5%.

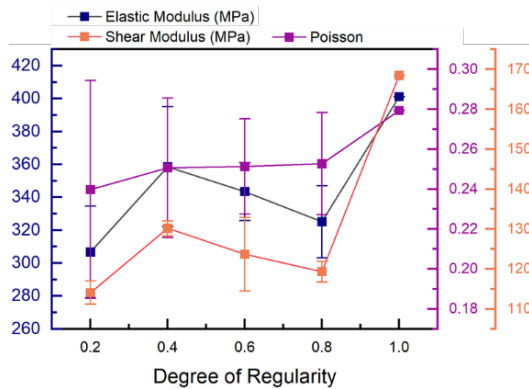


Fig. 6. Comparison of elastic properties of GFs with different regularities.

Here, the degree of anisotropy of different model with various regularity are discussed as shown in Fig 7. The degree of anisotropy (DOA) is obtained by the following formula [11].

$$DOA = \frac{2 * (S_{11} - S_{12})}{S_{44}} = \frac{2 * (1 + \nu) * G}{E} \quad (6)$$

Where S_{ij} is elastic constants; E is elastic modulus; ν is the Poisson ratio; G is the shear modulus.

The degree of anisotropy will be higher than several other irregularity models when a regularity model close to 0.6 is used.

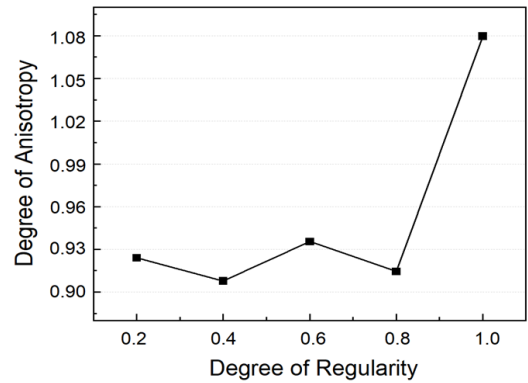


Fig. 7. Degree of anisotropy of GFs with different regularities.

CONCLUSION

This modelling approach allows the deformation of the RVE model to be used to analyse the influence of the microstructure on the material properties, while the periodic boundary method is used to predict the mechanical properties of the calculated macro size material. The construction of a suitable cell model is therefore the key to this approach. There are some differences between the BCC model and the real material structure, but these differences are reduced when the number of RVE cells in the macroscopic model of the material is sufficiently large. When the size of the macroscopic model is large enough, the effect of inhomogeneities in the microstructure of the material on the mechanical properties of the material is greatly diminished. However, this model can overestimate the mechanical properties of the material due to the relatively perfect structure. The anisotropic graphene foam model based on Voronoi lattice is closer to the real microstructure in terms of topology (distribution of faces, edges, and vertices). However, considering the actual computational workload, the prediction accuracy of the model constructed by this algorithm is not significantly better than that of the model constructed by BCC.

Both cell structure modelling methods still have a great potential for development, such as introducing defects and inhomogeneous material distribution present in real materials to bring the RVE model closer to the microstructure of the material. In addition, as the main constituent material of the material wall, the graphene sheet is also affected by the thickness and inhomogeneity of the material, etc., and its elastic property parameters need to be further considered.

Acknowledgments

The authors are grateful for the research support received from Chinese Scholarship Council No. 202106280043 and the financial support from Cardiff University.

Conflicts of interest

The authors declare no conflict of interest.

REFERENCES

- [1] Z. Qin, G. S. Jung, M. J. Kang, and M. J. Buehler, 'The mechanics and design of a lightweight three-dimensional graphene assembly', *Sci Adv*, vol. 3, no. 1, p. e1601536, Jan. 2017.
doi.org/10.1126/sciadv.1601536
- [2] S. P. Patil, P. Shendye, and B. Markert, 'Molecular Investigation of Mechanical Properties and Fracture Behavior of Graphene Aerogel', *J Phys Chem B*, vol. 124, no. 28, pp. 6132–6139, Jul. 2020.
doi.org/10.1021/acs.jpcc.0c03977
- [3] C. Wang, C. Zhang, and S. Chen, 'The microscopic deformation mechanism of 3D graphene foam materials under uniaxial compression', *Carbon*, vol. 109, pp. 666–672, Nov. 2016.
doi.org/10.1016/j.carbon.2016.08.084
- [4] S. Cranford and M. J. Buehler, 'Twisted and coiled ultralong multilayer graphene ribbons', *Modelling Simul Mater Sci Eng*, vol. 19, no. 5, p. 054003, Jul. 2011.
doi.org/10.1088/0965-0393/19/5/054003
- [5] C. Wang, D. Pan, and S. Chen, 'Energy dissipative mechanism of graphene foam materials', *Carbon*, vol. 132, pp. 641–650, Jun. 2018.
doi.org/10.1016/j.carbon.2018.02.085
- [6] C. Wang, C. Zhang, and S. Chen, 'Micro-Mechanism and Influencing Factors of Graphene Foam Elasticity' *Carbon*, vol. 148, pp. 267–276, 2019.
doi.org/10.1016/j.carbon.2018.02.085
- [7] D. Pan, C. Wang, and X. Wang, 'Graphene Foam: Hole-Flake Network for Uniaxial Supercompression and Recovery Behavior', *ACS Nano*, vol. 12, no. 11, pp. 11491–11502, Nov. 2018.
doi.org/10.1021/acsnano.8b06558
- [8] S. J. Yeo *et al.*, 'A Plesiohedral Cellular Network of Graphene Bubbles for Ultralight, Strong, and Superelastic Materials', *Advanced Materials*, vol. 30, no. 45, p. 1802997, Nov. 2018.
doi.org/10.1002/adma.201802997
- [9] S. L. Omairey, P. D. Dunning, and S. Sriramula, 'Development of an ABAQUS plugin tool for periodic RVE homogenisation', *Engineering with Computers*, vol. 35, no. 2, pp. 567–577, Apr. 2019.
doi.org/10.1007/s00366-018-0616-4
- [10] H. X. Zhu, J. F. Knott, and N. J. Mills, 'Analysis of the elastic properties of open-cell foams with tetrakaidecahedral cells', *Journal of the Mechanics and Physics of Solids*, vol. 45, no. 3, pp. 319–343, Mar. 1997.
[doi.org/10.1016/S0022-5096\(96\)00090-7](https://doi.org/10.1016/S0022-5096(96)00090-7)
- [11] H. X. Zhu and A. H. Windle, 'Effects of cell irregularity on the high strain compression of open-cell foams', *Acta Materialia*, vol. 50, no. 5, pp. 1041–1052, Mar. 2002.
[doi.org/10.1016/S1359-6454\(01\)00402-5](https://doi.org/10.1016/S1359-6454(01)00402-5)

Eaton M

*Cardiff University
School of Engineering*

Maillard JY

*Cardiff University
School of Engineering*

Ward B

*Cardiff University
School of Computer Science and Informatics*

Zare S

*Cardiff University
School of Engineering*

ADVANCED MANUFACTURING

Developing Antibacterial Nanocomposites

After the pandemic, we became more aware of microorganisms around us and realized how these creatures could affect our health and environment. In this regard, this project was planned to prepare polymer-based nanocomposites with antibacterial properties. This study selected a cationic polymer, poly (diallyl dimethylammonium) chloride (PDDA), along with graphene oxide reinforcement to achieve this goal. The mechanical and thermal properties of PDDA, GO, and the prepared PDDA-GO nanocomposite will be characterized by dynamic mechanical analysis (DMA) and differential scanning calorimetry (DSC). A high glass transition (T_g) (around 250°C) has been identified with DSC and DMA for the PDDA. The minimum inhibitory concentration (MIC) technique was used to study their antimicrobial activities against *Staphylococcus aureus* and *Escherichia coli*. The early results for the PDDA were shown to be moderately effective against *E. coli* and *S. aureus*, with values of 64 and 16 µg/mL, respectively.

Keywords:
Nanocomposites, PDDA, antibacterial, graphene oxide, cationic polymer.

Corresponding author:
EatonM@cardiff.ac.uk



M. Eaton, J.Y. Maillard, B. Ward, and Z. Zare, 'Developing Antibacterial Nanocomposites', *Cardiff University School of Engineering Research Conference 2023*, Cardiff, UK, 2023, pp. 105-108.

doi.org/10.18573/conf1.y

INTRODUCTION

Over the past decades, nanomaterials and polymer nanocomposites have gained massive engagement in various fields; For instance, biomedical applications [1], sensors and biosensors [2], and tissue and scaffold engineering [3]. Materials at the nanometre scale permit the designing and generating of new products with outstanding performance and enhanced characteristics [4].

Nanocomposites have a solid structure in which the distance between the phases includes at least a dimension with nanoscale size [5]. Composites generally have two “matrix” and “reinforcement” phases. There are three prevalent matrices, polymer, metal, and ceramic, with reinforcement in various forms such as lamina, fillers, fibre (short and continuous), flake, and particles.

Herein, we aim to prepare polymer-based with reinforcing graphene oxide nanocomposites with potential antimicrobial properties. Polymers as nanocomposite matrices can have almost the same mechanical and thermal properties as metal and ceramics matrices with easier and more affordable processing [6].

With the development of nanotechnology, novel nanomaterials have been proposed with considerable antimicrobial activity, especially in the nanocomposite forms [7]. Nanomaterials like graphene and its derivatives, oxide nanoparticles, carbon nanotubes, etc., have been used as fillers in nanocomposites with incredible outcomes [8].

Among them, graphene oxide (GO), Due to the presence of these functional groups such as epoxy, carbonyl and hydroxyl functional groups, is the most accustomed one and can be dispersed in water, which caused it to be favoured for biomedical applications [9].

Moreover, graphene oxide, has been successfully used as a reinforcement for polymers owing to its outstanding thermal, mechanical, and electrical properties. The exfoliation and good dispersion of GO, along with a strong interface interaction between GO and polymer, are crucial to observe such property enhancements [10].

Furthermore, graphene oxide, due to its outstanding thermal, mechanical and electrical properties, has been successfully used as a reinforcement for polymers. The deep interface interaction between GO and polymer, along with its exfoliation and good dispersion, are crucial to observe such property enhancements.

Moreover, owing to the exfoliation and good dispersion of GO, along with a strong interface interaction between GO and polymer, it has been successfully used as a reinforcement for polymer nanocomposites, along with outstanding thermal, mechanical, and electrical properties.

Numerous studies have been conducted on the potential antimicrobial activity of GO. The antibacterial property has been associated with the physical damage to cell membranes due to membrane stress which has been caused by sharp edges of the GO, Which results in leakage of RNA from bacteria membrane; Additionally, the oxidative stress has been identified as the most widely accepted mechanism via either a ROS-dependent or a ROS-independent pathway, which can interfere with bacterial metabolism and disrupt crucial cellular functions, eventually leading to inactivation or even cell death [11]. It was suggested that graphene may induce oxidative stress on neural pheochromocytoma-

derived PC12 cells [12]. Several research has been conducted on this antibacterial activity of GO, and inconclusive results have been reported. A recent report has shown that contact of *E. coli* and *Staphylococcus aureus* bacterial cells with GO can result in growth reductions of about 51 and 61%, respectively [13].

Given the above, the initial objective of the presented work was to identify a suitable polymer with antimicrobial properties. One of the most promising candidates is polycationic family of polymers, this is due to their mass and charge localization that promotes electrostatic interaction between the cationic structure and the negatively charged bacterial cell membrane, causing disruption of the cell membrane and/or wall, and reaction with the cytoplasmic membrane (lipid or protein) followed by membrane disorganization [14]. Amongst polycationic polymers, quaternary ammonium compounds (QACs) are the most valuable antiseptics and disinfectants. Furthermore, they are environment friendly which favours their usage [15]. Between all available QACs, poly (diallyl dimethylammonium) chloride (PDDA) was chosen in this study as it displayed an outstanding antimicrobial activity [16].

MATERIALS AND METHODS

Materials

PDDA (20% water solution, average $M_w = 100,000 - 200,000$) was purchased from Sigma Aldrich. Graphene oxide (1% aqueous dispersion, 1L) was acquired from GOgraphene and used as received. Distilled water (DI) was used in all the fabrication process, including solutions preparation and washing.

Preparation of PDDA-graphene oxide nanocomposite.

Graphene oxide sheets were functionalized with PDDA by non-covalent bonding by adding suitable amounts of 1 wt% GO to 20 wt% PDDA aqueous solutions and sonicated for half an hour.

Antibacterial Activity

In order to study the antimicrobial properties of the antimicrobial agents (PDDA and GO) and the prepared nanocomposite, the minimum inhibitory concentration (MIC) method was used. Two strains including Gram-negative *E. coli* ATCC 25922 and Gram-positive *S. aureus* ATCC 6538 were selected for antibacterial tests because they are usually associated with the medical-associated infections. The target *E. coli* and *S. aureus* cultures were grown overnight in a Luria-Bertani (LB) broth at 37 °C. The cultures were subsequently diluted in fresh medium and grown until 2h, which was confirmed by measuring the optical density at 600 nm. Afterward, the bacterial cells were suspended and diluted in sterile saline solution to 10^7 colony-forming units (CFU) mL^{-1} .

For the MIC tests, the antibacterial agents were diluted to serial dilutions (1028, 512, 256, 128, 64, 32, 16, 8, 4, 2 $\mu\text{g mL}^{-1}$) by sterile saline solution before being inoculated with the bacteria suspension. The lowest concentration that can satisfied, represented the MIC of the antibacterial materials.

Thermal and Mechanical properties

The thermal decomposition, curing temperature, and the glass transition temperature (T_g) of PDDA, GO, and the PDDA-GO nanocomposite were measured by differential scanning calorimetry (DSC) (Netzsch / DSC 200) instrument in the nitrogen atmosphere. For DSC analysis, specimens were heated with continuous increment in temperature from -80 to 360°C with a rate of 20°C/min.

Perkin Elmer DMA 8000 instrument at dual cantilever clamp mode at 1 Hz and 10 Hz of vibration frequency was used to measure the dynamic mechanical property and thermal properties of the PDDA, GO, and the PDDA-GO nanocomposite. The dynamic force was applied in the temperature from 30 to 360°C with heating rate 3°/min.

RESULTS AND DISCUSSION

Antibacterial Activity of PDDA.

The minimum inhibitory concentration (MIC) as a reference method, have been widely used to test the in-vitro antibacterial activity of antimicrobial agents that inhibits the visible and rapid growth of the bacteria for measuring the potential agents against specific pathogens. Target pathogens were chosen *E. coli* as Gram-negative bacteria, *S. aureus* as Gram-Positive bacteria. As displayed in the polymer activity after an overnight incubation toward both kinds of bacteria was examined for three times. Results showed PDDA was effective against both bacteria in a concentration-dependent manner values for *E. Coli* and *S. aureus* of 16 and 64 µg/ml, respectively. These observed MIC values are suggesting that the PDDA has antibacterial activity in concentrations from 16 (against *E. coli*) and 64 µg mL⁻¹ (against *S. aureus*).

Bacteria	PDDA concentration (µg mL ⁻¹)
<i>E. coli</i>	>16
<i>S. aureus</i>	>64

Table 1. Antibacterial activity of PDDA.

Thermal properties of PDDA

To investigate the thermal properties of PDDA, the DSC (Differential Scanning Calorimetry) was first used to determine the glass transition (T_g) and the polymer’s melting temperature.

Various weights and heating ranges were used to do the DSC analysis. Still, we have not found the exact data for the T_g and melting point of PDDA and there has not been any related data online to compare our results with them. But after trying multiple times the latest results are as shown in Fig. 1. DSC graph of PDDA.

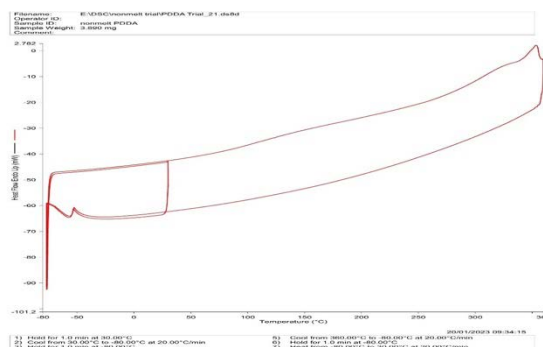


Figure 1. DSC graph of PDDA.

As can be seen, there is a peak around 360°C, which suggests the melting point. However, usually seeing a melting point on the DSC should give us a mutual peak on the other side of the spectrum as the crystallization peak. Since we cannot see that, we are uncertain to say this is the exact melting point. Also, T_g usually shows a slight shift. There is a slight shift around 100°C, but we consider that as water vaporizing from the polymer since PDDA is super water absorbent, and this shift changes each time with different samples using.

For further investigation, DMA (Dynamic Mechanical Analysis) has been used. This technique is usually used to study a polymer’s viscoelastic behavior by varying the temperature of the sample or the frequency of the stress applied to it. The analysis can give two graphs, the “modulus”, which measures the material’s overall resistance to deformation and the “tan delta”, measuring the material’s damping. We can determine the glass transition and melting point based on these two graphs.

The analysis was done at two frequencies (1 Hz and 10 Hz). The glass transition is frequency dependent; therefore, as seen in the Figure 2, the 1Hz and 10Hz modulus graphs have separated around 250°C. Also, the tan delta signal is the point in the transition region where the material has the most viscous response to deformation. This signal often shows a distinct peak in the transition region, and the T_g measured from the tan(δ) is simply the temperature at the peak. As shown in the Figure 3 this peak is also around 250°C suggesting the T_g of PDDA. Also, on continued heating, the melting point, is reached around 360°C both in modulus and tan delta graph suggesting the melting point which is the same result we seen in the DSC analysis graph.

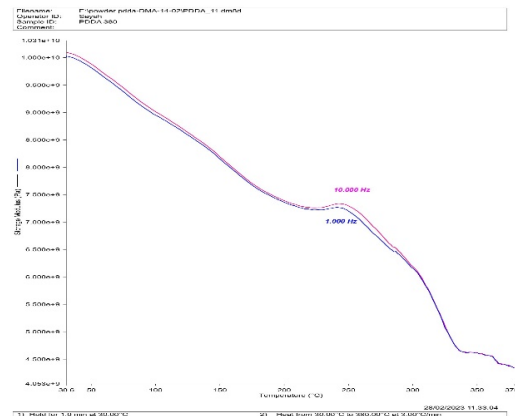


Figure 2. DMA of PDDA (the storage modulus graph).

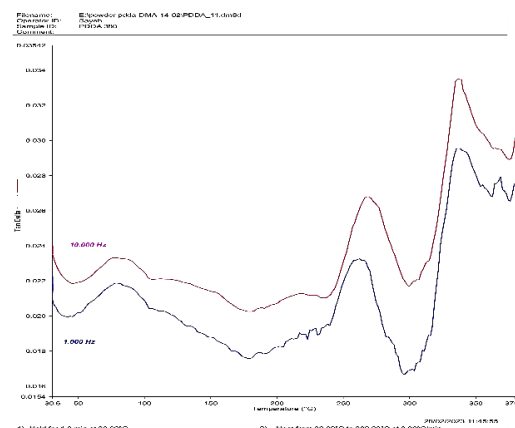


Figure 3. DSC of PDDA (the tan delta graph).

CONCLUSIONS AND FUTURE WORK

From these primary results it can be concluded that the PDDA has a high temperature melting point, which will cause problem for the process of our nanocomposite. Therefore, now we are mainly looking at how to shift these high temperatures to lower by adding additives to the polymer.

Conflicts of interest

The authors declare no conflict of interest.

REFERENCES

- [1] C. Sharma and N.K. Bhardwaj, 'Bacterial nanocellulose: Present status, biomedical applications and future perspectives' *Materials Science and Engineering: C*, Vol. 104, pp. 109963, 2019.
doi.org/10.1016/j.msec.2019.109963
- [2] S. Hameed and P. Bhattarai, 'Novel Nanomaterials for Biosensor Development', *Nanobiosensors: From Design to Applications*, pp.45-72, 2020.
doi.org/10.1002/9783527345137.ch3
- [3] J. Mahendran and J.-P. St-Pierre, 'Nanomaterials Applications in Cartilage Tissue Engineering', *Nanoengineering Materials for Biomedical Uses*, pp. 81-105, 2019.
doi.org/10.1007/978-3-030-31261-9_5
- [4] M. B. Ross, P. De Luna, Y. Li, C.-T. Dinh, D. Kim, P. Yang, et al., 'Designing materials for electrochemical carbon dioxide recycling', *Nature Catalysis*, Vol. 2, Issue 8, pp. 648-658, 2019.
doi.org/10.1038/s41929-019-0306-7
- [5] M.R. Rahimi and S. Mosleh, *Intensification of Sorption Processes: Active and Passive Mechanisms*. Elsevier, 2021.
- [6] M. Roy, P. Tran, T. Dickens and A. Schrand, 'Composite Reinforcement Architectures: A Review of Field-Assisted Additive Manufacturing for Polymers', *Journal of Composites Science*, vol. 4, no. 1, p. 1, 2019.
doi.org/10.3390/jcs4010001
- [7] M. Azizi-Lalabadi, H. Hashemi, J. Feng, and S. M. Jafari, 'Carbon nanomaterials against pathogens; the antimicrobial activity of carbon nanotubes, graphene/graphene oxide, fullerenes, and their nanocomposites', *Advances in Colloid and Interface Science*, vol. 284, p. 102250, Oct. 2020.
doi.org/10.1016/j.cis.2020.102250
- [8] O. Movil, L. Frank, and J. A. Staser, 'Graphene Oxide-Polymer Nanocomposite Anion-Exchange Membranes', *Journal of The Electrochemical Society*, vol. 162, no. 4, pp. F419-F426, 2015.
doi.org/10.1149/2.0681504jes.
- [9] L. Hui et al., 'Availability of the Basal Planes of Graphene Oxide Determines Whether It Is Antibacterial', *ACS App Mater Interfaces*, vol. 6, no. 15, pp. 13183-13190, Aug. 2014.
doi.org/10.1021/am503070z
- [10] M. Cobos, I. De-La-Pinta, G. Quindós, M. J. Fernández, and M. D. Fernández, 'One-step eco-friendly synthesized silver-graphene oxide/poly(vinyl alcohol) antibacterial nanocomposites', *Carbon*, vol. 150, pp. 101-116, Sep. 2019.
doi.org/10.1016/j.carbon.2019.05.011.
- [11] X. Zou, L. Zhang, Z. Wang, and Y. Luo, 'Mechanisms of the Antimicrobial Activities of Graphene Materials', *J Am Chem Soc*, vol. 138, no. 7, pp. 2064-2077, Feb. 2016.
doi.org/10.1021/jacs.5b11411
- [12] S. Liu et al., 'Antibacterial Activity of Graphite, Graphite Oxide, Graphene Oxide, and Reduced Graphene Oxide: Membrane and Oxidative Stress', *ACS Nano*, vol. 5, no. 9, pp. 6971-6980, Sep. 2011.
doi.org/10.1021/nn202451x
- [13] Q. Bao, D. Zhang, and P. Qi, 'Synthesis and characterization of silver nanoparticle and graphene oxide nanosheet composites as a bactericidal agent for water disinfection', *Journal of Colloid and Interface Science*, vol. 360, no. 2, pp. 463-470, Aug. 2011.
doi.org/10.1016/j.jcis.2011.05.009
- [14] L. D. Melo, E. M. Mamizuka, and A. M. Carmona-Ribeiro, 'Antimicrobial Particles from Cationic Lipid and Polyelectrolytes', *Langmuir*, vol. 26, no. 14, pp. 12300-12306, Jul. 2010.
doi.org/10.1021/la101500s
- [15] B. Issa, I. M. Obaidat, B. A. Albiss, and Y. Haik, 'Magnetic Nanoparticles: Surface Effects and Properties Related to Biomedicine Applications', *International Journal of Molecular Sciences*, vol. 14, no. 11, pp. 21266-21305, Nov. 2013.
doi.org/10.3390/ijms141121266
- [16] L. M. Sanches, D. F. S. Petri, L. D. De Melo Carrasco, and A. M. Carmona-Ribeiro, 'The antimicrobial activity of free and immobilized poly (diallyldimethylammonium) chloride in nanoparticles of poly (methylmethacrylate)', *Journal of Nanobiotechnology*, vol. 13, no. 1, p. 58, Dec. 2015.
doi.org/10.1186/s12951-015-0123-3

Silver K

*Cardiff University
School of Engineering*

Bestow S

*Cardiff University
School of Engineering*

Richardson J

*Cardiff University
School of Engineering*

Nagara C

*Cardiff University
School of Engineering*

Choi H

*Cardiff University
School of Engineering*

Li J

*Cardiff University
School of Engineering*

ADVANCED MANUFACTURING

Microwave Resonator-based Microfluidic Sensors Fabricated Using 3D-Printing Technology

Microwave resonators can be utilized as precision, fast, selective, and non-invasive sensors for reagent and material characterisation. The quality factor (Q-factor) of a microwave resonator determines its dielectric sensing performance, and the value of Q-factor can be improved by the resonator structure optimisation. However, conventional microwave resonator fabrication can be a complex, time-consuming process that constrains the device prototyping and development. Here we present a low-cost, fused filament 3D printing method to effectively fabricate integrated, split-ring microwave resonators with fluidic inducts, operating in the frequency range 2 to 4 GHz. Finite element modelling is employed to simulate the microwave resonance of sensing aqueous droplets in continuous mineral oil flow, using COMSOL Multiphysics software. We evaluate the sensing performance of different 3D-printed microwave resonators with geometrical variations of ring shapes, sizes, and numbers of split gaps, focusing on the increase of their Q-factors for improved sensitivity. Our work demonstrates a rapid prototyping approach to optimise microwave resonator, that can be applied to flow chemistry and engineering biology applications for functional soft material development purposes.

Keywords:

Split-ring resonator, microwave engineering, COMSOL modelling, 3D-printing, microfluidic.

Corresponding author:

LiJ40@cardiff.ac.uk



K. Silver, S. Bestow, J. Richardson, C. Nagra, H. Choi, and J. Li, 'Microwave Resonator-based Microfluidic Sensors Fabricated Using 3D-Printing Technology', *Cardiff University School of Engineering Research Conference 2023*, Cardiff, UK, 2023, pp. 109-112.

doi.org/10.18573/conf1.z

INTRODUCTION

Microwave resonators is the generic term for electronic devices resonant from 300 MHz to terahertz frequencies [1]. They have been widely applied to various research fields, including material characterisation and sensing, diagnosis, and healthcare applications [2]–[4]. Recently, integrated, microwave-microfluidic devices have been developed as miniaturised systems to sense and characterize low-volume reagents, flowing in a fine capillary, in real time [5]–[9]. Microwave resonators also can be used to heat samples to accelerate chemical reactions and excite biological specimens for chemistry and life science studies[10]–[13].

The performance of a microwave resonator can be quantified by its quality factor (Q-factor), a dimensionless number formed from the ratio of stored EM energy to energy loss per cycle. The Q-factor is governed by the microwave losses in the resonator substrate materials (plastic and metal) and can be maximised by using high conductivity metals (e.g. copper) of low surface roughness and dielectrics of low loss tangent. The fabrication of planar microwave resonator sensors can be a complex and time-consuming process that involves laser machining and clean room technologies [14]–[16]. Flexible microengineering and integration methods are required to form advanced microwave resonator with associated micro-sized components.

We have developed a rapid, 3D printing approach to fabricate microfluidic-microwave resonator devices based on split-ring resonators, incorporating a liquid metal as an electrode. Complex 3D microwave resonant structures with embedded droplet-forming fluid ducts can be devised and simulated using FEM (COMSOL) modelling. Optimised designs can be rapidly prototyped and tested to improve the device performance, e.g. via maximized Q-factors, by varying the resonator shapes, sizes, and number of gaps in the resonators' rings. Such devices are used for non-invasive characterization of liquid precursors and high-order emulsions, building towards functional soft matter materials.

MATERIALS AND METHODS

Cyclic olefin copolymer (COC) filament (CREAMELT) was used to fabricate microfluidic-microwave resonator devices using an Ultimaker S5 ProBundle 3D printer. We have shown that this material has a very low dielectric loss. The conductor part of microwave resonator was formed by the injection of gallium indium eutectic (Sigma Aldrich). A copper ground plane was applied to the chip base before soldering to two SMA connectors. Gallium Indium eutectic was then inserted into the ring cavity space. UV curable glue was used to seal the liquid metal and microfluidic inlets.

RESULTS

3D-printed, microfluidic-microwave resonator devices were used to sense the segmented flow of water in a continuous oil phase; the experiment setup is shown in Fig. 1. All reagents were purchased from Sigma Aldridge. Positive displacement syringe pumps were used to inject liquid into the 3D-printed device. An optical microscope was used to record the droplet movement within the fluidic duct.

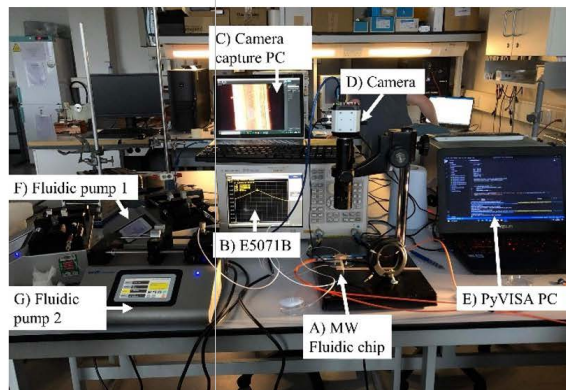


Fig. 1. Experiment setup. A is the MW and Microfluidic chip. B is the ENA. C and D are the camera control PC and imaging camera respectively. E is the PC running the automated script. F and G are the micro-litre pumps.

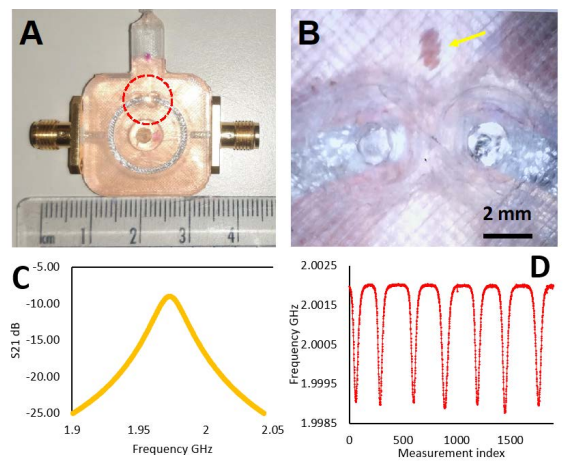


Fig. 2. A shows the microfluidic chip with two SMA connectors, two microfluidic inlet ports and a liquid metal ring (gap is highlighted). B is the droplet flow through the gap. C shows a resonant S21 plot for an empty duct, 1.975 GHz center frequency and Q of 100. D shows the repeatable 3 MHz change as droplets continually pass through the gap.

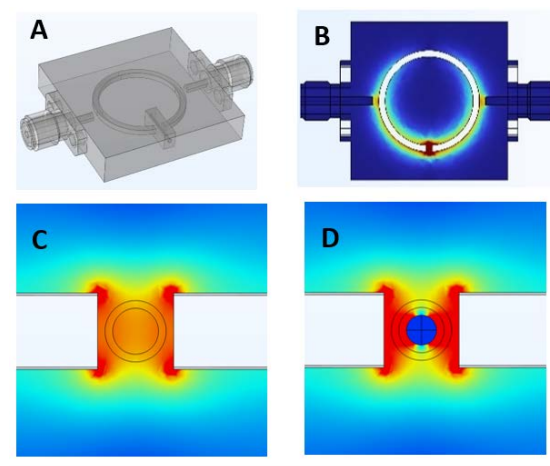


Fig. 3. COMSOL simulation geometry, electric field and droplet perturbation measurements. A. The 3D geometry rendered in COMSOL. B. E field with concentrated E field at the ring gap. C and D shows the electric field distribution between the gap with a CoC channel; with and without a droplet D respectively.

Finite element, multi-physics modelling was conducted using COMSOL (version 6.1). Fig. 2A shows an example printed device. The silver ring structure is formed by the injection of liquid metal. Split rings are coupled via pairs of SMA launchers, with a copper film ground plane, and measurements of S_{21} performed using a vector network analyser. Fig. 2B shows an aqueous droplet (brownish) flowing in an oil phase inside the fluidic duct through the gap of the split ring resonator. Fig. 2C shows the central resonant frequency (2.0906 GHz) of the 3D-printed microwave resonator device, when the duct is filled with air. Fig. 2D shows an example microwave resonance reading of water-in-oil emulsion. Each signal drop indicates a water droplet passing through the gap of the ring split.

Fig. 3 a COMSOL Multiphysics model and EM wave simulation of a split ring resonator, which was used to develop Table 1. The CoC channel in Fig C has no effect on the field distribution between the gap, retaining Q and hence sensitivity to droplets. Moreover, placing a droplet, as shown in Fig. D, depolarizes the field which subsequently changes the E field and resonant frequency. As a droplet passes through the ring gap, a periodic frequency shift of 3 MHz is observed.

Table 1 shows different microwave resonator structures that can be 3D-printed. The different design iterations were to study different concepts of split ring resonators. Rectangular resonators have greater uniformity of E-field within the gap. The number of gaps increases the resonant frequency and the corresponding Q-factor, compared with a single gap model. 3D plots for electric field were simulated to determine the effectiveness of these new designs for droplet sensing. The dual gap rectangular resonator was found to have the highest Q Factor. An increased aspect ratio, i.e. the length to width ratio of the resonator, accounts for the increase in Q. As the aspect ratio increases the electric field becomes more confined to edges of structure, leading to reduced radiation losses.



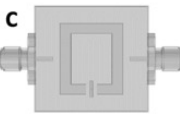


	Centre Frequency (GHz)	Quality Factor	E-field Max (V/M)
A 	1.97	128.06	12396.7
B 	1.81	145.11	16555.4
C 	2.03	177.97	20349.1
D 	2.31	170.77	18230.9
E 	3.83	498.91	18776.6

Table 1. A Single Split Ring Resonator Model, B Dual Ring Single Gap Split Ring Resonator, C Single Gap Rectangular Resonator D Single Gap Rectangular Resonator with Rounded Edges, E Dual Gap Rectangular Resonator.

DISCUSSION

The Q-factor of a microwave resonator sensor quantifies its sensitivity for dielectric measurement, with higher values giving greater sensitivity. In our experiments, we controlled the geometry of the split-ring resonator, such as shape, aspect ratio and dimensions. In theory, rectangular shaped resonators have a more uniform electric field and higher sensitivity in comparison with the circular shaped ones, as shown in the modelling results of Table 1. In addition, increasing the number of gaps can also improve the Q-factor, as the total energy stored in the increases via the electric field. A double split, setting up a higher order mode, as shown in Table 1:E, doubles Q factor and enables time dependent resolve of droplets in flow. However, single splits were chosen as the preferred geometry as the maximum electric field, to be utilized in microwave heating of droplets, shows no meritable improvements.

3D-printing provides a rapid prototyping approach to fabricate and test different microwave structures without significant post processing. Printable, dielectric substrate materials play a key role to determine the resonator performance. In our experiments, COC is selected as the substrate material, due to its low microwave losses. Additionally, COC is hydrophobic. This allows water segment flow in a continuous oil phase. High printing resolution and low surface roughness of liquid metal filling duct can improve the Q-factor, which can be achieved with high-end 3D printers and optimised printing settings, leading to more precise and efficient microwave sensing systems.

Our work demonstrates that monolithic, 3D-printed microfluidic-microwave devices can be applied to detect and analyse water-in-oil emulsions. This paves the way to non-invasive characterisation of aqueous droplet-based materials, such as hydrogel or cytoplasm for biological engineering applications. Sophisticated and high-performance electronic circuits will be built and integrated to develop functional fluidic manifolds, leading towards new capabilities and tools for life science studies as our future objectives.

CONCLUSION

This research demonstrates the potential of monolithic, 3D-printed microfluidic-microwave devices in detecting and analysing emulsions and aqueous droplets. Simulation was used to investigate novel ring geometries and aid in optimising conventional structures. Furthermore, analysis of field distribution has explained enhancements in Q and electric field leading to more sensitive resonant structures. These advancements offer for a non-invasive characterisation of droplet-based materials, which can be essential in biological engineering applications. The combination of 3D printing and microwave resonators holds promise for further advancements in diverse research areas, enabling innovative solutions for various scientific and technological challenges.

Acknowledgments

This work was partially supported and funded by the European Horizon 2020 project ACDC (Artificial Cells with Distributed Cores) under project award number 824060.

Conflicts of interest

The authors declare no conflict of interest.

REFERENCES

- [1] R. A. Alahnomi *et al.*, 'Review of Recent Microwave Planar Resonator-Based Sensors: Techniques of Complex Permittivity Extraction, Applications, Open Challenges and Future Research Directions,' *Sensors (Basel)*, vol. 21, no. 7, Apr. 2021. doi.org/10.3390/S21072267
- [2] M. Tiuri, 'Microwave sensor applications in industry,' *Conference Proceedings - European Microwave Conference*, pp. 25–32, 1987. doi.org/10.1109/EUMA.1987.333693
- [3] D. M. Elsheakh *et al.*, 'Rapid Detection of Coronavirus (COVID-19) Using Microwave Immunosensor Cavity Resonator,' *Sensors (Basel)*, vol. 21, no. 21, Nov. 2021. doi.org/10.3390/S21217021
- [4] H. Choi, J. Nylon, S. Luzio, J. Beutler, and A. Porch, 'Design of continuous non-invasive blood glucose monitoring sensor based on a microwave split ring resonator,' *Conference Proceedings - 2014 IEEE MTT-S International Microwave Workshop Series on: RF and Wireless Technologies for Biomedical and Healthcare Applications, IMWS-Bio 2014*, Feb. 2015. doi.org/10.1109/IMWS-BIO.2014.7032398
- [5] A. Ebrahimi, W. Withayachumnankul, S. Al-Sarawi, and D. Abbott, 'High-sensitivity metamaterial-inspired sensor for microfluidic dielectric characterization,' *IEEE Sens J*, vol. 14, no. 5, pp. 1345–1351, 2014. doi.org/10.1109/JSEN.2013.2295312
- [6] P. Velez, L. Su, K. Grenier, J. Mata-Contreras, D. Dubuc, and F. Martin, 'Microwave Microfluidic Sensor Based on a Microstrip Splitter/Combiner Configuration and Split Ring Resonators (SRRs) for Dielectric Characterization of Liquids,' *IEEE Sens J*, vol. 17, no. 20, pp. 6589–6598, Oct. 2017. doi.org/10.1109/JSEN.2017.2747764
- [7] A. A. Abduljabar, D. J. Rowe, A. Porch, and D. A. Barrow, 'Novel microwave microfluidic sensor using a microstrip split-ring resonator,' *IEEE Trans Microw Theory Tech*, vol. 62, no. 3, pp. 679–688, 2014. doi.org/10.1109/TMTT.2014.2300066
- [8] W. Ye, D.-W. Wang, J. Wang, S. Chen, G. Wang, and W.-S. Zhao, 'An Ultrahigh-Sensitivity Dual-Mode Microwave Sensor for Microfluidic Applications,' *IEEE Microwave and Wireless Technology Letters*, pp. 1–4, 2023. doi.org/10.1109/LMWT.2023.3252008
- [9] A. Secme *et al.*, 'High Resolution Dielectric Characterization of Single Cells and Microparticles Using Integrated Microfluidic Microwave Sensors,' *IEEE Sens J*, pp. 1–1, 2023. doi.org/10.1109/JSEN.2023.3250401
- [10] J. Sun, W. Wang, and Q. Yue, 'Review on Microwave-Matter Interaction Fundamentals and Efficient Microwave-Associated Heating Strategies,' *Materials*, vol. 9, no. 4, 2016. doi.org/10.3390/MA9040231
- [11] A. Folli *et al.*, 'A novel dual mode X-band EPR resonator for rapid in situ microwave heating,' *J Magn Reson*, vol. 310, Jan. 2020. doi.org/10.1016/J.JMR.2019.106644
- [12] M. Miyakawa, S. Kanamori, K. Hagihara, A. Itagaki, T. Nakamura, and M. Nishioka, 'Cylindrical Resonator-Type Microwave Heating Reactor with Real-Time Monitoring Function of Dielectric Property Applied to Drying Processes,' *Ind Eng Chem Res*, vol. 60, no. 25, pp. 9119–9127, Jun. 2021. doi.org/10.1021/ACS.IECR.1C00569
- [13] T. Markovic, G. Maenhout, M. Martinic, and B. Nauwelaers, 'Complementary Split-Ring Resonator for Microwave Heating of μL Volumes in Microwells in Continuous Microfluidics,' *Chemosensors 2021, Vol. 9, Page 184*, vol. 9, no. 7, p. 184, Jul. 2021. doi.org/10.3390/CHEMOSENSORS9070184
- [14] X. Shang *et al.*, 'W-Band Waveguide Filters Fabricated by Laser Micromachining and 3-D Printing,' *IEEE Trans Microw Theory Tech*, vol. 64, no. 8, pp. 2572–2580, Aug. 2016. doi.org/10.1109/TMTT.2016.2574839
- [15] S. Abadei, C. R. Cho, A. Grishin, and S. Gevorgian, 'Low frequency characterisation of laser ablation deposited thin $\text{Na}_0.5\text{K}_0.5\text{NbO}_3$ (NKN) films for microwave application,' <http://dx.doi.org/10.1080/00150190108225195>, vol. 263, no. 1, pp. 173–179, 2011. doi.org/0.1080/00150190108225195
- [16] X. Li, K. Y. Chan, and R. Ramer, 'Fabrication of through via holes in ultra-thin fused silica wafers for microwave and millimeter-wave applications,' *Micromachines (Basel)*, vol. 9, no. 3, 2018. doi.org/10.3390/MI9030138

Hejazi S

*Cardiff University
School of Engineering*

Packianather M.

*Cardiff University
School of Engineering*

Liu Y

*Cardiff University
School of Engineering*

ADVANCED MANUFACTURING

Using DCGAN and WGAN-GP to Generate Artificial Thermal RGB Images for Induction Motors

The paper investigates the feasibility of using GANs to create realistic induction motor thermal RGB image datasets for multimodal condition-monitoring systems. Generating high-quality thermal images presents computational challenges, and in this study, two GAN frameworks, DCGAN and WGAN-GP, were used under different health conditions. Firstly, DCGAN was used on three conditions using various hyperparameters, but the results required further improvement. Secondly, WGAN-GP was used with an extensive training duration of 11 hours, utilising 10,000 epochs and a batch size of 64, targeting the inner fault dataset, which resulted in generating artificial images that closely resembled real images. This study highlights the impact of hyperparameters on GAN performance and demonstrates the capability of GANs in creating artificial thermal image datasets.

Keywords:

Condition monitoring, generative adversarial networks, thermal images, DCGAN, WGAN-GP.

Corresponding author:

HejaziS@cardiff.ac.uk



S. Hajazi, M. Packianather, and Y. Liu, 'Using DCGAN and WGAN-GP to Generate Artificial Thermal RGB Images for Induction Motors', *Cardiff University School of Engineering Research Conference 2023*, Cardiff, UK, 2023, pp. 113-117.

doi.org/10.18573/conf1.aa

INTRODUCTION

In the era of Artificial Intelligence (AI) and smart manufacturing, having a reliable condition monitoring system for fault detection and recognition is essential for maintaining high-quality standards and controlling the production process [1] it is difficult to obtain a sufficient defect data set in terms of diversity and quantity. A new generation method called surface defect-generation adversarial network (SDGAN. This paper follows the paper published by Hejazi et al. published on December 2022. This study aims to highlight the importance of using a multimodal condition monitoring system utilising vibration and thermal images to increase the fault detection accuracy [2]. Thermal images are considered promising in induction motor condition monitor it can reach up to 100% if images are clear without further preprocessing [3], unlike vibration signal, which is regarded as the most famous metric in induction motor condition monitoring systems [2, 4].

However, thermal images are not commonly used in condition monitoring since defect data are limited or rare and are also subjected to a lack of fault diversity. It is common to use AI for classification or regression, and the neural network is expected to be trained on representative and balanced data for both. In fact, computers can also be used for data generation using generative models, such as variational autoencoders and generative adversarial networks. Therefore, the importance of using GANs arises when manufacturing needs a methodology that generates complex faults for better condition monitoring systems [1] it is difficult to obtain a sufficient defect data set in terms of diversity and quantity. A new generation method called surface defect-generation adversarial network (SDGAN. Generative Adversarial Networks (GANs) were introduced by Ian Goodfellow et al. in 2014 [5]. GANs use deep learning to generate fake images by mimicking the dataset distribution by playing a min-max game between two models, the Generator (G) and Discriminator (D) models. Hence, (G) learns to generate images very close to real images to fool D [6]. GANs are called generative because they generate something as an output, for example, images, videos domain adaptation, image super-resolution, etc., and adversarial because they have two networks fighting against each other (G) network (G) that capture the distribution and (D) model (D) that tries to figure the genuineness of generated data if it was fake or real [7].

Deep Convolutional Generative Adversarial Network (DCGAN) is a type of GANs that Radford discovered, Metz, and Chintala in 2014 [8]. DCGAN utilises Convolutional Neural Network (CNN) architecture with GANs [1] it is difficult to obtain a sufficient defect data set in terms of diversity and quantity. A new generation method called surface defect-generation adversarial network (SDGAN. One of the key innovations of DCGAN is the replacement of pooling layers with stride convolutions and fractionally-strided convolutions. This allows both the (G) and (D) to learn convolutional operations, spatial downsampling, and upsample individually. By doing this, DCGAN ensures (G) and (D) networks learn independently, which can help to stabilise the training process. It also uses batch normalisation (BN) to stabilise learning. BN is a technique used to normalise the input to a layer, which helps to solve the vanishing gradient problem and prevent the deep (G) from collapsing all samples to the same points. Finally, DCGANs use both ReLU and LeakyReLU activation functions to allow the model to learn quickly and perform well [9], [10] computer graphics, and computer vision problems can be treated as image-to-image translation tasks. Such translation entails learning to map one visual representation

of a given input to another representation. Image-to-image translation with generative adversarial networks (GANs. Followed by Data augmentation in fault diagnosis based on the Wasserstein Generative Adversarial Network with Gradient Penalty (WGAN-GP) deep architecture that can stabilise the training and generate high-quality images in 2017 [11]. WGAN-GP brings stability to the training model with almost no parameter tuning [12]. It also proved its capability in fault sample generation [13] a practical problem comes up in these studies, where deep learning models cannot be well trained and the classification accuracy is greatly affected because of the sample-imbalance problem, which means that there are a large amount of normal data but few fault samples. To solve the problem, an enhanced generative adversarial network (E-GAN, also in supplementing low dimensional fault data [14].

STATE-OF-THE-ART

DCGAN proved its efficiency in [15] which is called unbalanced dataset. Due to the existence of such unbalanced datasets, traditional methods are not easy to detect faults. Deep convolutional generative adversarial networks (DCGAN for image generation in solving imbalanced datasets in the chemical industry fault diagnosis field. It was also used in [4] for axial piston pump bearing fault diagnosis to mitigate data availability and missing fault labelling challenges. DCGAN was also used in induction motor fault classification using Case Western Reserve University's (CWRU) famous dataset in which CWT images were synthesised [14]. In January 2023, a paper was published focusing on WGAN usage in thermal images; fault creation in induction motors was also used to increase fault samples, namely, inner and outer faults also in healthy condition [16, 17]

It was clear from the literature that researchers tried to generate extra trustworthy data to enhance the training performance on limited fault types or generate look-like vibration signals without focusing on thermal image fault creation. Even the most recent paper explored generating thermal images on three conditions only to enhance the fault classification accuracy using a single input model. Unlike other projects, this paper explores the possibility of using GANs in induction motor thermal RGB image fault creation using DCGAN and WGAN. Hence, our condition monitoring thermal images are of high resolution and large size. The primary objective is to investigate the generation of an artificial thermal image dataset that resembles the existing dataset under various health conditions. The intention is to support the proposed multimodal condition-monitoring system outlined in the paper [2].

DATASET

Wolfson Magnetics Laboratory, located at Cardiff University School of Engineering. The laboratory conducted experiments to simulate six different failure modes and healthy conditions. To create these failure modes, a 2mm diameter drill was used to create holes in both the inner and outer parts of the bearing, as illustrated in Fig. 1 [3]. This paper aims to specifically investigate three conditions: inner, outer, which are (depicted in Fig. 1), and healthy. Healthy conditions refer to a bearing without any defects or faults.

However, Thermal images of bearing faults were collected using a Forward Looking InfraRed (FLIR) thermal camera

positioned 30cm from the centre of the housing, Fig. 2. The camera was connected to a computer to capture images of six artificially induced faults and one health condition. A total of 120 images were captured under three types of load, resulting in 360 images per condition. The data was split into 80% for training, equivalent to 288 RGB images, and 20% for testing, equal to 72 RGB photos [3, 18].

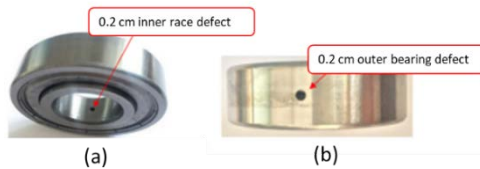


Fig. 1. Bearing faults (a) inner fault, (b) outer fault.

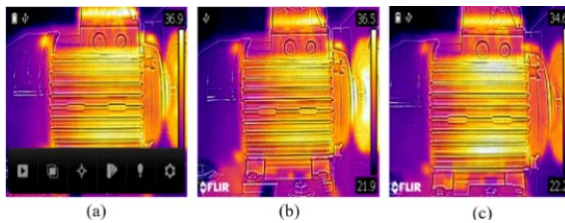


Fig. 2. Thermal images sample under three health conditions (a) inner fault (b) outer fault (c) healthy.

METHODOLOGY

In this study two GAN architectures were used. Firstly, the DCGAN model was trained on Google Colab using Tesla T4 GPU. Training and testing images of size 224 x 224 x 3 were located in the google drive directory. The (G) model takes a random noise vector of size 100 as input and generates an image. The (D) model predicts whether it is real or fake. Both models trained alternately with binary cross-entropy loss function and Adam optimiser. The DCGAN (G) has 40,635,715 parameters, and the (D) has 605,505 trainable parameters. The second architecture is WGAN-GP, a type of GAN architecture that uses a gradient penalty to enforce the Lipschitz continuity of the (D). The (D) is trained to output

a scalar value instead of a probability. The (G) is trained to minimise the Wasserstein distance between the distribution of real and generated samples. The (G) loss is the negative Wasserstein distance, and the (D) loss is the difference between the average of the (D) output on the real samples and the generated samples, plus a gradient penalty term. The gradient penalty term is added to ensure that the (D) satisfies the Lipschitz continuity condition with a 0.0001 learning rate and batch size of 64 and Adam optimiser [11].

RESULTS

Basic DCGAN was tested on three health condition datasets: inner fault, outer fault, and healthy. The experiments varied in terms of hyperparameters, such as Learning Rate (LR) (0.0001, 0.0002), batch size (16,32), and the number of epochs (50, 500). On the other hand, WGAN-GP was tested on the inner fault type only with advanced training parameters, as shown in Table 1.

To evaluate the performance of each experiment, the (G) and (D) losses were assessed. A lower (D) loss relative to the (G) indicates superior (D) performance. Conversely, a lower (G) loss suggests a better performance of the (G). These findings align with the results presented in Table 1, where the performance of each model can be observed based on their respective losses. The experiments were conducted in two stages: the first stage involved using basic DCGAN with simple parameters (Experiments 1-12) to test various health condition datasets, while the second stage focused on utilising WGAN-GP with advanced parameters specifically for the inner fault type.

Stage 1: Three conditions were tested, starting with the inner fault (Experiments 1-4): longer training time led to better performance, with the best result observed in experiment 2. It used 500 epochs, LR of 0.0001, a batch size of 32, and achieved a (G) loss of 4.627 and a (D) loss of 0.0002. Outer fault (Experiments 5-8), Increasing the batch size led to better performance, with the best result obtained in experiment 7, which used 50 epochs, LR of 0.0002, a batch size of 16, and achieved a (G) loss of 0.0021 and (D) loss of

No.	Model	Dataset	LR	Batch Size	Epochs	Training time (min)	(G) Loss	(D) Loss
1	DCGAN	Inner	0.0001	16	500	48	3.2172	5.537
2	DCGAN	Inner	0.0001	32	500	41	4.627	0.0002
3	DCGAN	Inner	0.0002	16	50	5	0.0019	3.5658
4	DCGAN	Inner	0.0002	32	500	40	5.0668	7.6786
5	DCGAN	Outer	0.0001	16	50	4	0.0045	3.0554
6	DCGAN	Outer	0.0001	32	50	4	0.0079	2.782
7	DCGAN	Outer	0.0002	16	50	4	0.0021	3.4129
8	DCGAN	Outer	0.0002	32	50	4	0.00308	3.2324
9	DCGAN	Healthy	0.0001	16	50	4	0.00681	2.8419
10	DCGAN	Healthy	0.0001	32	50	4	0.0068	2.8419
11	DCGAN	Healthy	0.0002	16	50	5	0.00681	2.84186
12	DCGAN	Healthy	0.0002	32	500	50	8.32011	5.0697
13	WGAN-GP	Inner	0.0001	64	10,000	660 (11 hours)	-1896.8600	Loss Fake: -1897.3366 Loss Real: -1548.9419

Table 1. GAN performance for fault detection experiments.

3.4129. Healthy conditions (Experiments 9-12) where longer training time resulted in improved performance, with the best outcome observed in experiment 12, which utilised 1000 epochs, LR of 0.0002, a batch size of 32, and achieved a (G) loss of 8.3201 and a (D) loss of 5.0697. However, visual inspection results were not as promising compared to the project objective.

Stage 2: the inner fault was exclusively tested using WGAN-GP (Experiment 13) with a higher number of epochs and longer training time. The experiment required 11 hours of training time. The (G) loss was a high negative number, while the (D) loss of -1897.3366 for fake samples and -1548.9419 for real samples. These findings suggest that the (D) network performed well in distinguishing between real and fake samples, with the loss being minimised during training. Similarly, the (G) loss was also a high negative number, specifically -1896.8599. This indicates that the (G) successfully generates samples that the (D) classifies as real samples with a high level of confidence.

DISCUSSION

The choice of hyperparameters significantly impacts model performance. Generating artificial fault images of large size and high complexity posed challenges requiring significant time and GPU capabilities. Table 1 provides insights into the performance of GANs using DCGAN. Implementing WGAN-GP with advanced hyperparameters (10,000 epochs, batch size 64) on a GPU yielded efficient generation of motor images closely resembling real images over time as shown in Fig. 3.

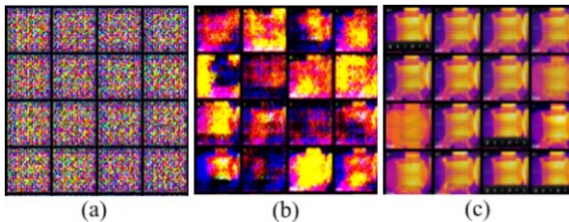


Fig. 3. WGAN-GP images (inner fault type): (a) at epoch 0, (b) at epoch 100, (c) at epoch 10,000.

CONCLUSION

This study has highlighted the significant impact of hyperparameters on GAN performance and has successfully demonstrated the remarkable capability of GANs in creating induction motor thermal images. This study has proved the applicability of WGAN-GP for generating artificial thermal images, although it requires high computational power. Future research will aim to optimise the process of dataset creation by training all fault types simultaneously using conditional GANs with higher image resolution.

Acknowledgements

This work was supported by the Saudi Arabian Cultural Bureau in London, the Saudi Arabian Ministry of Education, and Cardiff University.

Conflicts of interest

The authors declare no conflict of interest.

REFERENCES

- [1] S. Niu, B. Li, X. Wang, and H. Lin, 'Defect Image Sample Generation With GAN for Improving Defect Recognition,' *IEEE Trans Autom Sci Eng*, vol. 17, no. 3, pp. 1–12, 2020. doi.org/10.1109/TASE.2020.2967415
- [2] S. Hejazi, M. Packianather, and Y. Liu, 'Novel Preprocessing of Multimodal Condition Monitoring Data for Classifying Induction Motor Faults Using Deep Learning Methods,' in *2022 IEEE 2nd International Symposium on Sustainable Energy, Signal Processing and Cyber Security (iSSSC)*, Dec. 2022, pp. 1–6. doi.org/10.1109/iSSSC56467.2022.10051321
- [3] F. McGhan, 'Transfer Learning for Induction Motor Fault Diagnosis,' 2020. <https://github.com/frasermcghan/Year3Project> (accessed Sep. 24, 2022).
- [4] Y. He, H. Tang, Y. Ren, and A. Kumar, 'A semi-supervised fault diagnosis method for axial piston pump bearings based on DCGAN,' *Meas Sci Technol*, vol. 32, no. 12, p. 125104, Dec. 2021. doi.org/10.1088/1361-6501/ac1fbc
- [5] I. Goodfellow *et al.*, 'Generative adversarial networks,' *Commun ACM*, vol. 63, no. 11, pp. 139–144, Oct. 2020, doi.org/10.1145/3422622
- [6] A. Al-Qerem, Y. S. Alsalman, and K. Mansour, 'Image generation using different models of generative adversarial network,' *Proc - 2019 Int Arab Conf Inf Technol ACIT 2019*, pp. 241–245, 2019. doi.org/10.1109/ACIT47987.2019.8991120
- [7] D. Saxena and J. Cao, 'Generative Adversarial Networks (GANs),' *ACM Comput Surv*, vol. 54, no. 3, 2021. doi.org/10.1145/3446374
- [8] A. Kusiak, 'Convolutional and generative adversarial neural networks in manufacturing,' *Int J Prod Res*, vol. 58, no. 5, pp. 1594–1604, 2020. doi.org/10.1080/00207543.2019.1662133
- [9] A. Alotaibi, 'Deep generative adversarial networks for image-to-image translation: A review,' *Symmetry* (Basel), vol. 12, no. 10, pp. 1–26, 2020. doi.org/10.3390/sym12101705
- [10] Z. Wang, Q. She, and T. E. Ward, 'Generative Adversarial Networks in Computer Vision: A Survey and Taxonomy,' *ACM Comput. Surv.*, vol. 54, no. 2, 2021. doi.org/10.1145/3439723
- [11] I. Gulrajani, F. Ahmed, M. Arjovsky, V. Dumoulin, and A. Courville, 'Improved Training of Wasserstein GANs,' Mar. 2017, [Online]. Available: <http://arxiv.org/abs/1704.00028>
- [12] Z. Pan, W. Yu, X. Yi, A. Khan, F. Yuan, and Y. Zheng, 'Recent Progress on Generative Adversarial Networks (GANs): A Survey,' *IEEE Access*, vol. 7, pp. 36322–36333, 2019. doi.org/10.1109/ACCESS.2019.2905015

- [13] R. Wang, S. Zhang, Z. Chen, and W. Li, 'Enhanced generative adversarial network for extremely imbalanced fault diagnosis of rotating machine,' *Meas J Int Meas Confed*, vol. 180, no. April, p. 109467, 2021. doi.org/10.1016/j.measurement.2021.109467
- [14] H. Zhong, S. Yu, H. Trinh, Y. Lv, R. Yuan, and Y. Wang, 'Fine-tuning Transfer Learning based on DCGAN Integrated with Self-attention and Spectral Normalization for Bearing Fault Diagnosis,' *Measurement*, vol. 210, no. January, p. 112421, 2023. doi.org/10.1016/j.measurement.2022.112421
- [15] Y. Du, W. Zhang, J. Wang, and H. Wu, 'DCGAN based data generation for process monitoring,' *Proc. 2019 IEEE 8th Data Driven Control Learn Syst Conf DDCLS 2019*, pp. 410–415, 2019. doi.org/10.1109/DDCLS.2019.890892
- [16] H. Shao, W. Li, B. Cai, J. Wan, Y. Xiao, and S. Yan, 'Dual-Threshold Attention-Guided Gan and Limited Infrared Thermal Images for Rotating Machinery Fault Diagnosis Under Speed Fluctuation,' *IEEE Trans Ind Informatics*, pp. 1–10, 2023. doi.org/10.1109/TII.2022.3232766
- [17] J. Ma, X. Jiang, B. Han, J. Wang, Z. Zhang, and H. Bao, 'Dynamic Simulation Model-Driven Fault Diagnosis Method for Bearing under Missing Fault-Type Samples,' *Applied Sciences*, vol. 13, no. 5, p. 2857, Jan. 2023. doi.org/10.3390/app13052857
- [18] A. K. Al-Musawi, F. Anayi, and M. Packianather, 'Three-phase induction motor fault detection based on thermal image segmentation,' *Infrared Phys Technol*, vol. 104, p. 103140, Jan. 2020. doi: 10.1016/j.infrared.2019.103140

Condrea D
*Cardiff University
School of Engineering*

Clarke A
*Cardiff University
School of Engineering*

Ryan M
*Cardiff University
School of Engineering*

Hutt S
*Cardiff University
School of Engineering*

ADVANCED MANUFACTURING

Altering the Tribological Properties of Laser Powder Bed Fusion Materials through Various Methods: A Review

Additive Manufacturing has gained prominence in research due to its cost-effectiveness and design flexibility. However, the connection between tribology and Laser Powder Bed Fusion remains inadequately investigated despite its potential. This study examines various direct manufacturing methods (i.e., without post-processing), in order to identify the most effective technique for modifying tribological properties. The wear rate and coefficient of friction are influenced by densification, which is affected by the formation of melt pools and keyholes in the microstructure. Notably, there is conflicting evidence on the most influential processing parameter for wear. Some studies suggest that laser power holds the greatest significance, while others propose that scan angle has a more pronounced effect on wear behaviour. Additionally, texturing emerges as another tribology manipulation method, enabling the entrapment of lubricants and debris within the system. The study also explores the relationship between microhardness, volumetric energy density, wear, and friction.

Keywords:
Additive manufacturing, tribology, volumetric energy density, processing parameters, textured surface.

Corresponding author:
Email



D. Condrea, M. Ryan, A. Clarke and S. Hutt, 'Altering the Tribological Properties of Laser Powder Bed Fusion Materials through Various Methods: A Review', *Cardiff University School of Engineering Research Conference 2023*, Cardiff, UK, 2023, pp. 118-122.

doi.org/10.18573/conf1.ab

INTRODUCTION

Additive Manufacturing (AM) first emerged in the 1980s as a Rapid Prototyping technology [1] and has since been adopted as a manufacturing process in multiple industries, such as: medical, automotive, chemical, and aerospace [2]. AM fabricates parts using a layer-by-layer principle which allows far greater geometrical freedom in designs, therefore enabling highly complex products to be created, and has the potential to reduce design-to-manufacturing time through a single step process [3]. Metallic AM processes, such as Laser Powder Bed fusion (LPBF) and Electron Beam Melting (EBM), also allow the material properties to be tailored during manufacture.

One area where AM has the potential for significant improvement is applications where the wear characteristics of the material are critical. To date, however, there has been limited research between the relationship of Additive Manufacturing processing and the tribological properties of the materials and components produced. In this paper LPBF, which relies on metal powder and laser melting to build the final desired part, will be the primary focus.

TRIBOLOGICAL PROPERTIES AND THEIR SIGNIFICANCE

Tribological properties or behaviour (for example, coefficient of friction and slip ratio) is used to characterise states occurring in a system due to tribology. Wear, friction and lubrication are the three main elements of tribology with various sub-elements within, e.g., surface engineering [4]. There are many wear mechanisms, however, the predominant wear found in LPBF is abrasive as shown by Gopinath et al. [5]. AM has increased in usage in various industries where tribology must be manipulated in order to achieve the desired result and lifetime cycle.

There are several methods of manipulating the tribological properties of SLM materials for instance application of surface coatings, processing parameters, nanomaterials and textured surfaces. Material properties and the microstructure can easily be manipulated using altering processing parameters such as: hatch spacing; scan speed; laser power; scan angle; point distance; and exposure time [6], consequently varying the tribological behaviour of the part. Numerous research is currently being carried out inspecting the relationship between tribology and specifically density and microhardness, however, these properties are usually measured as a consequence of the materials and manufacturing conditions used, rather than designed as an output of the process. For example, Han et al. [7] purposefully manipulated scanning speed and hatch spacing predominately, after thermal behaviour simulations, and produced specimens that had a 39% increase in microhardness in comparison with as-fabricated composite samples. It is thought that the SLM produced components plastically deformed and resulted in grain elongation and deformation.

PROCESSING PARAMETERS AND TRIBOLOGY

The influence of Volumetric Energy Density

The relationship between tribological performance and processing parameters is not extremely clear in previous research. One possible issue is the adoption of the design parameter volumetric energy density ($VED, J/mm^3$) for comparison of results, which is calculated as follows:

$$ED_v = \frac{P}{v h t} \quad (1)$$

where P is laser power, v is the laser scanning speed, h is the hatch spacing between adjacent laser scanning tracks, and t is the layer thickness [8]. VED has restricted the potential of application because it does not have the ability to capture the complex physics of the melt pool, for example Marangoni flow and recoil pressure. Some studies will use different combinations of parameters, for instance using the laser beam diameter instead of hatch spacing [9]. Thomas et al. utilised a normalised ED which considers both processing parameters and material properties:

$$ED^* = \left(\frac{AP}{2 v t r} \right) * \left(\frac{1}{0.67 \rho C_p (T_m - T_0)} \right) * \left(\frac{1}{h^*} \right) \quad (2)$$

where A is the material's absorptivity, r is the laser beam radius, ρ is the material's density, C_p is the specific heat capacity, T_m is the melting point, T_0 is the initial temperature of the powder-bed, and h^* is the dimensionless hatch spacing derived from (h/r) [10]. It is immediately clear from the equation that the normalised ED takes into consideration more influential parameters on the specimen. Nonetheless, a limitation of the formula is the absence of absorptivity data for powder materials. Published absorptivity values are often produced using polished metal plates, and therefore have limited relevance to metallic powders. Furthermore, the absorptivity of materials is altered based on the processing parameters used in LPBF thus, published values can be immensely unreliable [11].

Other experimental work was done by King et al. [12] where a normalised melt pool depth as a function of normalised enthalpy was embedded, to consider the melt pool behaviour as well. Still, beyond the threshold, the normalised enthalpy does not include any other physics that are present in keyhole formation and can pose possible problems. Most formulas utilised in previous research do not explore scan or hatch patterns, the gas flow rate used in the gas chamber, the number of times a layer has been scanned, and various other components [3]. The energy density formula is useful for comparisons but if there are not greatly varying process parameters utilised (limiting different melt pool behaviour), it could lead to incorrect assumptions. Contradictory to most studies, Greco et al. [13] manipulated the volumetric energy density by adopting a constant VED value in experimentation even with varying laser power, layer thickness, and hatch spacing through altering the scanning speed accordingly. Consistent relative densities of up to 99.9% were achieved, further depicting that the VED does not portray the true phenomenon occurring during LPBF printing.

Current research of core processing parameters

Presently, there is a lot of contradictory research in the connection between the tribological behaviour of specimens and processing parameters applied. Li et al. [14] concluded that 316L stainless steel samples produced via SLM with differing laser powers and build-up directions do not considerably influence the coefficient of friction or the wear rate. It was noticeable that lower laser powers produced specimens with more pores and a lower hardness.

Theoretically, a higher wear rate should be expected yet, the results attained demonstrated that these samples, produced at lower laser powers, do not differ immensely from the other samples in their tribological properties, possibly due to plastic deformation eliminating the pores. Contradictory to Li et al.'s research, Sagbas et al. [15] demonstrated that laser power alongside scan speed, scan angle and hatch distance all manipulate the wear behaviour of specimens of Ti6Al4V. Scan angle was responsible for approximately 50% of the contribution ratio, with the other processing parameters having equal contribution. The coefficient of friction and hardness were noticeably affected by the processing parameters, thus the wear resistance of the SLM manufactured parts varied. Pant et al. [16] identified that laser power influences microhardness more in comparison to the core processing parameters. According to Taguchi design the laser power followed by hatch spacing and scan speed influence the specific wear rate the most, juxtaposing both Li et al. and Sagbas et al.

The effect of porous structures on tribology

There is current debate as to whether a controlled porous structure is more beneficiary to wear and friction over a fully dense part. Zhu et al. [17] stated that if material densification is increased (decreasing pores) the tribological performance of 316L stainless steel SLM samples should increase due to more refined grains in the microstructure. Another study by Li et al. [18] showed that, after dry sliding wear tests under different loads, the wear track morphology of the same material produced similar flats and high peak areas with no pores. During testing, the debris formed was forced into the pores due to a high contact pressure, possibly assisting the tribological behaviour of the component along its cycle. Li et al. [19] also witnessed the potential of pores in medical Ti6Al4V printed specimens. The porosity was amended to achieve a structure like that of bone for an orthopaedic application. Samples were printed using a laser power of 180-200W with wear being analysed throughout; it was found that finer and more ordered pores on the surface of the components produced a more desirable friction and wear result. This was a result of extra lubrication being captured in the pores allowing for a better resistance to wear.

Many studies prove that a higher density produces a less porous microstructure, thus a lower coefficient of friction and wear rate. A study by Rathod et al. [20] investigates the effect of SLM specimens built with a single melt (SM) and checkerboard (CB) scanning strategies on density and wear rate. SM samples produced a relative density of 96% while CB specimens were able to achieve a higher relative density of 98.5%. It was shown that the porosity significantly altered the wear rate, and SM samples exhibited a higher wear rate due to an increased number of pores present, therefore, a more predominant abrasive wear mechanism. Pekok et al. [21] depicts an inversely proportional relationship between VED and microhardness. Hence, at lower VEDs an increase in microhardness can be witnessed because of a decrease in melt pool size and temperature gradients allowing for an increase in cooling rate, to create a fine-grained microstructure and restricting dislocation movement. This is despite cracks being visible in the AA2024 SLM fabricated parts as a result of incomplete fusion and porosity. The main obstacle for these parts were small gas pores in the microstructure. On the other hand, fusion holes, unmelted power, alongside hot cracks and irregularly shaped pores were the primary concern for samples outside of the red line. AlMangour et al. [22] demonstrated similar results

with better mechanical and tribological properties found at higher densification with reduced scanning speed, since improved binding between the molten particles can be seen.

Printed textured surfaces and their tribological behaviour

Printed textured surfaces has the potential of altering the tribological behaviour of components, by creating pockets for lubrication and wear debris. Currently, there has been limited research in the relationship of printed textured surfaces and SLM specifically. Nonetheless, a study by Wang et al. [23] examines the potential of disc (DTS) and ring (RTS) textured surfaces on the coefficient of friction of 304 stainless steel. It was found that DTS provides a relatively low friction coefficient compared to that of RTS, aiding in the reduction of friction on the system (a pin-on-disk tribometer was adopted). Fielden-Stewart et al. [24] also altered the surface of specimens by modifying the printing angle (45°-90°); it was concluded that the printing angle and surface roughness increased in correlation to one another, the interfacial fracture toughness for adhesive wear also increased accordingly. Another study conducted by Gogolewski et al. [25], similar to that of Fielden-Stewart et al., investigated the formation of convex and concave hemisphere surface textures produced alongside an altering printing angle (0°- 90°). Printing irregularities were visible, such as flattened tops in convex bumps, occasional extra material between the texturing, and irregular powder particles found in the lower areas of the concave hemispheres. A correlation between printing angle, textured surface and surface roughness was not realised, due to an inaccurate metrological control and a varying distribution of the coefficient of friction for each specimen. However, it should be noted that the tribological behaviour was successfully altered using concave and convex hemisphere texturing. The addition of textured surface has the potential to largely manipulate the tribological properties of a component, especially with optimised processing parameter.

FUTURE RESEARCH WORK

Modifying processing parameters with both densification and the addition of pores both have the potential to significantly alter the tribology of a system. Alongside the addition of textured surfaces (for instance triangular and square structures) for an already optimised part could provide the perfect balance of tribological properties.

Conflicts of interest

The author declares no Conflicts of interest.

REFERENCES

- [1] T. Wohlers, and T. Gornet, 'History of additive manufacturing' in *Wohlers report 2014: 3D printing and additive manufacturing state of the industry annual worldwide progress report*, Fort Collins (Colorado): Wohlers Associates, p.118, 2014.
- [2] M. Averyanova, E. Cicala, Ph. Bertrand, and D. Grevey, 'Experimental design approach to optimize selective laser melting of martensitic 17-4 PH powder: part I – single laser tracks and first layer', *Rapid Prototyping Journal*, vol. 18, no. 1, pp. 28–37, Jan. 2012. doi.org/10.1108/13552541211193476
- [3] N. T. Aboulkhair, M. Simonelli, L. Parry, I. Ashcroft, C. Tuck, and R. Hague, '3D printing of Aluminium alloys: Additive Manufacturing of Aluminium alloys using selective laser melting', *Progress in Materials Science*, vol. 106, p. 100578, Dec. 2019. doi.org/10.1016/j.pmatsci.2019.100578
- [4] Y. Meng, J. Xu, Z. Jin, B. Prakash, and Y. Hu, 'A review of recent advances in tribology', *Friction*, vol. 8, no. 2, pp. 221–300, Apr. 2020. doi.org/10.1007/s40544-020-0367-2
- [5] V. M. Gopinath and S. Arulvel, 'A review on the steels, alloys/high entropy alloys, composites and coatings used in high temperature wear applications', *Materials Today: Proceedings*, vol. 43, pp. 817–823, 2021. doi.org/10.1016/j.matpr.2020.06.495
- [6] J. Delgado, J. Ciurana, and C. A. Rodríguez, 'Influence of process parameters on part quality and mechanical properties for DMLS and SLM with iron-based materials', *International Journal of Advanced Manufacturing Technology*, vol. 60, no. 5, pp. 601–610, May 2012. doi.org/10.1007/s00170-011-3643-5
- [7] Q. Han, R. Setchi, F. Lacan, D. Gu, and S. L. Evans, 'Selective laser melting of advanced Al-Al₂O₃ nanocomposites: Simulation, microstructure and mechanical properties', *Materials Science and Engineering: A*, vol. 698, pp. 162–173, Jun. 2017. doi.org/10.1016/j.msea.2017.05.061
- [8] Q. Han, R. Setchi, F. Lacan, D. Gu, and S. L. Evans, 'Selective laser melting of advanced Al-Al₂O₃ nanocomposites: Simulation, microstructure and mechanical properties', *Materials Science and Engineering: A*, vol. 698, pp. 162–173, Jun. 2017. doi.org/10.1016/j.addma.2019.04.018
- [9] U. Scipioni Bertoli, A. J. Wolfer, M. J. Matthews, J.-P. R. Delplanque, and J. M. Schoenung, 'On the limitations of Volumetric Energy Density as a design parameter for Selective Laser Melting', *Materials & Design*, vol. 113, pp. 331–340, Jan. 2017. doi.org/10.1016/j.matdes.2016.10.037
- [10] M. Thomas, G. J. Baxter, and I. Todd, 'Normalised model-based processing diagrams for additive layer manufacture of engineering alloys', *Acta Materialia*, vol. 108, pp. 26–35, Apr. 2016. doi.org/10.1016/j.actamat.2016.02.025
- [11] H. Li, M. Ramezani, M. Li, C. Ma, and J. Wang, 'Effect of process parameters on tribological performance of 316L stainless steel parts fabricated by selective laser melting', *Manufacturing Letters*, vol. 16, pp. 36–39, Apr. 2018. doi.org/10.1016/j.mfglet.2018.04.003
- [12] W. E. King *et al.*, 'Observation of keyhole-mode laser melting in laser powder-bed fusion additive manufacturing', *Journal of Materials Processing Technology*, vol. 214, no. 12, pp. 2915–2925, Dec. 2014. doi.org/10.1016/j.jmatprotec.2014.06.005
- [13] S. Greco, K. Gutzeit, H. Hotz, B. Kirsch, and J. C. Aurich, 'Selective laser melting (SLM) of AISI 316L—impact of laser power, layer thickness, and hatch spacing on roughness, density, and microhardness at constant input energy density', *The International Journal of Advanced Manufacturing Technology*, vol. 108, no. 5-6, pp. 1551–1562, May 2020. doi.org/10.1007/s00170-020-05510-8
- [14] H. Li, M. Ramezani, M. Li, C. Ma, and J. Wang, 'Effect of process parameters on tribological performance of 316L stainless steel parts fabricated by selective laser melting', *Manufacturing Letters*, vol. 16, pp. 36–39, Apr. 2018. doi.org/10.1016/j.mfglet.2018.04.003
- [15] B. Sagbas, G. Gencelli, and A. Sever, 'Effect of Process Parameters on Tribological Properties of Ti6Al4V Surfaces Manufactured by Selective Laser Melting', *Journal of Materials Engineering and Performance*, vol. 30, no. 7, pp. 4966–4973, Jul. 2021. doi.org/10.1007/s11665-021-05573-y
- [16] M. Pant, L. Nagdeve, G. Moona, H. Kumar, and A. Sharma, 'Tribological behavior investigation of 316L stainless steel samples processed by selective laser melting', *Proceedings of the Institution of Mechanical Engineers, Part J: Journal of Engineering Tribology*, vol. 237, no. 4, pp. 718–731, Apr. 2023. doi.org/10.1177/13506501221101797
- [17] Y. Zhu, J. Zou, X. Chen, and H. Yang, 'Tribology of selective laser melting processed parts: Stainless steel 316 L under lubricated conditions', *Wear*, vol. 350–351, pp. 46–55, Mar. 2016. doi.org/10.1016/j.wear.2016.01.004
- [18] H. Li, M. Ramezani, M. Li, C. Ma, and J. Wang, 'Tribological performance of selective laser melted 316L stainless steel', *Tribology International*, vol. 128, pp. 121–129, Dec. 2018. doi.org/10.1016/j.triboint.2018.07.021

- [19] P. Lu, M. Wu, X. Liu, W. Duan, and J. Han, 'Study on Corrosion Resistance and Bio-Tribological Behavior of Porous Structure Based on the SLM Manufactured Medical Ti6Al4V', *Metals and Materials International*, vol. 26, no. 8, pp. 1182–1191, Aug. 2020.
doi.org/10.1007/s12540-019-00506-w
- [20] H. J. Rathod, T. Nagaraju, K. G. Prashanth, and U. Ramamurty, 'Tribological properties of selective laser melted Al 12Si alloy', *Tribology International*, vol. 137, pp. 94–101, Sep. 2019.
doi.org/10.1016/j.triboint.2019.04.038
- [21] M. A. Pekok, R. Setchi, M. Ryan, Q. Han, and D. Gu, 'Effect of process parameters on the microstructure and mechanical properties of AA2024 fabricated using selective laser melting', *International Journal of Advanced Manufacturing Technology*, vol. 112, no. 1–2, pp. 175–192, Jan. 2021.
doi.org/10.1007/s00170-020-06346-y
- [22] B. AlMangour, D. Grzesiak, J. Cheng, and Y. Ertas, 'Thermal behavior of the molten pool, microstructural evolution, and tribological performance during selective laser melting of TiC/316L stainless steel nanocomposites: Experimental and simulation methods', *Journal of Materials Processing Technology*, vol. 257, pp. 288–301, Jul. 2018.
doi.org/10.1016/j.jmatprotec.2018.01.028
- [23] X. Wang, J. Liu, Y. Wang, and Y. Fu, 'Fabrication of friction-reducing texture surface by selective laser melting of ink-printed (SLM-IP) copper (Cu) nanoparticles(NPs)', *Applied Surface Science*, vol. 396, pp. 659–664, Feb. 2017.
doi.org/10.1016/j.apsusc.2016.11.003
- [24] Z. Fielden-Stewart, T. Coope, D. Bacheva, and B. C. Kim, 'Effect of the surface morphology of SLM printed aluminium on the interfacial fracture toughness of metal-composite hybrid joints', *International Journal of Adhesion and Adhesives*, vol. 105, p. 102779, Mar. 2021
doi.org/10.1016/j.ijadhadh.2020.102779
- [25] D. Gogolewski, T. Kozior, P. Zmarzły, and T. G. Mathia, 'Morphology of Models Manufactured by SLM Technology and the Ti6Al4V Titanium Alloy Designed for Medical Applications', *Materials*, vol. 14, no. 21, p. 6249, Oct. 2021.
doi.org/10.3390/ma14216249

Baramate KA

*Cardiff University
School of Engineering*

Lacan F

*Cardiff University
School of Engineering*

Ryan M

*Cardiff University
School of Engineering*

Gandopadhyay S

*Indian Institute of Technology Bhilai
Department of Mechanical Engineering*

Baduri D

*Cardiff University
School of Engineering*

ADVANCED MANUFACTURING

Development of a Net Zero Route for the Circular Production of Additive Manufacturing Powders

The research centres on the development of a Net Zero route for the sustainable production of metal additive manufacturing (AM) powders. In particular, the study involves recycling of waste machining chips to produce usable AM powders via solid-state crushing/ball milling (BM) at room temperature. Experimental work deals with the conversion of AA5083-H111 aluminium chips into powders using BM, followed by powder characterisation. It is observed that the particle size distribution and the powder morphology are influenced by the chip's length scale and BM parameters (such as ball-to powder ratio, ball diameter, milling speed and time). Finally, a framework of a novel circular hybrid manufacturing process chain to fabricate high value AM parts from the produced powders is proposed.

Keywords:

Net Zero, sustainable manufacturing, additive manufacturing, ball milling, aluminiums.

Corresponding author:

BaramateKA1@cardiff.ac.uk



K.A. Baramate, F. Lacan, M. Ryan, S. Gangopadhyay, and D. Badhuri, 'Generalizability of Deep Learning Models on Brain Tumour Segmentation', *Cardiff University School of Engineering Research Conference 2023*, Cardiff, UK, 2023, pp. 123-127.

doi.org/10.18573/conf1.ac

INTRODUCTION

The United Nations Framework Convention on Climate Change (UNFCCC) in their annual Conference of Parties (COP) addresses the issues of climate change by reducing greenhouse gas emissions and accelerating the Paris agreement. In 2015, the United Nations have adopted 17 Sustainable Development Goals (SDGs) as part of the 2030 Agenda for Sustainable Development. Of these, SDG 12 that states “Ensure sustainable consumption and production patterns” [1] is directly relevant to the theme of the current research activities on sustainable manufacturing, undertaken by the High-Value Manufacturing Group at Cardiff University. The research strategy further aligns with the UK Government’s ‘Net Zero’ targets to reduce the net CO₂ emissions from energy and industrial processes via greater promotion of circular economy and sustainable manufacturing [1, 2].

The global additive manufacturing (AM) market is expected to expand at a compound annual growth rate of 20.8% from 2022 to 2030 [3]. Research evidenced that metal powder cost is the largest continuous expense through the life of an AM machine. However, the standard metal AM powder production processes involve melting and atomisation of raw billets/ingots via water, gas, and plasma atomisation [4]. These processes and the powder supply chain makes them expensive. Substantially these techniques incur significant amount of energy consumption and generate carbon footprint. A recent study has compared the environmental impacts of metal AM processes against the conventional manufacturing (CM) technology. For example, 50-192 CO₂eq. is released to process aluminium material per kg by AM while CM releases 0.036-9.6 CO₂eq. compared to casting, extrusion, rolling, and wire drawing processes [5]. AM typically has a significantly higher carbon footprint per kilogram of material, sometimes by a factor of 10 or more. When accounting for embodied impacts in the materials, the environmental impact of AM can be multiplied by 1.4 to 8 times. However, this may not be an equitable comparison, as AM has the capability to produce certain components in a single step that would otherwise require multiple steps in conventional manufacturing processes [5]. A subject of exploration within this domain is the investigation of how employing remanufacturing or recycling purposes to this technology may diminish the ecological and economic impact of a component.

Research has been undertaken to recycle machining chips for powder metallurgy route [6, 7], and applications such as powder consolidation compaction and sintering [8–10]. With regard to the AM applications, ball milled (BM) chip powders or unprocessed chips were mainly tested in single-track melting via directed energy deposition (DED) [11, 12] and laser powder bed fusion (LPBF) processes [13]. The evidence of the fabrication of complete AM parts from ball milled powders is however extremely limited [14]. The majority of research on single-track melting/full part fabrication involved the DED process, partly because of the less stringent requirement on powder properties (sphericity, flowability, packing density..., compared to that needed for the LPBF process [15]. The current research therefore aims to generate AM powders via ball milling, for LPBF applications. A novel Circular Hybrid Manufacturing (CHM) route is developed to process and utilise BM powders in fabricating functional post-processed LPBF parts. Figure 1 shows the schematic of the CHM process chain.

MATERIALS AND METHODS

The chips of AA5083-H111 aluminium alloy of ~1-3 mm length scale was obtained from conventional milling operation on a vertical CNC milling machine. A representative image of the chips is shown in Fig. 2a. A 4-tooth carbide end mill cutter with 16 mm dia. was used for the milling operation at 85 m/min, 0.24 mm/rev feed rate and an axial depth of cut of 0.5 mm. The machined chips were cleaned with acetone and isopropyl alcohol in an ultrasonic bath to remove impurities originated from cutting fluid and grease. The cleaned chips were then dried in an oven at 90°C for 60 min to eliminate the moisture content. Subsequently, the chips were ball milled in a planetary ball mill, made by MECHMIN, Ltd., India (Fig. 2b).

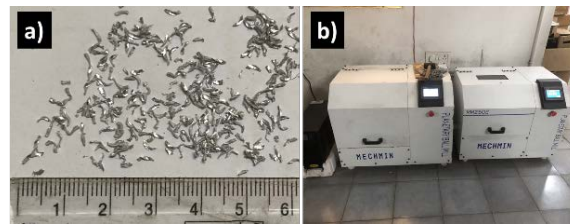


Fig. 2. a) Raw AA5083 chips, b) MECHMIN Planetary ball mill.

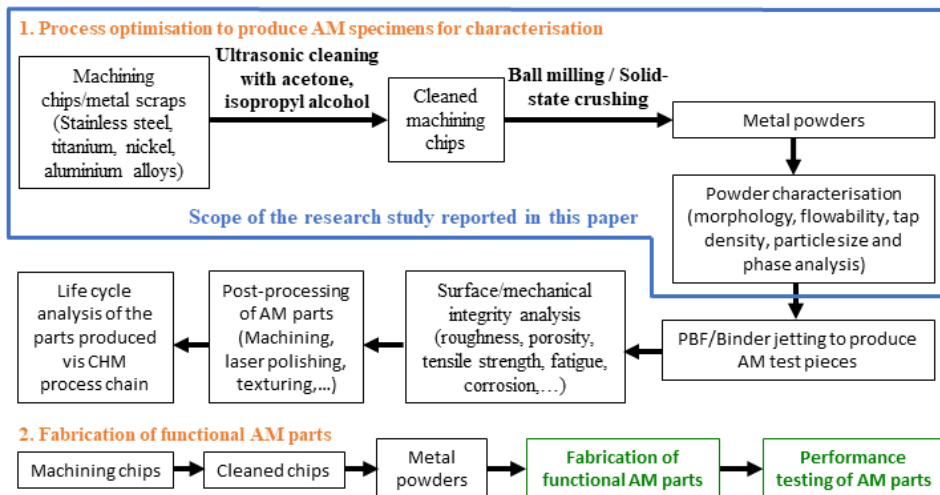


Fig. 1. Schematic of the CHM process chain.

On the dual working station ball mill, two hardened stainless steel cylindrical vials/jars with 250 ml and 100 ml volume and three different ball diameters (20 mm, 10 mm, 5 mm) were used. Approximately 50-60% of the jar volume was filled with the balls and the chip material. For BM operation, 15 balls of 20 mm dia., and 50 balls of 10 mm dia. were used in each of the 250 ml vials, and 250 balls of 5 mm dia. were used in each 100 ml jar. Three different ball-to-powder ratios (BPR), such as 15:1, 20:1, and 30:1 were utilised in different stages of BM. A 300 rpm BM rotational speed was typically used with 10 and 20 mm balls, however an exploratory trial involved 500 rpm speed when using 10 mm balls. A reduced BM speed of 150 rpm was employed when using the 5 mm balls.

There sets of multi-stage BM trials, involving 2 or 3 stages per set were undertaken in Phase 1, details given in Table 1. An on/off cycle of 15 min was applied when BM to avoid excessive heating of the milling media. So, the total machine cycle time for 30 min of BM run was 45 min, and 105 min for 60 min BM run.

Sets and Stages		BPR	Ball diameter (mm)	Jar volume (ml)	BM speed (rpm)	BM time (min)
Set 1.1	Stage 1	20:1	20	250	300	30
	Stage 2	20:1	10	100	300	30
	Stage 3	20:1	5	100	150	90
Set 1.2	Stage 1	30:1	20	250	300	30
	Stage 2	30:1	10	100	300	30
	Stage 3	30:1	5	100	150	90
Set 2.1	Stage 1	15:1	20	250	300	30
	Stage 2	15:1	5	100	150	90
Set 2.2	Stage 1	20:1	20	250	300	30
	Stage 2	20:1	5	100	150	90
Set 2.3	Stage 1	30:1	20	250	300	30
	Stage 2	30:1	5	100	150	90
Set 3	Stage 1	15:1	20	250	300	60
	Stage 2	10:1	10	250	500	30

Table 1. Phase 1 multi-stage BM parameters.

After Stage 1 in each set, ball milled powders were sieved to <math><180\mu\text{m}</math> and used for the next successive stages. It was observed in Set 3, that although a higher BM speed, i.e., 500 rpm, was safe to be used with 10:1 BPR, however the same speed caused considerable noise and vibration when used with larger balls (such as 20 mm).

Based on the visual inspection, particle size and powder morphology results from the Phase 1 BM powders, the Phase 2 BM parameters were selected and are shown in Table 2.

Sets and Stages		BPR	Ball diameter (mm)	Jar volume (ml)	BM Speed (rpm)	BM time (min)
Set 1	Stage 1	15:1	20	250	300	60
	Stage 2	10:1	10	250	300	30
	Stage 3	10:1	5	100	150	60
Set 2	Stage 1	15:1	20	250	300	60
	Stage 2	10:1	10	250	500	30
	Stage 3	10:1	5	100	150	60

Table 2. Selected BM parameters in Phase 2.

Assessing the scope of the study of the BM process to reduce the processing time and produce powders in sufficient quantity a 10:1 BPR was selected for Stage 2 and Stage 3 in both sets.

The powder morphology was analysed using a Carl Zeiss FEG scanning electron microscope (SEM). Particle size distribution was obtained via mechanical sieving with three sets of sieve size - 63, 150 and 180 μm . Phase detection on the powder particles was carried out using a Bruker D8 Advance X-ray diffractometer (XRD) with a Cu-K α target, 0.03° step size, 0.5 s/step scan speed, 40 kV voltage and 30 mA current, within a 2 θ range of 20°-90°.

RESULTS AND DISCUSSIONS

In the planetary ball milling technique, the process parameters play a vital role in producing fine powders. The particle sizes are influenced by BPR, BM time, and BM speed [16]. Fig. 3 shows the powder morphology of the BM AA5083 powders at different stages as mentioned in Table 1 and 2. The particles obtained with the 20:1 BPR in all stages were flattened and irregular in shape, possibly due to plastic deformation (Figs. 3a and 3c).

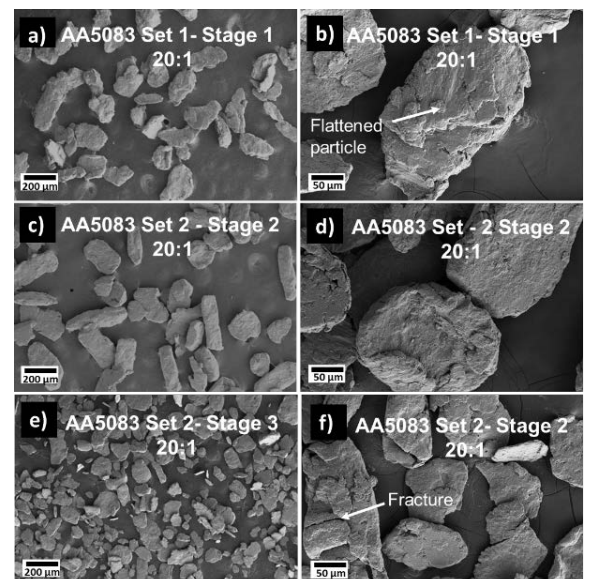


Fig. 3. SEM images of BM AA5083 powder particles after each stage of Set 1.1

It was observed adopting a multi-stage BM process aided in reducing the particle size. This is also recommended in [12]. Indeed, the particle size reduced from Stage 2 to Stage 3 in Phase 1, when using smaller 5 mm balls (Figs. 3e and 3f). This observation is corroborated by the particle size distribution analysis. In Phase 1, ~18% (by weight) of the BM particles were <180 μm after Set 1-Stage 1 with respect to the total BM chip weight. In contrast, ~63% of the BM powders were <180 μm after Set 2 Stage 2 in Phase 2. The particle size distribution in Fig. 4 reveals that ~70% of the particles were <180 μm after Set 2-Stage 3 BM. SEM images further reveal plastic deformation on the particles. This is possibly because the AA5083 alloy is typically a ductile material. A few cleaved fractured regions can also be seen which could be attributed to the material’s strain hardening ability due to the presence of ~4-4.9% Mg in the alloy. Phase analysis on the aluminium chips and the BM powders using XRD displayed Al and Al₂O₃ peaks at the standard 2θ positions, see Fig. 5.

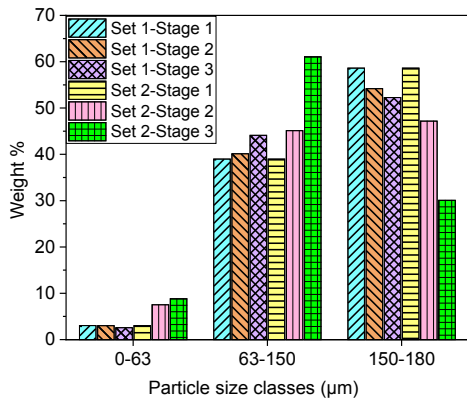


Fig. 4. Particle size distribution of BM AA5083 powders via sieving, obtained in Phase 2.

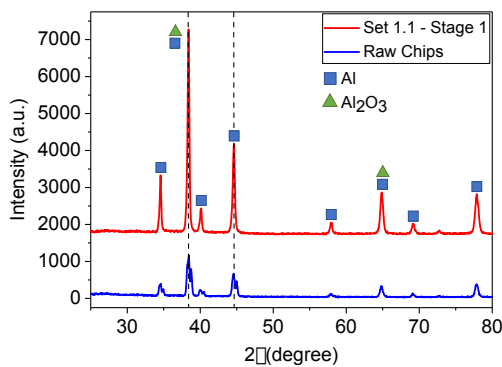


Fig. 5. XRD analysis of AA5083 powder particles.

Following the successful generation of powders via BM from machining chips, the next phase of the research aims at building AM parts using an in-house LPBF system. A new reduced build volume (RBV) kit has been designed and fabricated (Fig. 6) in order to be used in the in-house LPBF system.

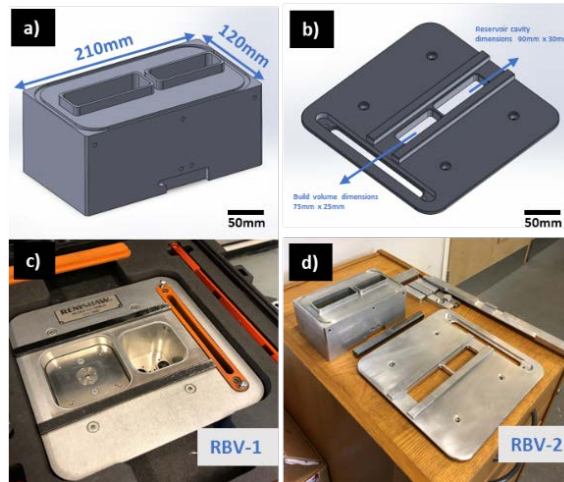


Fig. 6. Design and fabrication of the RBV kit for the in-house LPBF system: a) Build block, b) Top plate, c) Existing RBV kit (80 mm × 80 mm), d) Newly fabricated RBV kit (25 mm × 75 mm).

CONCLUSIONS

The research outlined in this paper is the cornerstone for implementing the net zero strategy to the circular manufacturing of AM powders. This work illustrates how BM can convert machining chips into powders suited for LPBF process. The results indicate that it is important to optimise the BM parameters (such as BPR, BM time, rotational speed, ball diameter and material) to produce powders with the targeted particle size and shape. The composition of the chips and their length scale also showed a considerable impact on the effectiveness of the BM process as well as on the particles’ morphology and size distribution. SEM images reveal flattened particles in Stage 1 of all trial sets, which became more spherical with reduced particle size when subject to multi-stage BM. Nonetheless, greater particle sphericity, suitable for LPBF process, is yet to be achieved. The next step of the current work will be the fabrication of AA5083 AM test pieces (particles sieved under 180 μm) on the in-house LPBF system. The parts’ surface integrity and mechanical properties will be compared with those built using commercial Al powders with comparable properties.

Acknowledgments

The research is supported by the Government of Maharashtra’s (India) PhD studentship award (Rajarshi Shahu Maharaj Foreign Scholarship) and the Net Zero Innovative Institute’s (NZII) Seedcorn fund. The authors acknowledge the ERDF (European Regional Development Fund) and Wolfson Foundation for funding the CCI (Cardiff Catalysis Institute) Electron Microscopy Facility.

Conflicts of interest

The authors declare no conflict of interest.

REFERENCES

- [1] Net Zero Strategy: <https://www.gov.uk/government/publications/net-zero-strategy> (accessed on 05.07.2022).
- [2] J.M. Allwood, 'Absolute Zero: Delivering the UK's Climate Change Commitment with Incremental Changes to Today's Technologies', UK FIRES: Engineering and Physical Sciences Research Council, UK, 2019.
- [3] 'Additive Manufacturing Market Size Report 2030', <https://www.grandviewresearch.com/industryanalysis/additive-manufacturing-market> (accessed on 16/02/2023).
- [4] J. Dawes, R. Bowerman, and R. Trepleton, 'Introduction to the Additive Manufacturing Powder Metallurgy Supply Chain', *Johnson Matthey Technology Review*, vol. 59, no. 3, pp. 243–256, Jul. 2015. doi.org/10.1595/205651315X688686
- [5] C. Van Sice and J. Faludi, 'Comparing environmental impacts of metal additive manufacturing to conventional manufacturing', *Proceedings of the Design Society*, vol.1, pp.671-680, Aug.2021. doi.org/10.1017/pds.2021.67
- [6] A. Mahboubi Soufiani, M. H. Enayati, and F. Karimzadeh, 'Fabrication and characterization of nanostructured Ti6Al4V powder from machining scraps', *Advanced Powder Technology*, vol. 21, no. 3, pp. 336–340, May 2010. doi.org/10.1016/j.apt.2009.12.018
- [7] S. R. Shial, M. Masanta, and D. Chaira, 'Recycling of waste Ti machining chips by planetary milling: Generation of Ti powder and development of in situ TiC reinforced Ti-TiC composite powder mixture', *Powder Technology*, vol. 329, pp. 232–240, Apr. 2018. doi.org/10.1016/j.powtec.2018.01.080
- [8] P. A. Pulido-Suárez, K. S. Uñate-González, J. G. Tirado-González, A. Esguerra-Arce, and J. Esguerra-Arce, 'The evolution of the microstructure and properties of ageable Al-Si-Zn-Mg alloy during the recycling of milling chips through powder metallurgy', *Journal of Materials Research and Technology*, vol. 9, no. 5, pp. 11769–11777, Sep. 2020. doi.org/10.1016/j.jmrt.2020.08.045
- [9] L. M. Rojas-Díaz, L. E. Verano-Jiménez, E. Muñoz-García, J. Esguerra-Arce, and A. Esguerra-Arce, 'Production and characterization of aluminum powder derived from mechanical saw chips and its processing through powder metallurgy', *Powder Technology*, vol. 360, pp. 301–311, Jan. 2020. doi.org/10.1016/j.powtec.2019.10.028
- [10] P. Jaya Teja, S. Ranjan Shial, D. Chaira, and M. Masanta, 'Development and characterization of Ti-TiC composites by powder metallurgy route using recycled machined Ti chips', *Materials Today: Proceedings*, vol. 26, pp. 3292–3296, 2020. doi.org/10.1016/j.matpr.2020.02.467
- [11] B. Fullenwider, P. Kiani, J. M. Schoenung, and K. Ma, 'Two-stage ball milling of recycled machining chips to create an alternative feedstock powder for metal additive manufacturing', *Powder Technology*, vol. 342, pp. 562–571, Jan. 2019. doi.org/10.1016/j.powtec.2018.10.023
- [12] J. W. Murray, A. Speidel, A. Jackson-Crisp, P. H. Smith, H. Constantin, and A. T. Clare, 'Unprocessed machining chips as a practical feedstock in directed energy deposition', *International Journal of Machine Tools and Manufacture*, vol. 169, p. 103803, Oct. 2021. doi.org/10.1016/j.ijmachtools.2021.103803
- [13] S. Dhiman *et al.*, 'Recycling of Ti6Al4V machining swarf into additive manufacturing feedstock powder to realise sustainable recycling goals', *Journal of Cleaner Production*, vol. 348, p. 131342, May 2022. doi.org/10.1016/j.jclepro.2022.131342
- [14] M. A. Jackson, J. D. Morrow, D. J. Thoma, and F. E. Pfefferkorn, 'A comparison of 316 L stainless steel parts manufactured by directed energy deposition using gas-atomized and mechanically-generated feedstock', *CIRP Annals*, vol. 69, no. 1, pp. 165–168, 2020. doi.org/10.1016/j.cirp.2020.04.042
- [15] I. E. Anderson, E. M. H. White, and R. Dehoff, 'Feedstock powder processing research needs for additive manufacturing development', *Current Opinion in Solid State and Materials Science*, vol. 22, no. 1, pp. 8–15, Feb. 2018. doi.org/10.1016/j.cossms.2018.01.002
- [16] S. Rosenkranz, S. Breitung-Faes, and A. Kwade, 'Experimental investigations and modelling of the ball motion in planetary ball mills', *Powder Technology*, vol. 212, no. 1, pp. 224–230, Sep. 2011. doi.org/10.1016/j.powtec.2011.05.021

Escudero-Ornelas AY

Cardiff University
School of Engineering

Bigot S

Cardiff University
School of Engineering

Davey E

Cardiff University
School of Engineering

Bhaduri D

Cardiff University
School of Engineering

Valera-Medina A

Cardiff University
School of Engineering

ADVANCED MANUFACTURING

A Study on the Surface Chemistry of Laser Textured Parts

The research investigates the changes in the surface properties and surface chemistry following laser microtexturing of stainless steel parts, in relation to their applications in the energy sector. In particular, the material compositions of the laser surface textured (LST) parts, together with the oxide compound formation on them are evaluated with respect to their wettability property. Wettability is crucial for heat exchange processes as it affects the efficiency of heat transfer by influencing surface contact and the formation of droplets on the heat exchanger surface. Here, two simple LST geometries, viz. channel and cross-hatch, were produced using a nanosecond fibre laser micromachining system. The wettability of the textured surfaces was then examined over a period of 45 days with an interval of 15 days. It was observed that the former geometry rendered a hydrophilic surface initially, which transformed to a hydrophobic surface after 45 days, whereas the latter LST design exhibited hydrophobic characteristic over the entire duration of the assessment. The material compositions and the oxide compound formation on the LST parts were analysed via energy dispersive spectroscopy, X-ray photoelectron spectroscopy and X-ray diffraction techniques and the results were correlated with the measured wettability data.

Keywords:

Microtexturing, laser manufacturing, micromachining, wettability, surface chemistry.

Corresponding author:

EscuderoOrnelasAY@cardiff.ac.uk



A.Y. Escudero-Ornelas, E. Davey, A. Valera-Medina, S. Bigot, and D. Bhaduri, 'A Study on the Surface Chemistry of Laser Textured Parts', *Cardiff University School of Engineering Research Conference 2023*, Cardiff, UK, 2023, pp. 128-132.

doi.org/10.18573/conf1.ad

INTRODUCTION

The British Petroleum Statistical Review of World Energy 2021 highlights the need of increasing renewable energy production by ~50% before 2050 [1] utilization, and storage; and nuclear power development. We used the annual 'British Petroleum statistical review of world energy 2021' report as our primary database. Globally, fossil fuels, renewable (primarily hydro, wind and solar. A viable approach to reach this goal is via reduction of energy consumption. In regard to the energy sector, microtextured surfaces can offer a viable passive mechanism for decreasing energy consumption by reducing drag and harnessing greater heat recovery in a turbulent and/or humid environment [2, 3] biomedical, transportation and aerospace sectors. In relation to the energy sector, microtextured surfaces provide an energy efficient and cost-effective passive mechanism for increased heat transfer during matter's phase change in energy recovery systems. This study explores the viability of laser microprocessing as an attractive manufacturing route for generating textured surfaces and compares with the results from a previous study involving microgeometries created by micro-wire electro discharge machining (μ WEDM).

One innovative approach to generate renewable energy from wind, gales, hurricanes, etc, is via developing High-Peak Perishable Energy Recovery systems that are capable of enhancing condensation heat transfer [4]. Such systems can be developed by producing microtextured surfaces on the components using various micromanufacturing techniques, e.g. electro-discharge machining, chemical machining and laser surface texturing (LST). The microtexture geometries, such as ridges grooves, and dimples can enhance the thermal capacity of the parts under isothermal fluid flow [5]. In wind energy applications, microtextures can improve the aerodynamic performance of wind turbine blades and increase the efficiency of energy generation [2]. As a passive energy-harvesting technology that requires no additional energy input or moving components, use of microtextured surfaces represent a promising pathway toward a sustainable future for the energy sector [6].

Over the past decade, manufacture of the microtextured surfaces has witnessed rapid growth. The correlation between microtextures and the boundary layer on the surfaces under turbulent fluid flow conditions has demonstrated the potential of minor surface modifications to significantly impact the fluid dynamics [7]. The primary aim of these microtextures is to alter surface properties, including wettability properties that can also be influenced by the surface chemistry [8, 9].

Previous research has proposed and analysed various computational fluid dynamics (CFD) software tools to identify the most effective simulations based on channel designs; however, the effects of the surface chemistry on the surface properties of the textured parts has not been considered [3]. Other studies have investigated the short- and long-term wetting behaviour of laser-textured stainless steel surfaces using femtosecond pulses and normal pulse mode, with applications in self-cleaning and anti-icing through homogeneous hydrophobic chemical modification [10]. The relationship between the surface microtexture and surface chemistry remains a topic of debate, as researchers strive to achieve desired wettability. Investigations into the surface chemistry of 2507 super duplex stainless steel in aerated, deaerated, and acidified artificial seawater have shown that the percentages of oxidised Cr, Fe(II), and hydroxides increase while film thickness decreases

with acidification [11]. A deeper understanding of the interactions among dispersive and non-dispersive chemical properties is still imperative [12]. A thorough analysis of the chemical compositions of the microtextured surfaces can enhance and contribute to the development of innovative surface modification techniques for other sectors, such as biomedical, marine, aerospace and automotive sectors [13, 14].

MATERIALS AND METHOD

Laser surface texturing was carried out on 316L stainless steel samples, of 35 mm \times 35 mm area and 2 mm thickness, on a Lasertec DMG-40 nanosecond fibre laser system.

To achieve a uniform and smooth surface prior to the laser texturing, the samples were cleaned with acetone and isopropyl alcohol, followed by drying in air. The nominal dimensions of the LST geometries are shown in Fig. 1 (a) while the CAD designs of the Channel and the Cross-hatch textures are displayed in Figs. 1 (b) and 1 (c), respectively. A 0.25 mJ laser energy at 80 kHz frequency were used to produce the textures, together with a 800 mm/s beam scanning speed and 100 μ m hatch distance. 50 scanning passes were given along machine X-axis to generate the Channel texture, whereas 50 passes were utilised along both X and Y-axes to produce the Cross-hatch pattern. The nominal laser beam diameter in all cases were fixed to 32 μ m.

The surface wettability tests were carried out by dropping 10 μ L of water from a syringe on the LST surfaces. The surfaces' wetting property was assessed over a duration of 45 days, with an interval of 15 days. Thus, the contact angles of the droplets were measured on Day 0, Day 15, Day 30, and Day 45, by using ImageJ software.

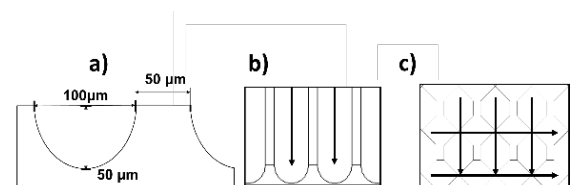


Fig. 1. (a) Texture dimensions, (b) Channel and (c) Cross-hatch designs.

The changes in the material compositions and the oxide compound formations on the LST surfaces over the duration of 45 days were analysed using different methods such as energy dispersive spectroscopy (EDS), X-ray photoelectron spectroscopy (XPS) and X-ray diffraction (XRD). A Thermo Fisher Scientific K-alpha+ spectrometer was utilised to conduct the XPS analysis. Samples were examined using a micro-focused monochromatic Al X-ray source (72 W) in the '400-micron spot' mode, where an analysis defining an elliptical X-ray spot of ~400 μ m \times 600 μ m was provided. The data was captured with pass energies of 150 eV for survey scans and 50 eV for high resolution scans, with step sizes of 1 eV and 0.1 eV, respectively. Data analysis was conducted using CasaXPS v2.3.24 software [15] discussions arising from a series of workshops have been a significant source for developing the overall XPS data processing concept and are the motivation for creating this work. These workshops organized by the Institut des Matériaux Jean Rouxel (IMN). The quantification was determined utilising a Shirley type background and Scofield cross-sections with an electron energy dependence of -0.6. XRD analysis was carried out

using a Siemens D5000 system using a CuK α X-ray target, from 20° to 90°, with a step angle of 0.02° and a scan step time of 1 s.

RESULTS AND DISCUSSION

The EDS analysis reveals that the LST specimens were prone to oxidation as they were produced under atmospheric conditions. As seen from Table 1, the oxygen content increased to 9.6 weight% in the Channel textured regions on Day 0, from a 5.3 wt% of oxygen content in the untextured areas. The same raised to 8.61 wt% in the Cross-hatched textures from 4.11 wt% in the untextured fields. The data also showed that the Fe content decreased in the textured areas, possibly due to the increased oxygen content. The higher oxygen content in the textured areas is attributed to the recast materials. Oxygen content was found to be less than 0.01% at the bottom of the Channels and 0.48% at the intersection of the grooves in the Cross-hatch design. However, the oxygen contents were ~24.54% and ~19.60% at the top of the riblets in the Channel and Cross-hatch textures, respectively. By comparing the chemical compositions of the Channel and Cross-hatch LSTs between Day 0 and Day 15, only minor changes were observed, except for the carbon content, which increased by over 1% in the Channel textures, but by only 0.46% in the Cross-hatch textures after 15 days.

	C	O	Fe	Si	Cr	Mn
Channel Day 0	5.77	9.60	57.87	0.34	16.02	1.38
Channel Day 15	6.89	9.86	57.80	0.36	15.79	1.39
Cross-hatch Day 0	4.13	8.61	60.35	0.33	16.93	1.76
Cross-hatch Day 15	4.59	8.02	60.53	0.34	16.76	1.62

Table 1. EDS results in wt% on the Channel and Cross-hatch textures after Day 0 and Day 15.

The SEM images of the textures are shown in Figs. 2 and 3. For the Channel specimens, the method of manufacturing was by removing layers along the X-axis, whereas for the Cross-hatch, the laser scanning was repeated along the Y-axis after completing scanning along the X-axis. This resulted in deeper craters in the Cross-hatch pattern, see Fig. 4.

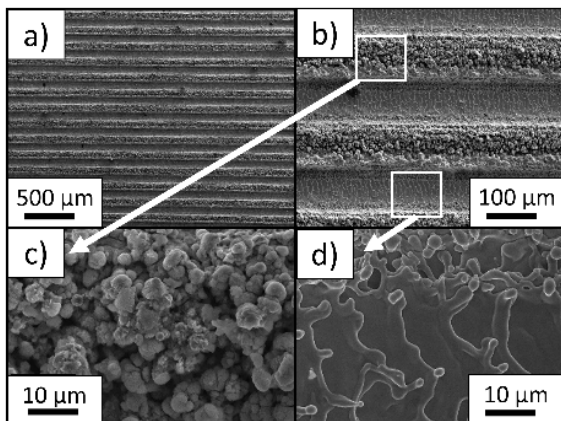


Fig. 2. SEM images of the Channel texture: Day 0.

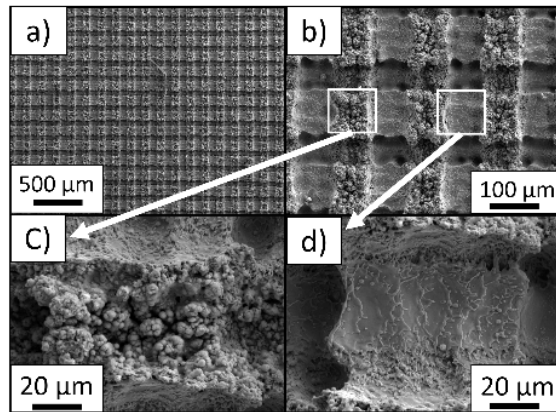


Fig. 3. SEM images of Cross-hatch texture: Day 0.

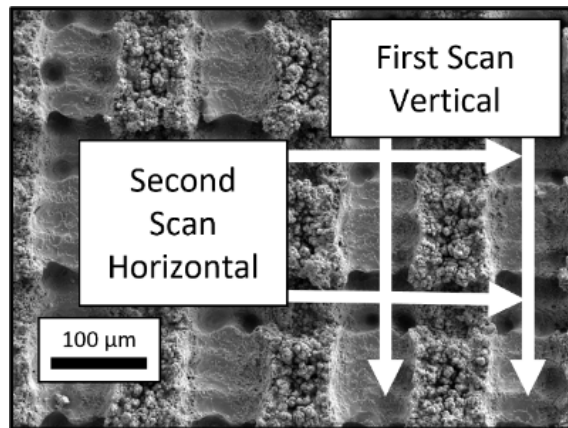


Fig. 4. Cross-hatch crater merge.

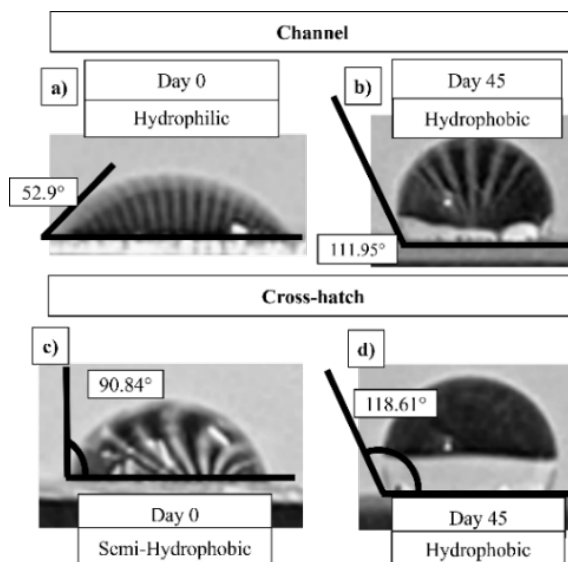


Fig. 5. Wettability contact angle results.

The images of the water droplets on the LST surfaces after Day 0 and Day 45 are shown in Fig. 5, together with the corresponding contact angles obtained via the ImageJ software. The changes in the measured contact angles over the period of 45 days are displayed in Fig. 6 overleaf. It is found that the contact angles for both textures increased considerably, by ~111.34% and ~30.57% for the Channel and Cross-hatch patterns, respectively.

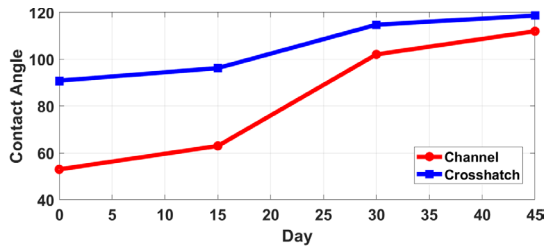


Fig. 6. Contact angles measured after Days 0, 15, 30, and 45.

The XRD spectra obtained from both Channel and Cross-hatch textures are shown in Fig. 7. The results show that iron (Fe), as well as the presence of Fe₂O₃ and Fe₃O₄, is in agreement with the EDS results, which indicates surface oxidation.

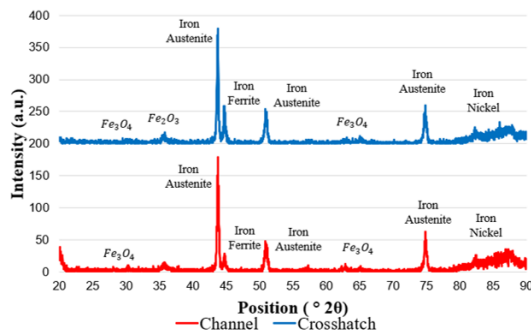


Fig. 7. XRD phase analysis on the Channel and Cross-hatch LST specimens.

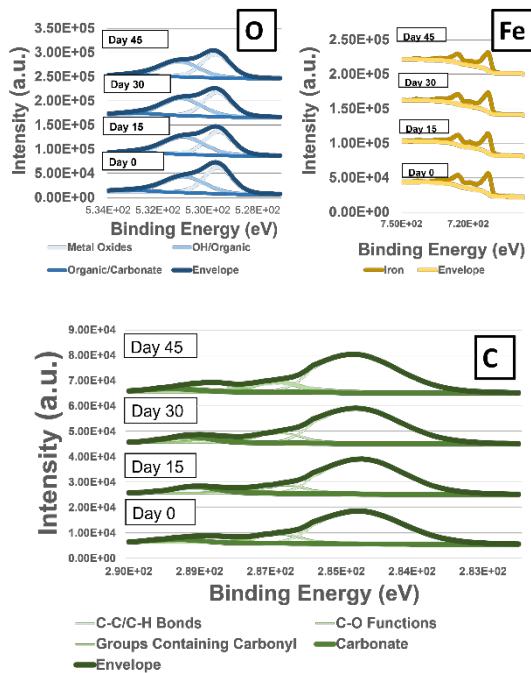


Fig. 8. XPS analysis of oxygen (O), iron (Fe) and carbon (C) on the Channel LST specimen.

The XPS results on the Channel design are shown in Fig. 8. Possibly the minor variation in the percentage of carbonyl groups attributed to the change in the wettability property of the Channel textures, i.e. from hydrophilic after Day 0 to become hydrophobic after Day 45.

CONCLUSIONS

The paper reports material composition and surface chemistry analysis of LST parts over a duration of 45 days after texturing. The effects of these two factors on the wettability property of the textured surfaces are evaluated. The data suggests that surface oxidation as well as the presence of certain carbon-based compounds (in particular, carbonyl groups) might play a crucial role in determining the hydrophilicity or hydrophobicity of the textured surfaces. Future work will involve an in-depth study investigating the effects of other elements present in the material, such as Cr, Mo, Ni, Mn and N, on the wettability property. A deeper insight in understanding of how surface chemistry changes via laser texturing will immensely aid in designing bespoke textured surfaces with controlled surface and material properties.

Acknowledgments

The research is supported by The Mexican National Council on Science and Technology (CONACYT) PhD scholarship.

Conflicts of interest

The authors declare no conflict of interest.

REFERENCES

- [1] J. L. Holecek, H. M. E. Geli, M. N. Sawalhah, and R. Valdez, 'A Global Assessment: Can Renewable Energy Replace Fossil Fuels by 2050?', *Sustainability*, vol. 14, no. 8, p. 4792, Jan. 2022.
doi.org/10.3390/su14084792
- [2] H. Martinez-Zavala, D. Bhaduri, P. Petkov, A. Valera-Medina, and S. Bigot, 'Effects of laser microtextured surfaces in condensation heat transfer', *Procedia CIRP*, vol. 95, pp. 927–932, 2020.
doi.org/10.1016/j.procir.2020.01.184
- [3] A. Yarden Escudero-Ornelas, D. Bhaduri, H. Martinez-Zavala, A. Valera-Medina, and S. Bigot, 'On the performance evaluation of microtextured surfaces using computational fluid dynamics: A comparative study', *World Congress on Micro and Nano Manufacturing - WCMNM 2022*, Leuven, Belgium.
- [4] H. Martinez Zavala, 'High peak, perishable energy recovery – foundation phase', PhD thesis, Cardiff University, 2022.
- [5] A. J. Mazaltarim, J. J. Bowen, J. M. Taylor, and S. A. Morin, 'Dynamic manipulation of droplets using mechanically tunable microtextured chemical gradients', *Nat Commun*, vol. 12, no. 1, p. 3114, May 2021.
doi.org/10.1038/s41467-021-23383-7
- [6] A. Sharma, D. Marla, S. S. Joshi, and R. Bathe, 'A Study of Femtosecond Laser Processed Microtextures on Silicon Wafers to Enhance Optical Absorption', *Lasers Manuf Mater Process*, vol. 9, no. 3, pp. 277–291, Sep. 2022.
doi.org/10.1007/s40516-022-00176-4
- [7] M. A. H. Al-fahham, S. Bigota, and A. Valera Medina, 'A Study of Fluid Flow Characteristics Using Micro Structured Surfaces Produced by WEDM', in *4M/ IWWMF2016 The Global Conference on Micro Manufacture: Incorporating the 11th International Conference on Multi-Material Micro Manufacture (4M) and the 10th International Workshop on Microfactories (IWWMF)*, 2016, pp. 247–250.
doi.org/10.3850/978-981-11-0749-8_708
- [8] F. Schell, S. Alamri, T. Steege, C. Zwahr, T. Kunze, and A. Lasagni, 'On the wetting behavior of laser-microtextured stainless steel using Direct Laser Interference Patterning', *Surface and Coatings Technology*, vol. 447, p. 128869, Oct. 2022.
doi.org/10.1016/j.surfcoat.2022.128869
- [9] S. Y. Misyura, G. V. Kuznetsov, D. V. Feoktistov, R. S. Volkov, V. S. Morozov, and E. G. Orlova, 'The influence of the surface microtexture on wettability properties and drop evaporation', *Surface and Coatings Technology*, vol. 375, pp. 458–467, Oct. 2019.
doi.org/10.1016/j.surfcoat.2019.07.058
- [10] G. Giannuzzi *et al.*, 'Short and long term surface chemistry and wetting behaviour of stainless steel with 1D and 2D periodic structures induced by bursts of femtosecond laser pulses', *Applied Surface Science*, vol. 494, pp. 1055–1065, Nov. 2019.
doi.org/10.1016/j.apsusc.2019.07.126
- [11] Z. Cui *et al.*, 'Passivation behavior and surface chemistry of 2507 super duplex stainless steel in artificial seawater: Influence of dissolved oxygen and pH', *Corrosion Science*, vol. 150, pp. 218–234, Apr. 2019.
doi.org/10.1016/j.corsci.2019.02.002
- [12] A. Samanta, Q. Wang, S. K. Shaw, and H. Ding, 'Roles of chemistry modification for laser textured metal alloys to achieve extreme surface wetting behaviors', *Materials & Design*, vol. 192, p. 108744, Jul. 2020.
doi.org/10.1016/j.matdes.2020.108744
- [13] C. Hu, D. Ashok, D. R. Nisbet, and V. Gautam, 'Bioinspired surface modification of orthopedic implants for bone tissue engineering', *Biomaterials*, vol. 219, p. 119366, Oct. 2019.
doi.org/10.1016/j.biomaterials.2019.119366
- [14] S. Arango-Santander, 'Bioinspired Topographic Surface Modification of Biomaterials', *Materials*, vol. 15, no. 7, p. 2383, Jan. 2022.
doi.org/10.3390/ma15072383
- [15] N. Fairley *et al.*, 'Systematic and collaborative approach to problem solving using X-ray photoelectron spectroscopy', *Applied Surface Science Advances*, vol. 5, p. 100112, Sep. 2021.
doi.org/10.1016/j.apsadv.2021.100112

Sustainable Energy



Sustainable Energy

- 135 Modelling and Simulation of a Hydrogen-Based Energy Storage System
- 140 Acoustic Noise Emission Detection and Location Analysis from a Scaled Laminated Transformer
- 145 Measuring the Coupled Effect of Heat and Stress on the Magnetic Properties of Electrical Steel
- 148 Development of a Multi-Community Peer-to-Peer Electricity Trading Mechanism
- 153 Double-ended Fault Location Method with Reduced Measurements
- 158 Spectroscopic Measurements of Light Emissions from High Current Arcs
- 163 Influence of Fuel Hydrogen Content and Atomisation Quality on Ultrafine Non-volatile Particulate Matter Emissions in RQL Gas Turbine Technology
- 168 Numerical Wave Flume with Lattice Boltzmann Method for Wave Energy Converters
- 173 Mathematical Modelling to Optimise an Urban Electric Vehicle Charging System
- 176 Plasma-assisted Ammonia Combustion: The Effect of Equivalence Ratio on NO Emissions
- 181 Exploring the Potential of Ammonia/Hydrogen Trigeneration Cycle

Sami S

*Cardiff University
School of Engineering*

Qaardan M

*Cardiff University
School of Engineering*

Zhou Y

*Cardiff University
School of Engineering*

Wu J

*Cardiff University
School of Engineering*

SUSTAINABLE ENERGY

Modelling and Simulation of a Hydrogen-Based Energy Storage System

In this study, a mathematical model of a Hydrogen-based Energy Storage System (HESS) was developed. The HESS includes sub-models of a Polymer Electrolyte Membrane (PEM) water electrolyser stack, a PEM fuel cell stack, hydrogen storage tanks, a compressor and AC/DC converters. For validation, simulation results were compared to results reported in the literature. The model of the HESS can be used for power systems dynamic simulation studies, such as providing ancillary services to the power system operator.

Keywords:

Hydrogen-based Energy Storage System, Proton Exchange Membrane electrolyser model, dynamic models.

Corresponding author:

SamiS1@cardiff.ac.uk



S. Sami, Y. Zhou, M. Qaardan, and J. Wu, 'Modelling and Simulation of a Hydrogen-Based Energy Storage System', *Cardiff University School of Engineering Research Conference 2023*, Cardiff, UK, 2023, pp. 135-139.

doi.org/10.18573/conf1.ae

INTRODUCTION

Hydrogen has the potential to contribute to tackling the climate change and reducing CO₂ emissions in power systems. A Hydrogen-based Energy Storage System (HES) is a long-term storage solution to decarbonise power systems as the excess electricity from renewables can be stored for later use in the form of hydrogen.

In this study, models of the HES components were developed and verified against experimental data from the literature [1]. The HES model can be used for dynamic simulation studies, where the HES, for example, is providing frequency support services to the power system operator. As shown in Fig. 1, the HES consists of a Polymer Electrolyte Membrane or Proton Exchange Membrane (PEM) electrolyser stack, low-pressure and high-pressure hydrogen storage tanks, a two-stage hydrogen compressor and a PEM fuel cell stack. The modelling of the HES accessories, such as gases purification systems, pressure regulators and flow regulators, is beyond the scope of this study.

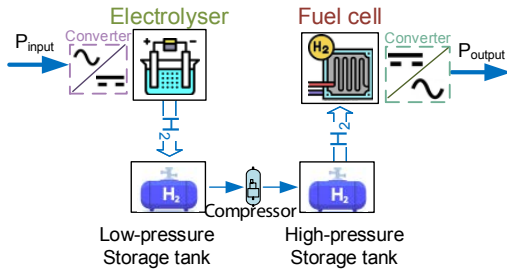


Fig. 1. The developed model of HES.

MODELLING OF HES COMPONENTS

Electrolyser and fuel cells stacks are the key parts of HESs. This study focused on the modelling of the electrolyser as exactly the reverse electrochemical processes are occurring in the PEM fuel cells.

Modelling of a PEM electrolyser stack

A mathematical model of the PEM electrolyser is developed based on [1-3]. Information listed in [1, 3] were based on HES projects in the USA and Germany. The dynamic model consists of three parts or sub-models, i.e. an electrochemical, hydrogen production and thermal sub-models. It is assumed that pressure effects and pressure drops are neglected, the temperature is uniform in the electrolyser stack and all cells have identical thermal behaviour [1]. Figure 2 shows the block diagram of the three sub-models of the developed electrolyser model. The dynamic behaviour of the thermal part impacts the other parts through the change in the temperature.

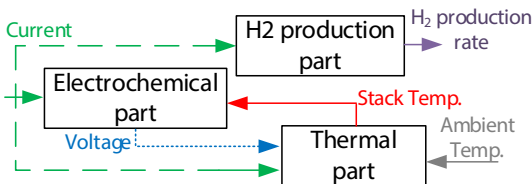


Fig. 2. The block diagram of interaction between the electrolyser sub-models.

Electrochemical part

The electrochemical part represents the current-voltage characteristics of the electrolyser cell. The mathematical description of the electrolyser cell voltage is given in equation (1) [1, 2]:

$$V_{cell} = V_{OC} + V_{act} + V_{ohm} + V_{diff} \quad (1)$$

where V_{OC} is the open-circuit voltage (V), V_{act} is the activation overpotentials at the anode and cathode (V_{act}), V_{ohm} is ohmic overpotential (V_{act}), V_{diff} is the diffusion or concentration overpotential (V).

Nernst equation is used to compute the open-circuit voltage for water electrolysis [2]:

$$V_{OC} = E_{rev} + \frac{RT}{zF} \left[\ln \left(\frac{p_{H_2} \sqrt{p_{O_2}}}{a_{H_2O}} \right) \right] \quad (2)$$

where E_{rev} is the reversible electrolyser cell voltage (V), R is the universal ideal gas constant ($J/mol K$), T is the electrolyser stack temperature (K), p_{O_2} and p_{H_2} are the partial pressures of oxygen and hydrogen (Pa), a_{H_2O} is the water activity between electrode and membrane, z is the number of moving electrons and F is Faraday's constant ($A sec/mol$).

The reversible voltage equals 1.229 V at standard temperature and pressure conditions. At other temperatures, it can be determined by [2]:

$$E_{rev} = 1.229 - 0.9 \times 10^{-3} (T - 298) \quad (3)$$

The activation overpotential or overvoltage describes the speed of the reactions taking place at the electrode surface. As electrons are transferred to or from the electrodes, part of the applied voltage is lost [2]. Different representations of the activation overpotential were found in literature, and Tafel correlation was adopted in this research [1]:

$$V_{act} = \frac{RT}{\alpha_{act} z F} \left[\ln \left(\frac{i}{i_0} \right) \right] \quad (4)$$

where α_{act} is the charge transfer coefficient, i_0 (A/m^2) is exchange current density and i (A/m^2) is the electrolyser stack current density, which is calculated by [1]:

$$i = \frac{I}{A_{cell}} \quad (5)$$

where I (A) is the electrolyser stack current and A_{cell} (m^2) is the electrolyser cell active area. The value of the charge transfer coefficient and the exchange current density were extracted from experimental data using non-linear regression analysis because the materials of the catalyst were unknown [1]. Additionally, the kinetics of the hydrogen reactions at the cathode occur faster than the kinetics of the oxygen reactions at the anode, and hence the activation overpotentials at the cathode are neglected [1].

The ohmic overvoltages or overpotentials are caused by the ohmic resistance of the bipolar plates, electrolytes and surfaces of the electrodes [1, 2]. Since the membrane resistance is about 10 times bigger than other resistances, other resistances are neglected in this research [1]. This study adopts the empirical correlations proposed by [4]:

$$V_{ohm} = \frac{t_m i}{\sigma_m} \quad (6)$$

where t_m (m) is the membrane thickness and σ_m (S/m) is the membrane conductivity. σ_m is a function of the protonic exchange, which in turn is a function of the temperature:

$$\sigma_m = (0.005139\lambda_m - 0.00326)e^{\left[1268\left(\frac{1}{303} - \frac{1}{T}\right)\right]} \quad (7)$$

where λ_m is the average membrane water content. It is considered that the membrane is completely saturated with water, and hence a value of 17 represents good hydration [1].

The diffusion or concentration overpotential or overvoltage occurs due to the mass transfer process that changes the concentration of the reactants at the surfaces of the electrodes [1, 2]. The diffusion overpotential can be described by [1]:

$$V_{diff} = \frac{RT}{\beta 2F} \left[\ln \left(1 + \frac{i}{i_{lim}} \right) \right] \quad (8)$$

where β is an empirical coefficient and i_{lim} in (A/m²) is called limit current density. Both values were extracted from experimental data using non-linear regression techniques [1].

Hydrogen production part

The production rate of the hydrogen is directly proportional to the transfer rate of electrons at the electrodes, according to Faraday's law [1-3]. For an electrolyser of (n) cells connected in series, the hydrogen production rate (\dot{n}_{H_2}) in (mol/s) is expressed by:

$$\dot{n}_{H_2} = \eta_F \frac{nI}{2F} \quad (9)$$

where η_F is Faraday's efficiency. Faraday's efficiency is the ratio of the actual to theoretical maximum amount of hydrogen produced by the electrolyser. This efficiency is often called current efficiency as it is caused by parasitic current losses along the gas ducts in the cell block [5]. Faraday's efficiency empirical expression is [1]:

$$\eta_F = -0.0922 + 0.0091I + 0.00003I^2 - 0.0000003I^3 \quad (10)$$

Thermal part

An equivalent thermal parameters model is used to simulate the overall thermal energy balance in the electrolyser cells stack [3]. An electrical analogy is used to represent the potential of heat storage in the electrolyser cells by a capacitance and heat transfer resistance from the cells to the surrounding. The rate of internal thermal energy generated (i.e. \dot{Q}_{gen} in W) in the electrolyser due to inefficiencies is partly stored in the surrounding mass (i.e. \dot{Q}_{store} in W). Part of the generated thermal energy is lost or transferred to the ambient (i.e. \dot{Q}_{loss} in W). A water-based auxiliary cooling system is assumed, which is responsible for transferring another part of the generated thermal energy to maintain the stack temperature stable (i.e. \dot{Q}_{cool} in W). The overall thermal energy balance is represented by:

$$\dot{Q}_{store} = \dot{Q}_{gen} - \dot{Q}_{loss} - \dot{Q}_{cool} \quad (11)$$

$$\dot{Q}_{store} = C_{th} \frac{dT}{dt} \quad (12)$$

$$\dot{Q}_{gen} = n(V_{cell} - V_{th})I \quad (13)$$

$$\dot{Q}_{loss} = \frac{T - T_a}{R_{th}} \quad (14)$$

$$\dot{Q}_{cool} = C_{cw}(T_{cw,i} - T_{cw,o}) = UA_{HX}LMTD \quad (15)$$

where C_{th} is the heat capacity of the electrolyser stack (J/°C), T_a is the ambient temperature (°C), R_{th} is the equivalent thermal resistance (°C/W), V_{th} is the thermoneutral voltage,

C_{cw} is the heat capacity of the water used for cooling per second (W/°C), $T_{cw,i}$ is the inlet temperature of the cooling water (°C), $T_{cw,o}$ is the outlet temperature of the cooling water (°C), UA_{HX} is the effective heat exchange coefficient for the cooling process, which is the product of the heat transfer coefficient by the exposed surface area (W/°C), LMTD is the Logarithmic Mean Temperature Difference between the cold and hot feeds at each end of the auxiliary cooling system (°C).

The capacity and resistance can be estimated experimentally using heating curves and they are related to the rated power of the electrolyser [1]. Based on values found in the literature [1], an average value of (3 J/°C W) for the capacity and (0.09 °C/W) for the resistance were considered [1]. Hence, for a 6 kW PEM electrolyser, 21 kJ/°C of thermal capacity and 0.09 °C/W of thermal resistance were considered.

The effective heat transfer coefficient can be calculated in terms of the electrolyser current, an empirical expression that considers the heat transfer by heat conduction and convection is used [3]:

$$UA_{HX} = a_{cond} + I b_{conv} \quad (16)$$

where a_{cond} is the conductive heat exchange coefficient (W/°C) and b_{conv} is the convective heat exchange coefficient (W/°C A). The LMTD is calculated by:

$$LMTD = \frac{(T_{cell} - T_{cw,i}) - (T_{cell} - T_{cw,o})}{\ln \left(\frac{T_{cell} - T_{cw,i}}{T_{cell} - T_{cw,o}} \right)} \quad (17)$$

If the LMTD is assumed to be of a constant temperature, the outlet temperature of the cooling water is:

$$T_{cw,o} = T_{cw,i} + (T_{cell} - T_{cw,i}) \left[1 - e^{-\frac{UA_{HX}}{C_{cw}}} \right] \quad (18)$$

It was assumed that the water-based auxiliary cooling system is identical to the system reported in the literature [3, 6]. Hence, the same model parameters were used. Table 1 list the values used for all parameters of the electrolyser.

Modelling of hydrogen storage tanks

Two tanks were assumed to store the produced hydrogen. Figure 3 shows the block diagram of both tanks and the hydrogen compressor.

Low and high-pressure storage tanks

It was assumed that the temperature of the stored hydrogen in both tanks is kept constant, i.e. equal to the electrolyser temperature during the production of the hydrogen, using cooling and heating processes. However, the cooling and heating processes are out of this research scope. The Beattie-Bridgeman equation was used to describe the relationship between values of the pressure, volume and temperature in both storage tanks, as follows [7]:

$$p_{tank} = \frac{\dot{n}_{H_2}^2 RT}{V_{tank}^2} \left[1 - \frac{c \dot{n}_{H_2}}{V_{tank} T^3} \right] \left[\frac{V_{tank}}{\dot{n}_{H_2}} + B_0 \left(1 - \frac{b \dot{n}_{H_2}}{V_{tank}} \right) \right] - \frac{A_0 \left(1 - \frac{a \dot{n}_{H_2}}{V_{tank}} \right) \dot{n}_{H_2}^2}{V_{tank}^2} \quad (19)$$

where p_{tank} in (atm) is hydrogen pressure in the tank, V_{tank} in (litre) is the volume of the tank and a , b , c , A_0 , B_0 are constants, for hydrogen gas they are (-0.00506 litre/mol, -0.04359 litre/mol, 504 litre·K³/mol, 0.1975 atm litre²/mol², 0.02096 litre/mol respectively).

The ideal gas law [5] was used to estimate the amount of hydrogen stored in both tanks:

$$n_{H_2} = \frac{p_{\text{tank}} V_{\text{tank}}}{RT} \quad (20)$$

where n_{H_2} in (mol) is the total amount of gas, p_{tank} is in Pa, V_{tank} is in m^3 , T is in K and R is in $kPa \cdot m^3 / kmol \cdot K$ [8]. For the volume of $25 m^3$, the buffer or low-pressure tank can hold approximately $245 Nm^3$ (10.91 kmol), i.e. when the pressure is 13 bar and the temperature is $85^\circ C$ (i.e. close to the electrolyser temperature at the rated power of 6 kW). While the volume of the high-pressure tank of $26 m^3$ can hold approximately $2349 Nm^3$ (104.8 kmol), i.e. when the pressure is 120 bar and the temperature is $85^\circ C$.

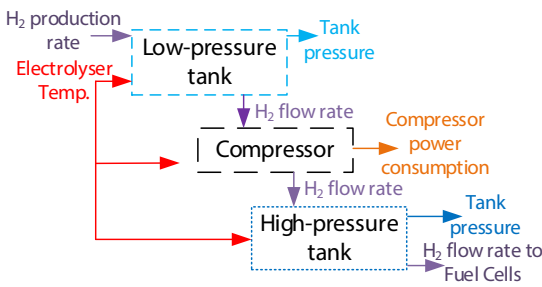


Fig. 3. The block diagram of the interaction between storage tanks and the compressor models.

Table 1. The values of parameters of the electrolyser.

E_{rev} (at standard conditions)	1.229 V	R_{th}	$0.09^\circ C/W$
R	$8.3145 J / mol K$	i_{lim}	$1401 A/m^2$
V_{th} (at standard conditions)	1482 V	F	$96485 A \text{ sec} / mol$
z	2	C_{th}	$21 kJ/^\circ C$
α_{H_2O}	1	T_a	$20^\circ C$
α_{act}	0.5316	β	0.315
i_0	$0.0004576 A/m$	C_{cw}	$697.67 W/^\circ C$
t_m	$0.00003306 m$	b_{conv}	$0.02 W / (^\circ C \cdot A)$
λ_m	17	T_{cw_i}	$14.5^\circ C$

Table 1. The values of parameters of the electrolyser.

Hydrogen compressor

A model of a two-stage polytropic compressor reported in [5] was adopted. The work done by the compressor ($P_{\text{compressor}}$) in (W) is [5]:

$$P_{\text{compressor}} = \frac{\eta_{H_2} (P_{\text{stage 1}} + P_{\text{stage 2}})}{\eta_{\text{compressor}}} \quad (21)$$

$$P_{\text{stage 1}} = \frac{k_{\text{plt}} R T}{k_{\text{plt}} - 1} \left[1 - \left(\frac{p_x}{P_{\text{stage 1}}} \right)^{\left(\frac{k_{\text{plt}} - 1}{k_{\text{plt}}} \right)} \right] \quad (22)$$

$$P_{\text{stage 2}} = \frac{k_{\text{plt}} R T}{k_{\text{plt}} - 1} \left[1 - \left(\frac{P_{\text{stage 2}}}{p_x} \right)^{\left(\frac{k_{\text{plt}} - 1}{k_{\text{plt}}} \right)} \right] \quad (23)$$

$$p_x = \sqrt{P_{\text{stage 1}} + P_{\text{stage 2}}} \quad (24)$$

where $\eta_{\text{compressor}}$ is the compressor efficiency (equal 63% [9]), k_{plt} is the polytropic coefficient (equal 1.4), p_x in (Pa) is the intermediate stage pressure, $P_{\text{stage 1}}$ in (Pa) is the first stage pressure (i.e. 1300 kPa (equal 13 bar)) and $P_{\text{stage 2}}$ in (Pa) is the second stage pressure (i.e. 12000 kPa (equal 120 bar)).

A compressor controller was modelled based on [5]. The compressor follows a simple controlling approach: it is switched ON when the pressure in the buffer tank rises above 10 bar and switched OFF when the buffer tank pressure drops below 6 bar. The compressor works with a constant hydrogen flow rate of $5 Nm^3/h$. The compressed hydrogen is stored in the high-pressure tank, as shown in Fig. 3.

Fuel cells stack model

The dynamic model of a fuel cell stack available in Simulink/Matlab® library was adopted in this study.

Modelling of AC/DC converters

Since both stacks of electrolyser cells and fuel cells are operating using the DC voltage, AC to DC converters are required. A simplified model of AC/DC converters developed in [10] was used.

SIMULATION RESULTS AND VALIDATION

The model of electrolyser was validated by comparison with experimental results from the literature and Root Mean Square Error (RMSE) was used to indicate the difference between the results. The data reported in [1] were presented in graphic form, and hence extracted data accuracy from these publications might be affected slightly. Regarding the validation of models of storage tanks and the compressor, the different experimental conditions in [5, 7] prevented the direct comparison of the results. The validation of the PEM electrolyser model was carried out by comparing polarization and hydrogen production curves against experimental data from a project in the USA [1]. Figure 4 shows the hydrogen production rate of the electrolyser, and the RMSE value is $0.0044 Nm^3/h$. Figure 5 depicts the V-I characterisation (polarisation) curve of the electrolyser, and the RMSE value is $0.027 V$.

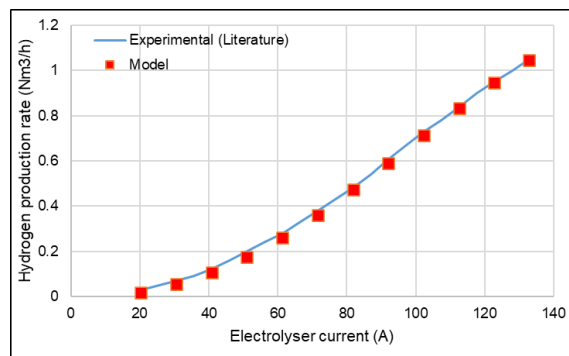


Fig. 4. The hydrogen production rate of the electrolyser.

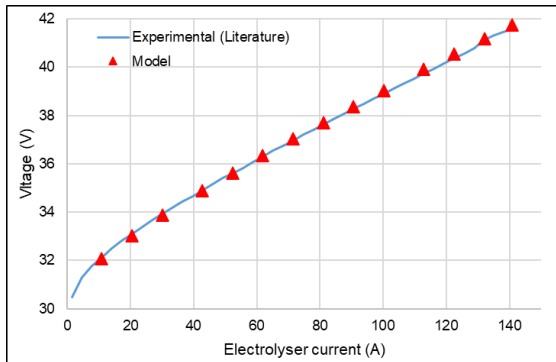


Fig. 5. The polarisation curve of the electrolyser.

CONCLUSIONS

Models of the components of a HESS, i.e. an electrolyser, hydrogen storage tanks and hydrogen compressor were developed, simulated and validated based on data reported in the literature. The model of the HESS can be used for dynamic simulation studies of power systems.

Acknowledgements

This work has been carried out in the framework of the European Union's Horizon 2020 research and innovation program under grant agreement No 957852 (Virtual Power Plant for Interoperable and Smart isLANDS'- VPP4ISLANDS). The work was also supported by FLEXIS, i.e. a project part-funded by the European Regional Development Fund (ERDF) through the Welsh Government (WEFO case number 80836).

Conflicts of interest

The authors declare no conflict of interest.

REFERENCES

- [1] P. Fragiaco and M. Genovese, 'Modeling and energy demand analysis of a scalable green hydrogen production system', *International Journal of Hydrogen Energy*, vol. 44, no. 57, pp. 30237–30255, Nov. 2019. doi.org/10.1016/j.ijhydene.2019.09.186
- [2] Z. Abidin, C. J. Webb, and E. MacA. Gray, 'Modelling and simulation of a proton exchange membrane (PEM) electrolyser cell', *International Journal of Hydrogen Energy*, vol. 40, no. 39, pp. 13243–13257, Oct. 2015. doi.org/10.1016/j.ijhydene.2015.07.129
- [3] Ø. Ulleberg, 'Modeling of advanced alkaline electrolyzers: a system simulation approach', *International Journal of Hydrogen Energy*, vol. 28, no. 1, pp. 21–33, Jan. 2003. doi.org/10.1016/S0360-3199(02)00033-2
- [4] T. E. Springer, T. A. Zawodzinski, and S. Gottesfeld, 'Polymer Electrolyte Fuel Cell Model', *Journal of the Electrochemical Society*, vol. 138, no. 8, pp. 2334–2342, Aug. 1991. doi.org/10.1149/1.2085971
- [5] Ø. Ulleberg, 'Stand-Alone Power Systems for The Future: Optimal Design, Operation and Control of Solar-Hydrogen Energy Systems', PhD, Norges teknisk-naturvitenskapelige universitet, Norway, 1999.
- [6] M.H. Nehrir, C. Wang, *Modeling and Control of Fuel Cells: Distributed Generation Applications*, John Wiley & Sons, USA, 2009. doi.org/10.1109/9780470443569
- [7] C. Wang, 'Modeling and Control of Hybrid Wind/ Photovoltaic/Fuel Cell Distributed Generation Systems', PhD, Montana State University, USA, 2006.
- [8] Y.A. Cengel, M.A. Boles, *Thermodynamics: an Engineering Approach*, McGraw-hill, USA, 9th ed, 2018.
- [9] T. Zhou and B. Francois, 'Modeling and control design of hydrogen production process for an active hydrogen/wind hybrid power system', *International Journal of Hydrogen Energy*, vol. 34, no. 1, pp. 21–30, Jan. 2009. doi.org/10.1016/j.ijhydene.2008.10.030
- [10] S. Sami, 'Virtual Energy Storage for Frequency and Voltage Control', PhD, Cardiff University, UK, 2017.

Lugg-Widger P

*Cardiff University
School of Engineering*

Pearson M

*Cardiff University
School of Engineering*

Anderson P

*Cardiff University
School of Engineering*

SUSTAINABLE ENERGY

Acoustic Noise Emission Detection and Location Analysis from a Scaled Laminated Transformer

In this paper the vibrational noise of a small scale laminated transformer core is measured to study the magnetic phenomena known as magnetostriction which generates its characteristic hum. Noise frequency measurements are recorded using traditional microphone arrangements and a highly sophisticated 2D acoustic camera array to trial its application. The recorded results examine the frequency harmonics of the transformer noise and analyze a method for specific frequency location detection.

Keywords:

Power transformer, noise, acoustics, magnetostriction.

Corresponding author:

WidgerP@cardiff.ac.uk



P. Lugg-Widger, M. Pearson, and P. Anderson, 'Acoustic Noise Emission Detection and Location Analysis from a Scaled Laminated Transformer', *Cardiff University School of Engineering Research Conference 2023*, Cardiff, UK, 2023, pp. 140-144.

doi.org/10.18573/conf1.af

INTRODUCTION

Electrical power transformers exhibit three sources of noise whilst in operation: core noise caused by a combination of the magnetostriction phenomena and Maxwell forces at joints, load noise caused by electromagnetic forces in the windings and structural components due to current leakage flux and noise generated by the operation of cooling and fan equipment [1]. It is beneficial to reduce the noise produced by electrical transformers as the continuous tone and character can cause irritation and discomfort to humans. This is especially important in urban areas where high density populations require increasing transformer size, and hence noise, in close proximity to many individuals. In some countries maximum permissible noise levels have been stipulated varying in values from normal levels in rural areas to lower values in large urban environments. Cities such as New York have even introduced ultra-low levels such is the importance of this issue [2].

Currently new transformer cores are designed to uniformly distribute magnetic flux with low levels of flux harmonics in the core and joints. Transformer cores are held by complex clamping structures and are designed to uniformly clamp laminations to avoid deformations. Transformer tanks must avoid noise and resonances therefore reducing sound radiation from the core and windings [3]. In order to meet future noise restrictions it is necessary to further examine and understand the total process of sound generation from magnetostriction, transmission and radiation in order to design and build future environmentally friendly ‘quiet’ transformers.

British and international standards, IEC 60076-10 [4] and IEC 61672 [5], detail how power transformer noise should be measured, however, varying methods of reporting results and equipment allows for a wide variation in results and evaluation. Currently some results measure total collective noise level of the transformer (dBA) and others the individual recordings from components such as core and fan noise, total noise level or loaded/unloaded transformer noise [1].

Core noise due to magnetostriction is caused by small mechanical deformations in the core laminations when a magnetic field is applied. These small changes in the dimensions of the core are independent of flux direction and therefore occur at double the supply frequency i.e 100Hz for a 50Hz supply. Furthermore, the effect of magnetostriction can introduce higher frequency harmonics of multiple orders above the initial 100Hz. Therefore, core noise has components at multiples of 100 or 120Hz (for 50Hz and 60Hz transformers respectively) [6,7]. In this paper the vibration of a small scaled laminated core transformer is measured whilst powered under no-load conditions and the magnetic phenomena known as magnetostriction further examined to generate a characteristic hum classified as “noise”. The noise measurements are recorded using a traditional microphone circular ring arrangement, a 2D traditional microphone array and finally a highly sophisticated 2D acoustic camera array to trial its application.

MATERIALS AND METHODS

The test arrangement used throughout experimentation in this paper consisted of a scaled three phase transformer, under no-load conditions, powered from a three phase regulator and individual variacs or variable transformers for each phase as shown in Fig. 1. Throughout testing the direct voltage and current from the scaled transformer was

monitored and recorded through a digital power meter. The voltage and current of the variacs that adjust the voltage induced in the transformer windings are directly adjustable using a National Instruments data acquisition card connected to a computer control system shown in Fig. 1. In this paper the scaled transformer dimensions were 550(W)x550(H)x80(D) and the clamping bolts of the support structure were intentionally left loose. The transformer has an applied phase voltage of 50V which is equivalent to an average 1.5T magnetic flux density.

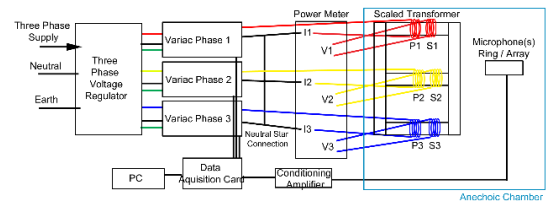


Fig. 1. Transformer noise electrical test arrangement and data measurement setup.

The conventional microphone ring arrangement consisted of 8 prepolarized condenser microphones and the array consisted of 9 of the same condenser microphones all with a frequency range of 8-12500 Hz with a response of 27.2 mV/Pa at 1000 Hz. Each of these microphones were fed into a preamplifier and then into a conditioning amplifier to enable the clearest and largest signal output. Individual signals from each microphone fed through the conditioning amplifier was monitored and recorded in real time using a data acquisition card and computer.

The conventional microphones are arranged in a ring or 2D array arrangement 70cm from the transformer core such as could be achieved using the anechoic chamber. For the ring arrangement there were six microphones positioned to directly oppose each side of each transformer limb and two microphones either end of the transformer as shown in Fig. 2. For the array arrangement each microphone was placed 22cm apart horizontally and 20cm apart vertically so that a total of 9 microphones in a 3x3 array was constructed in a 40cm(H) x 44cm(W) arrangement to directly oppose one side of each transformer limb as shown in Fig. 3 overleaf.

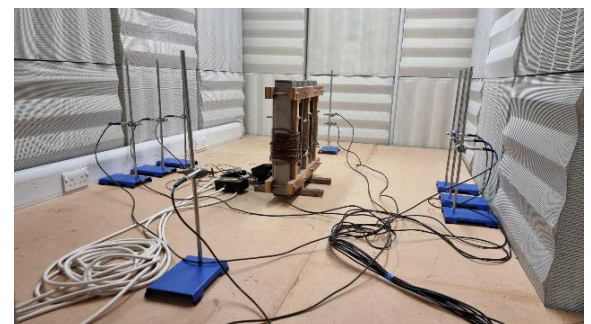


Fig. 2. Conventional eight microphone ring test arrangement placed 70cm from the transformer.



Fig. 3. Conventional nine microphone array test arrangement placed 70cm from the transformer.

The highly sophisticated near field 2D acoustic camera [8] that was utilized for the second half of the testing consisted of an array of 96 microphones with a frequency range of 40 Hz to 2 kHz for nearfield SONAH measurements (larger ranges are possible for far field measurements). This array was connected to a computer via a data acquisition system to record both microphone and camera data using the proprietary software.

The scaled transformer and microphone array are enclosed within an anechoic chamber to reduce background noise and interference and ensure the recordings taken refer specifically to the noise produced by the transformer as shown in Fig. 4. The transformer and acoustic camera were centered and placed 4cm apart as show in Fig. 5 providing maximum coverage of the transformer core.

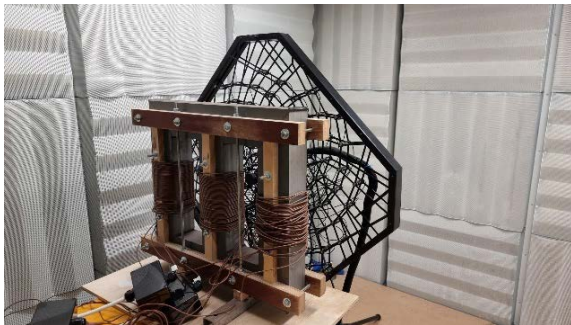


Fig. 4. Scaled electrical transformer and acoustic camera array inside the anechoic chamber.

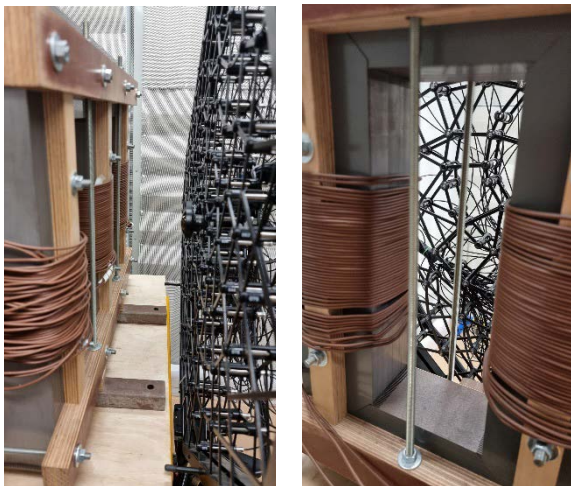


Fig. 5. Testing arrangement of acoustic camera and scaled electrical transformer.

RESULTS

Initially a background noise level recording was taken using the conventional microphones prior to any power being provided to the transformer as shown in Fig 6. The results from the background recording in Fig. 6 show that even in an anechoic chamber not all sources of background noise can be eliminated especially below 100Hz.

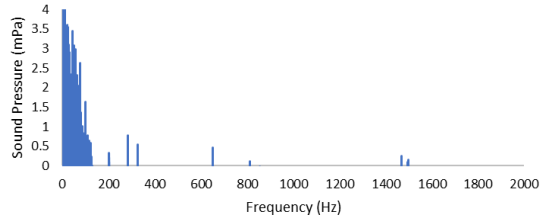


Fig. 6. Background noise level inside the anechoic chamber recorded using conventional microphones in array formation.

Following this the conventional microphones were arranged in a ring formation and a recording taken for the transformer at 1.5T as shown in Fig. 7 Next the same microphones were arranged in an array formation, as described in the methods section, and the data recorded for the transformer at 1.5T is shown in Fig. 8.

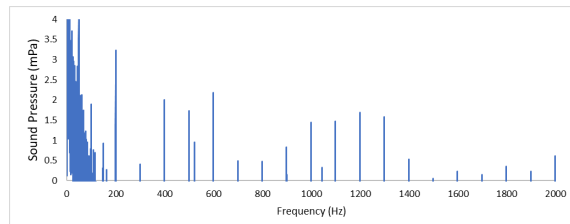


Fig. 7. Noise level of the transformer at 1.5T inside the anechoic chamber recorded using conventional microphones in ring formation.

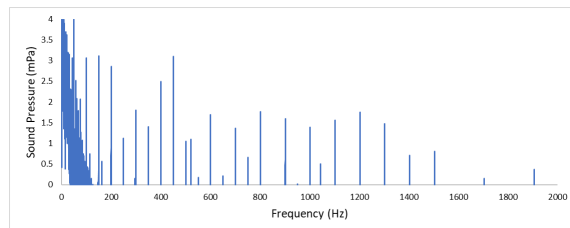


Fig. 8. Noise level of the transformer at 1.5T inside the anechoic chamber recorded using conventional microphones in array formation.

Following this the conventional microphones were replaced with the sensitive acoustic camera array and a new recording undertaken for the background noise level of the anechoic chamber without the transformer powered as shown in Fig. 9.

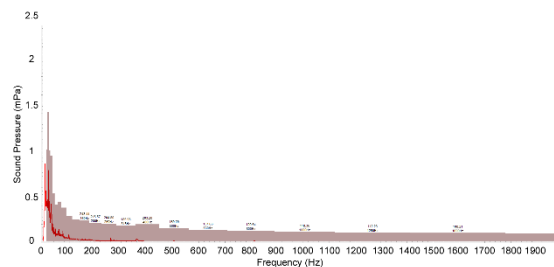


Fig. 9. Background noise level from inside the anechoic chamber recorded using the acoustic camera array.

Finally, the acoustic camera array was used to record the noise from the transformer at 1.5T inside the anechoic chamber as shown in Fig. 10.

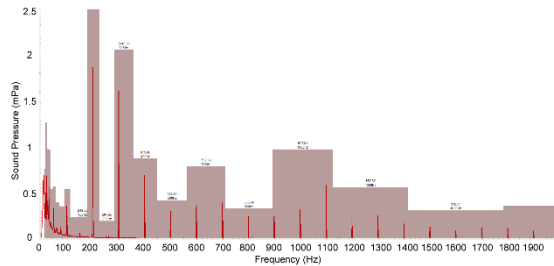


Fig. 10. Noise level of the transformer at 1.5T from the scaled transformer inside the anechoic chamber recorded using the acoustic camera array.

The results from Fig. 10 were further enhanced using the acoustic camera array to map the noise detection from the 96 microphone array to a precise location on the camera recordings using nearfield SONAH location detection. The acoustic camera location mapping results for the 300Hz peak in Fig. 10, with the transformer at 1.5T, is shown Fig. 11.

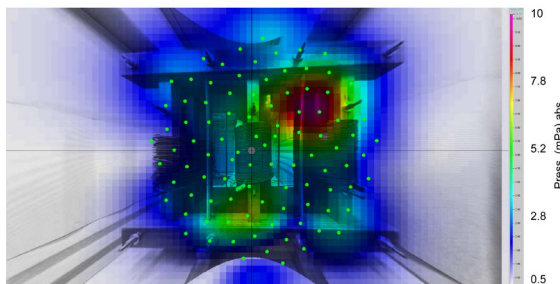


Fig. 11. 300Hz Noise detection for the scaled transformer at 1.5T inside the anechoic chamber recorded using the acoustic camera array.

DISCUSSION

In Fig. 6 and Fig. 9 the background noise levels in the anechoic chamber from two comparative sets of microphone arrays were recorded. The figures indicate that both sets of microphones were comparable and show the same background noise below 100Hz with small amounts of noise detected around 300Hz. Fig. 6 and Fig. 9 also show that the low levels of noise in the anechoic chamber allows for scientific experimentation and measurements to be undertaken from the noise produced by a magnetic transformer core when resonating due to magnetostriction.

In Fig. 7 and Fig. 8 the same conventional microphones were used in an array and ring formation to produce a recording of the noise from the transformer at 1.5T. Fig. 7 and Fig. 8 show the increased noise levels recorded at 100Hz caused by magnetostriction at double the supply frequency. The results also clearly show the harmonics produced at multiples of 100Hz including 200Hz, 300Hz etc all the way up to 1400Hz and beyond. These harmonics generally decline in magnitude as the frequency increases. In Fig. 8 the array formation also indicates additional harmonics at 150Hz, 250Hz etc up to 800Hz which do not appear in the ring formation and will require further examination and experimentation to understand.

In Fig. 10 the acoustic camera array is used to record the noise from the transformer at 1.5T. In comparison to Fig.

7 and Fig. 8, the results obtained by the acoustic camera in Fig. 10 are broadly equivalent and clearly show the transformer noise produced at 100Hz and the harmonic multiples at 200Hz, 300Hz and beyond. Furthermore, the acoustic camera array was used to highlight and identify sources of noise location overlaid on the photos from the camera which is possible due to the large number of microphones in the array. In Fig. 11 the noise for the 300Hz signal, taken from Fig. 10, detected from the acoustic camera array indicates the top right corner of the transformer core and structure was the source of noise which was resonating significantly.

CONCLUSIONS

In conclusion this research highlights the comparative noise measurements from a scaled transformer at 1.5T that can be undertaken using both a conventional microphone setup and a novel acoustic camera array. It indicates that the continued use of an acoustic camera array to further understand sources of resonating transformer harmonics can be undertaken and further examination is required to understand noise source location and frequency in greater detail. Future research will examine the location of transformer noise at varying magnetic flux densities with different degrees of clamping levels of the core structure to understand the fundamentals of magnetostriction in a complex structure and a transformer core.

Acknowledgments

The authors would like to acknowledge the support of the Welsh Government Welsh European Funding Office (WEFO) project MAGMA. The authors would also like to acknowledge the Cardiff University Research Infrastructure Fund that supported the acquisition of the acoustic camera utilized in the experimentation of this paper.

Conflicts of interest

The authors declare no conflict of interest.

REFERENCES

- [1] R. Girgis, J. Anger, and D. Chu, 'The sound of silence: Designing and producing silent transformers', *ABB Review*, vol. 2, pp.47-51, 2008.
- [2] R. Girgis, M. Bernesjo, S. Thomas, J. Anger, D. Chu, and H. Moore, 'Development of Ultra-Low Noise transformer technology', *IEEE Transactions on Power Delivery*, vol. 26, issue 1, pp. 228-234, Jan. 2011.
doi.org/10.1109/TPWRD.2010.2070812
- [3] G. Shilyashki, H. Pfurtner, P. Hamberger, M. Aigner, A. Kenov, and I. Matkovic, 'Spatial distributions of magnetostriction, displacements and noise generation of model transformer cores', *International Journal of Mechanical Sciences*, vol. 118, pp.188-194, 2016.
doi.org/10.1016/j.ijmecsci.2016.09.022
- [4] IEC/TC14 / PEL/14, *British / International Standard BS/IEC 60076-10, Power Transformer, Determination of sound levels*, Feb. 2020.
- [5] IEC/TC29 / EPL/29, *British / International Standard BS/IEC 61672, Electroacoustics. Sound level meters, Specifications.*, Dec 2013.
- [6] R.S. Masti, W. Desmet, and W. Heylen, 'On the influence of core laminations upon power transformer noise', *Proceedings of ISMA2004*, pp. 3851-3862, 2004.
- [7] H. Jingzhu, L. Dichen, L. Qingfen, Y. Yang, and L. Shanshan, 'Electromagnetic vibration noise analysis of transformer windings and core', *IET Electric Power Applications 2016*, vol. 10, issue 4, pp. 251-257, 2016.
doi.org/10.1049/iet-epa.2015.0309
- [8] gfai tech Fibonacci array acoustic camera, further specifications: www.gfaitech.com

Mallett P

*Cardiff University
School of Engineering*

Anderson P

*Cardiff University
School of Engineering*

Harrison C

*Cardiff University
School of Engineering*

SUSTAINABLE ENERGY

Measuring the Coupled Effect of Heat and Stress on the Magnetic Properties of Electrical Steel

The coupled effect of heat and stress on the magnetic properties of electrical steel laminations is measured using a novel single-strip tester (SST) that applies uniaxial stress and localised heating to a sample. Magnetic characteristics, such as hysteresis curves, power losses and permeability, are produced as a function of stress, whose effect varies with temperature. The proposed system improves on existing systems by removing the need for a furnace, ring samples and large stressing apparatus.

Keywords:
Magnetic properties, electrical steel, heat, stress.

Corresponding author:
MallettP@cardiff.ac.uk



P. Mallett, P. Anderson, and C. Harrison, 'Measuring the Coupled Effect of Heat and Stress on the Magnetic Properties of Electrical Steel', *Cardiff University School of Engineering Research Conference 2023*, Cardiff, UK, 2023, pp. 145-147.

doi.org/10.18573/conf1.ag

INTRODUCTION

Electrical or silicon steel is widely used in the construction of electric motors as magnetic material via excitation coils where permanent magnets are not suitable; hence the magnetic properties of this material are a very important aspect of motor efficiency. Stressing silicon steel affects magnetisation due to imposed restriction on domain movement through the Villari effect [1]; increasing the temperature has a complex effect on this behaviour, not only affecting electrical resistivity but also magnetisation and mechanical properties [2]. Therefore an environment, such as an electric motor in an automotive drive system, that applies both stress and temperature conditions to silicon steel changes the nominal magnetic performance of the material. This effect is largely not considered by motor designers when selecting a grade of electrical steel since this type of measurement is not conducted by manufacturers who market their material based on international standards that exclude variable temperature and stress.

The coupled effect of heat and stress on the magnetic properties of electrical laminations can be investigated using the novel apparatus presented here that applies localised heating to a uniaxially-stressed lamination. Magnetic property data are recorded during the measurement to enable stress- and temperature-dependent power loss and permeability analysis of the material, which is essential when designing or considering materials for automotive applications. Existing methods to conduct this type of measurement have used of ultra-high-pressure containers or furnaces [3], which are considerably more complex and larger than the proposed system shown in Fig. 1, which offers greater measurement repeatability and usability.

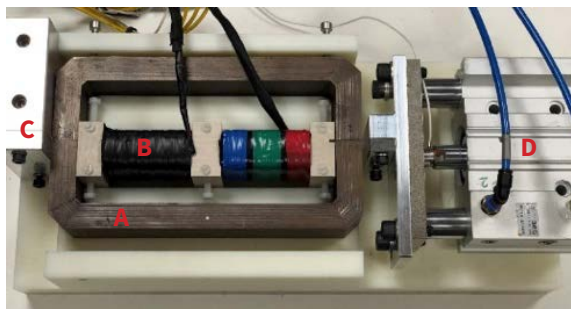


Fig. 1. SST apparatus to apply heat and stress while recording magnetic data; A = iron yoke, B = coil windings, C = aluminium grip, D = piston.

METHODOLOGY

An SST was designed and built to apply uniaxial stress and localised heating to a silicon steel Epstein lamination (30mm x 305mm) while magnetic measurements are conducted. A piston applies either tensile or compressive stress to one end of the clamped sample while a thin silicone heater strip is affixed to its surface as it lies inside coil windings that magnetise and measure the subsequent magnetic flux density. Different temperatures (from room temperature to 150°C) can be set while varying stresses (+/-100MPa) are imparted, during which inductions from 0.1-1.8T are measured at 5-1500Hz.

Stress application

The Epstein sample lies vertically between horizontal iron yokes to remove the compression applied by the top yoke in the conventional SST set up. This is essential for applying the intended stress condition which cannot

be effectively administered if a yoke lay atop the Epstein sample. Another issue with stress applications arises from inadequate gripping of the sample, leading to non-uniform stress distribution; this has been addressed by sintering the aluminium clamp faces that grip the ends of the sample. Additionally, the sample is sandwiched between the wall of the coil housing and a ceramic spacer which is held in place with screws to prevent sample buckling. A feedback system measures the pressure exerted on the load cell in the piston and adjusts the pressure in the piston accordingly to apply the desired stress to the sample.

Heat Application

Embedded into the spacer is a silicone heater strip whose temperature is set by a thermal controller using a thermocouple in contact with the sample. The resistive windings inside the strip are arranged so as not to interfere with the magnetic field in the sample.

RESULTS AND DISCUSSION

For the below measurements, data from magnetic measurements of 1.5T at 400Hz are presented in the tensile stress range of 0-35MPa and temperature range of 50-150°C. The stress range selected is to explore the effects of the Villari region at different temperatures, which typically occurs within the 1-25MPa boundary [4]. The material exhibited is a 3.3% silicon B32 0.5mm grade of non-oriented electrical steel.

Different stress inductions create different loss temperature profiles within the Villari region, as seen in Fig. 2, where the profiles with the most change are likely Villari boundaries for this material since the loss-temperature response is more consistent above 10MPa.

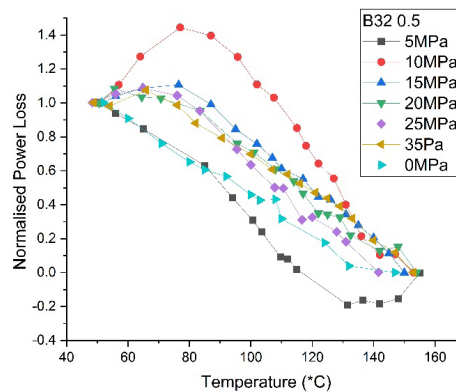


Fig. 2. Power losses at 1.5T, 400Hz due to different temperatures. Power losses normalised to lowest temperature recorded in each stress profile.

Figure 3 shows Fig. 2's data from the perspective of the loss-stress profile to contrast the small effect that large increases in temperature have on the loss-stress profile. Given the contribution of Eddy currents at 400Hz, increases in temperature will decrease power losses through increasing electrical resistance; however, this effect is marginal compared to the effects of stress. Figure 4 further demonstrates the dominance of stress over temperature effects with the increase in coercivity between stressed and unstressed states while temperature has a negligible effect on this. Moreover, the BH loop distortion is dominated by stress.

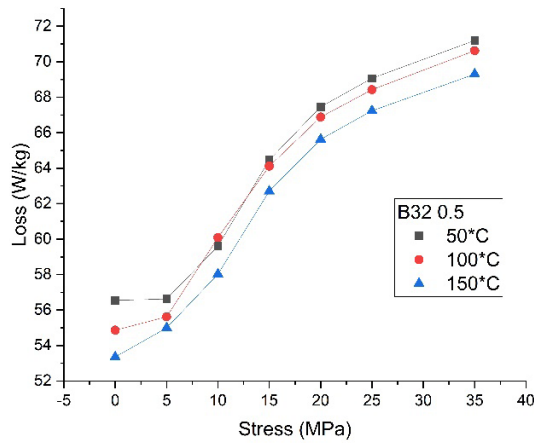


Fig. 3. Power losses due to stress at 1.5T, 400Hz and different temperatures.

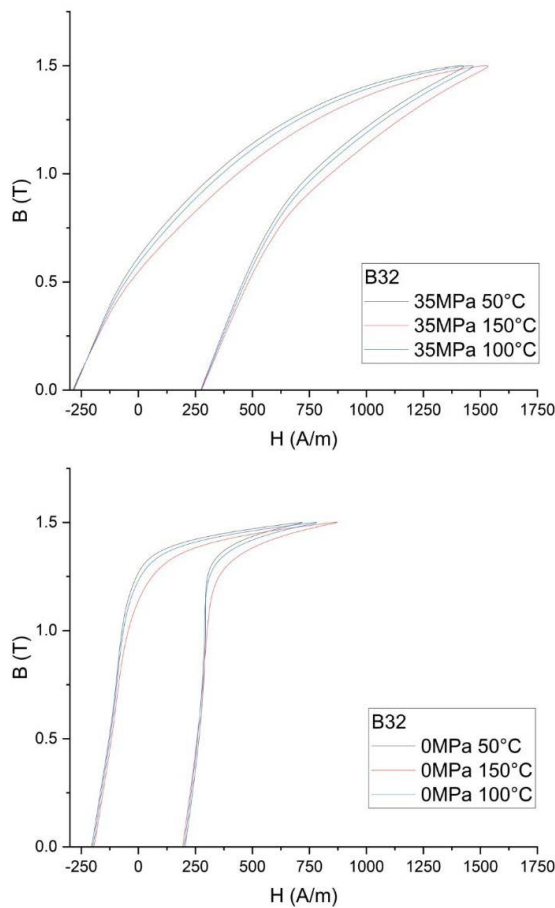


Fig.4. Magnetic hysteresis at 1.5T, 400Hz due to different temperatures in a stress (top) and unstressed (bottom) state.

CONCLUSIONS

The novel test jig presented is capable of measuring the magnetic properties of electrical steel laminations at different stresses and temperatures in conjunction, and could be used further to characterise the dependence of heat and stress effects on material factors that govern hysteresis.

Increases in both stress and temperature negatively impact magnetic permeability; however, within the operational environment of an electric motor the stress effects are dominant and increase power losses by ~30% at 35MPa, while temperatures of 150°C can reduce power losses by ~3% for the same stress due to Eddy current reduction.

Stress-dependent models could implement a temperature coefficient similarly.

Conflicts of interest

The authors declare no conflict of interest.

REFERENCES

- [1] D. Singh, P. Rasilo, F. Martin, A. Belahcen, and A. Arkkio, 'Effect of Mechanical Stress on Excess Loss of Electrical Steel Sheets', *IEEE Trans Magn*, vol. 51, no. 11, pp. 1–4, Nov. 2015. doi.org/10.1109/TMAG.2015.2449779
- [2] J. Chen, D. Wang, S. Cheng, Y. Wang, Y. Zhu, and Q. Liu, 'Modeling of Temperature Effects on Magnetic Property of Nonoriented Silicon Steel Lamination', *IEEE Trans Magn*, vol. 51, no. 11, pp. 1–4, Nov. 2015. doi.org/10.1109/TMAG.2015.2432081
- [3] L. Xiao, G. Yu, J. Zou, Y. Xu, and W. Liang, 'Experimental analysis of magnetic properties of electrical steel sheets under temperature and pressure coupling environment', *Journal of Magnetism and Magnetic Materials*, vol. 475, pp. 282–289, Apr. 2019. doi.org/10.1016/j.jmmm.2018.11.107
- [4] I. T. Gürbüz et al., 'Experimental characterization of the effect of uniaxial stress on magnetization and iron losses of electrical steel sheets cut by punching process', *Journal of Magnetism and Magnetic Materials*, vol. 549, p. 168983, May 2022. doi.org/10.1016/j.jmmm.2021.168983

Shafiekhani M

Cardiff University
School of Engineering

Zhou Y

Cardiff University
School of Engineering

Qadrdan M

Cardiff University
School of Engineering

Wu J

Cardiff University
School of Engineering

SUSTAINABLE ENERGY

Development of a Multi-Community Peer-to-Peer Electricity Trading Mechanism

Peer-to-peer electricity trading allows individual energy producers and consumers to trade electricity directly with one another. They can be managed as a single unit in the form of an energy community. However, in this study, a multi-community peer-to-peer electricity trading mechanism was developed to enable excess electricity from renewable sources to be traded between multiple communities. For this purpose, two energy communities were considered, in which there are generation and storage technologies such as PV panels, wind turbines, energy storage systems, and flexible and non-flexible loads. A Bill Sharing method was adopted to determine the price of electricity traded between different peers within each community and between the two communities and the suppliers. The efficacy of the proposed peer-to-peer electricity trading in decreasing the cost of satisfying the electricity demand in the communities was investigated. The proposed model reduces the average daily electricity costs by 64% compared with the case without peer-to-peer electricity trading.

Keywords:

P2P electricity trading, flexible load, heat pump, renewable energies, multi-community system.

Corresponding author:

ShafiekhaniM@cardiff.ac.uk



M. Shafiekhani, M. Qadrdan, Y. Zhou, and J. Wu, 'Development of a Multi-Community Peer-to-Peer Electricity Trading Mechanism', *Cardiff University School of Engineering Research Conference 2023*, Cardiff, UK, 2023, pp. 148-152.

doi.org/10.18573/conf1.ah

INTRODUCTION

Worldwide? approximately 50 billion tonnes of greenhouse gases are emitted annually, almost 75% of which are related to the electricity sector [1]. Total GHG emissions in the UK in 2020 were 405 million tonnes. 27% of the greenhouse gases emissions was from transport sector, 21% from electricity supply, and 17% from businesses (as the three most polluting sectors). The total emissions are nearly 50% lower than in 1990 which is significant progress towards the UK's goal of reaching net-zero emissions by 2050 [2].

The increase in the share of Distributed Renewable Energy Resources (DRER) is a response to policies and incentives aimed at reducing emissions and addressing global warming. However, this increase in DRER poses challenges, such as managing the variability and intermittency of renewable sources, as well as integrating DRER into the existing power grid. To address these challenges, peer-to-peer (P2P) electricity trading has the potential to offer a solution. P2P trading allows customers to trade excess electricity generated from their DRER directly with each other, which can help balance the grid. This causes consumers to appear in the role of prosumers. By providing a means for customers to participate in energy markets, P2P trading can also help democratize the energy system. While P2P trading is not a complete solution, it offers a promising approach to address the challenges associated with the increase in DRER and can help promote a more sustainable and resilient energy system. A prosumer is an electricity customer who could also generate electricity. The excess electricity can be fed back into the grid and/or be traded with other prosumers. New marketplaces and business models are required to enable/empower prosumers and market participants [3,4] to minimize the costs of the entire system as well as their own costs.

LITERATURE REVIEW

There are various P2P electricity trading mechanisms, such as Supply Demand Ratio [3-7], Mid-Market Rate [8,9], and Bill Sharing [10-12]. These P2P pricing mechanisms have been utilized in various research with different objectives.

A method has been developed in [3] to examine the effects of Distributed Energy Resource ownership on the benefit of each participant in the form of a single community microgrid in the P2P trading market. The Supply Demand Ratio method was used to calculate the P2P trading prices in this study. An energy management method is proposed in [4] that integrates demand-side management into the P2P electricity trading problem. Demand side management offers flexibility for community residents to participate in the P2P electricity market. They use a uniform pricing and electricity-allocation mechanism based on the Supply Demand Ratio method to ensure that every household within the community residents can participate fairly in P2P electricity trading. A smart bidding strategy is developed in [5] for a community of smart homes with different distributed energy resources, battery, electric vehicle, and smart appliances (thermal and electrical loads). The proposed algorithm involves a double auction mechanism, in which bidding occurs between the prosumers and consumers based on Supply Demand Ratio and real-time pricing. A deep learning-based P2P transaction method combined with Supply Demand Ratio is proposed in [6], which uses a data-driven approach to build a transaction behaviour model to optimize the energy consumption plans and P2P bids of prosumers in the community. The Supply Demand Ratio pricing mechanism has been utilized

in [7] to develop an approach to optimize the charging/ discharging schedule of battery energy storage systems in the microgrids of prosumers based on an energy router-based energy sharing structure.

A joint Mid-Market Rate-based P2P electricity and carbon allowance trading mechanism for a small building community is proposed in [8]. It claims to address (1) the increasing penetration of renewable energies and the complicated operation of coupling multi-energy sectors; (2) the lack of integration of the energy market and carbon emission trading scheme; and (3) privacy concerns in the energy system. The authors in [9] formulate P2P trading as a multi-agent coordination problem and propose a multi-agent deep reinforcement learning method to address it. They also utilize the Mid-Market Rate pricing mechanism to enable electricity trading among peers. Some studies have used the Bill Sharing method for P2P electricity trading.

Some studies have used Bill Sharing mechanism for P2P electricity trading. Two mechanisms are proposed in [10] to construct a stable grand coalition of a single community prosumers to adequately incentivize them to participate in P2P trading. The first involves a benefit distribution scheme, whereas the second involves a pricing mechanism based on the Bill Sharing method. The operational costs of an individual household and community are optimized in [11] using the Bill Sharing method for various degrees of PV penetration in the form of a P2P electricity trading problem. A systematic index system is developed in [12] to evaluate the performance of various P2P electricity-sharing mechanisms, such as the BS, Mid-Market Rate, and Supply Demand Ratio methods and three different technical indexes, i.e., energy balance, power flatness and self-sufficiency were investigated. The flaw in the BS method used in all these studies is that only the cost and income of buying and selling electricity from/to the supplier are considered. For example, when the community has excess electricity, the amount of excess electricity is sold to the supplier, and the income is divided between the producer peers. Consumer peers do not pay for their consumption and producer peers are not paid for supplying electricity within the community.

Here, we develop a multi-community P2P electricity trading mechanism in a multiple-community system as Fig. 1. In this structure, each community can compensate for its needs from other communities as well as suppliers.

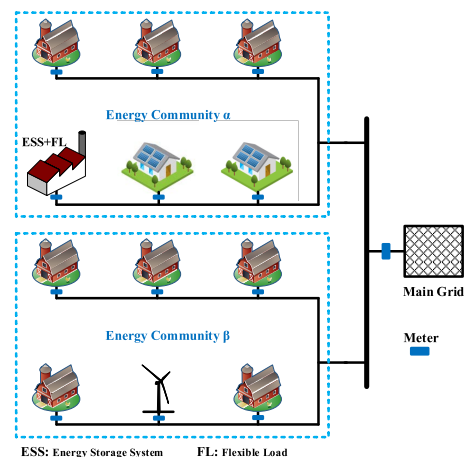


Fig. 1. Multiple-community structure.

FORMULATION OF A P2P ELECTRICITY TRADING PROBLEM

The P2P electricity trading was formulated as an optimization problem with an objective function to minimize the cost to all communities conducting P2P electricity trading (Eq. 1):

$$Cost = \sum_{k=1}^K \left(\sum_{t=1}^T \sum_{n=1}^N P_{k,n,t}^m \lambda_{k,t}^m - \sum_{t=1}^T \sum_{n=1}^N P_{k,n,t}^{ex} \lambda_{k,t}^{ex} \right) \quad (1)$$

where, $\lambda_{k,t}^m$ [€/kWh] and $\lambda_{k,t}^{ex}$ [€/kWh] represent electricity import and export prices in the community at time t , respectively. The amount of electricity imported by peer n in community k at time t , is denoted by $P_{k,n,t}^m$ [kW]. The amount of electricity exported is denoted by $P_{k,n,t}^{ex}$ [kW]. n is the index of peers and k is the index of communities. $P_{k,n,t}^m$ and $P_{k,n,t}^{ex}$ are calculated by Eqs. 2 and 3.

$$P_{k,n,t}^m = D_{k,n,t} + P_{k,n,t}^{Ch} + FL_{k,n,t} - M_{k,n,t}, \forall k \in K, \forall t \in T, \forall n \in N \quad (2)$$

$$P_{k,n,t}^{ex} = G_{k,n,t} + P_{k,n,t}^{Dch} - M_{k,n,t}, \forall k \in K, \forall t \in T, \forall n \in N \quad (3)$$

The electricity demand of peer n in the community k at time t is denoted by $D_{k,n,t}$ [kW]. Furthermore, the generation of peer n in the community k at time t is denoted by $G_{k,n,t}$ [kW]. The instantaneous overlapping of consumption and generation of peer n in community k at time t is denoted by:

$$M_{k,n,t} = \min(D_{k,n,t} + P_{k,n,t}^{Ch}, G_{k,n,t} + P_{k,n,t}^{Dch})$$

Air-source heat pumps have been considered as the Flexible Load (FL) [13]. They enable prosumers and also Energy Storage Systems to provide flexibility and exchange electricity with suppliers or other prosumers in response to P2P electricity trading prices. $FL_{k,n,t}$ [kW] represents flexible load's consumption of the n th peer in community k at time t . Details regarding the formulation of the Flexible Load can be found in [13].

$P_{k,n,t}^{Ch}$ [kW] and $P_{k,n,t}^{Dch}$ [kW] are positive variables and denoted the battery charging and discharging power of the n th peer in community k at time t . Details regarding the formulation of the Energy Storage System can be found in [13].

BILL SHARING METHOD

The Bill Sharing method is a cost sharing method that each peer inside a community pays for its individual electricity use. This cost is shared according to individual peer's total electricity consumption and export. The electricity use is calculated for individual peers. We have developed the BS's formulation used in literatures for multi-community systems. In the multi-community system, there is a coordinator that has access to all data of all peers and solves the optimization problem, which is related to the day-ahead market. By solving the P2P electricity trading problem by the coordinator, the energy exchanged between peers and communities and their prices are determined. In fact, exchanges between peers and communities happen simultaneously. The formulation of the Bill Sharing method is stated in Eqs. (4) and (5). $\lambda_{k,t}^{BS}$ [€/kWh] is the base price and it is assumed to be equal to Smart Export Guarantee (SEG) tariff rate [14] (a fixed payment for sending electricity to the grid which has been used in the UK since 1 Jan 2020) in this paper. $E_t^{S_k C_k}$ [kWh] represents the amount of electricity from a supplier to the community k at time t . $\lambda_t^{S_k C_k}$ [€/kWh] shows community k 's supplier price at time t . $E_t^{C_i C_k}$ [kWh] represents exported electricity from community i to community k at time t . $E_{k,t}^m$ [kWh] and $E_{k,t}^{ex}$ [kWh] show total electricity imported and exported by community k at time t , respectively.

CASE STUDY AND RESULTS

There are two energy communities: α and β as shown in Figure 1. In community α ($k=1$), there are 15 peers ($n=1, 2, \dots, 15$), and in community β ($k=2$), there are 18 peers ($n=1, 2, \dots, 18$). Figure 2 shows predicted generation, and demand of the communities and Fig. 3 shows the suppliers prices, and SEG tariff rate. Each community has got its own supplier. As Figure 2 shows, in the first 12 hours, there was excess electricity in community β , and this situation occurred for community α from 9:00 to 17:00. The SEG tariff rate is equal to 5.5 pence in the system [14]. There is an Energy Storage System in community α with a capacity of 100 kWh/50 kW. The proposed model is simulated using CPLEX solver in GAMS software.

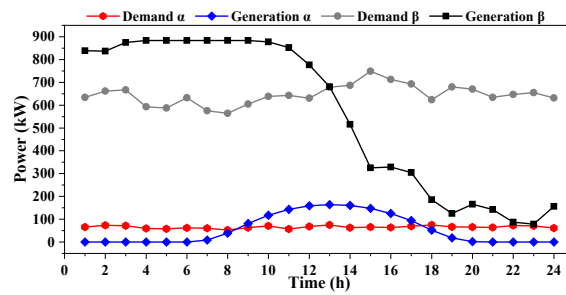


Fig. 2. Predicted generation and demand of communities.

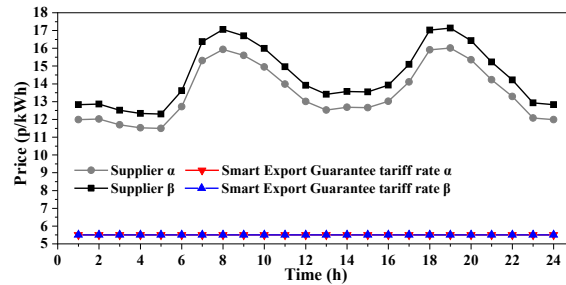


Fig. 3. Market prices

Figure 4 shows P2P prices in both communities. As is clear from Eqs. (4)-(5), the minimum import and export prices in each community are equal to the base price ($\lambda_{k,t}^{BS}$). The minimum import price in each community occurs when a community does not import electricity from its supplier or other communities. Community β has not imported any electricity from the supplier or community α during hours 1:00 to 13:00, so its peer's import price is equal to the base price. This happened to the community α during hours 9:00–18:00. Community β has been importing electricity from community α and its supplier since hour 14:00, so during these hours, the import price has exceeded the base price (red line in Fig. 4). Community α imports electricity from Community β during hours 1:00 to 8:00 and imports electricity from the supplier during hours 19:00 to 24:00, so the import price has exceeded the base price during these hours.

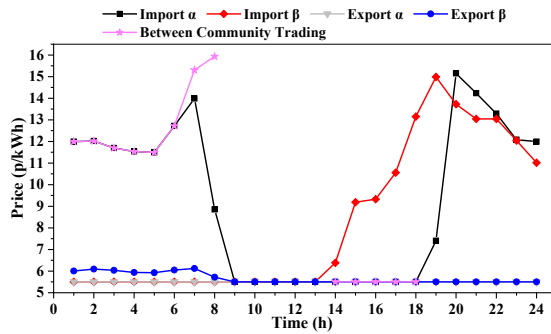


Fig. 4. P2P prices.

As it is clear from Eq. (4), the export price in each community depends only on the amount of electricity exported to another community and the export price. In the first eight hours and hour 13:00, community β exports electricity to community α , and during hours 14:00 to 18:00, community α exports electricity to community β . The between-community prices during these hours are illustrated in Fig. 4. Community α exports electricity to community β only during hours 14:00 to 18:00, so only during these hours its export price can exceed the base price; however, considering that the between-community prices are equal to the base price during these hours, the export price in this community is equal to the base price. It should be noted that during the hours when community α does not export electricity to community β , the export price is equal to the base price. Community β exports electricity to community α during hours 1:00 to 8:00 (blue line in Fig. 5), and the between-community price is higher than the base price during these hours (purple line in Fig. 4), so the export price in this community is higher than the base price (blue line in Fig. 4). Because community β does not export electricity to community α during other hours, the export price is equal to the base price.

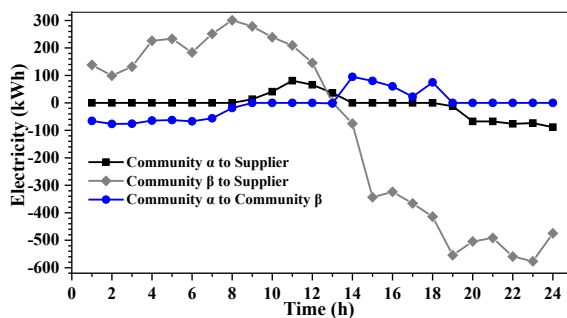


Fig. 5. Trading electricity in communities

The ambient air temperature and power consumption of the flexible load are presented in Fig. 6. It is known that as the temperature decreases, the amount of electricity consumed to maintain the inside temperature of houses within a comfortable range increase. The state of charge of the ESS is also shown in this figure. The Energy Storage System is charged at 12:00 and 13:00, because during these hours, the community α faces an excess of electricity. During hours 18:00 and 19:00, the Energy Storage System discharged all its electricity because during these hours, the community faced a deficit of electricity. Finally, it's charged at hour 24:00 to reach the initial state of charge.

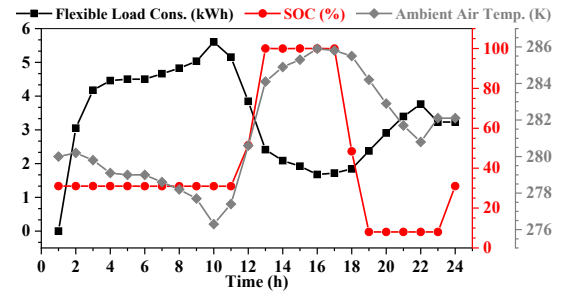


Fig. 6. SOC of the ESS and FL's consumption.

The total cost of the studied system is £599.66. In order to verify the advantage of between-community trading, another model was also solved without between-community trading. In that case, the total cost is £651.47, which is 8.6% higher than with community-community trading. In order to reveal the effect of P2P electricity trading compared to the traditional market, another model was also solved in the form of a traditional market, and the total cost in this case is £1646.68, which is almost triple that of the P2P case.

CONCLUSIONS

This paper describes a multi-community P2P electricity trading mechanism in a local electricity market. The Bill Sharing method, which is a cost-sharing method, was developed as the pricing mechanism for this structure. It was found that P2P in a multi-community system with between-community trading capability reduces the total cost of the electricity by 64% compared with the case without P2P electricity trading. It was also found that without between-community trading in the same system, the cost increases by more than 8%.

Conflicts of interest

The authors declare no conflict of interest.

REFERENCES

- [1] H. Ritchie, 'Sector by sector: where do global greenhouse gas emissions come from? - Our World in Data' [online], <https://ourworldindata.org/ghg-emissions-by-sector>. (Accessed 10 Feb 2023)
- [2] Department for Energy Security and Net Zero, 'Net Zero Government Initiative: UK roadmap to net zero government emissions', Dec. 2023, [online]. Available at <https://www.gov.uk/government/publications/net-zero-government-emissions-uk-roadmap> (Accessed 14 March 2024)
- [3] X. Luo, W. Shi, Y. Jiang, Y. Liu, and J. Xia, 'Distributed peer-to-peer energy trading based on game theory in a community microgrid considering ownership complexity of distributed energy resources', *Journal of Cleaner Production*, vol. 351, p. 131573, Jun. 2022. doi.org/10.1016/j.jclepro.2022.131573
- [4] F. Zhao, Z. Li, D. Wang, and T. Ma, 'Peer-to-peer energy sharing with demand-side management for fair revenue distribution and stable grid interaction in the photovoltaic community', *Journal of Cleaner Production*, vol. 383, p. 135271, Jan. 2023. doi.org/10.1016/j.jclepro.2022.135271
- [5] D. Kanakadhurga and N. Prabakaran, 'Peer-to-Peer trading with Demand Response using proposed smart bidding strategy', *Applied Energy*, vol. 327, p. 120061, Dec. 2022. doi.org/10.1016/j.apenergy.2022.120061
- [6] D. Peng, H. Xiao, W. Pei, H. Sun, and S. Ye, 'A novel deep learning based peer-to-peer transaction method for prosumers under two-stage market environment', *IET Smart Grid*, vol. 5, no. 6, pp. 430–439, Dec. 2022. doi.org/10.1049/stg2.12078
- [7] B. Gu *et al.*, 'Optimal Charge/Discharge Scheduling for Batteries in Energy Router-Based Microgrids of Prosumers via Peer-to-Peer Trading', *IEEE Trans Sustain Energy*, vol. 13, no. 3, pp. 1315–1328, Jul. 2022. doi.org/10.1109/TSTE.2022.3154145
- [8] D. Qiu, J. Xue, T. Zhang, J. Wang, and M. Sun, 'Federated reinforcement learning for smart building joint peer-to-peer energy and carbon allowance trading', *Applied Energy*, vol. 333, p. 120526, Mar. 2023. doi.org/10.1016/j.apenergy.2022.120526
- [9] D. Qiu, Y. Ye, D. Papadaskalopoulos, and G. Strbac, 'Scalable coordinated management of peer-to-peer energy trading: A multi-cluster deep reinforcement learning approach', *Applied Energy*, vol. 292, p. 116940, Jun. 2021. doi.org/10.1016/j.apenergy.2021.116940
- [10] J. Li, Y. Ye, D. Papadaskalopoulos, and G. Strbac, 'Computationally Efficient Pricing and Benefit Distribution Mechanisms for Incentivizing Stable Peer-to-Peer Energy Trading', *IEEE Internet Things J*, vol. 8, no. 2, pp. 734–749, Jan. 2021. doi.org/10.1109/JIOT.2020.3007196
- [11] S. Kuruseelan, and C. Vaithilingam, 'Peer-to-Peer Energy Trading of a Community Connected with an AC and DC Microgrid', *Energies*, vol. 12, no. 19, p. 3709, Sep. 2019. doi.org/10.3390/en12193709
- [12] Zhou, Y., Wu, J., & Long, C. Evaluation of peer-to-peer energy sharing mechanisms based on a multiagent simulation framework. *Applied Energy*, 2018, 222, 993-1022. doi.org/10.1016/j.apenergy.2018.02.089
- [13] W. Hua, Y. Zhou, M. Qadrdan, J. Wu and N. Jenkins, "Blockchain Enabled Decentralized Local Electricity Markets With Flexibility From Heating Sources," in *IEEE Transactions on Smart Grid*, vol. 14, no. 2, pp. 1607-1620, March 2023. doi.org/10.1109/TSG.2022.3158732
- [14] OFGEM, 'Smart Export Guarantee (SEG)', [online] <https://www.ofgem.gov.uk/environmental-and-social-schemes/smart-export-guarantee-seg> (Accessed 20 Feb 2023).

Jahanger HK

*Cardiff University
School of Engineering*

Haddad M

*Cardiff University
School of Engineering*

Robson S

*Cardiff University
School of Engineering*

Sumner M

University of Nottingham

SUSTAINABLE ENERGY

Double-ended Fault Location Method with Reduced Measurements

The double-ended impedance-based fault location Method (DEFLM) uses the wideband frequency content of the transient generated by the fault to determine the impedance from the point of measurement to the fault. This work evaluates the use of DEFLM in integrated power system such as those in More Electric Vehicles. Two approaches have been investigated with two measurements from two terminals and with one reduced measurement. The outcomes demonstrate that the DEFLM with full measurements provide a very high accuracy of the fault location with accuracy reaches 99% assuming the two end measurements are synchronized. On the other hand, the DEFLM with reduced current measurement from loads end shows less accuracy as the fault reaches the load terminal. However, the accuracy still high and within acceptable range utilizing more cost-effective approach.

Keywords:

Double-ended, fault location, high frequency, impedance-estimation, transient.

Corresponding author:

JahangerJ@cardiff.ac.uk



H.K. Jahanger, S. Robson, M. Haddad, and M. Sumner, 'Double-ended Fault Location Method with Reduced Measurements Double-ended Fault Location Method with Reduced Measurements', *Cardiff University School of Engineering Research Conference 2023*, Cardiff, UK, 2023, pp. 153-157.

doi.org/10.18573/conf1.ai

INTRODUCTION

Having a quick and accurate technique for locating faults is crucial in an integrated power system (IPS) because it reduces the time required to restore power to loads and enhances the system’s reliability [1]. Additionally, creating a fault location method that is affordable and requires minimal measurements is a challenging task to solve.

Double-ended impedance-based fault location is a widely used technique in the field of power system protection, enabling accurate and efficient fault location on distribution lines. The method is based on the measurement of impedance before and after the fault occurrence, and analysis of the difference in impedance measurements at both ends of the line to determine the location of the fault. Many studies have been conducted on the double-ended impedance-based fault location technique, demonstrating its effectiveness and reliability [2-5]. For example, a study by Aboshady (2017) [2] applied the technique to a distribution network, showing its ability to accurately locate faults even in such situations. Another study by Bahmanyar et al. (2017) [3] compared the performance of different fault location methods, demonstrating the advantage of the double-ended impedance-based method in terms of accuracy and robustness.

In summary, the double-ended impedance-based fault location technique has several advantages over other methods, including its non-intrusive nature, independence from line parameters, and ability to locate faults in both radial and meshed networks. Moreover, the technique has been implemented in studied for commercial protection relays, further demonstrating its practicality and reliability in real-world applications[4-5]. However, it requires full voltage and current measurements from both terminals of the faulted line. In this work, a double-ended impedance based with less measurements at non-fundamental frequencies is explored.

DOUBLE ENDED FAULT LOCATION METHOD (DEFLM)

In this section, a double-ended impedance based fault location method will be introduced based on full measurement and reduced measurement.

DEFLM

A single-phase circuit with a short circuit on the distribution line, is shown in Fig. 1(a), and is used to introduce the basis of this method. The supply impedance is represented by (Z_s), while Z_L is the equivalent load impedance. The cable impedance between the fault and the source end is Z_x and the remaining impedance Z_{l-x} represents the cable impedance from the fault point to the receiving end of the line. Note that the earth and the neutral are connected. The supply source at non-fundamental frequencies behaves as a short circuit, as shown in the Thevenin equivalent circuit of Fig. 1(b), while the fault is represented as a transient source which creates an equal and opposite voltage to the instantaneous pre-fault voltage (V_{pre-f}) at the fault location. POM1 is the point-of-measurement at the source end, while POM2 is the point-of-measurement at the receiving end.

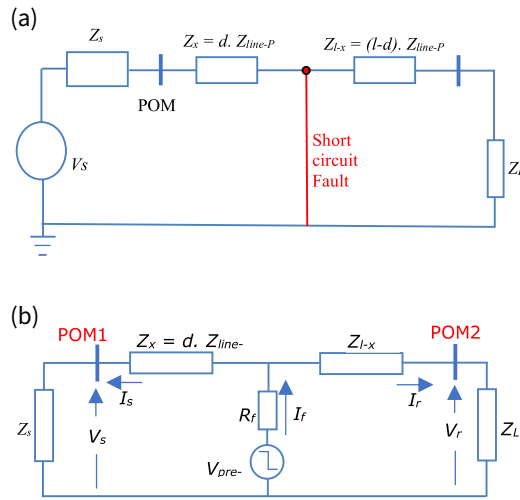


Fig. 1. Single line diagram with short circuit fault (a) Network at 50Hz, (b) Network at High frequency contents.

Kirchhoff’s laws are applied to the measured voltage and current during a fault for the measurements at both ends of the line to calculate the impedance between POM1 and the fault , yields (1) [6 - 8]:

$$V_s + I_s \cdot Z_x + I_f \cdot R_f = V_r + I_r \cdot Z_{l-x} + I_f \cdot R_f \tag{1}$$

where V_s, I_s are the voltage and current measurement at the source end of the line and V_r, I_r are the measured voltage and current at the receiving (load) end. The total impedance of the line is $Z_l = Z_x + Z_{l-x}$. Rearranging (1) for Z_x , gives (2):

$$Z_x = \frac{V_r - V_s + I_r \cdot Z_l}{I_s + I_r} \tag{2}$$

The fault distance is calculated by dividing Z_x by the per-meter impedance of the line (Z_{line-p}), as given in (3). The imaginary part of the impedance only is used because the reactance is not influenced by the fault resistance, and at higher frequencies, the reactance dominates the overall impedance more than the resistance. Furthermore, (2) shows that the fault resistance information, as well as the knowledge of the load impedance or the supply impedance are not required by the proposed DEFLM.

$$d = \frac{\text{imag}(\frac{V_r - V_s + I_r \cdot Z_l}{I_s + I_r})}{\text{imag}(Z_{line-p})} \tag{3}$$

DEFLM, ignoring I_r

It is proposed that the DEFLM can be implemented using only three measurements. In this approach, the source end voltage and current, as well as the receiving end voltage, will be required. Equation (2) is approximated by (4), which will be used in this section.

$$Z_x = \frac{V_r - V_s}{I_s} \tag{4}$$

Compared to (2), I_r is neglected in the denominator because at non-fundamental frequencies, it is assumed that $I_r \ll I_s$. Similarly, $I_r \cdot Z_l$ in the numerator of (2) will be very small compared to , hence, neglecting it has a limited influence on the estimated reactance and hence less measurement is required.

RESULTS

A model of a simple system was created using MATLAB/Simulink software. The single line diagram of the power system fault demonstrator at the ‘Flex Elec’ Laboratory-based IPS/microgrid at the University of Nottingham is shown in Fig. 2 [7,8], while the simulated demonstrator is shown in Fig. 3. The system consists of four sections with zone 1, 2 and 4 of 10m in length while zone 3 is 20 m. Each section is represented by lumped series resistance and inductance while the line capacitance is ignored due to the size and length of the cable used in the demonstrator. The current limiter and the load are also represented by pure resistance and inductance in series whereas the busbar and the power transformer are represented by a simple AC supply as shown in Fig. 3.

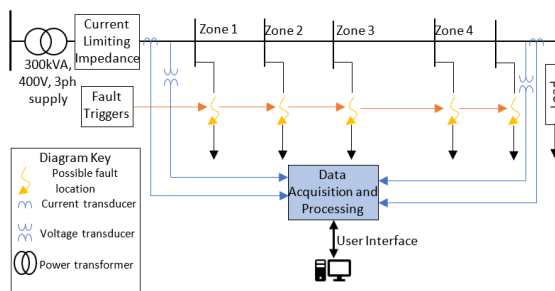


Fig. 2. Fault demonstrator at the University of Nottingham.

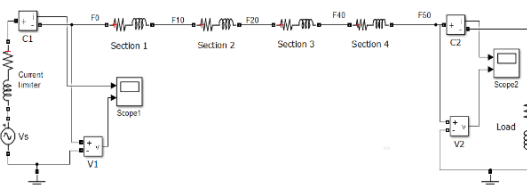


Fig. 3. MATLAB simulation of the Fault Demonstrator.

The per-unit-length resistance and inductance for each section are 1.15 mΩ/m and 0.82 μH/m [6-7], respectively. The load magnitude is (22+0.157j) Ω and the current limiting impedance is (0.5 + 0.0157j) Ω at 50Hz. Voltage and current transients measured at both ends, as shown in Fig. 4, are captured for 10ms at a sampling frequency of 50 kHz. The signals are then processed by multiplying it with a Blackman window. Finally, a Fast Fourier Transform (FFT) is used to transform the time domain signals to frequency domain and these are then used in (3). The frequency domain representation of these transients are derived using the FFT from the time domain signals and are shown in Fig. 5 with a frequency range up to 5 kHz.

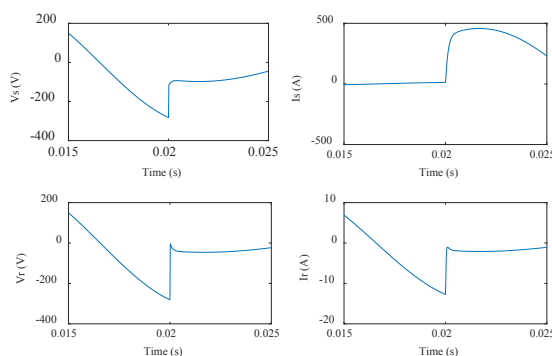


Fig. 4. Captured signals from POM1 and POM2 of the Simulated model.

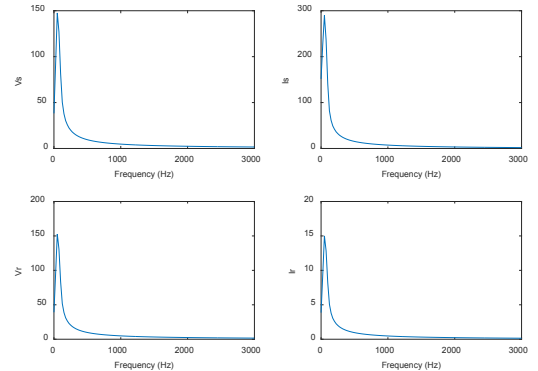


Fig. 5. Normalised Frequency domain representation of the measured signals from POM1 and POM2.

DEFLT Results

Five locations have been selected to create a line to ground fault through a 0.1Ω resistance as marked in Fig. 3: F0, F10, F20, F40, and F50. F0 represents a fault at the source end (POM1) while F50 is a fault at the receiving (POM2) end which is 50m from the source end. The data window is selected so that the fault transient is at the centre of the captured window as shown in Fig. 4. 5ms of pre-fault and 5ms of during-fault of data is utilized for the fault location algorithm.

The impedance estimated for the five fault locations in the frequency domain up to 3 kHz is shown in Fig. 6(a) which is the imaginary part while Fig. 6(b) is the real part of the impedance.

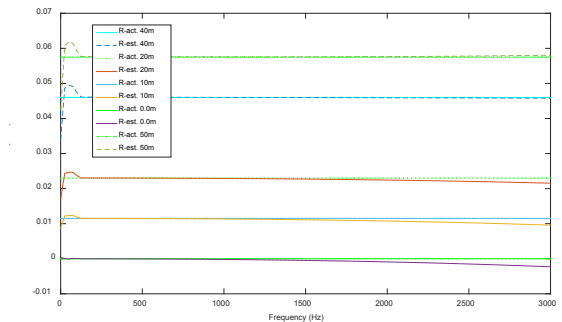
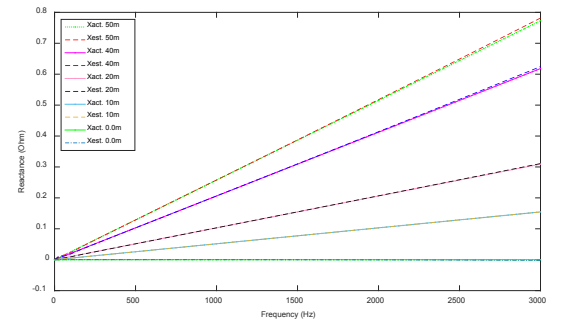


Fig. 6 Estimated impedance using DEFLM (a) Inductance part of the estimated Impedance (top), and (b) resistance part of the estimated impedance (bottom).

These estimated magnitudes represent the value of impedance between the source end and the fault location at non-fundamental frequencies, which is as indicated in Fig. 1. The solid lines represent the actual values used in

the model (Xact.), while the dashed lines are the estimated values (Xest.) using the DEFLM. It was found that the technique regarding the reactance part shows a strong match between estimated and actual values in the higher frequency range up to 3000 Hz while the resistance shows poorer accuracy than the reactance in the high frequency range. This is because in the high frequency range, the reactance is many times bigger than the resistance and any small error in the angle identified by the FFT process causes a significant error in the estimated resistance. However, the resistance can be ignored because the value of reactance is much higher than the resistance. Hence, the reactance is selected to locate the fault by dividing it with the per-metre reactance of the line at different frequencies.

DEFLM, ignoring I_r results

In this section, the DEFLT with one less measurement will be investigated. Receiving end current (I_r) is dropped and equation (4) is used to estimate the distance and consequently the distance.

Two line-neutral fault tests (F20 and F40) are imposed with $R_f = 4.5\Omega$ in order to demonstrate this approach. In Fig. 7 shown for F20, the estimated reactance using (4) (the solid blue line) is compared to the estimation using (2) (the dash-dotted red line). There is an obvious match between the two estimations. There is a small reduction in the accuracy when a fault was imposed 40m from the source-end (F40), which is shown in Fig. 8. However, the increase in the percentage error is less than 1%.

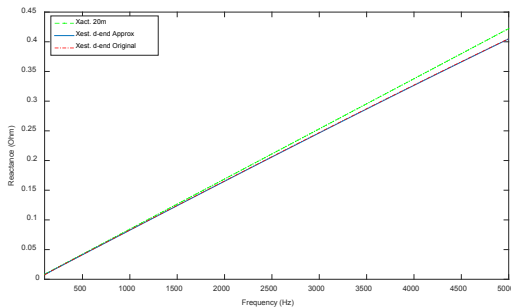


Fig.7. Estimated reactance using (2) versus (4) for fault at 10m.

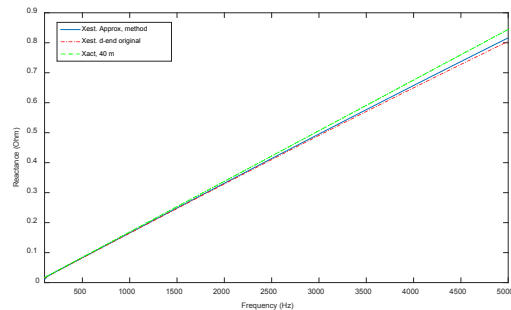


Fig. 8. Estimated reactance using (2) versus (4) for fault at 40m.

This behaviour is verified by looking at the frequency domain of the signals using in Fig. 9 which shows that $I_r(f) \ll I_s(f)$ as well as $I_r * Z_l \ll V_r - V_s$. Figure 9 shows the frequency domain representation of the measured signals for fault at 10m (top) I_s , I_r and $I_s + I_r$; and (bottom) $V_r - V_s$, $I_r * Z_l$, and $V_r - V_s + I_r * Z_l$.

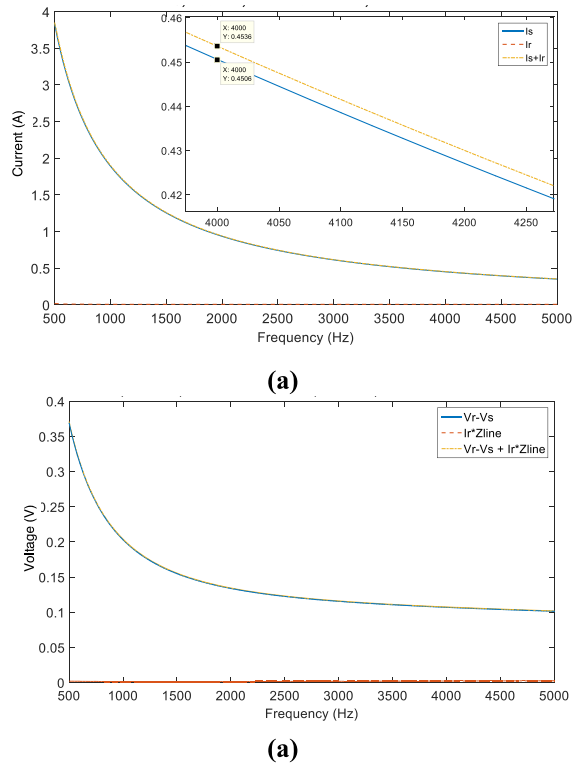


Fig.9. Frequency domain representation of the measured signals for fault at 10m.

CONCLUSIONS

A DEFLM based on higher frequency content of the fault generated transient utilizing full two ends measurements and reduced measurements is introduced and investigated. It has been shown that the DEFLM shows a very high accuracy when locating fault using the voltage and current measurements from the two terminals. Additionally, the proposed approach by reducing the required measurements from the load end, showed that the accuracy can drop. However, the accuracy of the proposed approach is still within acceptable rate.

Acknowledgments

This work was partially supported by EPSRC [Grant Number: EP/T021780/1].

Conflicts of interest

The authors declare no conflict of interest.

REFERENCES

- [1] R. Dashti, M. Daisy, H. Mirshekali, H. R. Shaker, and M. Hosseini Aliabadi, 'A survey of fault prediction and location methods in electrical energy distribution networks', *Measurement*, vol. 184, p. 109947, Nov. 2021. doi.org/10.1016/j.measurement.2021.109947
- [2] F. M. Aboshady, M. Sumner, and D. W. P. Thomas, 'A double end fault location technique for distribution systems based on fault-generated transients', in *2017 IEEE 26th International Symposium on Industrial Electronics (ISIE)*, Edinburgh, United Kingdom: IEEE, Jun. 2017, pp. 32–36. doi.org/10.1109/ISIE.2017.8001219
- [3] A. Bahmanyar, S. Jamali, A. Estebarsari, and E. Bompard, 'A comparison framework for distribution system outage and fault location methods', *Electric Power Systems Research*, vol. 145, pp. 19–34, Apr. 2017. doi.org/10.1016/j.epsr.2016.12.018
- [4] A. G. Phadke and J. S. Thorp, *Computer relaying for power systems*, 2nd ed., Chichester, West Sussex; Hoboken, NJ: Baldock, Hertfordshire: John Wiley & Sons; Research Studies Press, 2009.
- [5] M.M. SahaSaha, J. Izykowski, J. Rosolowski, 'Two-end and Multi-end Fault-location Algorithms', in *Fault Location on Power Networks*, London: Springer London, 2010, pp. 263–331. doi.org/10.1007/978-1-84882-886-5_7
- [6] H. K. Jahanger, M. Sumner, and D. W. P. Thomas, 'Combining fault location estimates for a multi-tapped distribution line', in *2017 IEEE PES Innovative Smart Grid Technologies Conference Europe (ISGT-Europe)*, Torino, Italy: IEEE, Sep. 2017, pp. 1–6. doi.org/10.1109/ISGTEurope.2017.8260187
- [7] H. K. Jahanger, D. W. P. Thomas, M. Sumner, and C. Rose, 'Impact of an inverter-based DG on a double-ended fault location method', *The Journal of Engineering*, vol. 2018, no. 15, pp. 1078–1083, Oct. 2018. doi.org/10.1049/joe.2018.0261
- [8] H. K. Jahanger, D. W. P. Thomas, and M. Sumner, 'An investigation into the robustness of a double-ended wideband impedance-based fault location technique', *Scientific Reports*, vol. 13, no. 1, p. 10001, Jun. 2023. doi.org/10.1038/s41598-023-36541-2

Hills M

Cardiff University
School of Engineering

Lugg-Widger P

Cardiff University
School of Engineering

Stone C

Cardiff University
School of Engineering

Peretto N

Cardiff University
School of Engineering

Haddad A

Cardiff University
School of Engineering

Mitchard D

Cardiff University
School of Engineering

SUSTAINABLE ENERGY

Spectroscopic Measurements of Light Emissions from High Current Arcs

Due to the destructive impact of lightning, and the risk of increasing strikes attributed to climate change on the natural and built environment, work has been carried out to study the temperature and light emitted by laboratory generated lightning using non-invasive light-based instrumentation, which will allow optimisation of lightning protection. Using spectroscopy, the optical emission spectrum of a 55 kA lightning arc with a copper fuse wire was obtained for study. The results showed the light radiated in the visible and infrared range, with strong copper emission lines seen, and determined a temperature of the arc of $8,531 \pm 577$ K. This is in preparation for sub-nanosecond resolution data to be recorded using a new streak spectrograph to create temporal data of lightning arcs. A new laboratory experimental set up is being developed to explore further electromagnetic emissions in the infrared, ultraviolet and x-rays, to derive other useful information about lightning phenomena.

Keywords:

Lightning phenomena, engineering, physics, spectroscopy, temperature, atomic emission lines.

Corresponding author:

HillsMT@cardiff.ac.uk



M. Hills, P. Lugg-Widger, N. Peretto, A. Haddad, and D. Mitchard, 'Spectroscopic Measurements of Light Emissions from High Current Arcs' *Cardiff University School of Engineering Research Conference 2023*, Cardiff, UK, 2023, pp. 158-162.

doi.org/10.18573/conf1.aj

INTRODUCTION

Lightning is one of the most unpredictable and destructive phenomena in nature, which can cause critical damage to infrastructure, transportation and power networks, and lead to natural disasters such as uncontrolled wildfires. As global temperature increases due to climate change, it is estimated that the energy of lightning strikes will also increase, as well as its frequency by 5 – 6 % per degree Celsius [1-3] but the impact of global warming on lightning rates is poorly constrained. Here we propose that the lightning flash rate is proportional to the convective available potential energy (CAPE). There is a growing scientific interest in understanding the interactions and further characteristics of lightning. The temperature, energy, arc initiation and duration of lightning arcs are all important parameters to study and improve their quantification to allow optimised lightning protection [4]. However, lightning is difficult to study in nature, as well as when generated in a laboratory, particularly because it can damage or destroy most instrumentation and analysis techniques. Therefore, non-contact, non-invasive techniques are required to ensure the safety of measuring equipment.

In this study, a detailed high-resolution spectroscopy and imaging was carried out to demonstrate the ability to obtain characteristic elemental interactions and arc temperature from a laboratory generated lightning strike. This type of technique will form the basis of a new laboratory experimental facility dedicated to the development of light-based measurement techniques, from soft x-ray to infrared. This will then allow further studies to be conducted, which may contribute towards other research areas, such as combustion.

BACKGROUND

Blackbody radiation is the spectrum of Electromagnetic (EM) energy emitted by all objects, with an ideally opaque, non-reflective body emitting a perfect curve. This continuous spectrum can indicate many characteristics of objects such as the temperature and the power radiated. As a body begins to rise in temperature, the total emitted radiation rises as given by Planck's Law (Eq. 1):

$$L(\lambda, T) = \left(\frac{2hc^2}{\lambda^5} \right) \left(\frac{1}{e^{\frac{hc}{\lambda k_B T}} - 1} \right) \quad (1)$$

where L is the spectral radiance [$\text{W m}^{-2} \text{sr}^{-1}$], h is Planck's constant (6.63×10^{-34} [J s]), c is the speed of light (3.00×10^8 [m s^{-1}]), λ is the emitted wavelength [m], k_B is the Boltzmann constant (1.4×10^{-23} [J K^{-1}]) and T is the temperature [K].

As well as an increase in radiation emitted, the wavelength at which the intensity is at its peak decreases due to Wien's Law (Eq. 2):

$$\lambda_{max} = \frac{b}{T} \quad (2)$$

where λ_{max} is the peak emitted wavelength [m] and b is Wien's displacement constant (2.90×10^{-3} [m K]).

An illustration of these laws is given in Fig. 1, where the spectral radiance in a lightning strike is several orders of magnitude higher than the radiance of a human. Also included are the radiation curves of the surface of the sun ($\approx 5,500$ K), and that of a large campfire or a Bunsen burner's flame ($\approx 1,500$ K). The area under these curves is proportional to the energy and, as such, indicates that the energy radiated by an object also increases as temperature rises.

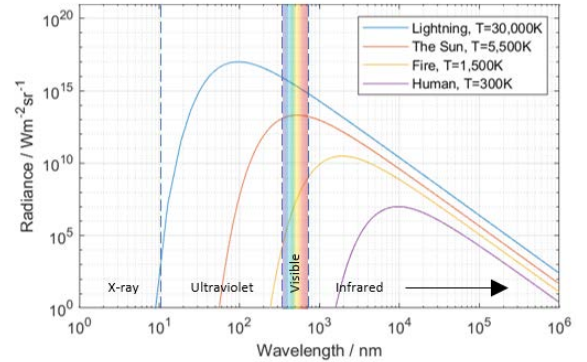


Fig. 1. The Blackbody Radiation Curves derived from the temperature of a lightning arc, the sun, a typical fire, and a human. Temperatures (T) are given in the legend.

With an average temperature of around 30,000 K, it can be seen that lightning primarily radiates in the ultraviolet range, unlike other objects. These low-wavelength electromagnetic waves are extremely high in energy but have not been studied in great detail. Studies of the blackbody radiation of lightning have primarily investigated the near-infrared (NIR) and visible wavelength of the EM spectrum.

Another characteristic phenomenon seen in the spectrum is atomic emission lines. When individual elements are excited by an energetic event, photons with certain wavelengths, specific to that element, are absorbed and re-emitted. By measuring the overall light emitted from an event, several elements can be identified with their respective emission lines. For example, if a spectrograph records a high intensity of photons with a wavelength of 777.4 nm, this can be identified as oxygen-I [5]. Many elements display a unique colour when heated due to having several prominent emission lines at a visible wavelength. Examples of this include copper burning blue-green with lines at 510.6, 515.3 and 521.8 nm to name a few, and sodium appearing yellow when energised due to prominent lines at 589.0 and 589.6 nm [6], which is why sodium street lamps glow yellow. One method of measuring the temperature using emission lines is the 'two lines method' [7-10]. When a plasma is in local thermodynamic equilibrium, the relative intensities of two spectral lines (of the same element) can be used to determine the temperature. Using two lines with different excited state energies, the temperature of an event can be found using Eq. 3 [9,10]:

$$T = \frac{E_2 - E_1}{k_B} \cdot \left[\ln \left(\frac{I_1 \lambda_1 A_2 g_2}{I_2 \lambda_2 A_1 g_1} \right) \right]^{-1} \quad (3)$$

where T is the temperature [K], E_i is the excited state energy of line i [J], λ_i is the wavelength of the line [nm], I_i is the intensity of the line, g_i is the statistical weight, A_i is the probability of transition [s^{-1}] and k_B is the Boltzmann constant (1.38×10^{-23} [J K^{-1}]).

EXPERIMENTAL METHOD

To generate lightning with characteristics similar to those of natural lightning, a 100 μs , 55.5 kA D waveform was used in accordance with the EUROCAE ED84 standard and its SAE equivalent [11]. A graph showing this measured current waveform is given in Fig. 2.

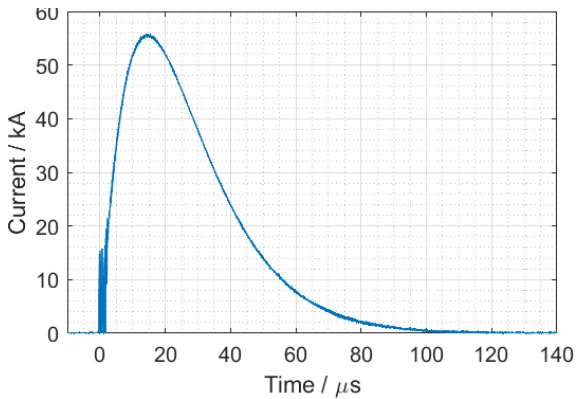


Fig 2. A 100 μ s, 55.5 kA D lightning waveform arc.

A stainless steel rod electrode with a diameter of 15 mm was placed 45 mm away from a flat aluminium grounding plate. These selected materials allow for minimal damage during repeated impulse testing. As per the ED105 Standard [12], an insulating ball is threaded onto the electrode and a 0.1 mm diameter copper initiation wire is attached from the end of the electrode to the grounding plane, which helps to create a conductive path for the arc and then vaporises early during the impulse front. However, the thin fuse wire can also be used to obtain prominent emission lines providing useful information for temperature calculations. Fig. 3 shows the electrode arrangement as well the Czerny-Turner integrated spectrographic system used to record the spectrum, observing and integrating all light emitted during the 100 μ s event. Light data is recorded from visible wavelengths at 390 nm to the infrared range at 950 nm. A sub-range of 560 nm allows many atomic lines to be seen and a more accurate calibration to be performed before recording the data. A wavelength resolution of 0.55 nm is achieved using a diffraction grating of 150 lines/mm and a blaze of 300 nm. An optic fibre is used to collect the light emitted, with a collimator to prevent oversaturation. Using a slit size of 50 μ m at the opening of the spectrograph, and an exposure time of 5 s, light is collected into the spectrograph and reflected using mirrors and a diffraction grating. It is then received by a CCD camera array of 1024 pixel bins.

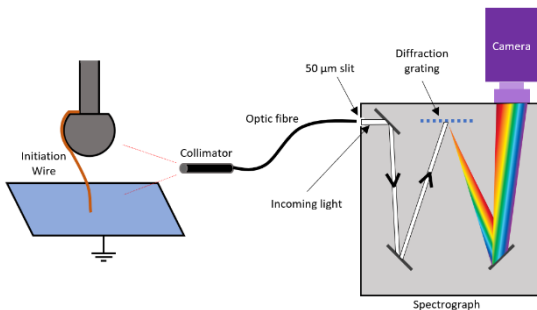


Fig 3. A schematic of the experiment set-up and the inner workings of the spectrograph. A stainless steel rod with an insulating ball was placed 45 mm away from the aluminium grounding plate, with a copper initiation wire connecting the two.

A mercury-argon light source was used to calibrate the system. To avoid any background noise, several spectra were taken when no event occurred, to subtract these values from the final results. This ensures all data analysed is from the event alone.

To capture the photographic image of the event, a full-frame DSLR was used with a shutter opening time of 6 s. Attached to the lens of the camera were two ND64 (neutral-density-6-stop) filters to reduce saturation in the image.

RESULTS AND DISCUSSION

A spectrum of a 55.5 kA lightning impulse was recorded and analysed to identify elemental emission lines. From this record, a temperature measurement was estimated.

Figure 4 shows a photographic image of the arc. The colours seen in the image already give an indication to the elements that will be seen in the spectrum. Copper vapour emits a blue-green colour due to prominent atomic emission lines in that section of the EM spectrum. The orange in the background is the vaporising wire, illuminated by the arc.



Fig 4. An image of a 55.5 kA lightning arc taken with a shutter opening time of 6 s.

Using an integrated spectrograph, Fig. 5 shows the total atomic emission obtained over the entire arc lifetime. Prior to studying the results, several post-data analyses were undertaken. A background spectrum was taken and subtracted from the final results, and other factors such as quantum efficiency and optic fibre attenuation (as well as anomalies such as cosmic rays) were taken into account. These peaks were then processed into an intensity plot. This allowed for clearer imaging of emission lines.

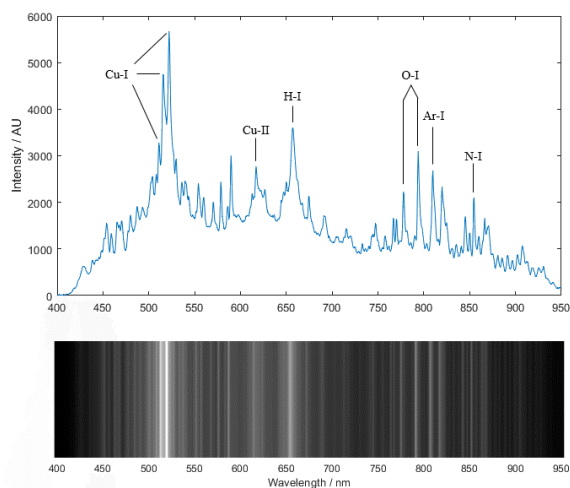


Fig 5. A spectrum and an intensity plot of the spectrum of a 55.5 kA lightning arc using a copper initiation wire.

By employing a coding script in MATLAB, the most prominent peaks in the spectrum were identified and recorded, with examples seen in Appendix A. Using a database of emission lines found in [5,13,14], prominent elements were then matched. These peaks may sometimes be broader than expected or may be different emission lines combined into one peak due to lack of resolution, especially when recording a wide wavelength range. To avoid misidentifying peaks, the three strongest copper-I peaks were used for temperature assessments. The wavelength of these peaks are in the blue-green section of the visible spectrum, hence the colour found in Fig. 4.

Examples of three prominent peaks of copper-I are found in Table 1. This includes the information required to calculate a temperature measurement of the arc.

Cu-I Peak	Wavelength [nm]	Energy [J]	Intensity [Counts]	g	A [s ⁻¹]
1	Cu-I	2558	3273	4	0.2 x10 ⁻⁹
2	Cu-I	3274	4749	4	6.0 x10 ⁻⁹
3	Ar-I	2677	5673	6	7.5 x10 ⁻⁹

Table 1. The emission line information for three peaks of Cu-I [5].

Using the values shown in Table 1 in Eq. (3), two different temperature values were calculated. When comparing peaks 1 and 2, a temperature of 9108±273 K was calculated and when comparing peaks 1 and 3, a temperature of 7954±239 K was found. Errors are estimated to be around 3% of the temperature value. These temperature values have a considerable difference, but this is due to the temperature being an average, integrated, value across the entire arc length (100 μs) and so the intensity of emission lines varies slightly during that duration. Measurements were also taken under the assumption of local thermodynamic equilibrium, which is likely not the case over the entire arc period. Additional analysis can be carried out to obtain a more accurate average value by comparing further peaks, examining the emission lines of other elements within the same arc, and by measuring the spectrum emitted at time intervals, with smaller ranges allowing for more accurate results.

CONCLUSIONS AND FUTURE WORK

Using integrated spectrograph systems, temperature values have been calculated for lightning arcs, but these measurements have relatively large differences (around 1,200 K, which is approximately 15%). As such, more detailed work would need to be undertaken to reduce this margin of error by primarily using a greater resolution and different emission spectra for the analysis. To improve the experimental results, streak spectroscopy measurements will be undertaken. This offers advanced and faster time-resolved measurements which improves accuracy. Such streak camera-based spectroscopy will allow temporal temperature measurements to be calculated at any point during the arc's lifetime, and thus a detailed variation in temperature can be obtained.

A new experimental set up will be developed to allow new more accurate experiments in this field to be completed. As well as detailed temporal spectroscopy, this next laboratory setup will allow x-ray emissions of an event to be measured

and further complement a schlieren imaging system. As lightning emits x-rays, this will give critical information to the blackbody radiation of such an event.

Acknowledgments

The authors gratefully acknowledge the financial support provided by the EPSRC DTC and NERC Project NE/X010848/1.

Conflicts of interest

The authors declare no conflict of interest.

Appendix A

Wavelength [nm]	Estimated Element [5]	Intensity [Counts]
503.7	Cu-I	2558
510.6	Cu-I	3274
515.4	Cu-I	4749
521.5	Cu-I	5673
529.4	Cu-I	2928
589.5	Ar-I	3005
617.0	Cu-II	2776
656.3	H-I	3604
793.8	O-I	3102
809.9	Ar-I	2677

Table 2. The intensity and wavelengths of prominent peaks found in a spectrum of a 55 kV copper-led lightning arc.

REFERENCES

- [1] D. M. Romps, J. T. Seeley, D. Vollaro, and J. Molinari, 'Projected increase in lightning strikes in the United States due to global warming', *Science*, vol. 346, no. 6211, pp. 851–854, Nov. 2014.
doi.org/10.1126/science.1259100
- [2] N. Michalon, A. Nassif, T. Saouri, J. F. Royer, and C. A. Pontikis, 'Contribution to the climatological study of lightning', *Geophysical Research Letters*, vol. 26, no. 20, pp. 3097–3100, Oct. 1999.
doi.org/10.1029/1999GL010837
- [3] C. Price and D. Rind, 'Possible implications of global climate change on global lightning distributions and frequencies', *J Geophys Res Atmospheres*, vol. 99, no. D5, pp. 10823–10831, May 1994.
doi.org/10.1029/94JD00019
- [4] M. A. Uman, 'Determination of lightning temperature', *J Geophys Res*, vol. 74, no. 4, pp. 949–957, Feb. 1969.
doi.org/10.1029/JB074i004p00949.
- [5] A. Kramida, Y. Ralchenko, J. Reader, and NIST ASD Team, *NIST Atomic Spectra Database (version 5.10)*, National Institute of Standards and Technology, 2022.
doi.org/10.18434/T4W30F
- [6] R. F. Barrow and E. F. Caldin, 'Some Spectroscopic Observations on Pyrotechnic Flames', *Proc Phys Soc B*, vol. 62, no. 1, pp. 32–39, Jan. 1949.
doi.org/10.1088/0370-1301/62/1/305
- [7] D. Clark, D. Carr, D. Mitchard, C. Stone, and A. Haddad, 'Spectroscopic techniques for temperature measurement of laboratory generated lightning arcs', *20th International Symposium on High Voltage Engineering*, Buenos Aires, Argentina, 2017.
- [8] R. Kozakov, M. Kettlitz, K.-D. Weltmann, A. Steffens, and C. M. Franck, 'Temperature profiles of an ablation controlled arc in PTFE: I. Spectroscopic measurements', *J Phys D: Appl Phys*, vol. 40, no. 8, pp. 2499–2506, Apr. 2007.
doi.org/10.1088/0022-3727/40/8/013
- [9] X. Li, J. Zhang, L. Chen, Q. Xue, and R. Zhu, 'Measuring Method for Lightning Channel Temperature', *Sci Rep*, vol. 6, no. 1, p. 33906, Sep. 2016.
doi.org/10.1038/srep33906
- [10] A. Descoedres, C. Hollenstein, R. Demellayer, and G. Walder, 'Optical emission spectroscopy of electrical discharge machining plasma', *Journal of Materials Processing Technology*, vol. 149, no. 1–3, pp. 184–190, Jun. 2004.
doi.org/10.1016/j.jmatprotec.2003.10.035
- [11] EUROCAE WG-31, SAE Committee AE-2, *ED-84A: "Aircraft Lightning Environment and Related Test Waveforms"*, EUROCAE, 2013.
- [12] EUROCAE WG-31, SAE Committee AE-2, *ED105A: "Aircraft Lightning Test Methods"*, EUROCAE, 2013.
- [13] D. Mitchard, D. Clark, D. Carr, and A. Haddad, 'Technique for the comparison of light spectra from natural and laboratory generated lightning current arcs', *Applied Physics Letters*, vol. 109, no. 9, p. 093502, Aug. 2016.
doi.org/10.1063/1.4962205
- [14] D. Mitchard, P. Widger, D. Clark, D. Carr, and A. Haddad, 'Optical emission spectra of high current and high voltage generated arcs representing lightning', *Applied Physics Letters*, vol. 114, no. 16, p. 164103, Apr. 2019.
doi.org/10.1063/1.5092875

Harper J
Cardiff University
School of Engineering

Johnson M
Rolls-Royce plc
Sin A-37, Derby

Durand E
Cardiff University
School of Engineering

Crayford A
Cardiff University
School of Engineering

SUSTAINABLE ENERGY

Influence of Fuel Hydrogen Content and Atomisation Quality on Ultrafine Non-volatile Particulate Matter Emissions in RQL Gas Turbine Technology

Aircraft engines are a source of harmful non-volatile Particulate Matter (nvPM) emissions, negatively affecting human health and the global environment. To mitigate this, new sources of fuel are being assessed for the commercial aviation sector. Sustainable Aviation Fuels (SAF) show significant promise as replacements to conventional aviation fuels, with the potential to reduce lifecycle CO₂ and nvPM emissions because of lower aromatic contents and higher hydrogen content. Towards better understanding of the nvPM emissions from aircraft combustors operating with SAF, this work outlines results from the RAPTOR experimental test campaigns performed at Cardiff University's Gas Turbine Research Centre (GTRC). Several aviation fuels of varying physiochemical properties were burned in a non-proprietary Rich-Quench-Lean (RQL) combustor rig. The nvPM emissions were measured using the European nvPM reference system, with data corrected for particle loss in the sampling and measurement system using additional particle size measurement. nvPM emission reductions were achieved for fuels of higher hydrogen content, and system loss correction was required to accurately quantify those reductions. Additionally, independent control of the air supply to the combustor rig allowed the impact of fuel spray quality to be decoupled from AFR, demonstrating that small improvements in spray droplet atomisation predicted from benchmarking fuel spray experiments (~5% reduction in SMD) consistently yielded significant reductions in nvPM emissions, ranging from 5-72% for nvPM EI_{mass}, 11-89% for nvPM EI_{number} and 1-7% for GMD.

Keywords:
Rich-quench-lean combustor,
particulate matter emissions,
sustainable aviation fuel,
atomisation, particle loss correction.

Corresponding author:
DurandEF@cardiff.ac.uk



J. Harper, E. Durand, M. Johnson, and A. Crayford, 'Influence of Fuel Hydrogen Content and Atomisation Quality on Ultrafine Non-volatile Particulate Matter Emissions in RQL Gas Turbine Technology', *Cardiff University School of Engineering Research Conference 2023*, Cardiff, UK, 2023, pp. 163-167.

doi.org/10.18573/conf1.ak

INTRODUCTION

Commercial aviation is currently responsible for around 2-3% of anthropogenic CO₂ emissions, with its global contribution expected to rise owing to predicted increases in flights and the challenges associated with decarbonising aircrafts compared to other sectors (e.g., Automotive) [1], [2].

Aircraft engines also produce other harmful emissions including NO_x and non-volatile Particulate Matter (nvPM). The production of nvPM is widely attributed to the presence of aromatic compounds in conventional Jet fuels, which are a carryover from the crude oil refinement process and have minimum requirements in current fuel specs [3]. The nvPM size from aviation gas turbines typically ranges between 10-100 nm [4]–[7], small enough to be absorbed by the lungs, resulting in cardiovascular and respiratory issues [8], [9]. Most commercial gas turbine engines use Rich-Quench-Lean (RQL) combustors, which were originally developed to mitigate NO_x emissions, however nvPM emissions are produced in fuel-rich primary zone [10] Gas Turbine Combustion: Alternative Fuels and Emissions, Third Edition provides an up-to-date design manual and research reference on the design, manufacture, and operation of gas turbine combustors in applications ranging from aeronautical to power generation. Essentially self-contained, the book only requires a moderate amount of prior knowledge of physics and chemistry. In response to the fluctuating cost and environmental effects of petroleum fuel, this third edition includes a new chapter on alternative fuels. This chapter presents the physical and chemical properties of conventional (petroleum-based with their burn out competing with NO_x reduction in the secondary lean zone.

Both CO₂ and nvPM emissions can be reduced using Sustainable Aviation Fuels (SAF). SAFs produce CO₂ during combustion but have the potential to offer reduced lifecycle CO₂ emissions through carbon capture at their feedstocks. Many SAF also allow for reductions in nvPM emissions due to the lower aromatic (higher hydrogen) content they typically exhibit [4], [11].

SAFs also have the potential to be used as drop-in fuels, meaning that they resemble conventional aviation kerosene closely enough to be used in existing aircraft with minimal modifications. This makes them promising to replace existing Jet-A fuels, with numerous pathways already approved to allow their use when blended with conventional Jet Fuel [12].

Towards better understanding the potential benefits of implementing SAF, the emissions of six Jet fuels of varying physiochemical properties were assessed using a non-proprietary RQL representative combustor as part of the RAPTOR (Research of Aviation PM Technologies, mOdeling and Regulation) research program. The RQL combustor is representative of a small aircraft combustor operating at low thrust conditions, such as idle on a runway. The nvPM and gaseous emissions were measured using the regulatory compliant European nvPM reference [13] and rigorous testing. Three reference systems for aircraft engine nvPM emissions measurement, compliant with the specifications for the standardized methodology, were independently developed. This paper reports the results of the first inter-comparison of these three reference systems using a CFM56-7B26/3 aircraft engine to establish repeatability and intermediate precision of the sampling and measurement systems as part of the multi-agency international collaborative projects: Aviation-Particle Regulatory

Instrumentation Demonstration Experiment (A-PRIDE, with additional particle size measurement performed for both particle loss correction, and to investigate the impact of fuel properties on particle size (i.e., Geometric Mean Diameter (GMD)). Additionally, the impact of atomisation quality on emissions was assessed via independent control of the air supplies to the fuel atomiser and primary zone cooling plate, affording maintenance of the primary and global Air to Fuel Ratios (AFR) whilst changing atomisation quality. As such, the results of this work facilitate better understanding of the impact of both fuel composition and atomisation properties on nvPM emissions, towards improving local air quality.

MATERIALS AND METHODS

Six fuels were assessed, including high-aromatic conventional Jet fuels (J-HA1 & J-HA2), a high aromatic SAF (A-HA), a low aromatic Gas-To-Liquid fuel (GTL), and blends of GTL and Jet fuels (B-HE & B-LA). In line with recent research in the field [11], [14], emphasis was given to fuel hydrogen content, which was determined using GCxGC-FID compositional data and represents the typical range encountered across Jet fuels meeting the aromatic and di-aromatic specifications prescribed by ASTM D1655 [3].

Fuel	Hydrogen Content (% wt.)	Total Aromatic Content (% wt.)	Di-Aromatic Content (% wt.)
J-HA1	13.43	24.24	1.07
A-HA	13.51	20.57	0.28
J-HA2	13.65	22.75	2.18
B-HE	14.51	12.82	0.14
B-LA	14.90	6.71	0.38
GTL	15.47	0.06	0.00

Table 1. RAPTOR fuel properties.

Experiments were undertaken at Cardiff University's Gas Turbine Research Centre (GTRC) using their bespoke 'Flexis' RQL combustor rig. Fuel and atomisation air were introduced using a purpose developed prefilming airblast atomiser produced using Additive Manufacturing (AM) [15], with secondary combustion air introduced through a fixed geometry combustion liner manufactured by traditional machining techniques. The combustor was housed in a High-Pressure Optical Chamber (HPOC), allowing for elevated temperatures, and pressure.

Two iterations of the combustor were used labelled Mk. II and Mk. II-A, with the Mk. II-A designed to afford an additional air supply feed to the primary zone via an internal transply cooling plate. Independent control of the air supplies to the atomiser and cooling plate allowed for variation in atomisation quality whilst maintaining constant primary AFR, thereby decoupling the impact of atomisation quality on emissions. Estimation of the atomisation quality was achieved using spray characterisation experiments carried out prior to combustion testing [15]. Measured droplet size data, over a range of operating conditions, were used to derive empirical constants for the developed AM atomiser, required as inputs for an established atomisation correlation [15]. Droplet sizes were measured for a range of fuels using a Dantec Fiber PDA system.



Fig. 1. RQL combustor atomiser and combustion chamber design.

Measurement of nvPM number and mass emissions was undertaken using the regulatory compliant European nvPM reference sampling and measurement system [16], [17], which contains several instruments used for the traceable determination of nvPM and gaseous emissions [13] and rigorous testing. Three reference systems for aircraft engine nvPM emissions measurement, compliant with the specifications for the standardized methodology, were independently developed. This paper reports the results of the first inter-comparison of these three reference systems using a CFM56-7B26/3 aircraft engine to establish repeatability and intermediate precision of the sampling and measurement systems as part of the multi-agency international collaborative projects: Aviation-Particle Regulatory Instrumentation Demonstration Experiment (A-PRIDE).

As per international standards [16] nvPM number and mass emissions are reported as Emission Indices (EIs) used to assess engine performance by giving emitted pollutants per unit mass of fuel burned. Particle loss correction was performed using a method PSD_B [18] to account for the significant losses of particles in a regulatory nvPM system, with particle size data determined using a Cambustion DMS-500. Each test point corresponds to a stable 30-second condition with error bars representative of ± 2 standard deviations of the scatter across the point.

RESULTS AND DISCUSSIONS

The impact of fuel hydrogen content on loss-corrected nvPM EI number and mass emissions are shown in Figure 2 for both combustor iterations. In agreement with the literature [4], [11], nvPM emissions are seen to decrease with increasing fuel hydrogen content, demonstrating a stronger correlation with nvPM emissions than any other single fuel property (e.g., aromatic content). System loss correction was critical to accurately quantify the nvPM reduction associated with cleaner fuels. This is because higher losses are associated with smaller particle sizes, typically witnessed for fuels of higher hydrogen content. Therefore, engine exit particle number concentrations tend to be underpredicted in the case of SAFs without correction, resulting in an overprediction in the effectiveness of high hydrogen content SAFs in mitigating nvPM. By comparing values of EI number before and after system loss correction, this overprediction was determined empirically as shown in Figure 3. As can be seen, without system loss correction, EI number reductions for higher hydrogen content fuels are overestimated by up to ~13%.

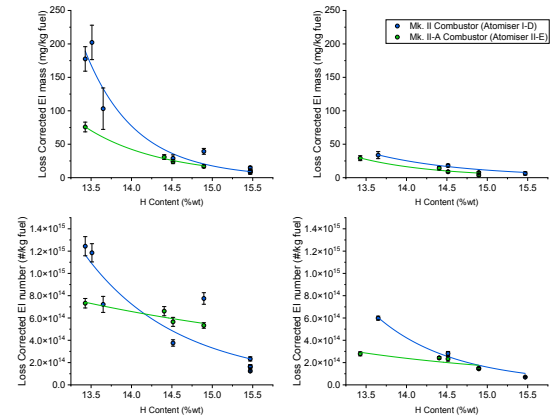


Fig. 2. nvPM EI number and mass emissions Vs fuel hydrogen content at rich (left) and lean (right) conditions.

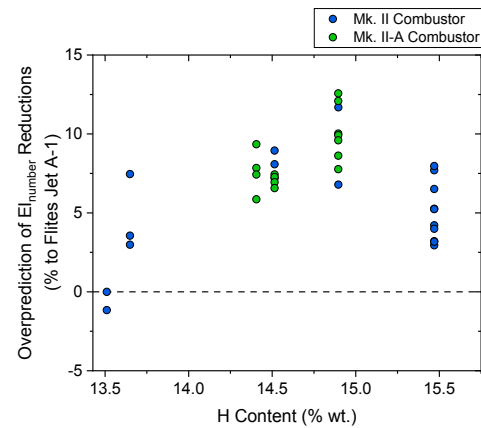


Fig. 3. Percent overprediction of EI number reduction associated with increased fuel hydrogen content without system loss correction.

Additionally, the impact of atomisation quality on nvPM emissions was assessed using the Mk. II-A by holding the primary and global AFRs constant at a given fuel hydrogen content, whilst decreasing the relative proportion of air supplied to the atomiser, resulting in worsened atomization performance (5% in SMD) as estimated using empirically validated correlations [15]. For the rich and lean conditions, switching to the reduced atomisation condition was achieved by reducing the mass flowrate of air through the atomiser by 8.5% and 8.7%, respectively. The results shown in Fig. 4 ovelaef highlight that the reduced atomisation performance corresponds to an increase in nvPM EI number (11-89%), mass (5-72%) and particle size (1-7% for GMD) across all the fuels and AFRs studied.

This finding is in agreement with the literature [19], suggesting improvements in atomisation quality led to higher numbers of smaller particles in the primary zone, which are more easily consumed in the secondary lean zone, leading to overall reduced PM emissions.

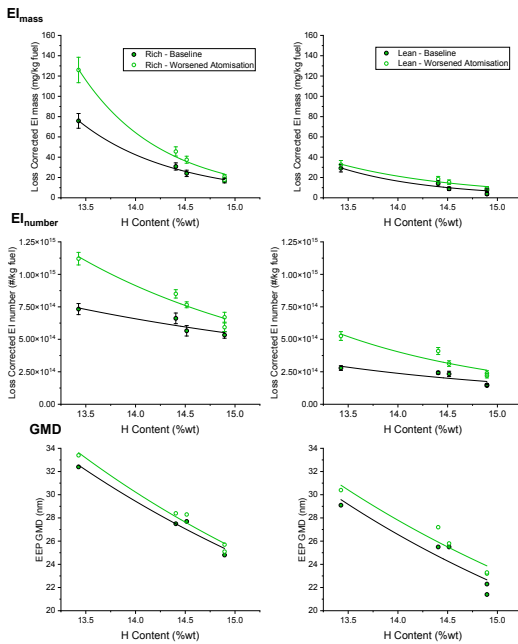


Fig. 4. Impact of reduced worsened atomisation quality on nvPM EI number, mass, and GMD.

Analysis of the gradients of the plotted trendlines in Fig. 4 3 suggests that higher increases in nvPM due to worsened atomisation are expected for fuels of lower hydrogen contents, implying that high aromatic conventional fuels could be more sensitive to changes in atomisation quality. The results also serve to experimentally demonstrate how small changes to atomisation quality can significantly impact nvPM number and mass, at least under the relatively low power conditions used for experimentation in this project.

CONCLUSIONS

- A non-proprietary RQL combustor rig with independent control of inlet air flows, representative of a small-scale aircraft engine operating at low thrust conditions, was successfully developed.
- The nvPM emissions from the RQL combustor were characterised using the European reference nvPM system for a range of Jet fuels with different hydrogen contents.
- System loss correction using particle size measurement was utilised to predict engine exit emissions, allowing for more accurate quantification of nvPM emission reductions achieved with SAFs of higher hydrogen contents.
- The influence of fuel physical properties affecting spray quality may significantly impact nvPM emissions, with small improvements in atomisation quality potentially resulting in significant decreases in nvPM emissions.

Acknowledgments

The experimental programme received funding from Clean Sky 2 Joint undertaking under the European Union's Horizon 2020 research and innovation RAPTOR (Grant agreement ID: 863969). The authors would also like to acknowledge EASA for the loan of the EUR nvPM mobile reference system under contract EASA. 2015.C01. AM01 and the WEFO ERDF FLEXIS project for the development of the RQL combustor rig.

REFERENCES

- [1] D. S. Lee *et al.*, 'The contribution of global aviation to anthropogenic climate forcing for 2000 to 2018', *Atmospheric Environment*, vol. 244, p. 117834, Jan. 2021. doi.org/10.1016/j.atmosenv.2020.117834
- [2] S. Becken and J. Shuker, 'A framework to help destinations manage carbon risk from aviation emissions', *Tourism Management*, vol. 71, pp. 294–304, Apr. 2019. doi.org/10.1016/j.tourman.2018.10.023
- [3] D02 Committee, 'ASTM D1655 - Specification for Aviation Turbine Fuels', ASTM International. doi.org/10.1520/D1655-19A
- [4] E. Durand, P. Lobo, A. Crayford, Y. Sevcenco, and S. Christie, 'Impact of fuel hydrogen content on non-volatile particulate matter emitted from an aircraft auxiliary power unit measured with standardised reference systems', *Fuel*, vol. 287, p. 119637, Mar. 2021. doi.org/10.1016/j.fuel.2020.119637
- [5] P. Lobo *et al.*, 'Measurement of Aircraft Engine Non-Volatile PM Emissions: Results of the Aviation-Particle Regulatory Instrumentation Demonstration Experiment (A-PRIDE) 4 Campaign', *Aerosol Science and Technology*, vol. 49, no. 7, pp. 472–484, Jul. 2015. doi.org/10.1080/02786826.2015.1047012
- [6] L. Durdina, B. T. Brem, D. Schönenberger, F. Siegerist, J. G. Anet, and T. Rindlisbacher, 'Non-Volatile Particulate Matter Emissions of a Business Jet Measured at Ground Level and Estimated for Cruising Altitudes', *Environ Sci Technol*, vol. 53, no. 21, pp. 12865–12872, Nov. 2019. doi.org/10.1021/acs.est.9b02513
- [7] A. M. Boies *et al.*, 'Particle Emission Characteristics of a Gas Turbine with a Double Annular Combustor', *Aerosol Science and Technology*, vol. 49, no. 9, pp. 842–855, Sep. 2015. doi.org/10.1080/02786826.2015.1078452
- [8] K. M. Bendtsen, E. Bengtsen, A. T. Saber, and U. Vogel, 'A review of health effects associated with exposure to jet engine emissions in and around airports', *Environmental Health*, vol. 20, no. 1, p. 10, Feb. 2021. doi.org/10.1186/s12940-020-00690-y
- [9] H. R. Jonsdottir *et al.*, 'Non-volatile particle emissions from aircraft turbine engines at ground-idle induce oxidative stress in bronchial cells', *Communications Biology*, vol. 2, no. 1, p. 90, Mar. 2019. doi.org/10.1038/s42003-019-0332-7

- [10] A. H. Lefebvre and D. R. Ballal, *Gas Turbine Combustion: Alternative Fuels and Emissions*, Third Edition. Taylor & Francis, 2010.
- [11] J. Harper, E. Durand, P. Bowen, D. Pugh, M. Johnson, and A. Crayford, 'Influence of alternative fuel properties and combustor operating conditions on the nvPM and gaseous emissions produced by a small-scale RQL combustor', *Fuel*, vol. 315, p. 123045, May 2022. doi.org/10.1016/j.fuel.2021.123045
- [12] D02 Committee, 'ASTM D7566 - Standard Specification for Aviation Turbine Fuel Containing Synthesized Hydrocarbons', ASTM International. Accessed: Mar. 14, 2023. [Online]. Available: <https://www.astm.org/d7566-20b.html>
- [13] P. Lobo *et al.*, 'Comparison of standardized sampling and measurement reference systems for aircraft engine non-volatile particulate matter emissions', *Journal of Aerosol Science*, p. 105557, Mar. 2020. doi.org/10.1016/j.jaerosci.2020.105557
- [14] B. T. Brem *et al.*, 'Effects of Fuel Aromatic Content on Nonvolatile Particulate Emissions of an In-Production Aircraft Gas Turbine', *Environ Sci Technol*, vol. 49, no. 22, pp. 13149–13157, Nov. 2015. doi.org/10.1021/acs.est.5b04167
- [15] J. Harper, 'An Experimental Study of the nvPM Emissions Produced by Alternative Aviation Fuels in a Newly-Developed RQL Research Combustor', Thesis (PhD), Cardiff University, 2022.
- [16] ICAO, 'Annex 16 - Environmental Protection Volume 2 - Aircraft Engine Emissions', Jul. 2017. Accessed: Feb. 18, 2019. [Online]. Available: <https://store.icao.int/annex-16-environmental-protection-volume-2-aircraft-engine-emissions.html>
- [17] SAE International, 'ARP 6320A - Procedure for the Continuous Sampling and Measurement of Non-Volatile Particulate Matter Emissions from Aircraft Turbine Engines', May 2021. doi.org/10.4271/ARP6320
- [18] E. Durand *et al.*, 'Correction for particle loss in a regulatory aviation nvPM emissions system using measured particle size', *Journal of Aerosol Science*, vol. 169, p. 106140, Mar. 2023. doi.org/10.1016/j.jaerosci.2023.106140
- [19] I. Zahmatkesh and M. Moghiman, 'Effect of liquid fuel droplet size on soot emission from turbulent spray flames', *Iranian Journal of Science and Technology, Transaction B: Engineering*, vol. 30, no. 3, pp. 339–351, 2006.

Guo B

*Cardiff University
School of Engineering*

Meng J

*STFC Daresbury Laboratory
Scientific Computing Department*

Pan S

*Cardiff University
School of Engineering*

Ning G

*Dalian University of Technology
State Key Laboratory of Coastal and Offshore Engineering*

SUSTAINABLE ENERGY

Numerical Wave Flume with Lattice Boltzmann Method for Wave Energy Converters

Based on Lattice Boltzmann Method, a free interface tracking model using volume of fraction (VOF) technique is built to explore the interaction of Oscillating Water Column (OWC) type of Wave Energy Converters (WECs) with waves. In the numerical wave flume, the momentum source is applied to generate incident waves and absorb reflected waves. After validation, one stationary OWC in the absence of Power take-off system (PTO) is then placed in the numerical wave flume to examine the performance of the numerical scheme. The simulation results show that the numerical stability is well achieved with the wave-structure interaction included and there is a strong vortex shedding at wall corner and nonlinearity with smaller amplitude in the present viscous flow model, compared with the linear potential flow solution.

Keywords:

Lattice Boltzmann method, numerical wave flume, wave-structure interaction, oscillating water column, wave energy converters.

Corresponding author:

GuoB5@cardiff.ac.uk



B. Guo, S. Pan, J. Meng, and D. Ning, 'Numerical Wave Flume with Lattice Boltzmann Method for Wave Energy Converters', *Cardiff University School of Engineering Research Conference 2023*, Cardiff, UK, 2023, pp. 168-172.

doi.org/10.18573/conf1.a1

INTRODUCTION

The wave energy capture efficiency (CWR) is indeed overestimated in the theoretical potential flow model developed. To study the hydrodynamic effects of viscosity and nonlinearity, a numerical wave flume is created using the Lattice Boltzmann method (LBM) to investigate the wave-OWC interaction. The LBM method possesses high expansibility on the parallel computing for the outstanding locality and stability, which can comparably improve the simulation efficiency on solving a viscous flow problem [1, 2].

MATERIALS AND METHODS

The present model uses MRT-LBM method to solve N-S equation, in which VOF-based free-surface capturing technique by Korner et al. [3] is adopted. Wave is generated by the momentum source and absorbed by the sponge layer [4], as shown in Fig.1. These algorithms are implemented using the High Level Mesoscale System [5].

Lattice Boltzmann method

Boltzmann equation describes the evolution of the density distribution function $f_\alpha(x, t)$. Its general form with the forcing term in the MRT (Multi-Relaxation-Time) model can be written as follows:

$$f_\alpha(x + \mathbf{e}_\alpha \delta t, t + \delta t) - f_\alpha(x, t) = -\mathbf{M}^{-1}[\mathbf{S}(\mathbf{m} - \mathbf{m}^{eq})] + \mathbf{M}^{-1}\Phi \delta t \quad (1)$$

where x is the spatial position and t is the time; \mathbf{e}_α is the discrete velocity; δt is the non-dimensional time step and non-dimensional grid spacing $\delta x = \delta t \cdot \sqrt{3}$; α ranges from 1 to 9 in two-dimensional space; \mathbf{M} and \mathbf{S} are transformation matrix and relaxation matrix, respectively. $\Phi = \mathbf{M}\bar{\mathbf{F}}$ is the forcing term in moment space, where the Guo Forcing Scheme is applied here:

$$\Phi = \left(\mathbf{I} - \frac{\mathbf{S}}{2} \right) \delta t (0, 6(\mathbf{F} \cdot \mathbf{u}), -6(\mathbf{F} \cdot \mathbf{u}), F_x, -F_x, F_y, -F_y, 2(F_x u_x - F_y u_y), F_y u_x + F_x u_y)^T \quad (2)$$

Then the macroscopic quantities can be calculated by the velocity moments,

$$\rho = \sum_\alpha f_\alpha, \quad \rho_0 \mathbf{u} = \sum_\alpha \mathbf{e}_\alpha f_\alpha + \frac{\mathbf{F}}{2} \delta t \quad (3)$$

Free-surface capturing method

Following Korner et al. [3], the single-phase VOF (volume of fluid) method is used to capture the gas-liquid interface. The fill level of each discrete cell with fluid is evaluated by the volume fraction,

$$\varepsilon = \frac{V_{fluid}}{V_{cell}} \quad (4)$$

It is clear that $\varepsilon = 0$ means the present cell is an empty cell and $\varepsilon = 1$ corresponds to a fill cell. The all interface cells with $0 < \varepsilon < 1$ separate liquid from gas. The fill level can be further expressed as,

$$\varepsilon = \frac{m_{fluid}}{\rho_{fluid}} \quad (5)$$

In the standard VOF-LBM model, we adopt the first-order explicit Euler time difference scheme,

$$m(\mathbf{x}, t + \delta t) = m(\mathbf{x}, t) + \sum_\alpha \Delta m_\alpha \quad (6)$$

The mass exchange Δm_α , associated with the convective term, between an interface cell at lattice node \mathbf{x} and its neighbor at $\mathbf{x} + \mathbf{e}_\alpha \delta t$ is calculated as,

$$\Delta m_\alpha(\mathbf{x}, t) = (f_{\bar{\alpha}}(\mathbf{x} + \mathbf{e}_\alpha \delta t, t) - f_\alpha(\mathbf{x}, t)) A_\alpha \quad (7)$$

$$A_\alpha = \begin{cases} 0, & \text{neighbor is empty cell} \\ \frac{\varepsilon(\mathbf{x}, t) + \varepsilon(\mathbf{x} + \mathbf{e}_\alpha \delta t, t)}{2}, & \text{neighbor is interface cell} \\ 1, & \text{neighbor is fluid cell} \end{cases}$$

where $\mathbf{e}_{\bar{\alpha}} = -\mathbf{e}_\alpha$.

Once the mass exchange has been evaluated, the VOF of each cell ε can be updated on Eq.5. In the advection step, the interface cells may be emptied or filled, corresponding to $\varepsilon < 0$ and $\varepsilon > 1$ respectively. For those interface cells, their state needs to be updated: the emptied cell to empty cell and the filled cell to fluid cell. To seal the gas-liquid interface, the surrounding empty cells at each filled cell must be converted to interface cells and surrounding fluid cells at each emptied cell must be converted to interface cells. Then, since there is no valid information at each gas cell (empty cell) in the present single-phase flow model, those new interface cells converted from empty cells needs to be initialized with equilibrium distribution $f_\alpha^{eq}(\rho^{avg}, u^{avg})$, in which the macroscopic quantities ρ^{avg} and u^{avg} are obtained from the average values of the surrounding fluid and interface cells at the moment $t + \delta t$.

Moreover, the mass conservation is required in the advection. That is to say, the excess mass from emptied $\varepsilon < 0$ and filled $\varepsilon > 1$ cells needs to be distributed to the neighbouring interface cells as,

$$m(\mathbf{x} + \mathbf{e}_\alpha \delta t) = m(\mathbf{x} + \mathbf{e}_\alpha \delta t) + m^{ex} \frac{v_\alpha}{v_{total}} \quad (8)$$

where excess mass $m^{ex} = \rho$ for the emptied cells and $m^{ex} = m - \rho$ for the filled cells.

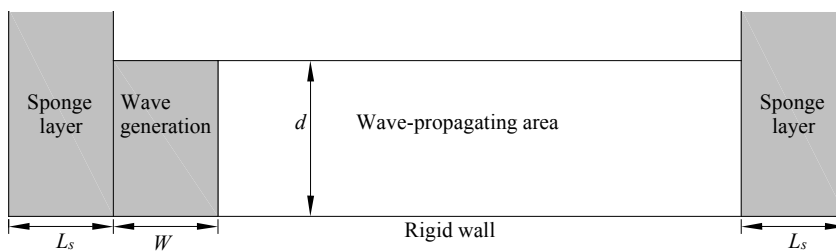


Fig. 1. Sketch of the numerical wave flume

Boundary conditions

For no-slip boundary conditions, a halfway bounce back scheme is used, the incoming unknown density distribution $f_{\bar{\alpha}}$ is reconstructed as,

$$f_{\bar{\alpha}}(\mathbf{x}, t + \delta t) = f_{\alpha}^{out}(\mathbf{x}, t) \quad (9)$$

Here f_{α}^{out} denotes the density distribution function after the collision step. At the slip boundary, the bounce forward scheme is adopted to reconstruct the missing distribution,

$$f_{\alpha^*}(\mathbf{x}, t + \delta t) = f_{\alpha}^{out}(\mathbf{x} - \mathbf{e}_{\alpha^*} t \delta t, t) \quad (10)$$

where α^* is the mirrored direction to α with $\mathbf{e}_{\alpha^*} t = \mathbf{e}_{\alpha} t$ and $\mathbf{e}_{\alpha^*} \mathbf{n} = -\mathbf{e}_{\alpha} \mathbf{n}$ (wall normal direction \mathbf{n} and tangential direction \mathbf{t}).

At a free surface boundary, it is obvious that the incoming distributions from empty cells are unknown as the dynamics of gas phase does not be considered in the present single-phase flow model. Therefore, the free surface kinetic boundary condition (FSK) proposed by Korner et al. [3] is applied here to reconstruct those missing distributions,

$$f_{\bar{\alpha}}(\mathbf{x}, t + \delta t) = -f_{\alpha}^{out}(\mathbf{x}, t) + f_{\alpha}^{eq}(\rho_A, \mathbf{u}(\mathbf{x}, t)) + f_{\bar{\alpha}}^{eq}(\rho_A, \mathbf{u}(\mathbf{x}, t)) \quad (11)$$

where $\rho_A = p_A$ in present LBM unit system is related to surrounding atmosphere pressure.

Smagorinsky LES

Free surface flows are characterized by high Reynolds numbers in the turbulent regime. Therefore, a large eddy model is used to simulate turbulent flows in the case of limited computing resource. The LBE-LES model is introduced in which the eddy viscosity ν_t is [2],

$$\nu_t = (C_s \delta x)^2 \|\bar{\mathbf{S}}\| \quad (12)$$

where C_s is the Smagorinsky constant, and mean strain rate

$$\|\bar{\mathbf{S}}\| = \sqrt{2\bar{S}_{ij}\bar{S}_{ij}}$$

which is calculated by the non-equilibrium part of the mean second-order moment $\bar{\mathbf{\Pi}}$,

$$\bar{S}_{ij} = -\frac{\bar{\Pi}_{ij}}{2\tau_{total}\rho RT} \quad (13)$$

where $\bar{\Pi}_{ij} = \sum_{\alpha} \mathbf{e}_{\alpha i} \mathbf{e}_{\alpha j} f_{\alpha} - f_{eq}$ and $\tau_{total} = \frac{\nu + \nu_t}{\delta t} + \frac{1}{2}$ represents relaxation time in the LBE-LES model.

Substituting Eq. 13 into Eq. 12 yields a solution of quadratic equation as,

$$\tau_{total} = \frac{1}{2}\tau + \frac{1}{2}\sqrt{\tau^2 + \frac{2(C_s \delta x)^2}{\rho RT} \|\bar{\mathbf{\Pi}}\|} \quad (14)$$

$$\text{where } \|\bar{\mathbf{\Pi}}\| = \sqrt{2\bar{\Pi}_{ij}\bar{\Pi}_{ij}}.$$

Wave generating and absorbing methods

The distributed momentum source is used to generate waves. The equivalent source term $\mathbf{S}_{\mathbf{g}}$ is,

$$\begin{cases} S_{g,x} = g(2\beta(x - x_s))e^{-\beta(x-x_s)^2} \frac{D}{\omega} \sin \omega t \\ S_{g,y} = 0 \end{cases} \quad (15)$$

where g is the gravity acceleration and $\beta = 20/W^2$ is a coefficient of source width W ; x_s is the centre of wave generating area; D is distribution source density [4].

Sponge layers are adopted to achieve wave dissipation in the two ends of numerical wave flume. In the sponge area with width L_s , the damping force \mathbf{S}_b is given as,

$$\mathbf{S}_b = -(B_1 \mathbf{u} + B_2 \mathbf{u}|\mathbf{u}|) \frac{e^{\left|\frac{x-x_0}{L_s}\right|^{n_s}} - 1}{e - 1} \quad (16)$$

where B_1, B_2 and n_s are empirical coefficient, and x_0 is the starting location of the sponge layer.

Dimensionless quantities in LBM system

Different from standard LBM, the present model uses the non-dimensional system associated with physical system as follows,

$$Ma = \frac{u_c}{\sqrt{RT}} \quad (17)$$

where u_c and \sqrt{RT} are the wave phase velocity (or maximum velocity) and characteristic velocities in physical system. For a specific Mach number we can evaluate \sqrt{RT} . And the characteristic length L_0 is chosen as the wave amplitude, Then the kinetic viscosity and gravity in lattice system can be calculated by,

$$\nu = \frac{\nu^* \sqrt{RT}}{RT L_0}, \quad g = \frac{g^* L_0}{RT} \quad (18)$$

where ν^* kinetic viscosity and g^* is the gravity acceleration in physical system.

RESULTS

Model validation

To validate the effectiveness of the present free-surface model, the Rider-Kothe single vortex test case [6] has been simulated. In the case, the collision and streaming do not be implemented. A given velocity field according to the following streaming function is used to calculate the equilibrium distribution functions as the simulation solution of each iteration.

$$\psi = \frac{2}{\pi} \sin^2 \pi x \cdot \sin^2 \pi y \cdot \cos \frac{\pi t}{T} \quad (19)$$

The flow field will restore to the initial state after one period. So the simulation results can be compared with the analytically filled level VOF to verify the purely advection case in absence of collision and streaming. The initial circle centre is located at (0.5, 0.75) and the wave period T is set as 2 s and 128 or 512 grid points is distributed in the 1m square domain. Relative errors of the two grid resolution are 4.5% and 1.4%, respectively.

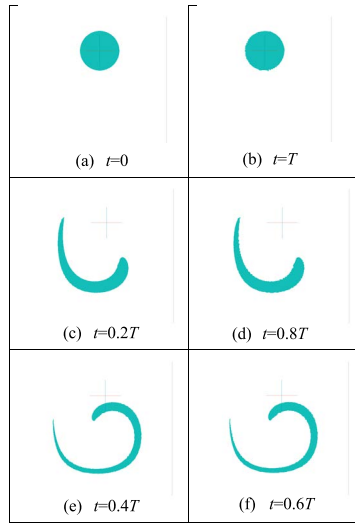


Fig. 2. Evolution of the fluid interface within one period (grid resolution: 512 by 512).

Waves propagation through an OWC

Following the model validation, waves propagating through an OWC without Power take-off system, as shown in Fig. 3, are modelled. In this case, the incident wave amplitude is 0.02m, and water depth h is 0.4m. The wave flume shown in Fig. 1 is used. The wave monitoring locations are also shown in Fig. 3 as WG1 and WG2, before and after the OWC respectively, and WG5 at the location of the OWC. Non-slip boundary condition is implemented in the body surface.

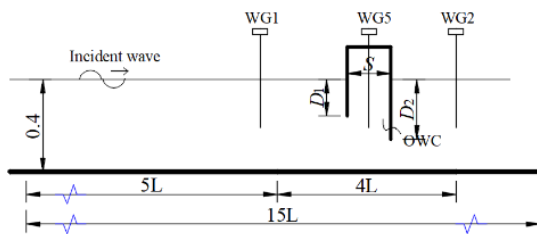


Fig. 3. Schematic diagram for OWC in wave flume.

Fig. 4 shows the wave profiles at $t=22T$ and $26T$, along the wave flume. The simulation results in general agree with each other, including the reflected wave in the upstream of the OWC and transmission wave in the downstream end, showing that the numerical stability has been achieved.

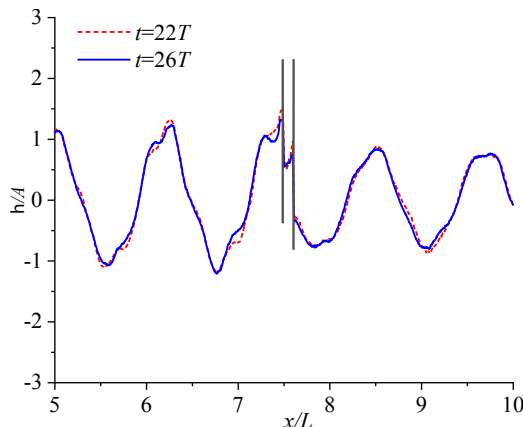


Fig. 4. Water surface elevation η along propagation direction at $t=22T$ and $26T$.

In addition, the temporal variations of wave elevation at $x=5L$ and $9L$ is presented in Fig. 5, where the potential-flow theoretical solutions are also shown. It is obvious that the maximum amplitude at the seaside is larger than that at the leeside, similar as the linear analytical solution.

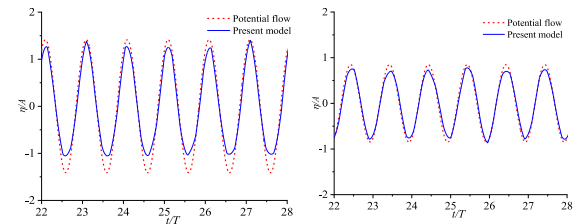


Fig. 5. Water surface elevation η at (a) $x=5L$ (left) and (b) $x=9L$ (right).

For the smaller wave amplitude in the present results, it is attribute to the vortex shedding at the sharp corner below walls and strong nonlinearity, as shown in Fig. 6. Moreover, the stronger nonlinearity in the upstream, due to the larger wave amplitude, causes the more significant discrepancy between linear potential-flow analytical solution and the present numerical results, compared with the transmission wave at the downstream of the OWC.

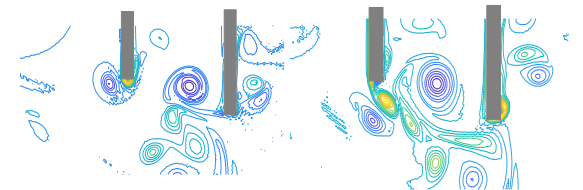


Fig. 6. Vortex contour below wall from the sharp corner (a) $t=t_1$ (left) and (b) $t=t_1 + 0.19T$ (right).

CONCLUSIONS

In this paper, a free surface model based on VOF-LBM method following [1] is established and is applied to wave-OWC interaction problem. The numerical results show that the present model can simulate complex free surface flow compared with those published works. By imposed momentum sources, the wave generation and absorption functions have been achieved and the numerical stability has been validated. In the wave-OWC interaction, the vortex shedding and strong nonlinearity cause the relatively small amplitude with respect to the linear potential-flow solution.

Acknowledgments

This work was partly supported by the scholarship provided by Cardiff University and China Scholarship Council (No. 202006060048). JM would like to thank the Engineering and Physical Science Research Council under EP/P022243/1 and EP/X035875/1. Thanks also go to the STFC Daresbury Laboratory for hosting the research visit for BG.

Conflicts of interest

The authors declare no conflict of interest.

REFERENCES

- [1] C. Janßen and M. Krafczyk, 'Free surface flow simulations on GPGPUs using the LBM', *Computers & Mathematics with Applications*, vol. 61, no. 12, pp. 3549–3563, Jun. 2011.
doi.org/10.1016/j.camwa.2011.03.016
- [2] G. Liu, J. Zhang, and Q. Zhang, 'A high-performance three-dimensional lattice Boltzmann solver for water waves with free surface capturing', *Coastal Engineering*, vol. 165, p. 103865, Apr. 2021.
doi.org/10.1016/j.coastaleng.2021.103865
- [3] C. Körner, M. Thies, T. Hofmann, N. Thürey, and U. Råde, 'Lattice Boltzmann Model for Free Surface Flow for Modeling Foaming', *J Stat Phys*, vol. 121, no. 1–2, pp. 179–196, Oct. 2005.
doi.org/10.1007/s10955-005-8879-8
- [4] J. Choi and S. B. Yoon, 'Numerical simulations using momentum source wave-maker applied to RANS equation model', *Coastal Engineering*, vol. 56, no. 10, pp. 1043–1060, Oct. 2009.
doi.org/10.1016/j.coastaleng.2009.06.009
- [5] <https://github.com/inmeso/hilemms>.
- [6] C. Janssen and M. Krafczyk, 'A lattice Boltzmann approach for free-surface-flow simulations on non-uniform block-structured grids', *Computers & Mathematics with Applications*, vol. 59, no. 7, pp. 2215–2235, Apr. 2010.
doi.org/10.1016/j.camwa.2009.08.064

Maybury L

Cardiff University
School of Engineering

Corcoran P

Cardiff University
School of Engineering

SUSTAINABLE ENERGY

Mathematical Modelling to Optimise an Urban Electric Vehicle Charging System

Many countries are embracing the adoption of electric vehicles for private transportation as a key measure in decarbonising their transportation sectors. In the UK, the Industrial Decarbonisation Strategy provides a blueprint for industry players to reduce carbon emissions, aligning with the nation's commitment to reach net zero emissions – a state where human generated greenhouse gases are balanced by their removal from the atmosphere. In line with this commitment, the UK is transitioning from conventional vehicles to electric vehicles, with a ban on the sale of new petrol and diesel vehicles slated for 2030. This transition underscores the need for reliable charging infrastructure and systems to support the growing demand for electric vehicles. In this article, a charging system for urban areas is proposed. An integer linear program model based on queuing theory is developed with the goal of minimizing congestion in the charging system. In the results section, a case study of Cardiff's urban centre, with a street network obtained from Open Street Map [1] is used to demonstrate the model's application of creating an assignment of apartment blocks to charging stations with the goal of minimizing the congestion of the charging stations in the urban area.

Keywords:

Electric vehicles, sustainable mobility, mathematical modelling, assignment problem, decarbonisation.

Corresponding author:

MayburyLE@cardiff.ac.uk



L. Maybury and P. Corcoran, 'Mathematical Modelling to Optimise an Urban Electric Vehicle Charging System', *Cardiff University School of Engineering Research Conference 2023*, Cardiff, UK, 2023, pp. 173-175.

doi.org/10.18573/conf1.am

INTRODUCTION

Many countries, including the UK, prioritize decarbonisation and have implemented policies such as the Net Zero Strategy [2] to decarbonise all sectors of the economy by 2050. The UK government’s Road to Zero policy [3] specifically targets cleaner road transport as part of this effort.

The UK has banned the sale of new petrol and diesel cars by 2030, prompting the transportation sector to transition towards electric vehicles (EVs) with the aim of achieving net zero emissions. This is a costly and ambitious transition that must be achieved with minimal expense and disruptions. Mathematical modelling can help optimise this transition.

As such, the approach presented in this paper is to mathematically optimise an urban EV charging system, with a specific focus on apartment blocks where residents typically lack designated parking spots in which to charge their vehicle. The optimisation problem incorporates an assignment problem and queuing theory to minimise the average wait time in the system by optimally assigning users to shared charging stations. By implementing the optimal solution, we believe congestion in the system can be reduced, as each urban resident is assigned a priority charging station that serves as their home station without incurring extra fees, with an assignment based on minimising queue times.

MATERIALS AND METHODS

The charging system proposed in this article is based on the assumption that those living in apartment blocks do not have access to individual home EV charging. As such, they will have priority access to a *shared home charging station*, which is a public charging station near the residence.

The model is formulated as an assignment problem where apartment blocks are assigned to charging station queues, which correspond to charging stations of fixed locations. This assignment is obtained using an ILP (integer linear program) optimisation model. The objective of the model is to minimise the average queue time over the set of charging station queues Q , whilst ensuring that users are not assigned to a charging station that is too far away from their residence. The ILP is solved using Gurobi Optimization, LLC [4].

RESULTS

In this section, the ILP described above is demonstrated using a simple example, and also applied to a street network of Cardiff City Centre.

Simple Example

In the simple example shown in Figure 1, the set of charging station queues is and the set of apartment blocks is . The edges represent the shortest path between each apartment block and each charging station.

Then the optimal assignment of apartment blocks to charging station queues is shown in Figure 2.

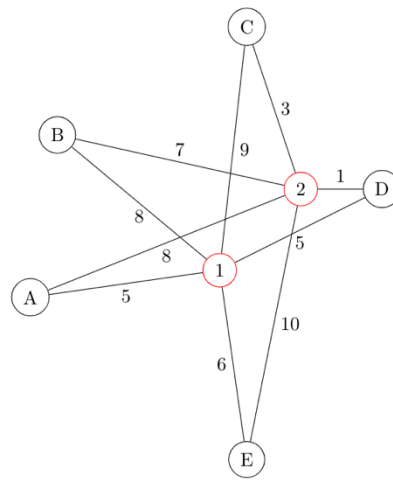


Fig. 1. Simple network of apartment blocks and charging stations.

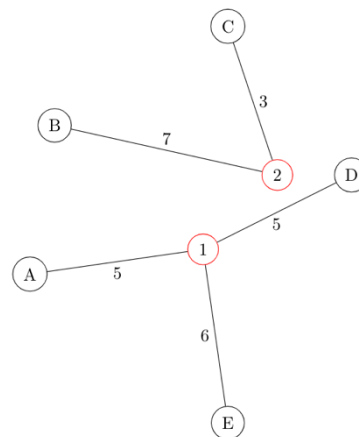


Fig. 2. Optimal assignment of apartment blocks to charging station queues.

Case Study: Cardiff City Centre

The method is applied to Cardiff’s urban centre. For the purpose of the study, a street network is modelled using a graph, where nodes are locations and edges are paths between the locations. As such, a street network of Cardiff is obtained from OpenStreetMap [1] using Python package OSMnx [5] which can be seen in Figure 3.

This street network is a bounding box of size 1100m containing the city centre. 9 apartment blocks are identified, along with 6 potential placements for charging stations to be installed. The apartment blocks are located at: Churchill Way, The Hayes, Westgate Street, Caroline Street, Bute Terrace and Cathedral Road. The carparks are located at St David’s Shopping Centre, Capitol Shopping Centre, Dumfries Place, Westgate Street, Adam Street, Sophia Gardens, Queen Street and Newport Road. These locations can be seen in Figure 3, with apartment blocks in blue and potential charging stations in red.



Fig. 3. Cardiff City Centre street network with apartment blocks and potential charging stations in blue and red points respectively.

The assignment ILP is applied to the street network shown in Figure 3, and the optimal assignment of apartment blocks to charging stations is calculated, and displayed in Fig. 4.

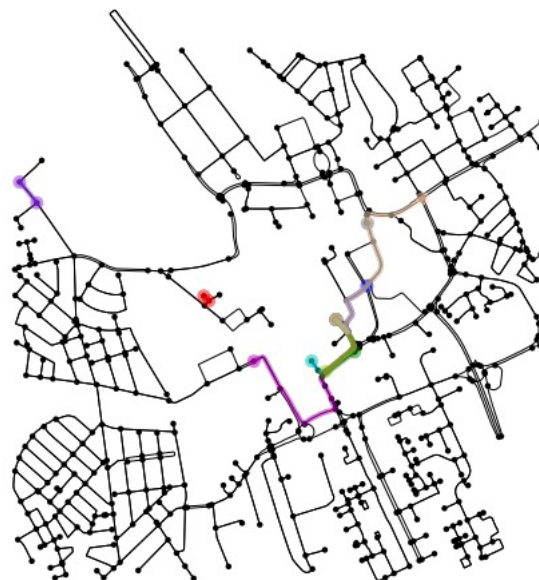


Fig. 4. Optimal assignment of apartment blocks to charging stations.

DISCUSSION

The method proposed in this article provides an optimal assignment of apartment blocks to charging station queues based on the constraints and parameters input, and has a number of applications, such as informing city planners how many charging points to install at different charging locations. It can also be used to compare overall system congestion for different charging station locations, by varying these locations in the model.

The method also has limitations. For example, the users are considered at an aggregated apartment block based level. Future research may employ household level data to complete the analysis at a finer scale.

Acknowledgments

This study is partly funded by an EPSRC DTP PhD studentship.

Conflicts of interest

The authors declare no conflict of interest.

REFERENCES

- [1] M. Haklay and P. Weber, 'Openstreetmap: User-generated street maps', *IEEE Pervasive Computing*, vol. 7, no. 5 pp. 12-18, Oct. 2008. doi.org/10.1109/MPRV.2008.80
- [2] HM Government, 'Net zero strategy: Build back greener', 2021[online]. Available: https://assets.publishing.service.gov.uk/government/uploads/system/uploads/attachment_data/file/1033990/net-zero-strategy-beis.pdf.
- [3] HM Government, 'The road to zero', 2021 [online]. Available: https://assets.publishing.service.gov.uk/government/uploads/system/uploads/attachment_data/file/739460/road-to-zero.pdf.
- [4] Gurobi Optimization, LLC, 'Gurobi Optimizer Reference Manual', 2022 [online]. Available: <https://www.gurobi.com>
- [5] G. Boeing, 'OSMnx: New methods for acquiring, constructing, analyzing, and visualizing complex street networks', *Computers, Environment and Urban Systems*, vol. 65, pp. 126-139, Sep. 2017 doi.org/10.1016/j.compenvurbsys.2017.05.004

Goktepe B
*Cardiff University
School of Engineering*

Morris S
*Cardiff University
School of Engineering*

Clark D
*Cardiff University
School of Engineering*

Mashruk S
*Cardiff University
School of Engineering*

SUSTAINABLE ENERGY

Plasma-assisted Ammonia Combustion: The Effect of Equivalence Ratio on NO Emissions

As a carbon-free fuel and hydrogen carrier, ammonia has gained increasing attention in the combustion community to support the global decarbonisation efforts. However, it has unfavorable flame properties and emissions characteristics such as low flammability and intrinsic trade-off between nitric oxide emissions and slip ammonia that hinders its widespread integration to the heat and power sectors. As a promising technology, non-thermal plasma has already presented the potential to assist swirling ammonia flames with significant improvements in NOx abatement and flammability, while eliminating the need for blending with other reactive fuels such as hydrogen and methane. For this study, a plasma burner was designed to explore plasma discharge interaction with a highly swirling premixed ammonia flame over a range of equivalence ratios, and its effect on NO emissions. The results revealed that average plasma power varied with the equivalence ratio and the reduced electric field affected the NO emissions characteristics of premixed ammonia flames.

Keywords:
Ammonia, plasma-assisted combustion, NO emissions, swirling flames.

Corresponding author:
GoktepeB@cardiff.ac.uk



A. Duman, J. Powell, S. Thomas, X. Sun, and E. Spezi, 'Generalizability of Deep Learning Models on Brain Tumour Segmentation', *Cardiff University School of Engineering Research Conference 2023*, Cardiff, UK, 2023, pp. 176-180.

doi.org/10.18573/conf1.an

INTRODUCTION

As a carbon-free fuel and hydrogen carrier, ammonia (NH₃) has the potential to support the clean energy transition in heat and power industries. Relatively easy to transport and store, NH₃ can also be regarded as a promising energy storage medium to leverage renewable energy sources in the electrical power generation mix. When produced from renewable energy, it provides a zero-carbon energy source to power gas turbines. However, burning NH₃ in gas turbines is a challenging task owing to the fundamental flame properties and emissions signature of NH₃, such as the low burning rate, high ignition energy and high tendency of elevated nitrogen oxides (NO_x) emissions[1,2]. The strategies for burning ammonia within the regulated NO_x emissions limits are therefore highly desirable and have become a key technological enabler to unleashing the vast potential use of ammonia for sustainable clean energy.

Co-firing ammonia with high-reactive fuels such as hydrogen is a proven strategy that can overcome the technical issues regarding the low burning rate while releasing zero-carbon emissions. As has been shown previously, ammonia flames doped with hydrogen (H₂) could conserve potential threats of flame stability and higher NO_x emissions depending on H₂ ratio in the blend and equivalence ratio (φ)[3]. Another potential strategy is the partial cracking of ammonia to hydrogen in a pre-combustion process. However, partially cracked NH₃ mixtures can produce an additional N₂ diluent component relative to NH₃-H₂ blends that reduce the efficacy of the burning rate enhancement and can elevate NO_x emissions with cracked H₂ fraction[4]. A new strategy is required that can simultaneously improve the fundamental flame properties and emissions performance of ammonia.

Plasma has emerged as a promising strategy with a proven track record of combustion enhancement, emissions abatement and fuel reforming, thanks to its unique chemistry that produces a rich pool of ions, electrons, other charged particles, neutral species, and heat[5]. Despite the relatively rich literature on plasma assisted hydrocarbon flames[5], the research on plasma-assisted ammonia combustion has lately started burgeoning with successful demonstration of applications for improved combustion and emissions mitigation[6–12]. The experimental studies [6–8,12] confirmed that plasma discharge has significantly extended the flammability limits of premixed swirling NH₃-air flames and reduced the NO emissions. However, the reduction has remained limited due to a series of factors such as plasma method, discharge gas, applied frequency and amplitude, and equivalence ratio.

In view of the above considerations, the aim of the research herein was to investigate plasma discharge-ammonia flame interactions over a range of equivalence ratios, with the primary focus on analysing discharge signal characteristics and its effects on NO emissions.

MATERIALS AND METHODS

The generic plasma burner used in the present work is based in Cardiff University's Gas Turbine Research Centre (GTRC) and shown schematically in Fig.1(a). The swirl manifold consists of eight tangential air supply ports of 3.5 mm ID, imparting a range of swirling motions to the upstream annular flow. The intensity of swirling motions can be quantified by a non-dimensional geometric swirl number given by [13]:

$$S_g = \frac{\pi r_0 D_0}{2A_t} \left\{ \frac{m_\theta}{m_\theta + m_A} \right\}^2 \quad (1)$$

where r_0 is the radius of the annular pipe into which the tangential flow is injected. D_0 is the diameter of the annular pipe at the throat. The terms, m_θ and m_A , are the mass flow rates of tangential and axial inlets, respectively. A_t is the total cross-sectional area of all tangential inlets. In the setup, the flame is confined into a quartz tube of 100 mm ID.

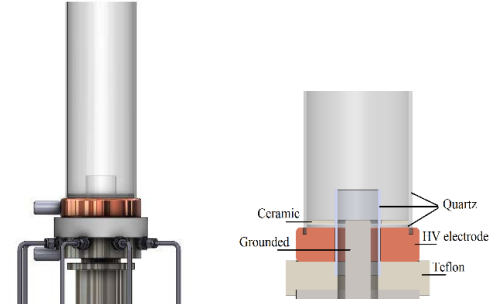


Fig.1. Plasma burner equipped with a coaxial DBD plasma generation system (a) CAD drawing and (b) cut-through view.

As shown in Fig.1 (b), a coaxial dielectric barrier discharge (DBD) plasma generation system was integrated to the swirl burner to produce volumetric non-thermal plasma in a discharge gap of 7.5 mm between two electrodes separated by a quartz nozzle of 40 mm ID serving as a dielectric or an insulator. A donut-shaped copper electrode received high voltage (HV) pulses while the stainless-steel swirl manifold was connected to the central stainless steel electrode of 25.4 mm which was connected to ground. The HV electrode was isolated from the grounded swirl manifold by a Teflon insulator. Before being applied to the discharge gap, a signal was first generated and then amplified using a waveform generator (Rigol 4000 series) and a high voltage amplifier (Trek 30/20), respectively. A HV probe (North Star PVM-5) and a current pulse transformer (Stangenes current pulse transformer) were used in combination with a high-speed oscilloscope (Lecroy HDO 6000) to monitor the discharge voltage and current waveforms included to measure the DBD pulses in the discharge gap. The electrical configuration of the rig is illustrated in Fig.2.

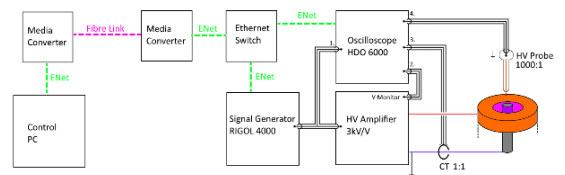


Fig.2. Electrical configuration of PAC tests at GTRC (burner detail omitted for clarity).

Gaseous emissions were sampled downstream of the confinement quartz tube using a 9-hole equal-area probe, regulated with a heat exchanger to maintain temperature at 433K. The gas extraction system includes a pump, filter block and sample lines maintained at the same temperature conforming to the specifications in ISO-11042[14]. The sample gas was split and delivered to multiple gas analysers housed in a single cabinet. NO concentrations were measured as hot and wet at 1 Hz using heated vacuum chemiluminescence (Signal 4000VM), whereas dry O₂ concentrations were quantified by using a paramagnetic analyser (Signal 9000MGA).

Chemiluminescence spectrum of ammonia flames was scanned by using a UV/visible-capable spectrometer (Stellernet Inc BLUE-Wave) with a 100-mm focal length and a 25- μm wide entry slit which was coupled with a UV/visible-capable optical fiber head (Stellernet Inc DLENS with F600 fiber optic cable). The spectrometer incorporates 600-grooves/mm grating and a Si-CCD detector (Sony ILX511b) with a spectral resolution of 0.5 nm. The detector's exposure time was set to 1 s and 20 scans were averaged to improve the signal-to-noise ratio (SNR).

In this study, the experiments were performed for premixed swirling NH_3 -air flames at equivalence ratios ranging from 0.8 to 1.2. For each case, the applied voltage was kept constant at 21 kVpk and 400 Hz which would reliably maintain a plasma over the measurement duration. The geometrical swirl number was maintained constant at 4.36 ± 0.012 across the equivalence ratio range by varying the ratio of m_g/m_A . Thermal power output of the ammonia flames was kept constant at 8 kW. In all the test points, the inlet mixture stayed at ambient temperature; no preheating was employed to sustain flame in the combustion zone.

RESULTS

Figure 3 shows the phase resolved DBD energy derived from the acquisition of 10,000 current pulses in discrete time windows for the equivalence ratios of 0.8, 1.0 and 1.2, respectively. Phase-resolved discharge colour map indicates the density of pulses occurring at a given energy and phase on the AC cycle. The figure shows that the individual pulse energy did not exceed 0.2mJ, and DBD occurred on both the positive and negative-going rising edge of the voltage, giving the total energy of 1.825 J, 1.588 J and 1.416 J for equivalence ratios of 0.8, 1.0 and 1.2, respectively.

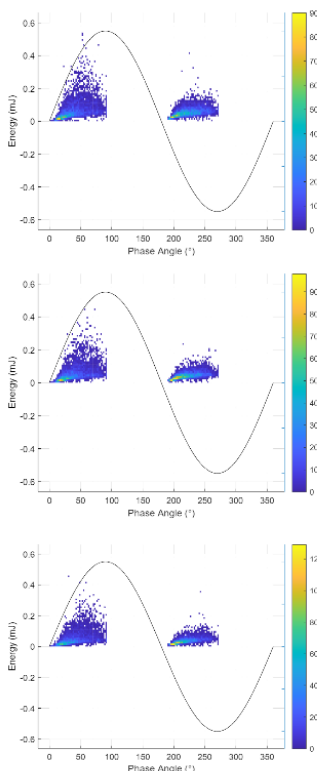


Fig.3. Phase-resolved pulse energy as a function of Equivalence Ratio, for P=8kW, V=21kVpk; (a) $\phi=0.8$ (top), (b) $\phi=1.0$ (middle), and (c) $\phi=1.2$ (bottom).

Figure 4 shows the average plasma power, P_{avg} (over 10,000 pulses) as a function of the equivalence ratio. There was a notable reduction in P_{avg} with ϕ , and this behavior merits further investigation.

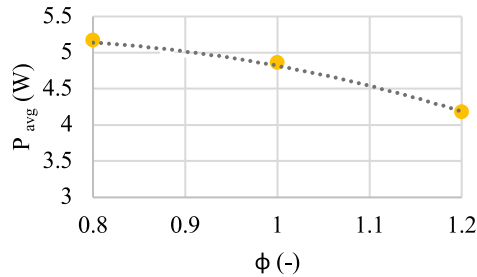


Fig.4. Average plasma power dependency on equivalence ratio.

Figure 5 shows the local variation of the reduced electric field, E/N in the discharge gap (E/N, the electric field (V/m) divided by the gas number density(1/m³) and given in the unit Townsend (Td) [5]) The calculated reduced electric field was varied in a range of 80-130 Td ($1\text{Td}=10^{-21} \text{ V}\cdot\text{m}^2$), regardless of equivalence ratio.

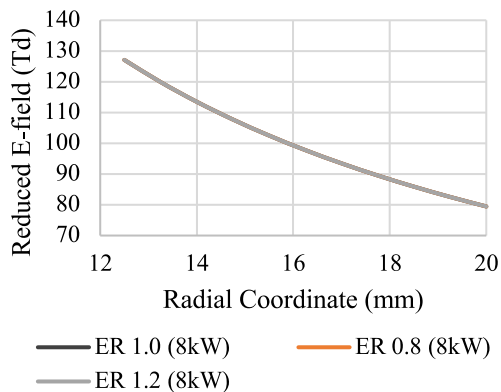


Fig.5. Reduced electric field in the space between the grounded central electrode and dielectric barrier. Note that E/N is nearly identical for all the equivalence ratios, which is expected given the fixed gas pressure.

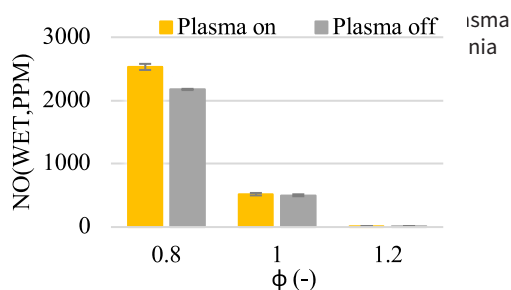


Fig.6. Comparison of NO emissions for plasma-assisted ammonia flames and conventional ammonia flames.

At fuel rich conditions, the plasma effect on NO emissions was negligible yet still more pronounced at the lean conditions, yielding higher NO concentrations than conventional ammonia flames. Regardless of the plasma activation, NO emissions notably abated at fuel rich conditions.

Figure 7 illustrates the peak intensity value of NH_2^* excited radicals at 630 nm (corresponding to NH_2 α band[15]) in the chemiluminescence spectrum of ammonia flames.

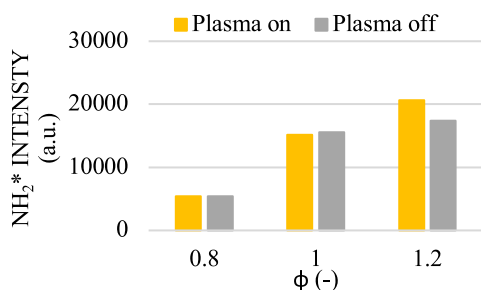


Fig.7. NH_2^* chemiluminescence intensity of plasma-assisted ammonia flames and conventional ammonia flames over the equivalence ratio range.

In general, the radical concentration increased with the equivalence ratio indicating the decomposition of excessive ammonia in the flame region. The plasma discharges enriched the radicals in the ammonia rich flames. However, the effect was diminished at fuel-lean conditions.

DISCUSSION

In conventional ammonia flames, NO consumption at fuel rich conditions is enhanced through the reactions between NH_2 with NO to form either N_2 or NNH , both of which are the key reaction pathways of Thermal De- NO_x [1]. The increase in NH_2^* chemiluminescence with equivalence ratio confirmed the reduction in NO concentrations as previously proposed in [6,16]. At lean conditions, NO formation is promoted through oxidization of NH and NH_2 to NO, mainly over the HNO intermediate [1]. However, the plasma discharge had no significant effect on NO emissions at rich conditions, even though yielding higher NH_2^* chemiluminescence. On the other hand, at lean conditions, the plasma effect became more stand-out, increasing NO emissions in the ammonia flames. The results are incongruent with others' findings [6,7] in which the plasma discharge ensured curbing NO emissions significantly in ammonia flames. This discrepancy might be related to the ratio of discharge power to thermal load. In the present study, this ratio was almost one third of the value in [6], corresponding to only 0.063% of the thermal load at $\phi=1.0$. Moreover, the E/N was varied in a range of 80-130 Td. As has been reported by other studies [10,17], for the $E/N \leq 100$ Td, the main fraction of the plasma energy goes into the vibrational excitation of N_2 , that does not produce effective plasma species to functionise ammonia flames. As the electric field varies with discharge gap, applied voltage and geometry of the electrode [17], the future study will focus on repeating the experiments at higher electric fields.

CONCLUSIONS

The effect of plasma discharge-ammonia flame interactions on NO emissions were experimentally investigated varying equivalence ratio at a constant thermal power output. NO emissions were compared against NH_2^* chemiluminescence intensity.

There is an apparent relationship between equivalence ratio and average plasma power, with lower equivalence ratio resulting in a measurably more energetic plasma.

In this study plasma discharges did not improve the NO emissions performance of premixed ammonia flames.

Acknowledgments

This work was supported by the UKRI Industrial Decarbonisation Research and Innovation Centre (IDRIC) and European Regional Development Funded project FLEXIS. The research was undertaken at Cardiff University's GTRC with invaluable technical support from Jack Thomas.

Conflicts of interest

The authors declare no conflict of interest.

REFERENCES

- [1] H. Kobayashi, A. Hayakawa, K. D. K. A. Somarathne, and E. C. Okafor, 'Science and technology of ammonia combustion', *Proceedings of the Combustion Institute*, vol. 37, no. 1, pp. 109–133, 2019. doi.org/10.1016/J.PROCI.2018.09.029
- [2] A. Valera-Medina, H. Xiao, M. Owen-Jones, W. I. F. David, and P. J. Bowen, 'Ammonia for power', *Progress in Energy and Combustion Science*, vol. 69, pp. 63–102, Nov. 2018. doi.org/10.1016/J.PECS.2018.07.001
- [3] A. A. Khateeb, T. F. Guiberti, X. Zhu, M. Younes, A. Jamal, and W. L. Roberts, 'Stability limits and NO emissions of technically-premixed ammonia-hydrogen-nitrogen-air swirl flames', *International Journal of Hydrogen Energy*, vol. 45, no. 41, pp. 22008–22018, Aug. 2020. doi.org/10.1016/J.IJHYDENE.2020.05.236
- [4] A. M. Elbaz, S. Wang, T. F. Guiberti, and W. L. Roberts, 'Review on the recent advances on ammonia combustion from the fundamentals to the applications', *Fuel Communications*, vol. 10, p. 100053, Mar. 2022. doi.org/10.1016/J.JFUECO.2022.100053
- [5] Y. Ju and W. Sun, 'Plasma assisted combustion: Dynamics and chemistry', *Progress in Energy and Combustion Science*, vol. 48, pp. 21–83, Jun. 2015. doi.org/10.1016/J.PECS.2014.12.002
- [6] J. Choe, W. Sun, T. Ombrello, and C. Carter, 'Plasma assisted ammonia combustion: Simultaneous NOx reduction and flame enhancement', *Combustion and Flame*, vol. 228, pp. 430–432, Jun. 2021. doi.org/10.1016/J.COMBUSTFLAME.2021.02.016

- [7] G. T. Kim, J. Park, S. H. Chung, and C. S. Yoo, 'Effects of non-thermal plasma on turbulent premixed flames of ammonia/air in a swirl combustor', *Fuel*, vol. 323, p. 124227, Sep. 2022.
doi.org/10.1016/J.FUEL.2022.124227
- [8] Q. Lin *et al.*, 'Controllable NO emission and high flame performance of ammonia combustion assisted by non-equilibrium plasma', *Fuel*, vol. 319, p. 123818, Jul. 2022.
doi.org/10.1016/J.FUEL.2022.123818
- [9] G. Faingold and J. K. Lefkowitz, 'A numerical investigation of NH₃/O₂/He ignition limits in a non-thermal plasma', *Proceedings of the Combustion Institute*, vol. 38, no. 4, pp. 6661–6669, 2021.
doi.org/10.1016/J.PROCI.2020.08.033
- [10] M. Shahsavari, A. A. Konnov, A. Valera-Medina, and M. Jangi, 'On nanosecond plasma-assisted ammonia combustion: Effects of pulse and mixture properties', *Combustion and Flame*, vol. 245, p. 112368, Nov. 2022.
doi.org/10.1016/J.COMBUSTFLAME.2022.112368
- [11] T. S. Taneja, P. N. Johnson, and S. Yang, 'Nanosecond pulsed plasma assisted combustion of ammonia-air mixtures: Effects on ignition delays and NO_x emission', *Combustion and Flame*, vol. 245, p. 112327, Nov. 2022.
doi.org/10.1016/J.COMBUSTFLAME.2022.112327
- [12] Y. Tang, D. Xie, B. Shi, N. Wang, and S. Li, 'Flammability enhancement of swirling ammonia/air combustion using AC powered gliding arc discharges', *Fuel*, vol. 313, p. 122674, Apr. 2022.
doi.org/10.1016/J.FUEL.2021.122674
- [13] D. Feikema, R.-H. Chen, and J. F. Driscoll, 'Enhancement of flame blowout limits by the use of swirl', *Combustion and Flame*, vol. 80, no. 2, pp. 183–195, May 1990.
[doi.org/10.1016/0010-2180\(90\)90126-C](https://doi.org/10.1016/0010-2180(90)90126-C)
- [14] British Standard ISO 11042-1:1996 Gas Turbines. Exhaust Gas Emission Measurement and Evaluation British Standards Institution, UK, 1996.
- [15] S. Mashruk, X. Zhu, W. L. Roberts, T. F. Guiberti, and A. Valera-Medina, 'Chemiluminescent footprint of premixed ammonia-methane-air swirling flames', *Proceedings of the Combustion Institute*, vol. 39, no. 1, pp. 1415–1423, 2023.
doi.org/10.1016/J.PROCI.2022.08.073
- [16] D. Pugh *et al.*, 'An investigation of ammonia primary flame combustor concepts for emissions reduction with OH*, NH₂* and NH* chemiluminescence at elevated conditions', *Proceedings of the Combustion Institute*, vol. 38, no. 4, pp. 6451–6459, 2021.
doi.org/10.1016/J.PROCI.2020.06.310
- [17] D. A. Lacoste, 'Flames with plasmas', *Proceedings of the Combustion Institute*, vol. 39, no. 4, pp. 5405–5428, 2023.
doi.org/10.1016/J.PROCI.2022.06.025

Jiang H

*Cardiff University
School of Engineering*

Alnajideen M

*Cardiff University
School of Engineering*

Valera-Medina A

*Cardiff University
School of Engineering*

SUSTAINABLE ENERGY

Exploring the Potential of Ammonia/Hydrogen Trigeneration Cycle

Numerous low-carbon energy initiatives are adopting ammonia as an energy source, with a particular focus on combining ammonia and hydrogen in a 70%/30% volume ratio for gas turbine systems. The ammonia-hydrogen triple generation cycle, a hybrid of a humidified Brayton cycle and a reverse Brayton cycle, has demonstrated outstanding performance, achieving zero carbon and low NO_x emissions, while boosting overall efficiency to around 59%, comparable to conventional fossil fuel-based power generation systems. The Aspen Plus software was used to simulate and calculate the system's efficiency, mainly focusing on the humidification Brayton cycle, reverse Brayton cycle, and waste heat recovery phase of the ammonia-hydrogen triplex production cycle. Three scenarios were developed to evaluate the efficiency of different steam condensation recovery processes, with all three yielding efficiencies of at least 59%, confirming the cycle's effectiveness and feasibility. Advancements in the system's structure in the future could further enhance the system's efficiency.

Keywords:

Gas turbine, ammonia combustion, thermodynamic cycles, aspen plus, waste heat recovery.

Corresponding author:

AlnajideenMI@cardiff.ac.uk



H. Jiang, M. Alnajideen, and A. Valera-Medina, 'Exploring the Potential of Ammonia/Hydrogen Trigeneration Cycle', *Cardiff University School of Engineering Research Conference 2023*, Cardiff, UK, 2023, pp. 181-184.

doi.org/10.18573/conf1.ao

INTRODUCTION

The world today is facing unprecedented needs to meet energy demand while reducing energy costs and pollution levels. Fossil fuels, which have been the dominant energy source for decades, are becoming increasingly scarce and expensive to extract, posing a significant challenge to meeting this growing demand. This has prompted a shift towards renewable energy sources such as solar, wind, and hydropower, and alternative energy fuels like ammonia and hydrogen, which are sustainable and emit fewer pollutants. In this paper, we present the progress that has been so far in evaluating the performance of our previously proposed ammonia-hydrogen trigeneration power cycle [1, 2]. The thermodynamic cycle, including its three different scenarios, was processed and simulated using Aspen Plus Software. Efficiency calculations were subsequently performed using the resulting data.

SIMULATION METHODS

The ASPEN Plus software, an advanced system for process engineering, is used to model and simulate thermodynamic engineering cycles. It has been extensively used and its ability to simulate real-world power plant applications has been proven and demonstrated in many research articles [3-5].

Three different scenarios were utilised to simulate the trigeneration cycles. In each scenario, the water vapour from the combustion gases was separated by cooling at different stages within the system. These included i) the separation of the water stream from the exhaust gases behind the first heat exchanger (Scenario 1, Fig. 1), ii) the separation of the water stream from the exhaust gases behind the second heat exchanger (Scenario 2, Fig. 2), and iii) the complete absence of condensate (Scenario 3, Fig. 3 overleaf).

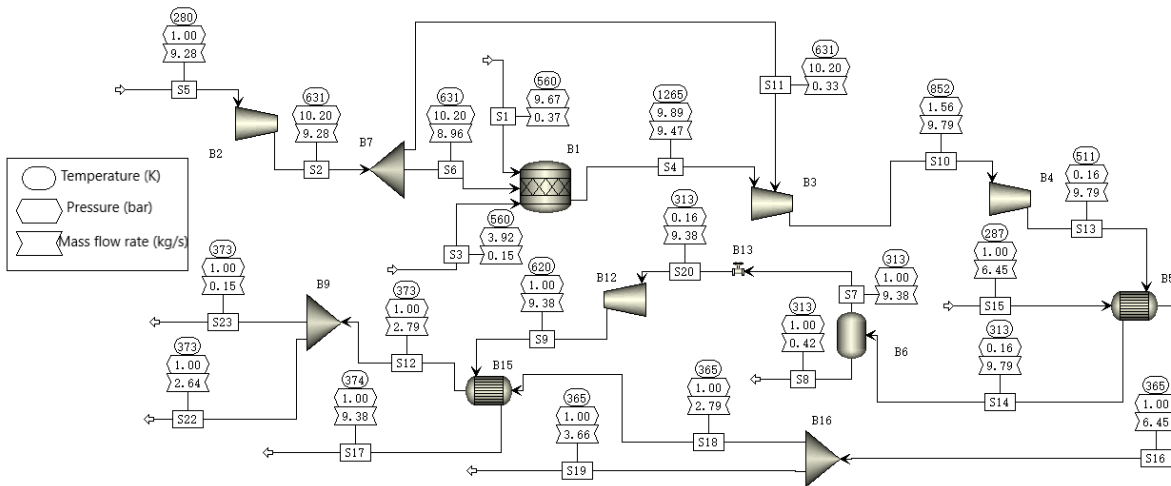


Fig. 1. Scenario 1: separation of water stream from the exhaust gases behind the first heat exchanger.

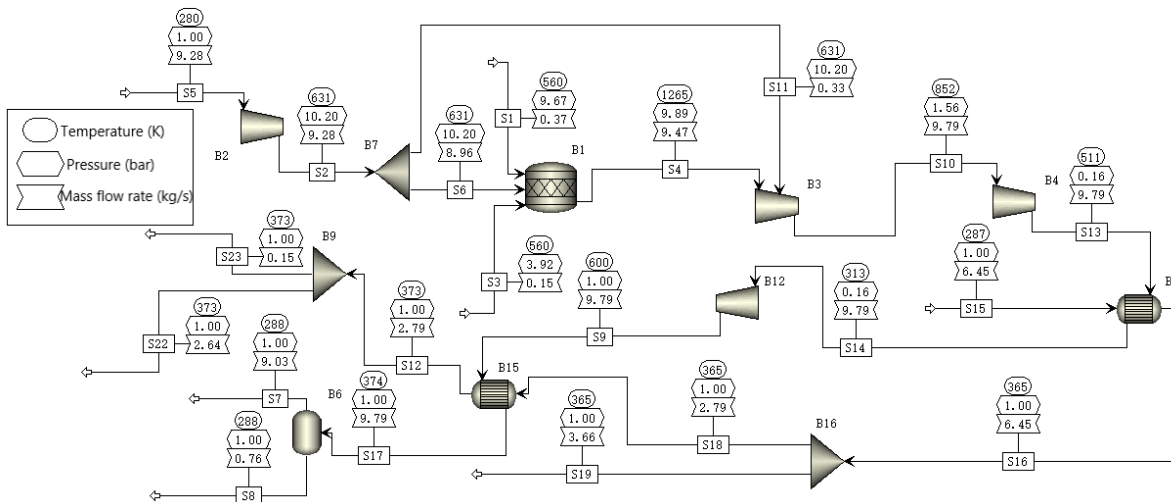


Fig. 2. Scenario 2: separation of water stream from the exhaust gases behind the second heat exchanger.

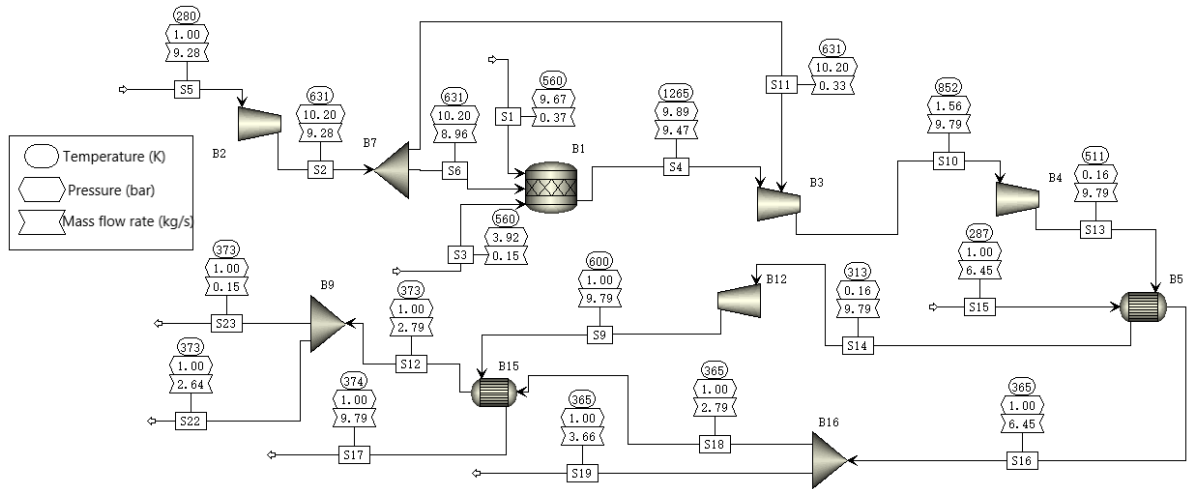
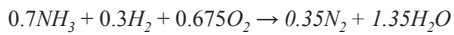


Fig. 3. Scenario 3: no water was separated.

Initially, the incoming atmospheric air (with a mass flow rate of 9.28 kg/s, temperature of 280K and pressure of 1.00 bar) was compressed by the compressor (B2). Subsequently, the compressed air was split into two distinct streams with different amounts of \dot{m} via a splitter (B7). One of the streams was directed to the gas turbine (B3) to facilitate the cooling of its blades, while the second stream was fed into a combustion chamber (B1) to undergo combustion with an NH₃-H₂ mixture by 70%/30% (vol.%). In order to reduce the production of nitrogen oxides, water vapour was added to the combustion chamber (B1). The chemical reaction inside the combustion chamber can be given as:



The flue gases resulting from the combustion process were expanded by both the first gas turbine (B3) and the second gas turbine (B4), respectively. It is to be noted that the exhaust gases from the second gas turbine (B4) were found to still contain a significant amount of heat, which could be harnessed to heat water and ultimately increase the thermal efficiency of the system. Consequently, the turbine's exhaust gasses are directed towards the first heat exchanger (B5) to elevate the temperature of the liquid water from 287K to 365K, while the exhaust gases were cooled to 313 K. A splitter (B16) was employed to divide the resulting hot water into two streams with varying mass flow rates. One of the streams was utilised for dynamic district heating, while the second stream was heated using the second heat exchanger (B15). The resulting water flow was then divided into two streams using splitter (B9), with one having a mass flow rate of 2.64 kg/s intended for industrial heating, and the other having a mass flow rate of 0.147 kg/s, which was heated to 560 K and directed back to the combustion chamber for the subsequent triple generation cycle. Once the exhaust gasses had passed through the first heat exchanger (B5), the variations among the three simulation scenarios would become apparent.

In the first simulation scenario (Fig. 1), the exhaust gases that passed through the first heat exchanger were directed to the separator. Here, a portion of the water vapor present in the exhaust gases underwent condensation, resulting in the formation of a liquid under standard atmospheric pressure and was then separated in accordance with the two-phase flow. The recovered liquid water was utilised as part of the feed water for the waste heat recovery process after passing through separator (B6). The residual gasses were then passed through the expansion valve

(B13), followed by compression in compressor (B12). This sequence of processes led to an increase in the gasses' temperature to 620K at 1.00 bar. Finally, the exhaust gases were cooled to 374K in the second heat exchanger (B15), utilising a water stream with a temperature of 365K, and subsequently released.

In the second scenario (Fig. 2), the exhaust gases exited the first heat exchanger (B5) at 313K and 0.16 bar was fed directly into the second compressor (B12). The pressurised gas was then directed into the second heat exchanger (B15), where it underwent a heat exchange process with the supply water. Within separator (B6), the exhaust gases were completely cooled down to 288K, with the majority of the water vapour undergoing cooling and condensation into liquid water. The resulting liquid water, with a mass flow rate of 0.76 kg/s, was subsequently retrieved in a subsequent stage as part of the supply water for heating work, while the remaining exhaust gases were discharged.

The final simulation scenario (Fig. 3) involved no separation of water from the exhaust gases. Once the exhaust gases exited the first heat exchanger (B5), it was directly routed into the second compressor (B12), without undergoing any treatment. The exhaust gases at 0.16 bar were then compressed to 1.00 bar, which was the same as in the second scenario. Subsequently, the exhaust gases underwent a heat exchange (B15) with the supplied liquid water from the second splitter (B16). Following this step, the exhaust gases were directed to the subsequent processes.

RESULTS AND DISCUSSION

The present study involves an evaluation of the performance of a trigeneration thermodynamic cycle through three different simulation scenarios. The overall efficiency was determined by taking into account various parameters, such as the thermal power supplied by fuel combustion, the mechanical efficiency and work output of the gas turbines, and the power consumed by the compressors.

In the first scenario, a mass flow rate of 0.42 kg/s was utilised to condense and separate water, leading to a computation of a water circulation efficiency of 6.51%. In terms of the first heat exchanger (B5), 2.14 MW of heat was released from the gas, and an enthalpy change of 2.11 MW was achieved for the heated water, resulting in an efficiency of 98.35%. Similarly, in the second heat exchanger (B15),

approximately 2.51 MW of heat was released from the gas, and an enthalpy change of 2.10 MW was attained for the warmed water, which led to an efficiency of 82.21%. The input thermal power provided 1.07 MW to the system, the two gas turbines (B3 and B4) delivered a total of 7.12 MW with 90% mechanical efficiency, and the two compressors (B2 and B12) consumed a total of 6.47 MW of power. This resulted in an overall system efficiency of 60.69% and recovery of 0.42 kg/s of water.

In the second scenario, the efficiency of the first heat exchanger (B5) was found to be the same as in the first scenario, at 98.35%, owing to their identical processes. Nonetheless, other differences emerged in the efficiency calculations between the two scenarios. The mass flow rate of the condensate in scenario 2 was 0.76 kg/s, producing a water circulation efficiency of 11.78%. The second heat exchanger (B15) in scenario 2 released approximately 2.48 MW of heat during combustion and cooling, and the enthalpy change of the water during heating was 2.02 MW, leading to an efficiency of 81.71%. The simulation revealed that the input thermal power provided 1.07 MW to the system, and the gas turbines (B3 and B4) delivered a total of approximately 7.12 MW with a mechanical efficiency of 90%. The total power required to operate the two compressors (B2 and B12) was approximately 6.49 MW. Consequently, the system's overall efficiency was found to be 59.04% with 0.76 kg/s of recovered water.

In the third scenario, the sole distinction from Scenario 2 is the absence of water vapor condensation and separation in the exhaust gas downstream of the second heat exchanger (B15). Therefore, with the exception of the water circulation efficiency, all other efficiencies in Scenario 3, namely the first heat exchanger (B5) efficiency, the second heat exchanger (B15) efficiency, and the system efficiency, are in agreement with the calculations in Scenario 2. As the mass flow rate of the condensate is zero in Scenario 3, the water circulation efficiency is also zero. The efficiency of the system in Scenario 3 closely approximates that of Scenario 2, at 59.04% without any water recovered from the system.

CONCLUSIONS

The present study aimed to investigate the feasibility of an ammonia-hydrogen trigeneration cycle, which integrates a humidified Brayton cycle and a reverse Brayton cycle, as a competitive and promising option for ammonia-based energy utilisation in the contemporary energy market. The system's efficiency was analyzed using Aspen Plus software under various scenarios, followed by validation and efficiency calculations.

The simulation results demonstrated that the efficiency of the system, heat exchanger efficiency, compressor power consumption during waste heat recovery, and water circulation efficiency were significantly affected by the water condensation and recovery at different stages. The first scenario exhibited a lower water circulation efficiency of 6.51% compared to the second scenario, which achieved an efficiency of 11.78%, due to the differences in the condensation methods employed at different stages in the two scenarios. However, the second heat exchanger in Scenario 1 exhibited the highest efficiency of 82.21% among the three scenarios. In contrast, the third scenario showed a 0% water circulation efficiency due to the absence of water condensation and separation in the system. Nevertheless, all other efficiencies in Scenario 3 were consistent with

those in Scenario 2. Moreover, the overall system efficiencies remained at approximately 59%, despite the variations in water condensation and recovery at different stages. Among the three scenarios, Scenario 1 achieved the highest system efficiency of 60.69% by performing water condensation and separation after the first heat exchanger.

In conclusion, the study found that condensing and separating water vapour between the first heat exchanger and the second compressor in the ammonia-hydrogen trigeneration cycle system is the most effective way to improve the system's efficiency, even though it may not be the most efficient water cycle in the simulation. However, this can be improved by adding another separator after the second heat exchanger. The simulation results also confirmed the feasibility and high efficiency of the ammonia-hydrogen trigeneration cycle, which can compete with current fossil fuel-based power generation systems. The study suggests that with further technological development, the ammonia-hydrogen trigeneration cycle can become even more efficient and play a significant role in the low-carbon energy structure. Nevertheless, there is an immediate need to evaluate the exhaust gas emission levels of the cycle across the three scenarios.

Acknowledgements

The authors would like to acknowledge the funding support by EPSRC under the project SAFE Pilot - AGT/ EP/T009314/1.

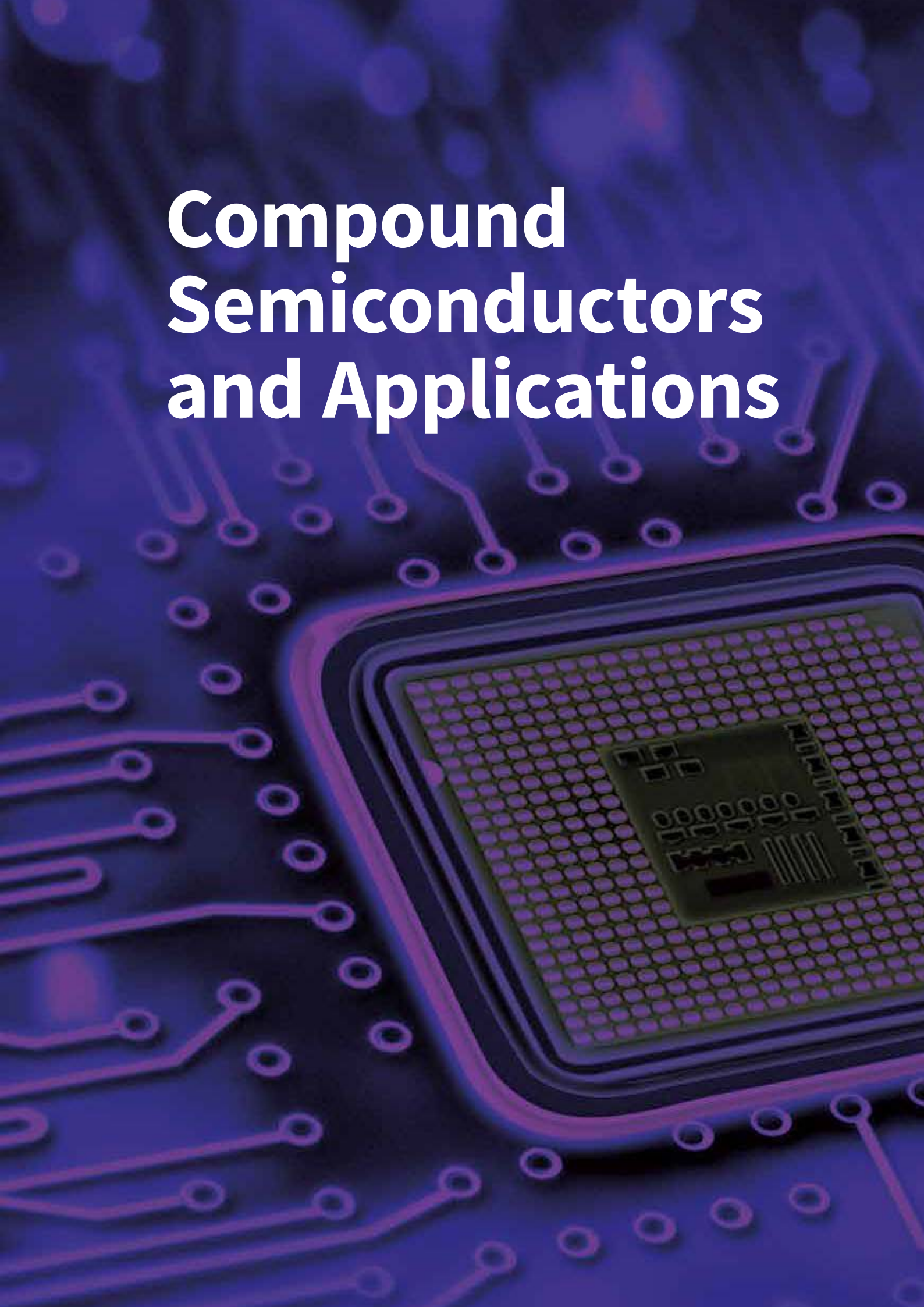
Conflicts of interest

The authors declare no conflict of interest.

REFERENCES

- [1] M. Guteša Božo, S. Mashruk, S. Zitouni, and A. Valera-Medina, 'Humidified ammonia/hydrogen RQL combustion in a trigeneration gas turbine cycle', *Energy Conversion and Management*, vol. 227, p. 113625, Jan. 2021.
doi.org/10.1016/j.enconman.2020.113625
- [2] M. Guteša Božo *et al.*, 'A novel trigeneration gas turbine cycle powered by humidified ammonia/hydrogen with ammonia refrigeration', presented at *1st Symposium on Ammonia Energy*, 2022.
- [3] Ö. Ç. Mutlu and T. Zeng, 'Challenges and Opportunities of Modeling Biomass Gasification in Aspen Plus: A Review', *Chem. Eng. & Technol.*, vol. 43, no. 9, pp. 1674–1689, Sep. 2020.
doi.org/10.1002/ceat.202000068
- [4] M. Garcia, H. K. Knuutila, and S. Gu, 'ASPEN PLUS simulation model for CO₂ removal with MEA: Validation of desorption model with experimental data', *Journal of Environmental Chemical Engineering*, vol. 5, no. 5, pp. 4693–4701, Oct. 2017.
doi.org/10.1016/j.jece.2017.08.024
- [5] C. Panda, 'ASPEN PLUS simulation and experimental studies on biomass gasification', B Tech thesis, National Institute of Technology, Rourkela, India, 2012.

Compound Semiconductors and Applications



Compound Semiconductors and Applications

- 187 Numerical Investigation of Size Effects in Tension and Torsion of Micro-scale Copper Wires using a Strain Gradient Modified Johnson-Cook Constitutive Model
- 191 Electro-Thermal Coupling for Simulation of 52 kV Polymeric Bushing with Nonlinear ZnO Microvaristor Under Different Environmental Conditions

Zhu S

*Cardiff University
School of Engineering*

Brousseau E

*Cardiff University
School of Engineering*

COMPOUND SEMICONDUCTORS AND APPLICATIONS

Numerical Investigation of Size Effects in Tension and Torsion of Micro-scale Copper Wires using a Strain Gradient Modified Johnson-Cook Constitutive Model

While material behaviour on the micro to nanoscale may be investigated using various experimental methods, it is of interest to develop complementary 3-dimensional (3D) numerical approaches to simulate material deformation at such small scales. In particular, these simulations provide a means to shed further light on key mechanisms at play, especially in the region of plastic strain. The size effect in tension and torsion of micro-scale copper wires is numerically investigated in this study using a strain gradient modified Johnson-Cook method. This 3D algorithm is implemented by self-compiled subroutines using the ABAQUS/Explicit solver. The simulated flow stress and yield stress in torsion of micro-scale copper wires were observed to increase with the decrease of the wire diameter, which correlates well with experimental findings reported in the literature. A similar size effect, although not as significant as that in torsion, was also observed in the simulated tension experiments, again in line with existing experimental reports. This work contributes to the efforts of the research community in the simulation material behaviour at the micro- to nanoscale, especially when considering the combined influence of both size effect and strain rate.

Keywords:

Tension/torsion simulation, johnson-cook theory, strain gradient plasticity, size effect, finite element method.

Corresponding author:

YaoS8@cardiff.ac.uk



S. Zhu and E. Brousseau, 'Numerical Investigation of Size Effects in Tension and Torsion of Micro-scale Copper Wires using a Strain Gradient Modified Johnson-Cook Constitutive Model', *Cardiff University School of Engineering Research Conference 2023*, Cardiff, UK, 2023, pp. 187-190.

doi.org/10.18573/conf1.ap

INTRODUCTION

The knowledge of material properties on the micro- to nanoscale is of great importance for the predictable and reliable manufacture of small-scale structures. Different from the meso-macro scale, where material properties can be considered constant and relatively easy to calibrate when implementing numerical simulations, establishing accurate material constitutive models at smaller scale remain challenging due to increased instrumentation requirements and the prevalence of more complex mechanisms such as the size effect. This effect, which results in the increase in the flow stress of material as the volume of the deformed region reduces, has been reported in many experiments [1] such as tension, compression, torsion, indentation and scratching of various metal/polymer wires and foils.

Numerical tools such as molecular dynamics modelling (MD), crystal plasticity finite element method (CPFEM), multiscale approaches including finite element combined with atomistic method (FEAt), bridging scale method (BSM), coupled atomistic and discrete dislocation plasticity (CADD) approaches and quasi-continuum (QC) method have been developed by the research community to investigate and model this size effect. However, prohibitive computational cost, unrealistic space/time scale involved, and implementation complexity can hinder the applications of these methods. On the other hand, the low-order strain gradient plasticity theory (SGP), which is built on the framework of von Mises plasticity, considers the size effect by introducing a material characteristic length and strain gradient. The relative ease of implementation and robust physical derivation render SGP an efficient and reliable method to investigate material behaviour at the micro to sub-micro scale. In addition, the Johnson-Cook (JC) theory [2] which considers the effect of strain hardening, strain rate and the temperature has been widely utilised in the simulation of meso to macro scale deformation of metallic materials.

To solve the aforementioned issues in numerical simulations at micro and sub-micro scales, this study reports the implementation of a 3D Finite Element (FE) approach whereby the material constitutive model is described by combining the JC and the SGP theories. The combination of these theories forms a novel framework within which the effect of strain hardening, strain rate, temperature and size effect could be investigated thoroughly. As a result, the bridge between different scales is expected to be facilitated and the material library at small scales is expected to be enriched for future simulations.

MATERIALS AND METHODS

The FE simulations carried out in this work concern the torsion and uniaxial tension of copper wires. The numerical studies are performed using the ABAQUS/Explicit module and the SGP-modified JC algorithm is realised using the embedded subroutines. The copper wires are constrained on all degrees of freedom (DOF) on the base part and only the x direction of the grip part is ascribed to move under a quasi-static strain rate of 0.1 in tension (see Fig. 1). The stress in tension is calculated as an average value of the von Mises stress of the gauge section. For the torsion simulations, the grip and base parts are subjected to a rotation of 1.57 (radians) in the $UR1$ direction and the remaining DOFs are constrained. The shear strain is calculated using $a\theta/L$, where L is the gauge length, a is the radius of the wire and θ is the torsion angle. The diameters of the simulated copper wire were varied and included the

following values: 18 μm , 30 μm , 42 μm and 105 μm . These values were selected to be able to compare the simulation results against the experimental data published in [1]. The material properties used in this work can be found in [2].

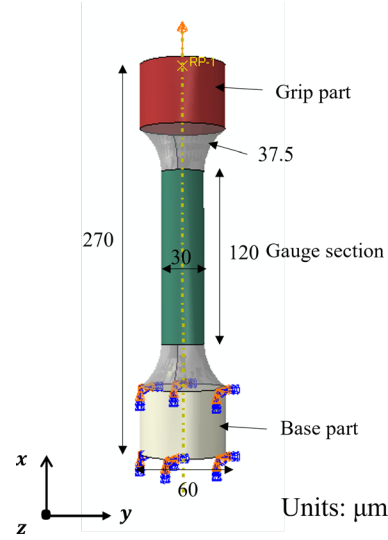


Fig. 1. Schematic illustration of one of the simulated dog-bone-shaped specimens.

The classical JC model describes the flow stress as:

$$\sigma_{JC} = [A + B(\bar{\epsilon}^{pl})^n][1 + C \ln(\frac{\dot{\bar{\epsilon}}^{pl}}{\dot{\epsilon}_0})](1 - \hat{\theta}^m) \quad (1)$$

Based on the SGP theory, the flow stress using Taylor's model is given as:

$$\sigma = M\alpha G b \sqrt{\rho_s + \rho_g} \quad (2)$$

ρ_s can be determined by material tests where the strain gradient is negligible and thus classic JC is applicable:

$$M\alpha G b \sqrt{\rho_s} = \sigma_{JC} \quad (3)$$

Substituting (3) into (2), the flow stress becomes:

$$\sigma = \sigma_{JC} \sqrt{1 + \frac{\rho_g}{\rho_s}} \quad (4)$$

ρ_g is calculated as:

$$\rho_g = \bar{r} \frac{\eta}{b} \quad (5)$$

Substituting (3) and (5) into (4), the flow stress is now [3]:

$$\sigma_{flow} = \sigma_{JC} \sqrt{1 + \left(\frac{18\alpha^2 G^2 b}{\sigma_{JC}^2} \eta\right)^\mu} \quad (6)$$

where $\frac{18\alpha^2 G^2 b}{\sigma_{JC}^2}$ is defined as material characteristic length l . μ is introduced to represent the density of GNDs needed to accommodate the strain gradient in the deformation zone. Equation (6) describes the material constitutive model which combines the JC and the SGP theories. The incremental plastic strain gradient $\Delta\eta_{ijk}^p$ can be calculated using the formulation below [4].

$$\Delta\eta_{ijk}^p = \Delta\epsilon_{ik,j}^p + \Delta\epsilon_{jk,i}^p - \Delta\epsilon_{ij,k}^p \quad (7)$$

In this work, (7) is reformulated as:

$$\Delta\eta_{ijk}^p = \sum_{k=1}^8 N_k(\xi, \eta, \zeta)(\Delta\bar{\varepsilon}_{ij}^{pl}) \quad (8)$$

Similar to the effective strain which can be expressed as

$\varepsilon = \sqrt{\frac{2}{3}\varepsilon_{ij}\varepsilon_{ij}}$, under rate-proportional loading, $\Delta\eta^p$ can be calculated as:

$$\Delta\eta^p = \sqrt{\frac{1}{4}\Delta\eta_{ijk}^p\Delta\eta_{ijk}^p} \quad (9)$$

The JC shear failure criterion is also included in the developed model. More specifically, the failure strain $\bar{\varepsilon}_f^{pl}$ is calculated as follows:

$$\bar{\varepsilon}_f^{pl} = (d_1 + d_2 e^{d_3 \frac{p}{q}})(1 + d_4 \ln(\frac{\dot{\bar{\varepsilon}}^{pl}}{\dot{\varepsilon}_0}))(1 + d_5 \hat{\theta}) \quad (10)$$

Next, a summation of incremental failure strain is performed over all increments to calculate the failure criterion as follows:

$$\omega = \Sigma\left(\frac{\Delta\bar{\varepsilon}_f^{pl}}{\bar{\varepsilon}_f^{pl}}\right) \quad (11)$$

Once ω exceeds a critical threshold, i.e., a value over 1, the affected elements are deleted in the next solver step. The equivalent plastic strain $\bar{\varepsilon}^{pl}$, von Mises stress q and hydro stress p that are needed for the algorithm are obtained by the VGETRM utility subroutine at the end of each increment.

RESULTS

All the simulated stress-strain curves of copper wires in tension are displayed in Fig 2. Following the notation reported in [5] the normalized torque Q/a^3 is also plotted against the surface shear strain κa in torsion as shown in Fig 3, where κ is the twist per unit length of the wire.

From Fig. 2, it is observed that the stress-strain curves of wires with different diameters in tension are all superimposed when using only the classical JC method built in Abaqus. This is expected because the classical JC approach does not take strain gradient into account and thus, cannot simulate the size effect. The maximum simulated flow stress in tension using the classical JC model was found to be around 231.8 MPa. In torsion, the simulated flow stress using the built-in JC method fluctuated slightly between 277.3 MPa-290.9 MPa. For this reason, in Fig. 3, only the average value of 283.3 MPa is plotted for the classical JC simulation.

When using the SGP-modified JC method, both the flow stress and Q/a^3 increased in different proportions with the decreasing of wire diameters. In tension, the simulated stress-strain data are the highest for the 18 μm wire, i.e., that with the smallest diameter. This was expected and is aligned with the experimental results in [1], which are also reported in both Fig. 2 and Fig.3. The same observation can be made for the simulations in torsion. The stress-strain data in torsion for the 30 μm and 42 μm wires are relatively close, which is similar in trend to the experimental findings. Although a good agreement between the trends and the order of magnitude of the numerical and experimental data is observed, actual values differ. This may be due to the fact that the experimental results in [1] were achieved on copper wires that had been annealed. The annealing process likely resulted in an enlarged grain size and smaller dislocation density [6] compared to standard copper wires which have been considered as the baseline when implementing the proposed SGP-modified JC constitutive model.

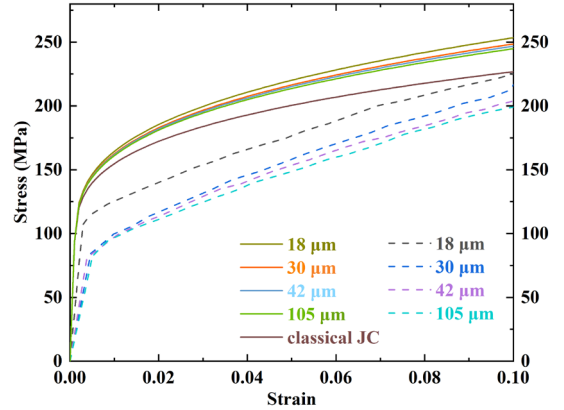


Fig. 2. Stress-strain curves for copper wires in tension with diameters of 18 μm , 30 μm , 42 μm and 105 μm . The dashed curves show the experimental results reported in [1].

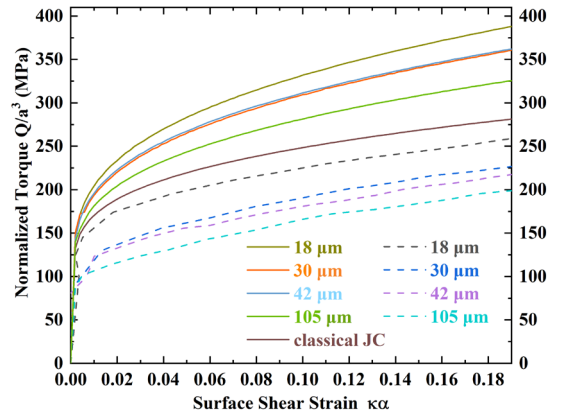


Fig. 3. Plots of normalized torque-twist curves for copper wires with diameters of 18 μm , 30 μm , 42 μm and 105 μm . The dashed curves show the experimental results reported in [1].

The extracted yield stress data in tension at the strain of 0.1 and in torsion at the surface shear strain of 0.19 are displayed in Fig. 4 for all wire diameters considered. The yield stress using the classical JC theory remains nearly identical (around 231.8 MPa for tension and 271 MPa for torsion) regardless of the diameter. When using the proposed SGP-modified JC model, it is clearly noted from Fig. 4 that the simulated yield stress increases with a reduction in the wire diameter. This size effect is also observed to be more pronounced in torsion than that in tension, as was also reported in [1] based on experimental findings.

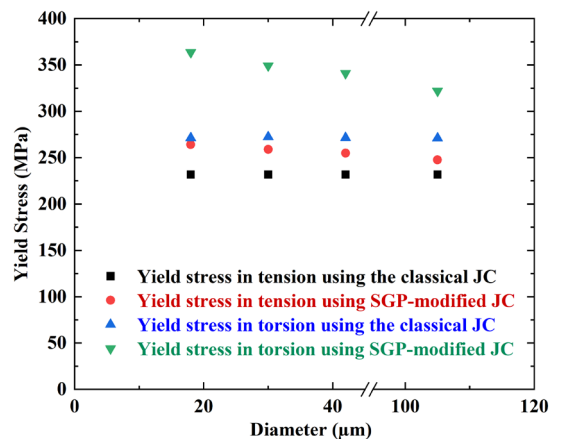


Fig. 4. Simulated yield strength data (for a strain of 0.1 in tension and a surface shear strain of 0.19 in torsion) for copper wires with diameters of

DISCUSSION

Using the developed SGP-modified JC constitutive model in the FE simulations, the numerical results were found to be consistent with the experimental findings from [1] which reported the existence of a size effect for micro-scale copper wires. As expected, such size effect cannot be simulated using the classical JC theory only. Fleck et al. [5] pointed out that, the size effect was more prominent in torsion. This was also observed in the simulations presented here.

The reason behind this difference in material behaviour between tension and torsion is that, in uniaxial tension, the hardening is mainly due to the statistically stored dislocations which can be relatively moderate for a given wire diameter. In torsion, and for the same wire diameter, the strain gradient = and more pronounced non-homogeneity of deformation introduce an increased amount of geometrically necessary dislocations (GND). For a given surface shear strain, a thinner wire i.e., a smaller a , would introduce a larger strain gradient and greater density of GND. A faster and greater hardening in thinner wires would thus be observed. The material characteristic length, which is a homogenous representation of internal structures and dislocations, and the equivalent plastic strain/ shear strain are attributed to this size effect.

One should also notice that the developed model does not capture the size effect in the initial elastic region. This is the reason why the simulated yield point (around 94MPa in tension) and normalized torque (around 140 MPa in torsion) values are constant in Fig. 2 and Fig. 3.

CONCLUSIONS

The presented results demonstrate that the developed SGP-modified JC model and its implementation via 3D FE simulations can be used to study the size effect in micro-scale tension and torsion of copper wires. Given that the model also intrinsically considers the influence of the strain rate, strain hardening and temperature, it paves the way for the further simulation of micro and nano-scale manufacturing processes which are not taking place in a quasi-static mode, such as in ultraprecision machining for example.

In future simulations, the contribution of the strain rate and processing temperature against that of the strain gradients will also be investigated based on the developed model. As stated by Pañeda [7], for a typical dislocation density of $10^{15}/\text{m}^2$, equation (6) holds at a scale above 100 nm. This means that the developed model should be used in future studies where the size of the processed material region is above this threshold.

Acknowledgements

Shuai Zhu would like to thank the support of China Scholarship Council for sponsoring his PhD study at Cardiff University. The authors would like to thank the support of Supercomputer Wales and all the IT staff at Cardiff University. Shuai Zhu would like to thank Dr Emilio Martínez Pañeda, Dr Zhang Yin, Dr Oliver Pantale, Dr David Morin and Dr Martin Baeker for their help in subroutines. The authors are open to possible collaborations. The developed subroutines (classic_JC_dynamic_damage.f, JC_dynamic_damage_SGP.f) and inp files in this work are available upon reasonable requests (email: zhushuaihit0712@gmail.com).

Conflicts of interest

The authors declare no conflict of interest.

APPENDIX

A, B, C, m, n coefficients of the JC model
 $\Delta \bar{\epsilon}^{pl}$ incremental equivalent plastic strain
 $\dot{\epsilon}_0$ reference strain rate
 $\dot{\bar{\epsilon}}^{pl}$ equivalent plastic strain rate
 $\hat{\theta}$ temperature term
 d_1, d_2, d_3, d_4, d_5 parameters of JC failure criterion
 ρ_s density of statistically stored dislocation
 ρ_g density of geometry necessary dislocation
 G shear modulus (GPa), b burgers vector (nm)
 a empirical coefficient which takes value between 0.3 and 0.5
 \bar{r} Nye-factor which is assumed to be 1.90 for face-centred cubic (fcc) polycrystals
 M Taylor factor, 3.06 for fcc metals
 $N_k(\xi, \eta, \zeta)$ shape function vector
 $\Delta \epsilon_{ik,j}^p$ plastic strain components

REFERENCES

- [1] D. Liu, Y. He, X. Tang, H. Ding, P. Hu, and P. Cao, 'Size effects in the torsion of microscale copper wires: Experiment and analysis', *Scripta Materialia*, vol. 66, no. 6, pp. 406–409, Mar. 2012. doi.org/10.1016/j.scriptamat.2011.12.003
- [2] G. R. Johnson and W. H. Cook, 'Fracture characteristics of three metals subjected to various strains, strain rates, temperatures and pressures', *Engineering Fracture Mechanics*, vol. 21, no. 1, pp. 31–48, Jan. 1985. doi.org/10.1016/0013-7944(85)90052-9
- [3] X. Lai, H. Li, C. Li, Z. Lin, and J. Ni, 'Modelling and analysis of micro scale milling considering size effect, micro cutter edge radius and minimum chip thickness', *International Journal of Machine Tools and Manufacture*, vol. 48, no. 1, pp. 1–14, Jan. 2008. doi.org/10.1016/j.ijmactools.2007.08.011
- [4] H. Gao, Y. Huang, W. D. Nix, and J. W. Hutchinson, 'Mechanism-based strain gradient plasticity— I. Theory', *Journal of the Mechanics and Physics of Solids*, vol. 47, no. 6, pp. 1239–1263, Apr. 1999. doi.org/10.1016/S0022-5096(98)00103-3
- [5] N. A. Fleck, G. M. Muller, M. F. Ashby, and J. W. Hutchinson, 'Strain gradient plasticity: Theory and experiment', *Acta Metallurgica et Materialia*, vol. 42, no. 2, pp. 475–487, Feb. 1994. doi.org/10.1016/0956-7151(94)90502-9
- [6] P. A. El-Deiry and R. P. Vinci, 'Strain Rate Dependent Behavior of Pure Aluminum and Copper Micro-Wires', *MRS Online Proceedings Library*, vol. 695, no. 1, p. 421, Mar. 2011. doi.org/10.1557/PROC-695-L4.2.1
- [7] E. Martínez-Pañeda and C. Betegón, 'Modeling damage and fracture within strain-gradient plasticity', *Int J Solids Struct*, vol. 59, pp. 208–215, May 2015. doi.org/10.1016/j.ijsolstr.2015.02.010

Aboshwerb M

*Cardiff University
School of Engineering*

Albano M

*Cardiff University
School of Engineering*

Haddad M

*Cardiff University
School of Engineering*

COMPOUND SEMICONDUCTORS AND APPLICATIONS

Electro-Thermal Coupling for Simulation of 52 kV Polymeric Bushing with Nonlinear ZnO Microvaristor Under Different Environmental Conditions

Bushings are considered as one of the main components of power transformers, a key element of the transmission network. Recently, bushings with composite housings have been adopted because of their advantages over ceramic bushing, e.g., reduced weight, reduced explosive hazard and better performance under polluted conditions and under seismic activity. However, excessive electric field intensity can originate tracking and erosion effects on the insulating material affecting the withstand capabilities of the bushing. This paper investigates the electric field distribution coupled with temperature distribution on a 52 kV polymeric bushing to determine any vulnerable areas. The simulation evaluates the electrical and thermal stress reduction in these identified areas by introducing ZnO-microvaristor material, as a possible solution to mitigate these damages. A suitable bushing design using this field grading material is proposed for effective stress control near the flange ground terminal to offer the manufacturers additional confidence for applying novel insulating materials.

Keywords:

Polymeric bushing, Non-linear field grading composites, Stress control, Finite element method, ZnO microvaristor.

Corresponding author:

AboshwerbMA@cardiff.ac.uk



M. Aboshwerb, M. Albano, and M. Haddad, 'Electro-Thermal Coupling for Simulation of 52 kV Polymeric Bushing with Nonlinear ZnO Microvaristor Under Different Environmental Conditions', *Cardiff University School of Engineering Research Conference 2023*, Cardiff, UK, 2023, pp. 191-195.

doi.org/10.18573/conf1.aq

INTRODUCTION

Polymeric materials have been widely used for outdoor insulation in transmission and distribution systems for economic and technological reasons. Compared to analogous ceramic insulation systems, polymeric insulation provides a substantial weight reduction, less fragile properties and better performance under pollution [1]. However, composite insulation materials suffer from degradation and aging issues from surface partial arcing due to localized high electric field magnitudes. The organic nature of polymeric materials determines a vulnerability to degradation and aging under various electrical, environmental, mechanical and thermal stresses [2]. Therefore, it is important to design the polymeric insulation system without any high electric stress areas under all possible in-service environmental conditions.

Recently, the utilization of resistive field grading materials using specific ceramic powders for stress control has been introduced [3,4]. Developments and improvements in the manufacture of ZnO microvaristors and compounding with silicone materials provide a promising solution for reducing electric fields across polymer insulating surfaces [5]. This resistive non-linear electric field grading material based on ZnO microvaristors displays high field-dependent conductivity characteristic, which allows redistribution of the electric field, hence prevents localized field enhancements. Cardiff University High Voltage Research Team [4-6] showed how the formulation of ZnO microvaristors can offer the possibility to adjust nonlinear switching parameters such as field switching thresholds, especially in HV applications including high voltage composite insulators.

In this paper, a polymeric bushing with field grading material has been investigated to identify optimal parameters that impact electric field distribution on the bushing surface. These include thickness, length, position and the switching parameters of field grading material such as initial conductivity, non-linearity coefficient, and field switching threshold. The simulation work was performed using COMSOL Multiphysics 5.5 and 2D axisymmetric models [7]. The simulation results show the impact of the optimal parameters field grading material in reducing the high electric stresses present in the initial bushing design.

ZNO MICROVARISTOR PROPERTIES

ZnO microvaristors are semiconducting particles having high nonlinear voltage-current properties. These may be utilized as a filler to produce nonlinear features to the insulating matrix, impart its nonlinear characteristics and form field grading composites. They are utilized for stress control in several HV applications, like power modules [8], induction motor stator coils [9] bushings [4], cable accessories [3], and composite insulators [4-6]. Moreover, micro-scaled electroceramic particles exhibiting highly nonlinear electrical properties like ZnO varistor in high voltage arrester applications have been developed [10].

A Scanning Electron Microscope (SEM) picture of such material is shown in Fig. 1 [5].

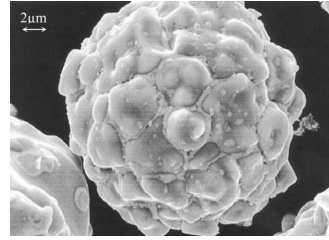


Fig. 1. Microvaristor structure viewed using SEM [5].

COMPUTATIONAL MODELLING

Design of polymeric bushing with non-linear resistive field grading material

Medium voltage distribution polymeric bushings consist of three main parts: the insulation housing body including the weather sheds that are made of silicone rubber insulation, the energised HV copper conductor core onto which the polymeric housing is molded, and an aluminum flange (ground terminal).

A simplified 52 kV silicone rubber bushing was investigated in this work. The key components of this bushing are shown in Fig. 2.

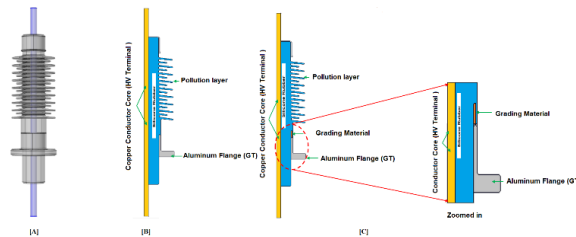


Fig. 2. 52 kV polymeric bushing (A) assembled bushing parts (B and C) computational axis-symmetric model of the proposed design adopting ZnO microvaristor material (details in C).

The pollution layer over the polymeric bushing surface is assumed to be uniform with 0.5 mm thickness [4]. The material properties of the polymeric bushing with ZnO microvaristor material are summarized in Table 1.

Materials	Relative Permittivity ϵ_r	Conductivity σ [S/m]
Air background	1	1×10^{-14}
Silicone rubber	4.3	1×10^{-15}
Conductor core	1	15.998×10^7
Aluminum flange	1	5.96×10^7
Transformer oil	2.2	9×10^{-12}
Pollution layer	81	1×10^{-6}

Table 1. Material properties adopted for polymeric bushing modelling.

The electrical conductivity of the nonlinear field grading material based on ZnO microvaristor exhibits a high degree of nonlinear behavior, and it can be expressed by the exponential function as given in (1).

$$\sigma(E) = \sigma_0 \left[1 + \left(\frac{E}{E_0} \right)^\alpha \right] \quad (1)$$

Where $\sigma(E)$ is the non-linear conductivity of field grading material, σ_0 is the low field conductivity, E_0 is the intensity

of the electric field, E_0 is the field switching threshold, and α is the nonlinearity coefficient. The dielectric constant of the field grading material is assigned as ϵ_r , [5].

Furthermore, the switching threshold value identifies the electric field magnitude at which the field grading composite electrical characteristics start to vary, changing very quickly from very low-loss insulator state to fairly-good conductor operation mode. This threshold magnitude is a crucial parameter for achieving efficient field grading in different HV applications. Figure 3 shows an example of conductivity-field characteristic illustrating the point of switching threshold E_0 . Beyond the switching threshold value, any slight rise in the magnitude of the electric field leads to a significant rise in the conduction current.

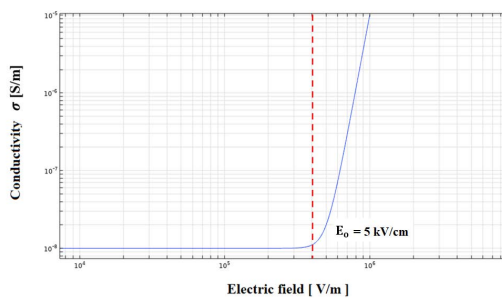


Fig. 3. Field-dependent conductivity of non-linear field grading material with switching threshold value.

Finite Element Analysis

In this study, field computations and modelling have been carried out by the commercially available FEM package COMSOL Multiphysics 5.5 [7]. Because of the symmetrical shape of the polymeric bushings, we adopted an axis-symmetric model with Electric Currents (EC) interface to decrease memory requirements and processing time [7]. The polymeric bushing model in Fig. 2 was implemented for the simulation study. The simulation of this simplified configuration under pollution condition shows that the most non-uniform electric field distribution with highest magnitudes is near the flange ground terminal and thus reflects the worst-case scenario.

The applied voltage on the HV conductor core is phase-to-ground value equivalent to 30 kV at 50 Hz, while the flange terminal is grounded. The axial symmetric line in the r-z plane was assigned as the polymeric bushing symmetry line. This study is performed under dry and clean, and pollution conditions, according to conditions specified in IEC 60507 standard [12]. The mesh density is assigned manually to improve the accuracy, especially near the critical regions of the flange ground terminal, as shown in Fig. 4.

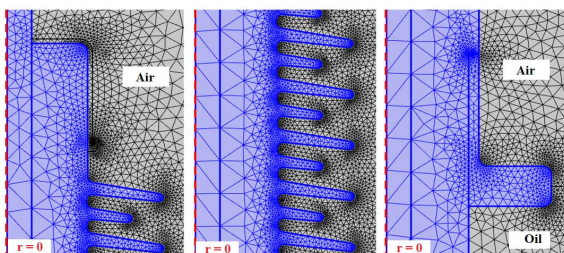


Fig. 4. Mesh discretisation of polymeric bushing domain.

SIMULATION RESULTS AND DISCUSSION

Equipotential lines along polymeric bushing surface with and without ZnO microvaristor material under uniform wet pollution conditions

The simulation results have shown that the different thicknesses and lengths of grading material, as well as the switching parameters of the field grading material have a crucial role in obtaining effective field grading along the polymeric bushing surface. In this simulation, the evaluated performance of the new graded bushing was obtained with the following parameters of field grading material: length and thickness of grading material; $L=30$ mm and $T=4$ mm respectively, switching field threshold $E_0 = 5e5$ V/m, conductivity at point of threshold $\sigma(\rho) = 1 \times 10^{-8}$ S/m, coefficient of non-linearity $\alpha = 10$. These values offered a better performance near the flange ground terminal compared to other values found in literature. Figure 5 shows the computed equipotential lines on the polymeric bushing model when the surface is wet pollution conditions without and with the addition of grading material.

As can be seen on the figure, the application of the non-linear field grading material clearly changes the distribution of the equipotential lines near the flange ground terminal. Such redistribution suppresses field enhancements along the bushing surface in the region of the grounded flange. Of particular interest is the triple junction region where the polymeric material, air and the metal of the flange meet. The field is significantly reduced to magnitudes below air ionisation threshold, hence suppressing initiation of electrical discharges on the bushing surface.

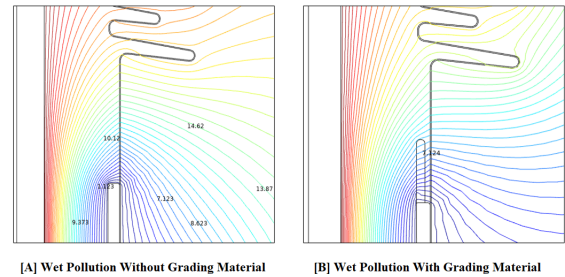


Fig. 5. The equipotential lines along the polymeric bushing surface without (a) and with grading material (b) under wet polluted condition.

Electric field distribution along the polymeric bushing surface with and without ZnO microvaristor under wet pollution condition.

Figure 6 illustrates the tangential of electric field distribution over the polymeric bushing leakage distance without and with grading material. The polymeric bushing with ZnO microvaristors shows a significant reduction of the tangential electric field distribution agreeing with the observation from equipotential lines plot. The tangential component of the electric field with the grading material is more uniform along the surface, preventing extreme electrical stress at the triple junction point near the flange ground terminal.

Figure 7 shows that the maximum electric field magnitude decreases from 0.57 kV/mm to 0.39 kV/mm near the flange ground terminal, representing a 31.5 % electric field reduction.

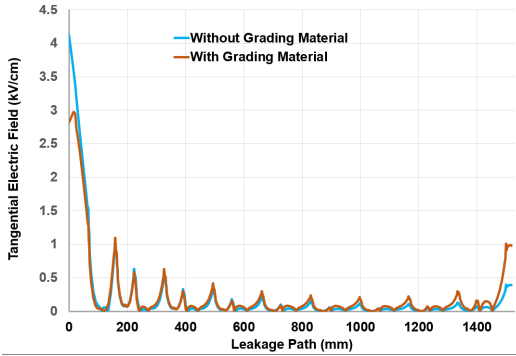


Fig. 6. The distribution of the tangential electric field over the polymeric bushing leakage path without (in blue) and with grading material (in brown).

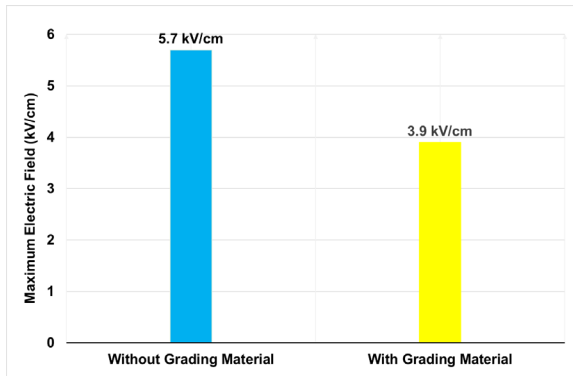


Fig. 7. The maximum electric field magnitude near the flange ground terminal of the studied polymeric bushing.

Temperature distribution of polymeric bushing without ZnO microvaristor material

As a bushing is operating, a portion of the current through the conductor of the bushing dissipates power and converts the losses into heat, and this raises the temperature of the bushing [13]. The chemical nature of the insulator can change if the bushing is overheated, or if it is exposed to high temperatures for prolonged time. This situation leads to changes in the physical bushing electrical properties and accelerates its degradation and ageing rates [13]. It was shown that the Hot Spot Temperature (HST) of a bushing is inversely proportional to its lifetime [14]. Moreover, calculating the HST and the temperature distribution of the bushing is thus very useful in identifying the best design and performance of the bushing.

Figure 8 shows the two- and three-dimensional temperature distributions on the studied polymeric bushing under the rated bushing current of 1250A. The 3D model has been developed for further simulations with a non-uniform pollution layer non-axially symmetrical, not presented in this work. The highest temperature obtained from the simulation of the polymeric bushing is 55°C, which is inside the oil tank in the vicinity of the copper conductor. The reason for different temperature distributions on the bottom and top of the polymeric bushing is due to the top part being surrounded by ambient air and cooled by convection, while the bottom of the polymeric bushing is located in the transformer oil tank, at 80°C at full load conditions.

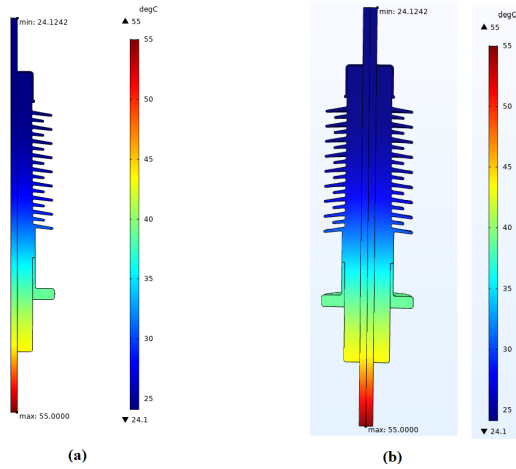


Fig. 8. (a) Two-dimensional temperature distribution in the polymeric bushing (b) Three-dimensional view of the polymeric bushing temperature distribution (°C).

Effect of current magnitude on the polymeric bushing temperature distribution

The temperature distribution on the conductor under different current magnitudes is calculated to identify the effect of the current magnitude on the magnitude and location of the HST. The application of 700, 1250, 2000, and 2500 A currents to the composite bushing, have been investigated and the results are shown in Fig. 9.

The temperature distribution is evaluated from the top region (air-sided part) to the lower region of the transformer (oil-sided part). As seen in Fig.8, the temperature distribution along the conductor and hence the bushing length is nonlinear and non-constant. As expected, the temperature value for each location appears to be affected by the current magnitude. It can be observed in Fig. 9 that higher increases are seen in the high current range.

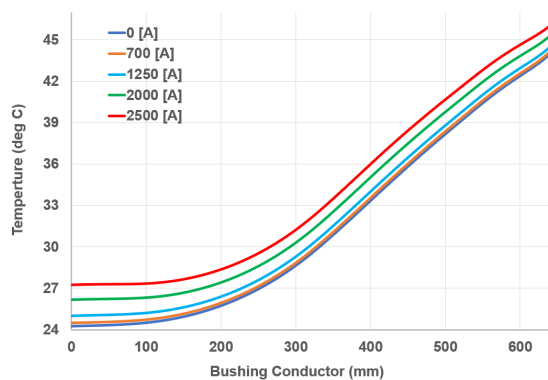


Fig. 9. Temperature distribution on the conductor for different currents (°C).

CONCLUSION

The influence of non-linear resistive field grading material based on ZnO microvaristors for stress control on a 52 kV polymeric bushing is investigated. The proposed graded material performance exhibits best performance compared to the typical polymeric bushing, and the electric field enhancements at the triple junctions are successfully reduced. The maximum electric field magnitude reduced from 5.7 kV/cm to 3.9 kV/cm near the flange ground terminal, representing a 31.5% electric field reduction. These promising results indicate that it is possible to reduce the risk of corona and surface electric discharge initiation over the polymeric bushing surface, reducing the possibility of dry bands formation and arcing, which may eventually lead to tracking and erosion of the polymeric bushing surface. Furthermore, the temperature distribution and heat analysis are essential investigation for such bushings. The bushings can have a reduced lifespan and are prone to malfunction due to the highest heat load resulting from power dissipation in the inner conductor. The temperature distribution and hottest spot temperature of the bushing are impacted by this power dissipation, along with other factors such as the flowing current, conductor material, and insulation material. A two-dimensional temperature distribution of the bushing was obtained. The hottest spot on the conductor, located near the flange, was then identified. Next, the current through the conductor was varied in four discrete values, and the temperature of the conductor was measured and the impact of the current on the hottest spot temperature was determined. It was concluded that increasing the current led to a slight increase in the temperature of the conductor and in the hottest spot, and no significant thermal stress was observed in the studied polymeric bushing.

REFERENCES

- [1] D. A. Swift, C. Spellman, and A. Haddad, 'Hydrophobicity transfer from silicone rubber to adhering pollutants and its effect on insulator performance', *IEEE Trans Dielect Electr Insul*, vol. 13, no. 4, pp. 820–829, Aug. 2006. doi.org/10.1109/TDEI.2006.1667741
- [2] P. Bonhôte, T. Gmür, J. Botsis, and K. O. Papailiou, 'Stress and damage analysis of composite–aluminium joints used in electrical insulators subject to traction and bending', *Composite Structures*, vol. 64, no. 3–4, pp. 359–367, Jun. 2004. doi.org/10.1016/j.compstruct.2003.09.005
- [3] L. Donzel, F. Greuter, and T. Christen, 'Non-linear resistive electric field grading Part 1: Theory and simulations', *IEEE Elect Insul Mag*, vol. 26, no. 6, pp. 47–59, Nov. 2010. doi.org/10.1109/MEI.2010.5599979
- [4] R. Abd-Rahman, A. Haddad, N. Harid, and H. Griffiths, 'Stress control on polymeric outdoor insulators using Zinc oxide microvaristor composites', *IEEE Trans Dielect Electr Insul*, vol. 19, no. 2, pp. 705–713, Apr. 2012. doi.org/10.1109/TDEI.2012.6180266
- [5] H. Ahmad, A. Haddad, H. Griffiths, S. Robson, T. Nishimura, and N. Tsukamoto, 'Electrical properties of field grading material', in *Proceedings of the International Symposium on High Voltage Engineering*, Pilsen, Republic Czech, 23 – 28 August 2015.
- [6] M. Aboshwerb, M. Albano, M., and A. Haddad, 'Fabrication of Nonlinear ZnO Microvaristor Field Grading Materials for High-Voltage Applications', in *Fifteen Universities High Voltage Network - UHVNet 2023, Colloquium on Technologies for Advances in Insulation Technologies and High Voltage Phenomenon*, Glasgow, UK, 17 February 2023.
- [7] COMSOL Multiphysics. User's Manual, Version 5.5; COMSOL AB: Stockholm, Sweden, 2019.
- [8] M. M. Tousei and M. Ghassemi, 'Combined geometrical techniques and applying nonlinear field dependent conductivity layers to address the high electric field stress issue in high voltage high-density wide bandgap power modules', *IEEE Trans Dielect Electr Insul*, vol. 27, no. 1, pp. 305–313, Feb. 2020. doi.org/10.1109/TDEI.2019.008493
- [9] J. Song, C. Li, L. Lin, Z. Lei, X. Bi, and H. Yang, 'Slot discharge pattern of 10 kV induction motor stator coils under condition of insulation degradation', *IEEE Trans Dielect Electr Insul*, vol. 20, no. 6, pp. 2091–2098, Dec. 2013. doi.org/10.1109/TDEI.2013.6678857
- [10] F. Greuter et al., 'Microvaristors: Functional Fillers for Novel Electroceramic Composites', *J Electroceram*, vol. 13, no. 1–3, pp. 739–744, Jul. 2004. doi.org/10.1007/s10832-004-5185-9
- [11] B. Boettcher, R. Lietzke, G. Malin, R.P. Glembocki, and M.H. Spalding, 'Electrical insulators, materials and equipment'. United States Patent 6864432, 2005.
- [12] IEC 60507:2013, Artificial pollution tests on high-voltage ceramic and glass insulators to be used on a.c. systems.
- [13] IEC 60137:2017, Insulated bushings for alternating voltages above 1000 V.
- [14] Z. Ahmed, 'Analysis of Partial Discharge in OIP Bushing Models', Electromagnetic Engineering School of Electrical Engineering, Kungliga Tekniska Hogskolan, Stockholm, 2011.



Cynhadledd Ymchwil
Peirianeg Caerdydd

Cardiff Engineering
Research Conference

School of Engineering
Cardiff University
Queen's Buildings
The Parade
Cardiff, CF24 3AA